The Evolution and Structure of Composite Meso-Alpha-Scale Convective Complexes

By
Ming-sen Lin

Department of Atmospheric Science
Colorado State University
Fort Collins, Colorado

Colorado State University

Department of Atmospheric Science

Paper No. 721

THE EVOLUTION AND STRUCTURE OF COMPOSITE MESO-ALPHA-SCALE CONVECTIVE COMPLEXES

by

Ming-Sen Lin

Research supported by the

National Science Foundation
under Grants ATM-8113082, ATM-8312077 and ATM-8512480

Department of Atmospheric Science
Colorado State University
Fort Collins, Colorado

Atmospheric Science Paper No. 404

ABSTRACT OF DISSERTATION

THE EVOLUTION AND STRUCTURE OF COMPOSITE MESO-ALPHA-SCALE CONVECTIVE COMPLEXES

The CSU Regional Atmospheric Modeling System (RAMS) data assimilation and analysis package is implemented to study the evolution and the structure of composite Meso-α-scale Convective Complexes (MCCs). Seven years of North American MCC cases are sampled and normalized into seven evolutionary sub-periods according to the temporal life-cycles of the storm systems.

The composite MCC shows some general features, such as the lower-tropospheric convergence and cyclonic vorticity associated with the upper-tropospheric divergence and anticyclonic vorticity during the MCC's initial to mature stages, the cold-core structure in the upper troposphere, and the characteristic warm core at middle levels. The low-level convergence, aligned with the intensified cyclonic vorticity, lifts and extends to the middle troposphere at the mature stage. A middle-level jet-like inflow is accompanied by a strengthening middle-level convergence which reaches its maximum intensity at the MCC's mature stage. This middle-level jet-like inflow, located slightly above the melting layer and near the lowest θ_e level which might reinforce the downdraft.

The vorticity budget of the composite MCC shows that the residual of grid-scale vorticity exhibits a vorticity sink in the lower troposphere and reaches its maximum intensity at the MCC mature stage. On the other hand, a mid- to upper-level vorticity source exists during the MCC early and dissipation stages. The imbalance can be attributed to

the removal of vorticity-rich air from low levels and its upward transport and deposition aloft by convection.

The composite MCC exhibits a apparent heat source of 10-20° day^{-1} at about the 400 mb level and a moisture sink of -9 to -14° day^{-1} equivalent heating below the 700 mb level throughout most of the MCC life-cycle. The water vapor budget of the composite MCC indicates that water vapor is mainly provided by MCC-scale convergence and the atmospheric storage term. At the MCC mature stage, the precipitation efficiency reaches 113% such that the moist atmosphere provides an extra 13% from its storage, which is accumulated from the MCC early stages.

A hypothesized MCC evolution obtained from this composite study suggests that for system development to occur, the low-level convergence must be aligned horizontally with the cyclonic vorticity pattern in the presence of larger Convective Available Potential Energy and/or smaller vertical wind shear.

Ming-Sen Lin
Dept. of Atmospheric Science
Colorado State University
Fort Collins, Colorado 80523
Fall 1986

ACKNOWLEDGEMENTS

I would like first of all to express my appreciation to my dissertation advisor, Professor William R. Cotton, for his continued support, guidance, and encouragement throughout the course of this research. He and the other committee members, Professors William M. Gray, Roger A. Pielke, and Robert N. Meroney, also made valuable suggestions and constructive criticisms which have helped to fulfill the study and to shape the final version of this manuscript.

Significant contributions from a number of other individuals helped make a comprehensive study such as this possible. I owe a great deal of thanks to Professors Wayne H. Schubert, Richard H. Johnson and Paul W. Mielke for their stimulating discussions during the research. Mr. Craig J. Tremback is gratefully acknowledged for assistance with and suggestions concerning data assimilation and objective analysis. My appreciation is also extended to Mr. Ray McAnelly for his cooperation in sampling MCCs, allowing me to use his composite MCC precipitation, and comments on the dissertation draft. I am indebted to Dr. Robert A. Maddox, Mr. Dennis M. Rodgers, and Mr. John Augustine of NOAA-ERL for kindly allowing me to use their satellite images during the study. I would also like to express my appreciation to Mr. Mike Moran for his considerable help in proof reading and correcting the dissertation draft. Mrs. Brenda Thompson and Ms. Annette Claycomb contributed to the manuscript preparation and editing, also Ms. Judy Sorbie and Mrs. Lucy McCall helped in drafting figures appearing in this dissertation. Finally, I wish to thank my wife Sue and son Ben for their continuous encouragement and forbearance during my doctoral program.

The Central Weather Bureau and the National Science Council of the Republic of China initially supported me in this study. Primary support for this research was obtained by the U.S. National Science Foundation under Grants ATM-8113082, ATM-8312077 and ATM-8512480. All computations were performed on the National Center for Atmospheric Research (NCAR) Cray-1A computers. NCAR is supported by the National Science Foundation.

TABLE OF CONTENTS

LIST OF TABLES

LIST OF FIGURES

LIST OF SYMBOLS AND ACRONYMS

Symbol or Acronym	Meaning
AIMCS	Airborne Investigations of Mesoscale Convective Systems
CAPE	Convective Available Potential Energy
CCOPE	Cooperative COnvective Precipitation Experiment
CISK	Conditional Instability of Second Kind
DR	Decay Region
EL	Equilibrium Level
EMCC	Eastern Mesoscale Convective Complex
ERL	Environment Research Laboratory
f	Coriolis parameter
FCE	Flux Convergence of available moist static Energy
GARP	Global Atmospheric Research Program
GATE	Global Atmospheric Research Program's Atlantic Tropical Experiment
GMT	Greenwich Mean Time
GR	Genesis Region
h	hour
H	scale height of circulation
IR	InfraRed
ITCZ	Intertropical Convergence Zone
km	kilometer
kPa	kiloPascal
L	physical scale length of system
LCL	Lifting Condensation Level
LFM	Limited Fine Mesh model

$\underline{U}$	density-weighted mean wind speed taken over the lowest 6 km minus the mean wind speed taken over the lowest 0.5 km
V	rotational component of wind
WMCC	Western Mesoscale Convective Complex
WMONEX	Winter Monsoon Experiment
WRP	Weather Research Program
Z	Zulu time, same as GMT
z	height, the vertical coordinate
%	percentage
o	degree
^{o}C	degree Celsius
θ	potential temperature
θ_e	equivalent potential temperature

1.0 INTRODUCTION

During the months of June, July, and August, a period of the year when daytime convective precipitation might be expected to dominate, more than 60% of all precipitation falls between the hours of 2000 and 0800 local time within an area covering Nebraska, Kansas, Iowa, and northern Missouri (U. S. Weather Bureau and U. S. Corps of Engineers, 1947). Although some investigators have assumed that certain physical mechanisms must act to trigger storms *in situ*, satellite imagery clearly illustrates the frequent movement of meso-α-scale convective complexes (MCCs) across this region during the nighttime (e.g., Maddox 1980, 1981; Bosart and Sanders 1981; Cotton *et al.*, 1983a).

MCCs are the source of many summertime severe weather events across North America. Maddox *et al.* (1979) found that significant flash floods in the eastern two-thirds of the U. S. often occur during the nighttime hours of the summer season, and they suggested that MCCs are largely responsible for this nocturnal flash flood phenomenon. A climatology of heavy precipitation events investigated by Crysler *et al.* (1981) also showed that heavy precipitation events in Missouri and Illinois had a maximum frequency near local midnight -- the time when MCCs normally reach their mature stage. Despite the benefits of significant rainfall, a variety of severe convective phenomena, including hailstorms, tornadoes, electrical storms, and high winds, accompany MCCs and may inflict a broad range of damage on industry, commerce, and agriculture throughout the High Plains during the summer season.

Moreover, quantitative precipitation forecasts associated with MCCs have been a particularly difficult problem for operational numerical weather prediction models. Maddox et al. (1981) claimed that even if synoptic-scale predictions are essentially correct, corresponding forecasts of the resulting weather can still fail miserably. They found that LFM model predictions not only did not correctly forecast the impact of organized, intense convective storms on the 500 mb level vorticity and 200 mb level wind fields, but they also provided very poor quantitative precipitation predictions while the MCC developed. The problem of forecasting and understanding the development, movement, and eventual demise of intense convective weather systems has been considerably complicated by the fact that the spacing of conventional upper air observations has been far too coarse to observe the life-cycle of such systems adequately. For instance, the separation of rawinsonde stations is about 400 km, but the atmospheric circulations and features associated with MCC convective weather are on the scale of 10-500 km. These scales are usually detected by satellite or radar, but are not clearly defined by the traditional rawinsonde data set alone.

As to the predictability of MCCs, there still exist some controversies. Cotton (1983) noted that it is possible that "once the synoptic scale conditions set up a region which is ripe for the genesis of MCC's, any random set of diurnally-forced convective events could lead to the explosive development of an MCC." If indeed this is the case, then the prediction of the genesis is likely to be a tractable problem for us. However, "if it is necessary to predict the initiation and evolution of the meso-β-scale disturbances, their merging processes,

etc.", then the prediction of MCC genesis represents a major challenge to meteorologists.

The research described herein is an attempt to understand the physical processes of the MCC evolution via a composite study. The fundamental assumption is that a composite analysis technique can be used to detect the dynamic and thermodynamic mechanisms which control the MCC life-cycle. It was postulated that an MCC forms in an environment with synoptic- to meso-α-scale forcing having sufficient moisture and potential instability to generate convective clouds and to provide for their up-scale development. Thus, MCCs result from quasi-stationary frontal or upslope flow which could produce the widespread lifting needed to release existing potential instability. Furthermore, some mesoscale mechanisms are needed to concentrate the favorable high moisture content and potential instability within a mesoscale region for MCC initiation and development.

A background review of MCC climatology, evolution, and structure is summarized briefly in Chapter 2. Data analysis and composite techniques are described in Chapter 3. In Chapter 4, the detailed MCC's climatology, kinematic structure, dynamics, and thermodynamics obtained from the composite study are presented. The evolution of the MCC's budgets are examined in Chapter 5. Some favorable conditions which were hypothesized to affect MCC genesis and development are then discussed in Chapter 6. A conceptual model of MCC evolution is presented in Chapter 7; and finally, conclusions and recommendations are given in Chapter 8.

2.0 BACKGROUND

A rigorous dynamical definition of the MCC has yet to be adopted. The term, MCC, first defined by Maddox (1980), refers specifically to a system of intense convection which is characterized by a particularly large, long-lived, cold-topped, and quasi-circular thick stratiform cloud as observed by satellite. Thus, MCCs represent a relatively consistent, better-defined, and probably more significant subset of mesoscale convective systems (MCSs), a term that is defined only generally by the scientific community as referring to any system of intense convection which is organized on the mesoscale.

2.1 MCC climatology

What are some of the climatological characteristics of MCCs? According to Maddox's (1981) definition of an MCC, the areal extent of infrared (IR) temperature $\leq -32^{o}C$ and $\leq -53^{o}C$* must be $\geq$ 100,000 and $\geq$ 50,000 km^2, respectively, for a period $\geq$ 6 hours. Furthermore, the eccentricity (minor/major axis ratio) of the cloud shield must be $\geq$ 0.7 at the time of maximum size. Based on these areal and temporal criteria, he found that about one-third of the MCCs he examined (23 of 71 cases) had their origins over the Rocky Mountains or their eastern slopes (such systems are referred to as "orogenic" in this study, i.e., "mountain-born"). The other two-thirds of his MCCs (48 of 71

---

* From an enhanced MB curve described by Clark (1983), the value should be $-53^{o}C$ instead of $-52^{o}C$

cases) initiated over the Plains. The preferred location for MCC occurrence was over the south-central states during April to June. As the warm season progressed, the favored region shifted slowly northward; by July and August the systems primarily affected the north-central states.

In addition, Maddox found that the average times of occurrence of the MCC's first thunderstorms, MCC initiation, maximum extent, and termination were 2000, 0145, 0730, and 1230 GMT*, respectively (1400, 1945, 0130, and 0630 LT, respectively). He emphasized that the first thunderstorms typically developed during the afternoon, and an average of 16.5 hours elapsed between the development of the first thunderstorms and the beginning time that the MCC decayed. In the same study, he noted that the average area of cloud top temperature $\leq -32\ ^{o}C$ at maximum extent was $300 \times 10^3\ km^2$.

2.2 Similarities and differences between MCCs and other MCSs

Meso-α-scale (Orlanski, 1975), convectively-driven weather systems can be further classified according to their physical characteristics and organization as "linear types" and "circular types". Bosart and Sanders (1981), Maddox and Doswell (1982), and Wetzel et al. (1983) suggested that the continental middle-latitude MCC was in many large-scale aspects more akin to the oceanic tropical cloud cluster (Williams and Gray, 1973; Ruprecht and Gray, 1976; Gray and Jacobson, 1977; Frank, 1978; McBride and Zehr, 1981; Tollerud and Esbensen 1985; Lee, 1986) than to the meso-α-scale mid-latitude squall line. They confirmed that MCCs and tropical cloud clusters have similar structures such as

---

* Local Central Standard Time (LT) is 6 h earlier than the universal time convention used throughout this paper.

overshooting top echoes and thick stratiform precipitation clouds shield associated with the middle to upper tropospheric mesoscale updrafts. They also demonstrated that these two systems exhibit a general convergence throughout the lower to middle troposphere, and they showed that a narrow layer of relatively strong divergence centered around 200 mb level is associated with the storm outflow. Wetzel et al. (1983) noted that both systems attained their maximum upward vertical motion in the upper troposphere. Maddox (1981) pointed out that MCCs, like tropical cloud clusters, exhibit a warm core in the middle to upper troposphere related to cumulus heating plus strong subsidence warming. Gray and Jacobson (1977) and McBride and Gray (1980) presented evidence and showed that tropical cloud clusters reach maximum intensity in the early morning; McAnelly and Cotton (1986) found similar results for MCCs. Moreover, Wetzel et al. (1983) emphasized that MCCs and tropical cloud clusters generally exist in an environment having a weak north to south temperature gradient, such that meridional sensible heat transport is slight and the system is quasi-barotropic. In general, it is fair to conclude that MCCs are something of a hybrid but are basically more like tropical cloud cluster systems than mid-latitude linear systems.

When contrasting MCCs with other MCSs, Maddox (1981, 1983), Fritsch and Maddox (1981), Sanders and Emanuel (1977), and Ogura and Liou (1980) revealed that MCCs had distinctly different dynamical structure and characteristics from the squall line. Often, strong forcing by vigorous baroclinic waves with embedded surface fronts and jet streams forces primarily squall-line-type organized convection. To some extent, the pre-frontal squall line and the MCC represent opposing ends of the spectrum of mesoscale system types. In general, a severe pre-frontal

squall line system is associated with a strong vertical wind shear throughout the lower- to middle-atmosphere and with the line of active convective cells oriented perpendicular to the lower-level wind shear (Klemp and Wilhelmson, 1978). This contrasts to an MCC which occurs in a weakly sheared environment and in which the active convective cells are aligned in a variety of patterns (e.g., arc-shaped or popcorn convection pattern described by Leary and Rappaport, 1983) including parallel to the mid-level steering winds (Maddox, 1981). Furthermore, pre-frontal squall lines are commonly associated with a stronger inflow in the lower troposphere and outflow in the upper-level troposphere than are MCCs. The squall line also has significantly drier air (low θ_e) in the mid-level of the troposphere, and are found to be vertically tilted upshear.

2.3 Synoptic- to meso-β-scale features during MCC evolution

A frequent question related to MCCs is why do "look-alike" synoptic settings sometimes support development of an MCC, but sometimes not. What are the major dynamic and thermodynamic factors controlling the gensis and development of MCC's? The evolution of an MCC from its initiation through maturity to decay involves not only the synoptic- to meso-α-scale, but also the finer meso-β-scale features.

Conceptually, the evolution of any MCS depends on at least four components: moisture content, conditional and potential instability, lifting mechanisms, and the up-scale development (organization) of neighboring meso-β-scale convective elements.

2.3.1 Moisture content

The importance of low-level moisture convergence to the amount and intensity of convective rainfall is well known (e.g., Frank, 1978;

Ulanski and Garstang, 1978; Tripoli and Cotton, 1980; Tao and Simpson, 1984). Frank (1978) found that large-scale convergence precedes the formation of MCSs observed in the GATE area by several hours. He suggested that the large-scale convergence favors the buildup of mid-level moisture which allows the convection to survive the drying influences of entrainment. Ulanski and Garstang (1978) revealed that surface convergence patterns nearly always precede the development of convective radar echo for periods as long as 90 minutes over southern Florida. They suggested that the most crucial factor in determining the amount of rainfall produced by a given storm was the size of the area of surface convergence. Based on investigations begun by Culverwell (1982), Cotton et al. (1983a) investigated an episode of 1977 in which MCCs occurred on 8 consecutive days. They found that the presence of a deep moist atmosphere, that is, a low-level flow of high moist content associated with a mid-level flow of monsoon-like circulation, helped to sustain the MCCs.

In order to efficiently support the large-scale moisture content to develop an MCS, much of the moist inflow needs to be narrowed into meso-α- to meso-β- scaled regions. This process is performed through some forcing mechanisms (discussed in Section 2.3.3) such that a narrow favored region is provided for helping MCC development. For instance, Banta (1984) and Banta and Barker (1984) claimed that a "leeside convergence zone" propagated eastward from the Rockies against the prevailing upslope flows and was deemed to be responsible for the initiation and maintenance of cumulus cloud resulting in the development of MCS. Toth and Johnson (1985) also found that the mesoscale convergence zone to the lee of mountain barriers, operating on both the

scales of ridge/valley and Rocky Mountain barriers/eastern High Plains, acted as a triggering mechanism for late afternoon thunderstorms. Purdom and Marcus (1982) postulated that cumulus-scale moisture convergence resulting from cloud mergers or from the intersection of thunderstorm outflow boundaries could contribute to the concentration of moisture content for up-scale development.

2.3.2 Conditional and potential instability

Wallace and Hobbs (1977) stated that potential (convective) instability occurs when the top part of a moist air layer cools much more rapidly through dry adiabatic lifting than the bottom part, and the lapse rate quickly becomes destabilized. Therefore, sufficient lifting may cause the layer to become conditionally unstable, even if the entire sounding is relatively stable to begin with. On the other hand, if the actual lapse rate of the atmosphere lies between the saturated adiabatic lapse rate and the dry adiabatic lapse rate, a parcel of air that is lifted sufficiently far above its equilibrium level will become warmer than its environment and behave as conditionally unstable. Fritsch and Chappell (1980) calculated the Convective Available Potential Energy (CAPE, i.e., the positive area of an environmental sounding) and found that it is closely related to the intensity of cumulus convection or conditional instability. On a larger scale, Maddox and Doswell (1982) showed that for MCCs the strong large-scale, low-level warm advection was pronounced near 700 mb level, and they pointed out that the unstable air to the south and east of an MCC accounted for MCC development. Maddox (1981) claimed that the mesoscale convective systems which developed within a relatively weak and stagnant large-scale setting were usually closely linked to the eastward progression of a weak middle

tropospheric short-wave trough which transported cool air aloft to destabilize the atmosphere. These studies imply that the formation of a mesoscale convective system is favored by processes which transport warm moist air into the lower level or cold dry air into the upper level of a particular region and concentrate the potential instability into a mesoscale area.

2.3.3 Lifting mechanisms

The elegant review by Emanual and Sanders (1983) suggested that some kind of synoptic to mesoscale lifting mechanisms were imperative for an organized convective system to be formed from sporadic cumulus and to develop into a long-lasting system. The following forcing mechanisms were considered to represent some of the possible candidates.

(a) Baroclinic frontal system: Maddox (1983) illustrated from his composite study that MCC formation took place within a region of preexisting weak frontal forcing which provided a region of low-level convergence. In fact, 47% of the cases of MCCs studied by Merritt and Fritsch (1984) were found to occur along or adjacent to a stalled frontal zone. However, Wetzel et al. (1983) did emphasize that an MCC was a quasi-barotropic system which transported little sensible heat meridionally. Although an MCC might be compatible with a certain amount of baroclinicity, it is believed that the MCC would be modified rapidly as baroclinicity increases. Particularly, given a strong vertical wind shear, the convection tends to organize itself more into either the classical squall-line structure studied by Palmen and Newton (1969) or the more comma-shaped cloud patterns described by Reed (1979).

(b) Mid-level short-wave trough: Maddox (1981) indicated that the initiation and development of an MCC is closely tied to the eastward

progression of a weak middle-tropospheric short-wave trough. He even illustrated that the advancing mid-level short wave associated with positive vorticity advection could serve solely as a forcing mechanism without the accompaniment of a surface front.

(c) Upper jet streak and low-level jet (LLJ): Because the warm air advection caused by the low-level jet and the cold air advection caused by the upper jet streak both provide a destabilizing influence conducive to the occurrence of thunderstorms, both jets have been connected to MCS initiation in the literature since Newton (1950). Moreover, the moist air advected by the LLJ provides a source of conditional instability. Uccellini and Johnson (1979) and Brill et al. (1985) further confirmed that the coupling of an upper jet streak and LLJ is sometimes responsible for the initiation of a mesoscale system. Matthews (1983) concluded that what he called a mesosynoptic event was favored in the vicinity of maximum lifting associated with upper jet streak divergence in the entrance (right rear quadrant) and exit (left front quadrant) regions. However, it has been rather clearly shown that the nocturnal precipitation maximum is related to the LLJ (Means, 1952; Blackadar, 1957). Although the strength of the MCC is usually modulated by the moisture and momentum source of the LLJ (Maddox, 1985), the inertial oscillation causes the LLJ to veer with time but the convergence into the system to decrease; hence, the MCC decreases in intensity and often dissipates by the early morning.

As a matter of fact, Maddox (1980, 1983) and Wetzel et al. (1983) have explained that the LLJ could provide a mechanism for focusing the moisture, mass, and heat into a narrow zone; then the mechanism induces sufficiently large vertical motion to release the convective

instability, which benefits initiation or intensification of the mesoscale system. Bosart and Sanders (1981) proposed a mechanism in which a transverse circulation in the lower tropospheric jet gave positive feedback between the convection and the warm moist air feeding it. In addition, the nocturnal LLJ could serve as a conveyor belt and provided a steady, high-speed influx of low-level moisture just above the nocturnal inversion.

(d) Topography: Although there still exists some suspicion that MCC formation could be directly initiated by the convergence of dry Rocky Mountain westerly downslope flow with potentially unstable southerly flow off the Gulf of Mexico (or with easterly diurnal upslope flow), there is no doubt that steep topography plays a role in promoting the onset of severe weather events. The pervasive feature of local hot spots, arising from peculiarities of the rugged terrain (Cotton et al., 1983a), triggers convection in Colorado and with it the potential for development into an MCC. Topography is also capable of inducing some local wind circulations thermally or mechanically, such as daytime upslope flow, nocturnal downslope flow, and mountain lee waves. These local wind systems may ultimately lead to the formation of MCSs (Tripoli, 1986).

(e) Gravity wave interaction: Gravity waves can interact with convective systems synergistically, sometimes producing convection, but usually convection can initiate gravity waves. Uccellini (1975), for instance, has shown that gravity waves can initiate convective storms. Also, Tripoli (1986) implicated gravity oscillations in the forcing of meso-β convective elements.

(f) Outflow boundary and density current: Purdom (1976) and Purdom and Marcus (1982) used satellite imagery to show that collisions of the thunderstorm outflow boundaries from previous convection could be responsible for initiation of new convection and for subsequent thunderstorm formation. Additionally, the density current (Charba, 1974), produced when a cold shallow pool of air spreads laterally by the force of gravity and lifts relatively warm air as it moves, could force convection and serve as a meso-β or meso-α discontinuity for developing a mesoscale system.

(g) Symmetric instability: Nehrkorn (1985) used a Wave-CISK model as the basis to show that symmetric instability could contribute significantly to developing a mesoscale mode with a maximum growth rate.

2.3.4 Up-scale development of neighboring meso-β-scale elements

Besides the aforementioned moisture content, conditional and potential instability, and lifting mechanisms, preexisting meso-β systems are necessary for the initiation and development of the MCC. Indeed, these meso-β systems provide the mid-level heat source from which the mid-level cyclonic circulation could spin up (Tripoli, 1986). Cotton et al. (1983a) inferred the existence of a mountain-related wave disturbance which provides an organizing influence on convection. They hypothesized that solar heating along the Rocky Mountain barrier and/or in the Great Basin generates a convectively-reinforced wave disturbance which organizes convection on the meso-α-scale over high Plains. Wherever this eastward-propagating wave disturbance overlaps low-level conditions capable of supporting moist deep convection on the mesoscale, locally generated meso-β clusters converge and organize themselves as an MCS, thereby reinforcing the deep-tropospheric wave disturbance.

McAnelly and Cotton (1986) concluded that MCCs originating on the High Plains often develop from the growth, interaction, and merger of multiple discrete meso-β convective clusters. These meso-β components tend to originate along larger meso-α-scale features, such as the eastern slopes of the Rockies, surface troughs and fronts, extensive mesoscale outflow boundaries, and axes of residual convection and mid-level moisture. In fact, they emphasized that the region of most intense meso-β convective development and rapid MCC growth occurred near the point where two such meso-α features intersect.

Some processes thought to account for the merger of meso-β-scale elements are:

(a) Storms decoupling from the surface: Schmidt (1985) studied a pair of CCOPE meso-β-scale storms and hypothesized that if the second storm was decoupled from the frictional surface by a cool surface layer, it might catch up with the first storm and result in a merger.

(b) Rear storm acceleration: Rockwood et al. (1984), in their study of a dual MCCs case, found that whenever the rear storm accelerated under the strong steering-level flow but the antecedent storm decelerated under the weak steering flow due to the resultant blocking of the storm ahead; it could cause a merger process.

(c) Mesocyclogenesis mechanism: Fritsch and Chappell (1980) demonstrated that certain configurations of convective activity might produce focused areas of forced subsidence warming aloft. The warming in turn would then cause an increase of thickness aloft, which creates a favorable circulation for mesocyclogenesis and an enhancement of the convection growth (Song, 1986). This mesolow area would be favored for the merger of meso-β-scale elements.

(d) Collision of thunderstorm outflow boundaries: Purdom and Marcus (1982) showed that either the outflow boundary of the previous thunderstorm convective lines or arc cloud lines might collide and merge, giving rise to intense convective development. Rockwood et al. (1984) presented a dual MCC case study and found that an intense meso-β-scale circulation resulted when the westward-moving outflow boundary from the first MCC collided with the eastward-moving flow from the second MCC and intensified the second MCC. Tao and Simpson (1984) found from their two-dimensional, multi-cell model that the most unfavorable environmental conditions for cloud merger are (1) weakly unstable stratification of the atmosphere and (2) weak large-scale lifting. They further pointed out that the dominant cloud merger mechanism is the cumulus downdraft and its associated cold outflow.

(e) Convection act with upslope flow: Tripoli (1986) pointed out that the low-level convergence between thermally generated slope flows and large-scale wind flows could act to initiate mountain convective systems.

2.3.5 Variations of moisture content, conditional and potential instability, and lifting mechanisms during the MCC MCC life-cycle

Moisture content, conditional and potential instability, lifting mechanisms, and up-scale development (organization) of neighboring meso-β-scale elements are favored overall during the initial and growth stages of MCCs, but these four components are unfavorable during the decay stage. For instance, at the initial stage, low-level southerly flow provides a large-scale influx of moisture concentrated into a mesoscale tongue of moist air (12-16 g kg^{-1}) from the Gulf of Mexico to

the eastern portion of the Genesis Region (GR) (Maddox, 1981). He also found that the atmosphere was distinctly moist over the eastern portion of the GR up to 500 mb level, which delineated a high moisture content. A distinct pocket of potentially very unstable air was present over the Plains. In his study, the other critical conditions include a pronounced LLJ (850 mb level wind speed > 20 kts) and an upper jet streak embedded within a weak middle tropospheric trough.

During the mature stage of an MCC, the aforementioned conditions seem to be effective and even more significant. For example, Maddox (1981) pointed out that the absolute moisture content increased significantly at low layers while the MCC reached its maturity. Moist air (RH > 85%) was transported vertically to 500 mb level through the convective towers. The stability analysis showed a much more stable air mass over the MCC Region (MR) resulting from precipitation stabilization, although forcing mechanisms were still strong enough to temporarily overcome the stability but the MCC gradually decayed. Also, the differential radiational cooling near the boundary of the MCC's dense cloud shield and surrounding clear areas might act to enhance the meso-circulations and to prolong the life of the system. Some intriguing features over the MR were pronounced, such as a substantially veering wind at 850 mb level, an amplified LLJ resulting from both the advance of the short-wave trough and inertial oscillation, an apparent low-level warm advection, and a distinct middle- to upper-level warm ridge.

Up to the decay stage of an MCC, there are significant changes related to the four processes favoring storm development. The system itself progresses into an increasingly unfavorable environment for deep

convection which inevitably leads to the demise of the MCC. For example, such environments are characterized by: 850-700 mb layer cool advection, absence of a pronounced LLJ at 850 mb level, a pronounced 500 mb level short-wave trough (i.e., baroclinicity is too strong), and 300 mb level up-gradient flow associated with a less pronounced anticyclonic jet streak.

2.4 MCC structure

Recently, scientific, engineering, and numerical modelling technology has progressed enough to make it feasible to simulate mesoscale convective systems. Modelling results from Fritsch and Chappell (1980), Fritsch and Maddox (1981), Perkey and Maddox (1985), Zhang and Fritsch (1985), and Tripoli (1986) have shown the possibility of using a numerical model to make inferences about the dynamical structures and evolution of a middle-latitude convective system. Nevertheless, the major findings concerning MCC structure are still deduced from observations. Maddox (1981) performed an objective analysis of composite meteorological conditions attendant to ten MCC weather systems. Some of the more important aspects of the structure of the mature MCC weather system are as follows:

(a) MCC relative inflow enters the system from all sides within the lower half of the troposphere (especially near 700 mb level); however, the system is not directly coupled to the surface layer.

(b) MCC relative flow at middle levels is quite weak, since the system is moving nearly with the middle tropospheric flow. In the upper troposphere, relative flow diverges around the system and is much stronger downwind than upwind. Occasionally, mid-level jets of low θ_e

air can be seen entering the storm (Wetzel et al., 1983; Gamache and Houze, 1985; Chen, 1986).

(c) The strongest convective elements often occur within the right-rear quadrant of the system, occasionally assuming line orientations parallel to the system's direction of movement.

(d) A large region of lighter precipitation and showers also occurs, usually to the left of the region of intense convection, within the area of mean mesoscale ascent.

(e) The MCC occurs within a region of strong warm advection and significant convergence at the nose of a southerly low-level wind maximum.

(f) The system is cold-core within a shallow boundary layer, warm-core through much of the mid-troposphere, and then cold-core again in the upper troposphere.

(g) The thermal structure produces a mesohigh within the boundary layer, a mesolow just above the mesohigh, and an upper tropospheric mesohigh capping the system. The mesolow acts to enhance inflow into the system, while the upper mesohigh tightens the height gradient along the northern edge of the system and helps an intense anticyclonically-curved outflow jet streak to form.

Cotton et al. (1983a) and Wetzel et al. (1983) investigated various meso-β-scale aspects of an MCC within the context of its convective to meso-α-scale evolution and found a structure similar to Maddox (1981), but they also found that:

(h) Mid-level divergence fields show a convergence/divergence couplet centered upwind of MCCs and separated by an east/west line of null divergence. This feature is found to be a manifestation of a

cross-contour flow toward higher heights, which seems to represent the rigorous adjustment process as mid-level air encounters the "obstacle" of the MCC.

(i) MCCs develop vertical velocities comparable in magnitude to developing middle-latitude winter cyclones, but without any of the characteristic features associated with cyclogenesis, such as decreasing surface pressure and northward transport of sensible heat.

From vorticity studies, Bosart and Sanders (1981) found that

(j) An MCC develops in association with a cyclonic circulation of substantial intensity in the lower and middle troposphere, and an anticyclonic circulation in the upper troposphere.

2.5 MCC-related precipitation pattern

The precipitation produced by an MCC is largely confined to the meso-β convective features. An analysis of their hourly precipitation characteristics by McAnelly and Cotton (1986) revealed a consistent, well-defined precipitation life-cycle relative to the MCC's satellite appearance. Generally, the precipitation rate increased throughout the initial development stage and reached a peak near the meso-α "cellular" appearance. During the cellular stage, the volumetric rain rate of the MCC reached a well-defined maximum; then shortly after this maximum, the MCC reached its maximum size and lost its organized meso-α-scale "cellular" appearance. The active rain area continued to expand for a short time, indicating a prolonged, weakening mesoscale circulation.

Kane et al. (1985), studying the precipitation characteristics of mesoscale convective weather systems, found that most of the heavy precipitation occurred between the time of MCC initiation and

maturation. They further disclosed that, in the right rear quadrant, 96% of the events produced $\geq$ 26 mm of rain over 58,000 km^2 and 85% of the events produced $\geq$ 51 mm of rain over 23,000 km^2. Also, they noted that every MCC produced $\geq$ 26 mm of rain over an average area of 112,000 km^2, and 95% of the events produced $\geq$ 51 mm of rain over an average area of approximately 34,000 km^2. Maddox (1981) showed that the composite MCC produced an average precipitation of 20 mm in an average rain rate of 1.66 mm/h.

2.6 MCC energy and moisture budgets

Very few kinetic energy studies have considered the subsynoptic scale, mainly due to the lack of appropriate data, as indicated by Fuelberg and Jedlovec (1982). The kinetic energy budgets of an MCC studied by Maddox (1981) showed that the residual term resulting from all the subgrid effects including friction was very large and the physical interpretation very difficult because the temporal evolution of these systems was extremely non-steady. Fuelberg and Printy (1984) studied the kinetic energy budget of meso-β-scale severe storms and showed that the mesoscale wind maximum formed in the upper troposphere on the poleward sides of convective areas, whereas speeds decreased south of the storm region. They further explained that there existed a strong generation of kinetic energy north of the storm by cross-contour flow, this being the primary mechanism by which the upper-level jet was formed. By the same token, there was a strong destruction of kinetic energy south of the storm.

In terms of the moisture budget, Maddox (1981) revealed that during the genesis period a significant increase in water vapor in the lower level results from vapor convergence. At the time of the MCC, a

significant rate of increase in the amount of moisture from the surface up to 500 mb level results from advection and convergence. After the system has decayed, advection is counteracted by divergence in lower levels, while the converse is true in the mid-level troposphere. Maddox showed that the MCC system processed nearly twice as much water vapor as was supported by its large-scale environment, probably through the localized regions of strong low-level inflow.

2.7 Problems to be solved

Based on this review, it is apparent that there is a number of ways in which Maddox's (1983) composite analysis could be extended. These posibilities are as follows:

(1) The composite data sample he employed could be expanded to include a statistically representative number of cases (Maddox's results are based on only 10 systems).

(2) The methodology for compiling data from Genesis Region, MCC Region and Decay Region (GR, MR, and DR of his study) needs to be refined. Maddox simply assumed 00Z to be the MCC generation stage, 12Z to be the mature stage, and 00Z of the next day to represent the decay stage. This approach can be refined to increase the temporal resolution by normalizing the MCC life-cycle and dividing it into more sub-periods.

(3) Maddox's MCC relative flow calculation simply assumed the analysis grid to move at the average velocity of his ten systems. He adopted the systems' motions as determined by tracking the centroid of the $-32^{o}C$ cloud shield during a 6-hour period, centered upon the time of the MCC's maximum extent. Such averaging of system motion has serious problems when the system undergo a curved or accelerated/decelerated

motion. Therefore, it can be improved by taking the benefits of ample data and precise MCC tracks.

(4) More detailed dynamic and thermodynamic structures in the context of finer temporal and spatial resolutions can be improved to produce a more thorough understanding of the MCC.

In this comprehensive study, it is attempted not only to compile a large amount of data for composite analysis, but also to categorize the MCC's life-cycle into 7 sub-periods. Based on these composite structures, we can create some hypothetical favorable conditions for MCC genesis and development as well as develop a conceptual model for MCC evolution.

2.8 Summary

In this background chapter, the results obtained in previous studies of MCCs were briefly reviewed. It is suggested that the definition of a "classical" MCC should meet the conditions for areal extent and shape of the thick stratiform cloud shields as discerned from IR satellite images. It is also recognized that the MCC is in many large-scale aspects more akin to the tropical cloud cluster than to the pre-frontal, mid-latitude squall line system. Indeed, MCCs are somewhat of a hybrid system, but they are basically tropical in nature, distinctly differing from the squall line by having weak vertical wind shear, weak baroclinicity, and absence of the pronounced lower to middle tropospheric dry layer.

Furthermore, in this chapter we discussed the importance and variations of the four controlling factors concerning the evolution of any MCS, namely moisture content, conditional and potential instability, lifting mechanisms, and the up-scale development (organization) of

neighboring mesc-β-scale convective elements. Next, the MCC kinematic structure, dynamic and thermodynamic features, and MCC-related precipitation patterns were considered to reveal the relevant characteristics of MCC evolution. Mention was also made of the controversies surrounding the predictability of MCCs and its important contribution to kinetic energy and moisture budgets. Finally, an approach to refine the previous research and to understand MCC evolution via a composite analysis were presented.

3.0 PROCEDURE

The philosophical approach of this research is to employ an objective analysis technique that will produce a composite of the synoptic- to meso-α-scale structure of an MCC during its evolution.

3.1 Objective definition of an MCC

In this study, Maddox's (1981) definition of an MCC was slightly modified by using the $-53^{o}C$ IR temperature area as the sole basis for identification. Although Maddox (1980) used both $-32^{o}C$ and $-53^{o}C$ IR temperature areas as criteria for his composite analysis, analyses of hourly precipitation data by McAnelly and Cotton (1986) and Kane et al. (1985) strongly suggested that the $-53^{o}C$ area correlated well with the active rainfall rate and appeared to be the core of the MCC. On the other hand, the $-32^{o}C$ area was largely indicative of thick stratiform cloud. Therefore, based on these definitions of the $-53^{o}C$ area, the "initiation" of the mature MCC is defined as when the contiguous area within the $-53^{o}C$ IR isotherm first exceeds 50,000 km^2. An MCC is considered to have reached its "maturity" when this area attains its largest size. It "ends" or "dissipates" when this area again becomes less than 50,000 km^2.

3.2 Objective analysis and data assimilation

Daley (1984) pointed out that the main purpose of an objective analysis scheme is to implement a method for reducing the data errors and increasing the data resolution for further data assimilation. The observational data usually contain errors which could result from

(1) problems with observing the system due to level of technical competence difference, instrument difference, and practice variance, or

(2) problems with communication due to coding and electronic features.

In addition to these errors, the distribution of observational data is usually non-uniform in space and time. Principally, by employing the objective analysis, we are trying to

(1) minimize the error through data-checking procedures and

(2) increase the data resolution through special data ingestion and interpolation procedures.

3.2.1 Objective analysis selection

Objective analysis provides numerical algorithms and methods used in the estimation of atmospheric state variables on 3- or 4- dimensional regular grids from data available at discrete locations and times. There is one generalized representation of an analysis process for which all individual schemes can be considered as linear transformations thereof. During the objective analysis, the instrumental or transmissional noises and scales which are not considered of interest are filtered out.

According to Daley (1984), there are five kinds of objective analysis methods used in operational numerical analysis schemes. In this research, we adopt the Barnes (1973) objective analysis method which is a successive correction method. Generally, the successive correction method does not take into account the redundancy of information, and it does not minimize the data error either. The scheme itself is simple, and no matrix inversion is involved; therefore, it is computationally inexpensive, which makes it attractive.

3.2.2 Barnes objective analysis

The Barnes (1973) objective analysis scheme, similar in some respects to the Cressman (1959) method, uses weighted averages of observed data to determine two-dimensional distributions of interpolated values at grid points. The scheme interpolates fields in an iterative fashion, and the attained convergence is a function of wavelength and the number of iterations.

Barnes assumes a continuum of observations regarding f(x,y), and filters these data according to their distance from an arbitrary point (x,y). That is,

$$g(x,y) = \int_0^{2\pi}\int_0^{\infty} f(x + r \cos\theta , y + r \sin\theta) w(r,k) r \, dr \, d\theta, \quad (1)$$

where r,θ are distance and position angle, and the weighting function is

$$w(r,k) = (1/ 4 \pi k) \exp(- r^2 / 4 k), \quad (2)$$

where k is an arbitrary parameter. We wish to determine the relationship between the observed value f and the weighted average value g at the same point. That is,

$$g(x,y) = D(a,k) f(x,y), \quad (3)$$

where D(a,k) is the response function and is wavelength-dependent.

Compared to the Cressman (1959) method, Barnes' method has four advantages:

(1) The weight factor can be chosen prior to the analysis so that pattern scales supportable by the data distribution will be revealed.

(2) The influence of data can be extended any distance without changing the weight function and the response characteristics.

(3) Small-scale irregularities are adequately suppressed by this technique, so that further smoothing by application of additional numerical filters is not necessary.

(4) The desired pattern resolution can be achieved in two passes, instead of the four or more required with Cressman's technique, thus effecting a modest saving in computer time.

Achtemeier (1986) further analyzed this successive correction technique for a limited-area dataset and revealed some important points:

(1) Data boundaries have an impact on the objective analysis by reducing the amplitude of long waves and shifting the phase of short waves.

(2) The distance that boundary effects intrude into the interior of the grid is inversely proportional to the weighting function shape parameter.

(3) The boundary effects intruded into the interior of the analysis domain a distance equal to the average separation between observations.

Therefore, in the analysis of the limited-area dataset used in this study, data were acquired over a larger domain in order to minimize the impacts of the boundaries' intrusion on the data field. For this reason, weighting coefficients for the Barnes scheme were chosen so that a 1500 km wavelength (after convertion of the 4k value to the equivalent wavelength, personal communication with Craig Tremback) retained 90% response (Fig. 3.1) while retaining less than 20% of the amplitude of 500 km wavelength features was retained so that undesired noise was filtered out. Also, a grid of 16^{o} latitude by 16^{o} longitude within a

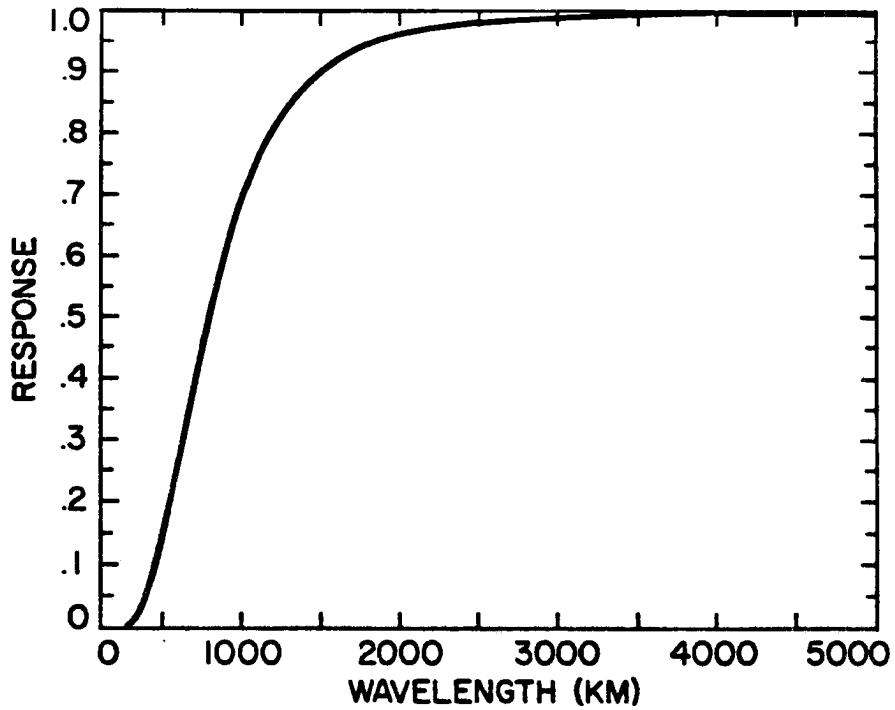

Fig. 3.1. Response curve for the filter used for the objective analyses of composite data.

60^{o} latitude by 60^{o} longitude area was analyzed to prevent boundary contamination.

3.2.3 Data assimilation and analysis

A package of data assimilation and analysis programs (Cotton et al., 1983b) has been designed and developed as part of the CSU Regional Atmospheric Modeling System (RAMS) to give a general and flexible data analysis system which produces data sets that can be used for synoptic- to meso-scale analysis. The updated version of the package has the ability to assimilate data from several sources: the National Meteorological Center's (NMC) 2.5^{o} latitude-longitude mandatory level pressure data, NMC mandatory and significant level rawinsonde reports, and U.S. Air Force 1^{o} or 30' average surface elevation data.

The data assimilation procedure is as follows:

(a) Access NMC 2.5^{o} pressure level data: these are originally hemispheric fields which are reduced to a domain and grid spacing that are specified by the user.

(b) Interpolate the NMC pressure level data onto the isentropic surfaces: interpolation combines the transformed NMC data with the surface elevation data to form a complete, synoptic-scale, 2.5^{o} latitude-longitude isentropic data set on the user-specified grid.

(c) Access the rawinsonde reports and interpolate onto the isentropic surfaces: options exist at this point to include specifying only a certain number of the NMC reports, eliminating any of the NMC reports, or including any special observations and bogus data at the analysis time which were not included in the NMC data set.

(d) Objective analysis: objective analysis could be done within the same or different resolution horizontal latitude-longitude grid. This

grid could be coarser than 2.5° for synoptic studies, or finer resolution for mesoscale analysis or model initialization. The objective analyses are done on the isentropic surfaces using the Barnes technique (details described in Section 3.2.2), utilizing both the selective rawinsonde reports and the 2.5° resolution data as observations. Optionally, the rawinsonde reports may be either exclusively or partially included in the objective analyses if the data coverage is adequate.

(e) Enhanced isentropic data set on latitude-longitude grid: this final product can be further analyzed and plotted or used as the initial conditions for a numerical model.

This data assimilation package was employed for each MCC case individually in the isentropic surface. It was then feasible to composite groupings of MCCs either in isentropic or other vertical coordinates. Because the MCCs frequently form over the Rockies and then move onto the High Plains over varying topography, the sigma-p coordinate (the surface and the tropopause pressure are chosen as lower and upper boundaries) is finally selected as the vertical coordinate for compositing, similar to McNab's (1976) budget study.

3.3 MCC composite analysis

In this section, the philosophy and the technique of composite analysis is outlined.

3.3.1 The philosophy of composite analysis

The idea of the composite algorithm used herein mainly follows from Gray et al. (1982), who have successfully carried out tropical composite analyses. They realized from experience that the best method of analyzing an atmospheric phenomenon from observations is to perform

detailed, quantitative case studies of a large sample of similar systems and then to statistically compare the cases. This provides information on both the mean characteristics and the variability of individual systems. Frequently, however, the observations have insufficient resolution to adequately depict perturbations created by a single disturbance.

One method of improving spatial data resolution is the compositing of data from weather systems showing similar behavioral characteristics. A composite analysis of a number of similar well-defined systems can present a clear, meaningful representation of the perturbations generated by such a weather system. A disadvantage of the method is that it tends to damp the magnitude of features present in individual situations so that characteristics of the composite system generally are not as intense as in the specific cases.

3.3.2 Composite analysis of temporal behavior of MCCs

The objective of this research is basically to expand and refine the results of Maddox's (1981, 1983) MCC composite studies. Generally speaking, his composite results were very coarse in temporal resolution, i.e., GR is similar to our pre-MCC and initial stages, MR to decay stage, and DR to about 10 hours after dissipation stage. The working hypothesis is: given enough MCC cases, their natural variability with respect to their time of occurrence will provide 0000 and 1200 GMT observations at many points along the generic MCC life-cycle for the standard upper-air observing times of 0000 and 1200 GMT. By compositing these observations into several time brackets spanning the system life-cycle, it is proposed that one can define the meso-α- to synoptic-scale life-cycle of MCCs.

Eight years (1977-1984) of MCC cases have been screened from data archived by Maddox's group at NOAA/WRP in Boulder. The detailed procedure of screening MCC cases is described in Appendix A, which also contains the basic characteristics and tracks of individual MCC cases. This study focuses on the MCCs occurring in June, July, and August; such a focus attempts to minimize the influences of strong baroclinicity as distinguished from the usual barotropic nature of the summer season. The first seven years of data are utilized for the composite sample, and the last year is reserved for testing the conceptual model originally. However, we found that there were not enough cases in certain MCC sub-periods for statistical significance; therefore some of the last year's data were also used for sampling. The cases have been screened according to how large and "classical" the MCC appears and by considering nearby meso-β- to meso-α-scale activity as undesirable "contaminants" to the meso-α environment of the MCC. According to an individual case's evolution, duration, size, cellular characteristics, and proximity to other mesoscale convection, each MCC was graded according to a subjective "MCC purity scale" with ten (0 to 9) categories for compilation purposes. For example, category 9 is reserved for the perfect MCC case, characterized by a large maximum cloud-shield size, a long mature duration, an ideal "cellular" appearance, little environmental contamination, and a clear evolution through its life-cycle. By the same token, category 0 is reserved for MCC case having a complex or "messy" evolution, an irregular "cellular" appearance, a short-lived mature diuration, and/or small cloud-top areal coverage at maximum extent. The "MCC purity scale" is

then used to distinguish between the organized MCCs (category 5 to 9) and the marginal MCCs (category 0 to 4).

Due to the natural variability of MCC's, some systems may be at, or two-to-four hours after or before MCC maturity at the time of standard 1200 GMT soundings are taken. Likewise, some systems may be at, or within several hours of initiation at the time of 0000 GMT. If a significant amount of MCC samples are compiled, each sub-period of MCC may occur within one and one half hours of either 0000 or 1200 GMT. Thus, a composite model of an MCC life-cycle can be obtained even though high time resolution soundings may be lacking (see Tables 3.2 and 3.3). Based on the "normalized" MCC temporal life-cycle, each MCC was then stratified into seven sub-periods: pre-MCC, initial, growth, mature, decay, end (dissipation), and post-MCC. The classification scheme is summaried in Table 3.1. Because the NMC pressure-level and rawinsonde data are only available at 0000 and 1200 GMT, cases selected for the same sub-period are always limited to either 0000 or 1200 GMT, in order to eliminate the diurnal variations discussed by Gray and Jacobson (1977). Each sub-period of the MCC life-cycle is roughly 2.5-3.0 hours long. Here, an extra period about 12 hour prior to the MCC initial stage is also included (i.e., MCC-12h) so as to be able to examine whether some synoptic conditions tend to occur prior to MCC initiation.

The MCCs' specific characteristics for these eight sub-periods are outlined in Table 3.2. Also, characteristics of the "marginal MCCs" sample set (detailed discussion in Section 4.1) are summarized in Table 3.3. Here, the position of each MCC's initial stage is used for the earlier "MCC-12h" stage in order to examine the presence of preexisting conditions. Since the individual MCC case may last more

Table 3.1. MCC life-cycle classification

Sub-period	Temporal Center of Sub-period	Remarks
MCC-12H	10-15 hours before INITIAL sub-period	Consists of data taken from the 12Z sounding (06 LT)
PRE-MCC	3 hours before INITIAL sub-period	Consists of data taken from the 00Z sounding (18 LT)
INITIAL	shield area $\geq 50 \times 10^3$ km^2 of $\leq -53^{\circ}$C IR temperature	Consists of data taken from the 00Z sounding (18 LT)
GROWTH	Mid-point between INITIAL and MATURE sub-periods	Consists of data taken from the 00Z sounding (18 LT)
MATURE	Maximum areal extent of region with $\leq -53^{\circ}$C IR temperature	Consists of data taken from the 12Z sounding (06 LT)
DECAY	Mid-point between MATURE and DISSIPATION sub-periods	Consists of data taken from the 12Z sounding (06 LT)
DISSI.	shield area $\leq 50 \times 10^3$ km^2 of $\leq -53^{\circ}$C IR temperature	Consists of data taken from the 12Z sounding (06 LT)
POST-MCC	3 hours after DISSIPATION sub-period	Consists of data taken from the 12Z sounding (06 LT)

than 12 hours from its pre-MCC to post-MCC stages, each of the MCC case can provide both of 0000 and 1200 GMT data for the different MCC sub-periods. Therefore, the total number of cases shown in Tables 3.2 and 3.3 usually exceed the real number of MCC cases.

The analysis procedure then utilizes the objective analysis and assimilation package of the CSU RAMS mentioned in Section 3.2.3. Each synoptic time (0000 and/or 1200 GMT) associated with an MCC has been grouped into one of the seven sub-periods. The initial isentropic objective analysis was done over a domain of 60° latitude-longitude, centered on the storm, with the purpose of displaying features within a central 16° latitude-longitude subgrid (Fig. 3.2).

Table 3.2. Characteristics of Organized MCCs grouped into sub-periods for 1977-1984 sample.

Sub-period	MCC -12H	PRE-MCC	INIT.	GROW.	MAT.	DECAY	DISSI.	POST-MCC	TOTAL
00 or 12 GMT	12	00	00	00	12	12	12	12	
No. of cases	22	12	31	8	8	17	20	18	136
Mean Rating	7.3	6.5	6.8	7.0	6.5	6.8	6.5	6.8	6.8
MCC latitude	42.3	42.2	42.3	42.4	42.3	42.2	41.9	41.6	42.2
MCC longitude	98.1	99.6	98.1	96.5	94.9	93.5	91.8	89.8	95.3

Table 3.3. Characteristics of Marginal MCCs grouped into sub-periods for 1977-1984 sample.

Sub-period	MCC -12H	PRE-MCC	INIT.	GROW.	MAT.	DECAY	DISSI.	POST-MCC	TOTAL
00 or 12 GMT	12	00	00	00	12	12	12	12	
No. of cases	14	8	12	3	4	7	11	11	70
Mean Rating	2.7	2.4	2.7	2.0	2.8	2.9	2.3	2.8	2.6
MCC latitude	39.8	39.8	39.8	39.7	39.7	39.5	39.2	38.9	39.5
MCC longitude	98.2	99.5	98.2	97.3	96.4	95.2	93.8	92.4	96.4

First, each MCC case has been subdivided and normalized according to its life-cycle, regardless of the MCC's movement or the ambient mid-

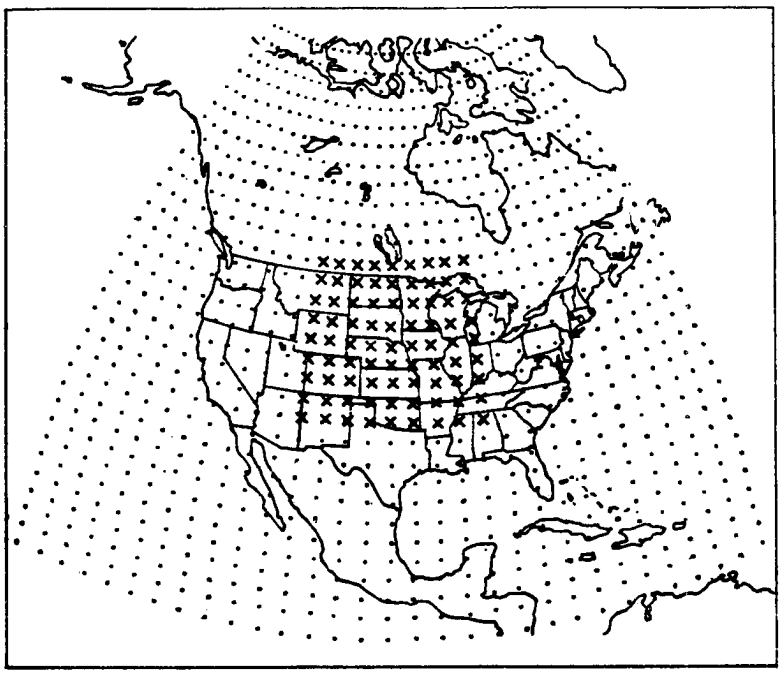

Fig. 3.2. A representative domain of the analysis field at the initial stage. X denotes the domain of 16^{o} latitude by 16^{o} longitude, and illustrates the domain of 60^{o} latitude by 60^{o} longitude.

level wind (called the non-rotated case). Maddox (1981, 1983) observed that MCC is tended to move with the mean flow in the 700-500 mb layer. The MCC's dynamics may also be modulated by the environment in which the MCC is embedded. In order to consider this influence, the entire analysis domain was first rotated and oriented along the path of MCC movement before the compositing procedure was performed. In the "rotated" case, the x-axis is positive along the MCC track (usually nearly west to east), with the origin placed at the MCC's centroid. The positive y-axis is 90^{o} counterclockwise from positive x (approximately north). The MCC track-relative velocity components were denoted by u and v in the x and y directions, respectively, as per conventional usage. Therefore, a positive value of u represents an along-MCC-track flow from the rear side, while a positive value of v indicates a cross-MCC-track flow from the right flank.

With the analyses generated for all of the MCCs in any given sub-period, two general composite analysis approaches were then followed. The first of these was to spatially average or composite the individual analyses, employing filtering techniques to eliminate smaller-scale noise and to maintain large-scale and mesoscale features. This approach is analogous to Maddox's (1981, 1983) composite studies, except that it provides a better time resolution of the MCC life-cycle by using seven sub-periods rather than his two. Thus, the composite evolution of such fields as horizontal and vertical winds, vorticity, divergence, mixing ratio, equivalent potential temperature, instability index, Richardson number, etc., can be examined. Because of the case-to-case variability of the synoptic settings (e.g., shear, jet-stream strengths and orientations, etc.), however, it is expected that any spatial averaging

scheme would severely reduce the mean amplitude of the perturbation features that are seen for the individual cases. Therefore, the second analysis approach involves a statistical treatment of the individual data sets, but they are still grouped by composite sub-period. In this method, spatial fields were first averaged or integrated over the MCC region for each individual case, to produce such variables as area-integrated convergence, divergence, vorticity, wind fields, thermodynamic variables, etc. These individual case representative values were then averaged, with the result retaining much of the amplitude information (this refers only to such variables as weighted convergence, weighted divergence, etc., it should not make any difference in regard to variables averaged over grid points, i.e., non-weighted) that is lost in the spatial compositing due to the spatial variation is generally greater than the individual case variation. Watson and Blanchard (1984) used a similar method to evaluate the area-averaged divergence and found that it was closely related to the area rainfall collected during the Florida Area Cumulus Experiment (FACE).

3.4 Summary

In this chapter, the principal approach of compositing the synoptic to meso-α-scale structure of MCC evolution via an objective analysis technique was described. First of all, comparing the different kinds of objective analysis methods used in recent numerical analysis schemes, we found that the successive scheme correction is simple and involves no matrix inversion; therefore computation is inexpensive for the successive correction scheme. Based on this advantage, the Barnes (1973) objective analysis was adopted and implemented in the RAMS data assimilation package. For a full analysis, the accessed NMC pressure

level data are first interpolated onto isentropic surfaces; then the rawinsonde reports are accessed in order to carry out an objective analysis over a finer resolution for detailed mesoscale analysis. Seven years of MCC cases based on a modified definition are compiled and each individual MCC is ranked into one of ten categories; each MCC's temporal life-cycle is also normalized into seven sub-periods. Finally, with the analyses collected from all of the MCC's for a given sub-period, two general composite analysis approaches are performed in the sigma-p coordinate, i.e., grid-point compositing and area-average method.

The major tasks of this comprehensive study are illustrated by a flow chart shown in Fig. 3.3. The detailed dynamic and thermodynamic analyses will be discussed in Chapter 4. Then, the vorticity, heat, and moisture budgets are presented in Chapter 5.

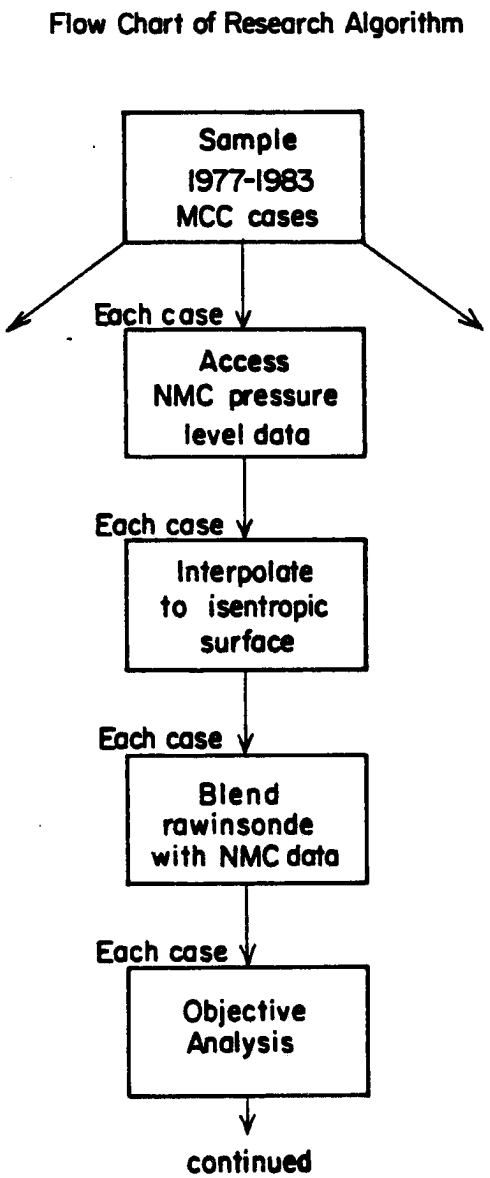

Fig. 3.3. Flow chart of study methodology.

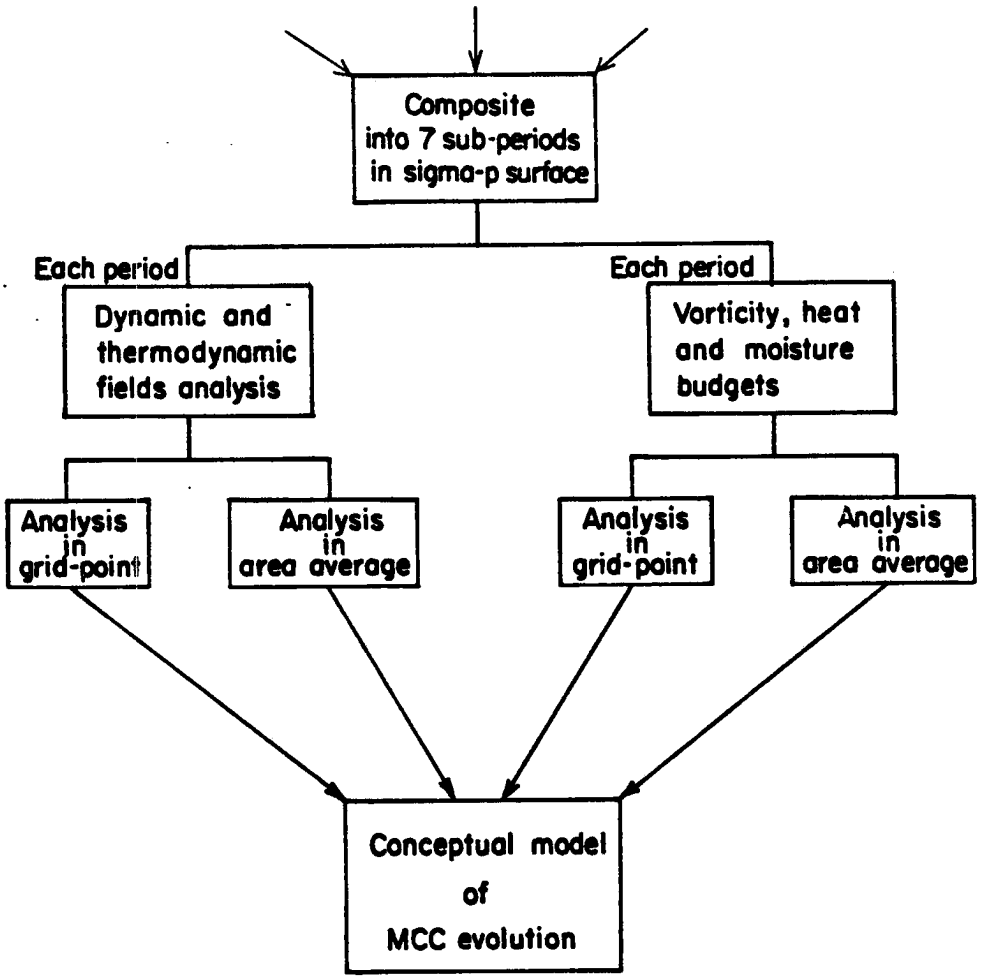

Fig. 3.3. Flow chart of study methodology (Continued).

4.0 MCC CLIMATOLOGY, KINEMATIC STRUCTURE, DYNAMICS, AND THERMODYNAMICS

The primary objective of this chapter is to address in detail the climatology, kinematic structure, dynamics, and thermodynamics of MCC evolution via a composite study.

4.1 MCC climatology derived from the composite study

Before we become deeply involved in the detailed analyses of the composite results, we present some statistics for the MCC sample utilized in this research.

Enhanced IR satellite imagery during June to August of 1977-1984 has been compiled to develop an MCC climatology. Although the image set was far from complete, images encompassing life-cycles of 134 MCCs were collected. Detailed information concerning these systems are documented in Table A.1 of Appendix A. Based on this information, certain specific "MCC purity scale" categories were then assigned according to some selection criteria. Table 4.1 shows that for the eight-year MCC developmental sample, the first thunderstorms typically developed during the afternoon (2041 GMT), and the development into an organized MCC usually did not occur until early evening (0214 GMT). An average of 16.1 hours elapsed between first thunderstorm development and the time that the MCC terminated. The size of these systems was indeed huge with an average cold-cloud shield area ($T_{BB} \leq -32^{o}C$) of more than 301 X 10^3 km^2 at the time of maximum extent. Centroid track coordinates for individual MCCs are presented in Table A.2, with the basic information of Table A.1 indicating that MCCs are likely to be responsible for the

Table 4.1 Statistics of Mesoscale Convective Complexes during 1977-1984.

			Time (GMT)							Cloud-top area at maximum extent ($\times 10^3$ km^2)	
			First			Cell.			Cell.		
Category	Case	Rank	Storm	Ini.	Mat.	End	Ini.	O-Top*	End	$\leq -52^\circ$C	$\leq -32^\circ$C
Overall	134	5.3	2041	0214	0736	1248	0449	0625	0836	186.2	301.0
Orogenic	32	6.8	1942	0140	0727	1305	0444	0546	0833	189.7	297.2
Plains	29	6.6	2256	0250	0815	1306	0513	0711	0917	211.6	336.5
Organized MCCs	90	6.7	2044	0210	0747	1305	0452	0632	0847	204.4	325.4
Marginal MCCs	44	2.4	2034	0223	0713	1214	0448	0610	0813	147.1	251.5

* Overshooting Top

nocturnal maximum in thunderstorm and precipitation frequencies over the central U.S. (Wallace, 1975).

The mean characteristics of separate sets of orogenic[1] and Plains MCCs were compiled as suggested by George (1979) in an attempt to discern the impact of geographical origin on MCC evolution. The orogenic MCC (or WMCC) is defined to be a system which initiates west of

[1] Following McAnelly and Cotton (1986), we introduce orogenic, literally meaning "produced by mountains," as a more precise replacement for orographic, literally meaning "describing mountains."

100°W longitude, while the Plains MCC (or EMCC) is defined to initiate east of 95°W longitude. Table 4.1 indicates no significant differences between these two systems, except that the Plains systems exhibit a broader cloud shield but shorter life-cycle.

The MCC developmental sample can also be stratified into two groups called marginal MCCs and organized MCCs according to the ranked purity scale of each MCC (see Section 3.3.2 and Appendix A); notice that the organized MCC is chosen when its purity rate is greater than or equal to 5. Table 4.1 indicates some significant differences between these two groups; in particular, organized MCCs are longer-lived and larger in cloud shield coverage than are marginal MCCs. The tracks of 67 organized MCCs (during 1977-1983) used in the composite sample are depicted in Fig. 4.1a, and the tracks of 39 marginal MCCs (during 1977-1983) are illustrated in Fig. 4.1b. Moreover, the composite tracks of each sub-period for organized (marginal) MCCs are shown in Fig. 4.2a (Fig. 4.2b). We see that the tracks of the organized MCCs favored a narrow channel across northern Nebraska and northern Iowa, but the tracks of the marginal MCCs covered a broaden channel, with a southward shift to Kansas and Missouri. Furthermore, Table 4.1 summarizes some gross features of the organized MCCs versus marginal MCCs used in the composite study. Generally speaking, it illustrates that the composite organized MCCs has initiated by about 0210 GMT (2010 LT) and terminates near 1305 GMT (0705 LT); these times are similar to those found by Maddox (1983).

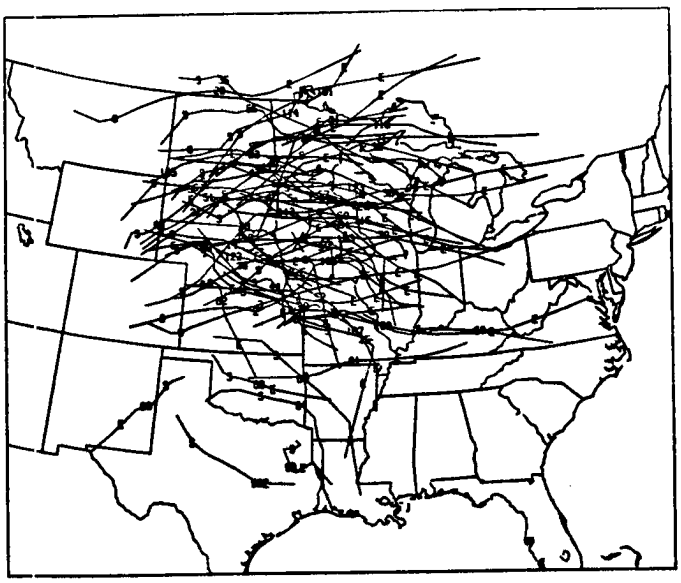

Fig. 4.1a. Tracks of organized MCCs during 1977-1983. The track of each MCC is based on 3-hour centroid positions shown in Table A.2, and the number associated with each track is the MCC case number from Table A.1. S denotes the MCC initial stage, E the dissipation stage.

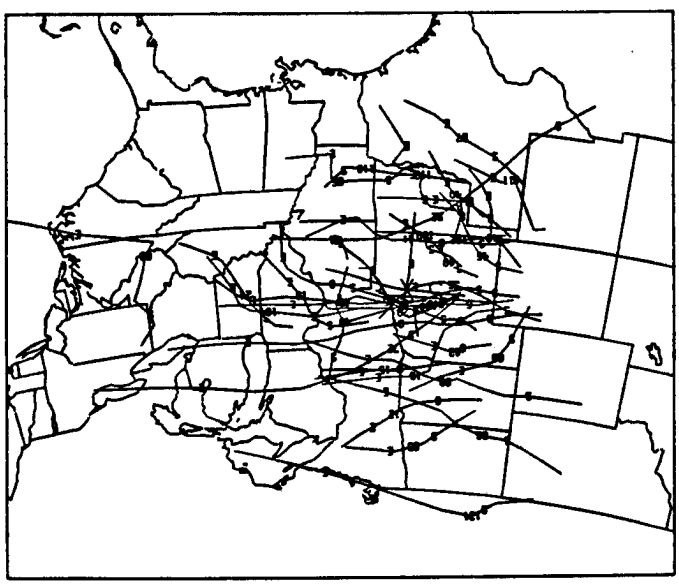

Fig. 4.1b. As in Fig. 4.1a, except for marginal MCCs.

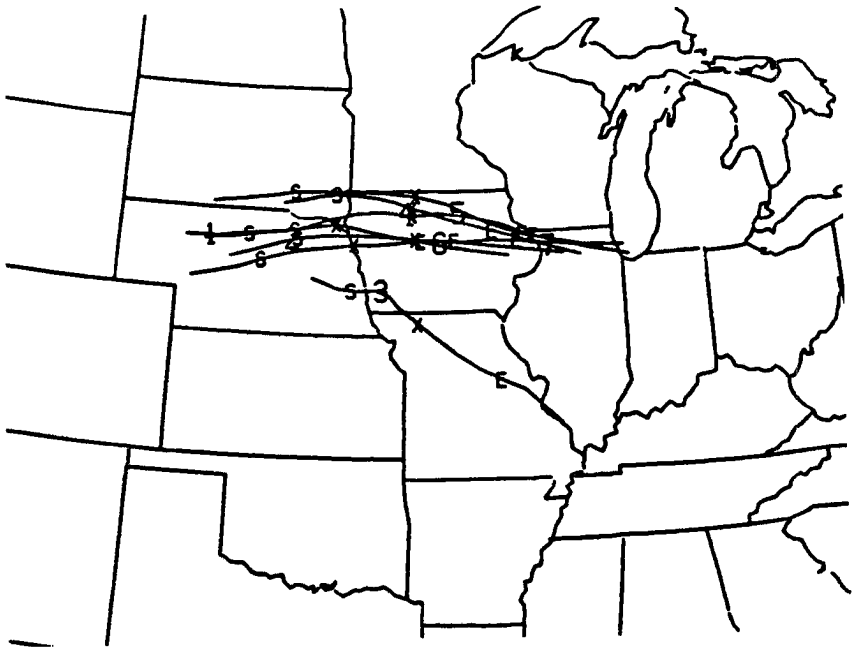

Fig. 4.2a. The composite tracks for each sub-period of organized MCCs during 1977-1983. The tracks are based on the average positions of the MCCs for each sub-period from Fig. 4.1a. The number "1" denotes pre-MCC stage, "2" the initial stage, "3" the growth stage, "4" the mature stage, "5" the decay stage, "6" the dissipation stage, and "7" the post-MCC stage.

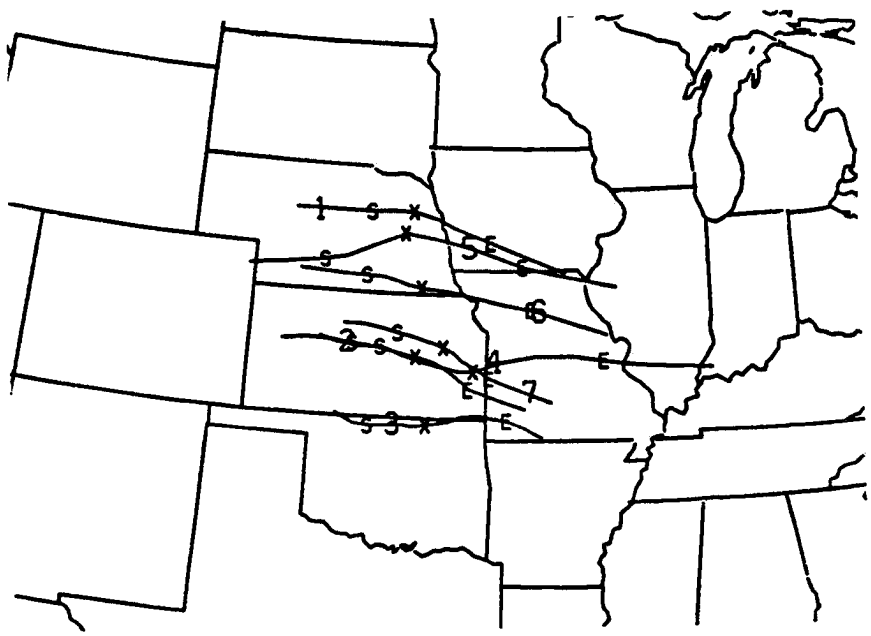

Fig. 4.2b. As in Fig. 4.2a, except for marginal MCCs.

4.2 Evolutionary variations of MCC moisture content, conditional and potential instability, lifting mechanisms, and the up-scale development (organization) of neighboring meso-β-scale convective elements.

In the following sections, we will discuss in detail the results of compositing MCC evolution.

4.2.1 Moisture content evolution

The spatial and temporal distributions of mixing ratio, equivalent potential temperature, mid-level mixing ratio, flux convergence available moist static energy (FCE), and moisture advection have been composited to identify the energy source and sink of an evolving MCC system. Fig. 4.3a shows a tongue of high moisture values (10 g kg^{-1}) at 850 mb level which curves north-northwestward from the Gulf of Mexico into the south to southeast portion of the threat area (i.e., Nebraska and Kansas) at the MCC-12h stage. The west-east cross section of the mixing ratio distribution along the future MCC's centroid (Fig. 4.4) clearly shows that this high moisture air is brought into the sloping threat area. As the MCC evolves, these discernable high moisture-content features are gradually sharpened and narrowed into a mesoscale region. Wetzel (1973) suggested that the moisture injected into middle levels by mountain convection moving over the plains during the afternoon (the pre-MCC stage in this study) could further destabilize the atmosphere and stimulate convection such that a selective focus for another set of deeper meso-β convective elements could develop.

By the time the MCC has reached its initial stage, the continued support of abundant moisture can be seen from the distribution of mixing ratio at 850 mb level (Fig. 4.3b). The time evolution chart (Fig. 4.5)

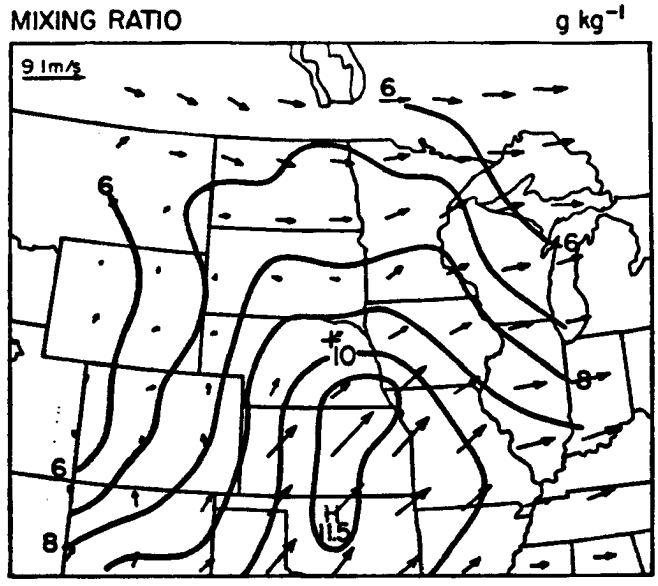

Fig. 4.3a. Analysis of 850 mb level mixing ratio and wind vectors at the MCC-12h stage. The length of the background wind arrows is proportional to the wind speed and the and the wind arrows point downwind. "+" marks the MCC centroid. Units: g kg^{-1} and m s^{-1}.

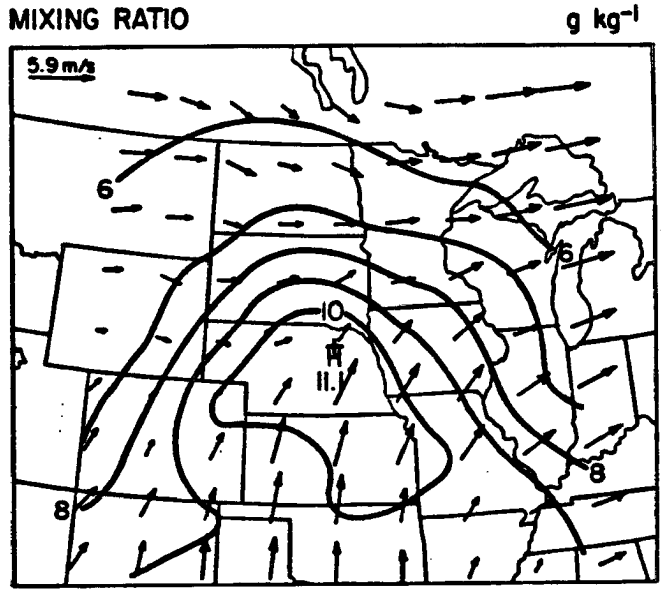

Fig. 4.3b. As in Fig. 4.3a, except for the initial stage. Units: g kg^{-1} and m s^{-1}.

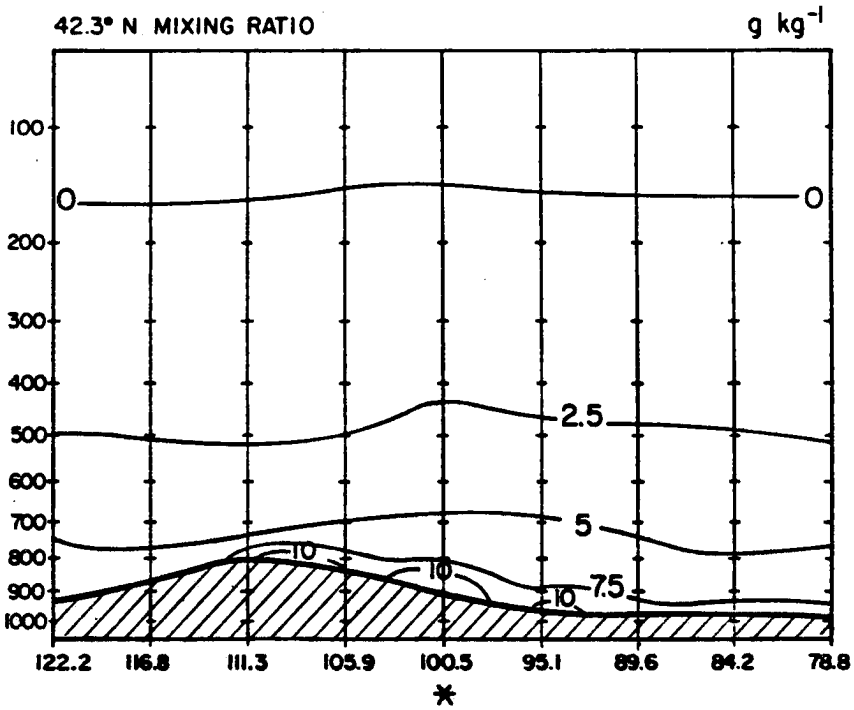

Fig. 4.4. Mixing ratio along the west-east cross-section through the MCC centroid at the MCC$_{-1}$12h stage. * denotes the MCC centroid. Units: g kg^{-1}.

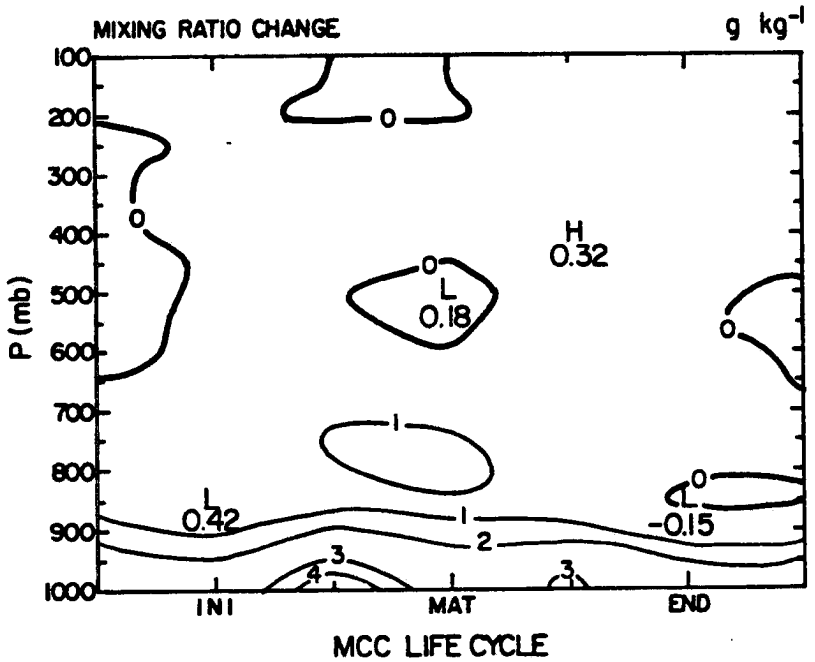

Fig. 4.5. Height-time plot of the mixing ratio difference from its corresponding value at the MCC-12h stage. The mixing ratio field is obtained by applying a 9-grid-point area average over a 6° X 6° lat.-long. domain every 50 mb. The central point of the 9-point average is located at the MCC centroid. Units: g kg^{-1}.

of moisture change (compared to MCC-12h sub-period) indicates that the moisture content increases with time within the lower troposphere, fueling MCC development; moisture content reaches its maximum value at the growth stage (secondary maximum at decay stage). A 3 X 3 grid-mesh areally-averaged (6^{o} X 6^{o} domain centered at the MCC centroid) has been frequently used in this study as a kind of spatial representation of any parameter related to the MCC property. The slightly decreasing of moisture content at the mature stage reflects the drying effect of the precipitation-induced downdraft. However, the positive anomaly of moisture content in lower to middle levels spans the MCC's early life-cycle, in part due to the action of cumulus convection embedded within the MCC. Cloud-top and/or lateral detrainment of water and ice from convection updrafts into the environment appear to be the most likely causes of this moistening.

Fig. 4.6 depicts the time evolution of the equivalent potential temperature profile. It clearly illustrates that the θ_e distribution possesses a secondary maximum close to the surface throughout the MCC's early stages and a minimum in middle levels at the MCC mature stage. The low-level convergence (discussed in Section 4.4.2) of this higher θ_e air is conducive to the convection burst. Incidentally, the extremely high θ_e values at upper levels are due to lower pressure rather than to increased moisture content. The low-level, high θ_e air is crucial to supporting the initiation and maintenance of a mesoscale system, while the middle tropospheric (500 mb level) minimum of θ_e indicates that the potential instability is conducive to driving the mesoscale downdraft. Gamache and Houze (1985) found a minimum of θ_e is located at about 700 mb level in their study of a tropical squall line. However, Ogura and

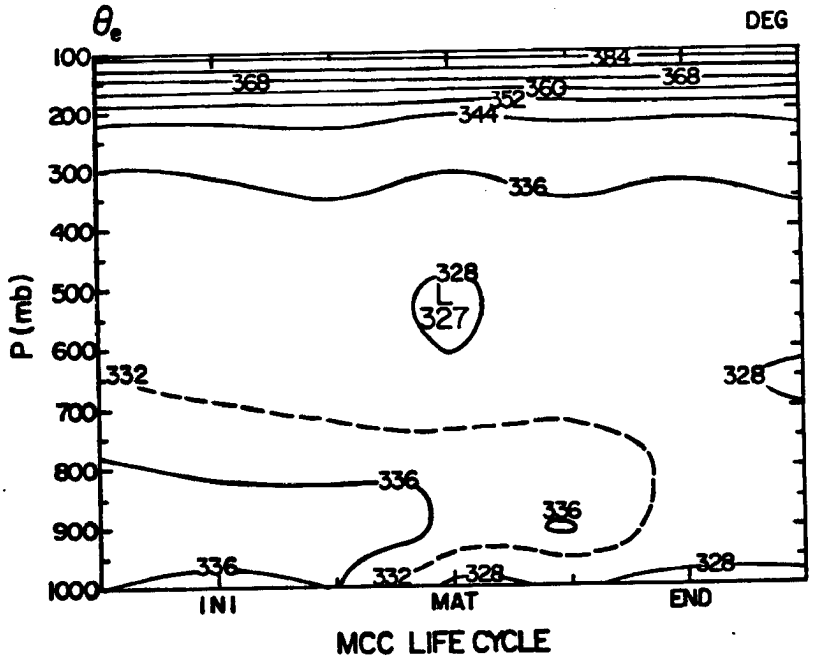

Fig. 4.6. Height-time plot of the equivalent potential temperature (θ_e). The θ_e field is obtained by applying a 9-grid-point area average over a 6° X 6° lat.-long. domain every 50 mb. Units: K.

Liou (1980) found that the environmental atmosphere ahead of the squall line shows the minimum of θ_e located at the 550 mb level. It is not clear whether this difference in the height of the θ_e minimum is due to fundamental differences between squall lines and MCCs or whether it results from regional differences.

The plan view of θ_e at 850 mb level during the initial stage (Fig. 4.7) indicates that the warm, moist air is gradually concentrated into a narrowing mesoscale region over the upstream side of the threat area. Winkler and Charba (1985) showed that MCS-induced heavy precipitation occurs at the southern edge of the steepest north-south gradient of surface θ_e and immediately to the north of a center of maximum surface θ_e. Meanwhile, the θ_e distribution at 500 mb level (Fig. 4.8) shows that the relatively cold, dry air (compared to low-level atmosphere) is enhanced as the MCC develops and reaches minimum magnitude at the MCC mature stage.

The literature review in Chapter 2 suggests that the relatively high mid-level (averaged 700-400 mb layer) moisture content in MCCs may be a significant difference between MCCs and squall lines. Indeed Fig. 4.9 indicates that a concentration of 700-400 mb layer moist air corresponds closely to the center of subsequent MCC initiation, partially due to the vertical advection of moisture from lower layers via deep convection. A more moist mid-level atmosphere will inhibit the mid-level entrainment of the dry air, thereby the moist environment can stimulate the deep convection. The time evolution of the middle-tropospheric (700-400 mb layer) mixing ratio (Fig. 4.10) further shows a tendency to increase as the system evolves, and it exhibits a maximum magnitude at the MCC growth stage resulting from vertical transport by

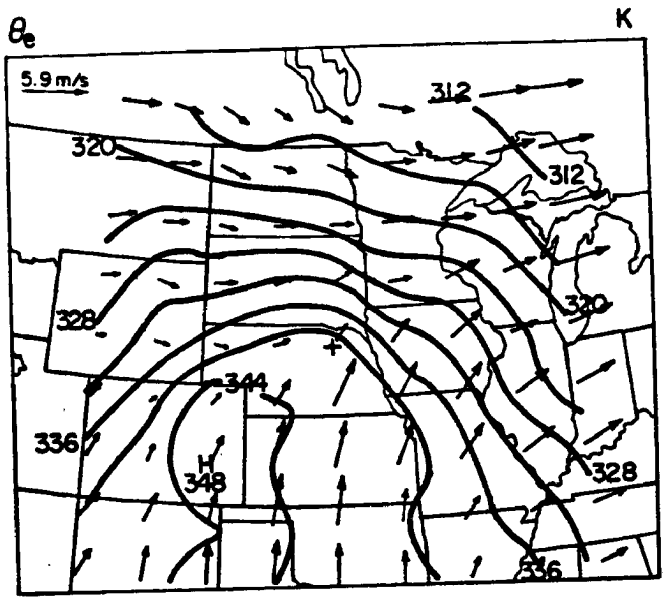

Fig. 4.7. Analysis of 850 mb level equivalent potential temperature (θ_e) and wind vectors at the initial stage. Units: K and $m\,s^{-1}$.

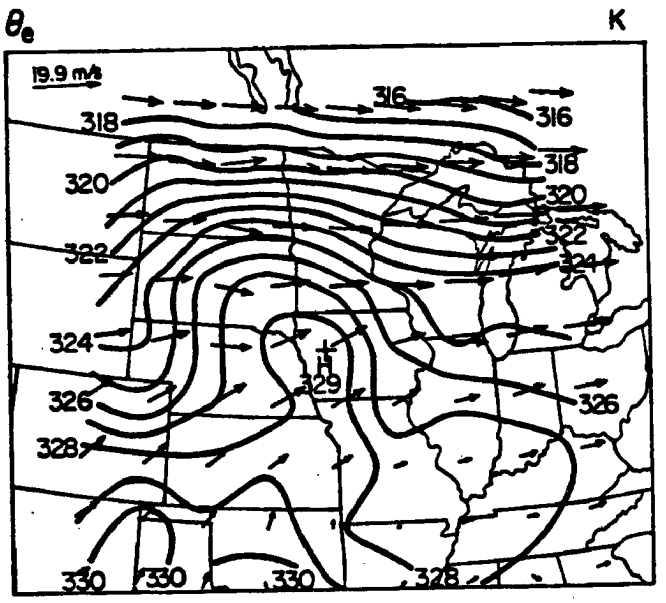

Fig. 4.8. Analysis of 500 mb level equivalent potential temperature (θ_e) and wind vectors at the mature stage. Units: K and $m\,s^{-1}$.

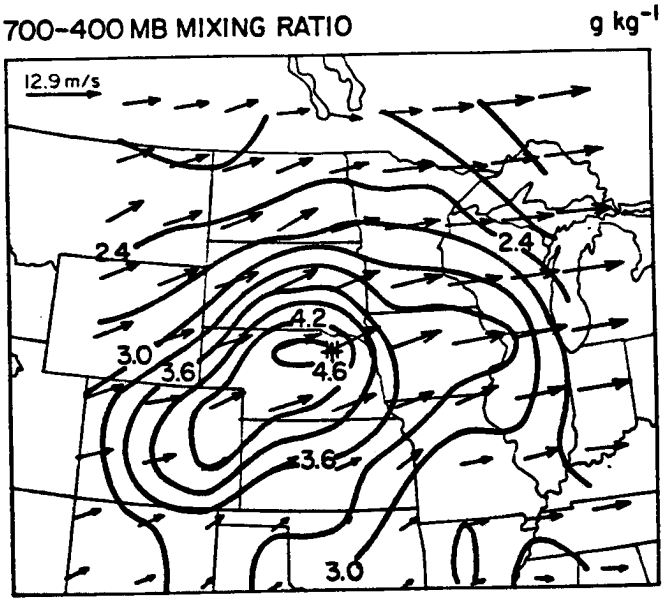

Fig. 4.9. Analysis of the average 700-400 mb layer mixing ratio and wind vectors at the initial stage. The layer mean mixing ratio and wind vectors are calculated by averaging over 9 grid points every 50 mb. Units: g kg^{-1} and m s^{-1}.

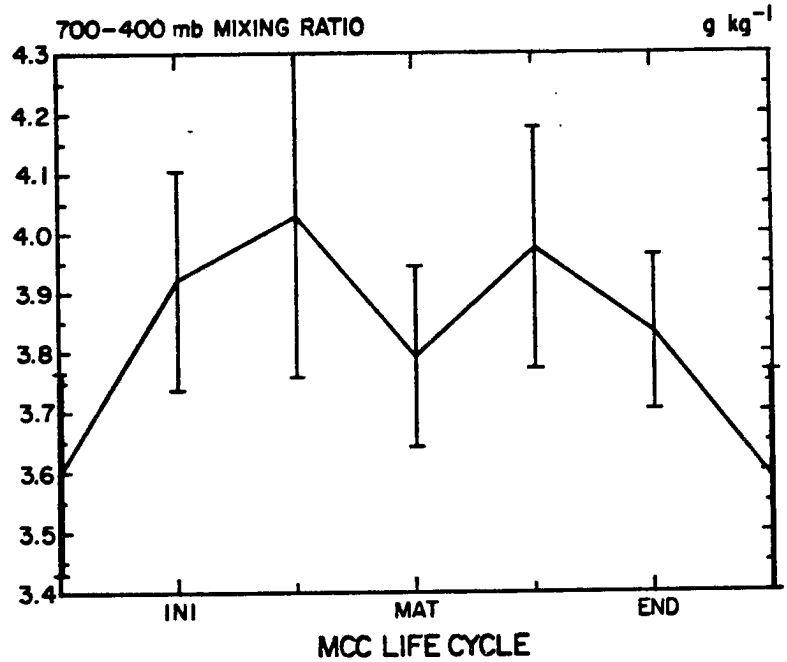

Fig. 4.10. Time evolution plot of the average 700-400 mb layer mixing ratio. The error-bar represents one plus/minus standard deviation of the 9-point average. Units: g kg^{-1}.

deep convection and horizontal advection of moist air by the ambient wind.

Indeed, large-scale circulations supply the moist air through horizontal advection for MCC genesis and development, as can be seen from Fig. 4.11. The change with time of the moisture advection field, shown in Fig. 4.12a, clearly illustrates that the low-level positive moisture advection into the threat area spans most of the MCC's life-cycle, except very close to the surface during the MCC's mature stage. This diagram also shows that the maximum positive moisture advection occurs at about the 700 mb level during the MCC's growth stage, when meso-β convective elements and meso-γ convection coexist. The evolution of the total moisture flux distribution (moisture advection plus moisture convergence), shown in Fig. 4.12b, illustrates the close linkage between moisture content and MCC evolution. Whenever the moisture support is substantially reduced (e.g., MCC decay stage), the system will weaken. In addition, the flux convergence of available moist static energy (FCE) has been calculated at the top of the boundary layer in an attempt to evaluate the concept of frictional CISK (cf. Koch, 1985). FCE is defined as follows.

$$FCE = c_p \bar{V}_{PBL} \cdot \nabla (\partial\theta_e/\partial z) + c_p (\partial\theta_e/\partial z)(\nabla \cdot \bar{V}_{PBL}) \ , \qquad (1)$$

where $\bar{V}_{PBL}$ is the horizontal wind vector averaged within the planetary boundary layer and $(\partial\theta_e/\partial z)$ is the vertical gradient of equivalent potential temperature over the second lowest data-available layer. It follows that low-level moisture convergence within a potentially unstable air mass and horizontal advection of moist static instability are the two component processes that can contribute to a net positive

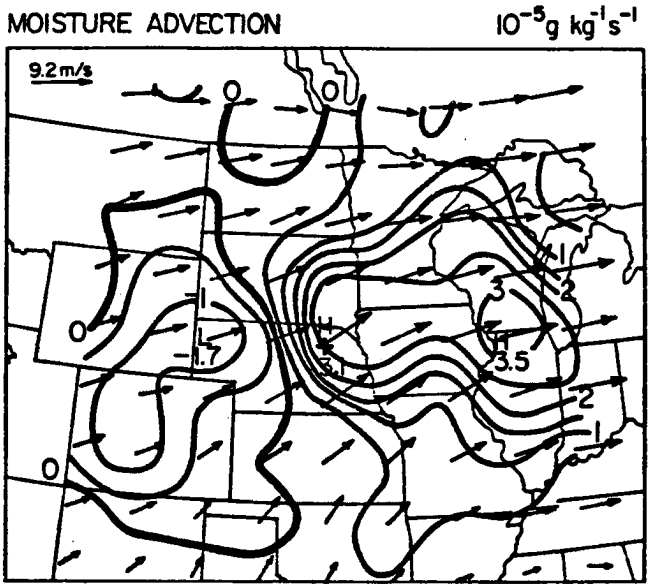

Fig. 4.11. Analysis of 700 mb level moisture advection and wind vectors at the initial stage. Units: 10^{-5} g kg^{-1} s^{-1} and m s^{-1}.

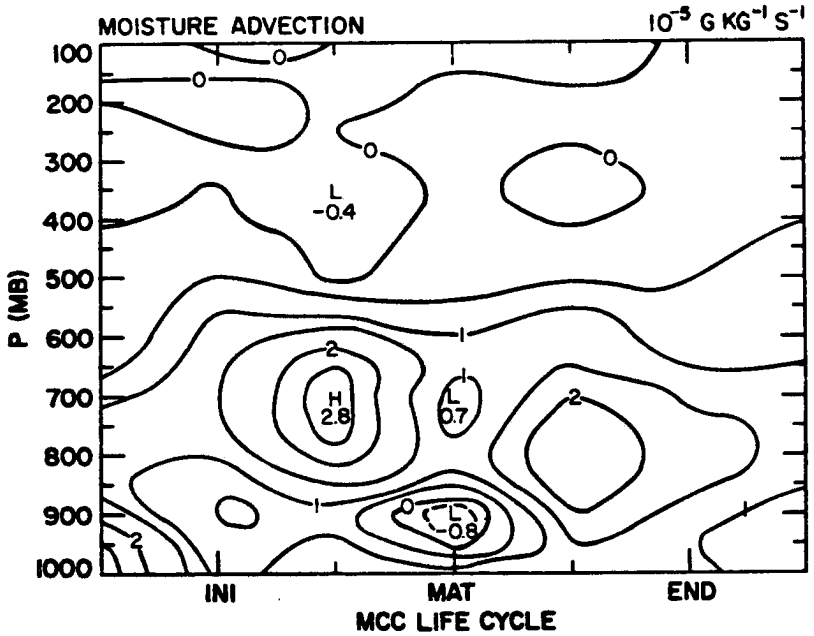

Fig. 4.12a. Height-time plot of the moisture advection. The moisture advection field is obtained by applying a 9-grid-point area average over a 6° X 6° lat^{-1}-long. domain every 50 mb. Units: 10^{-5} g kg^{-1} s^{-1}.

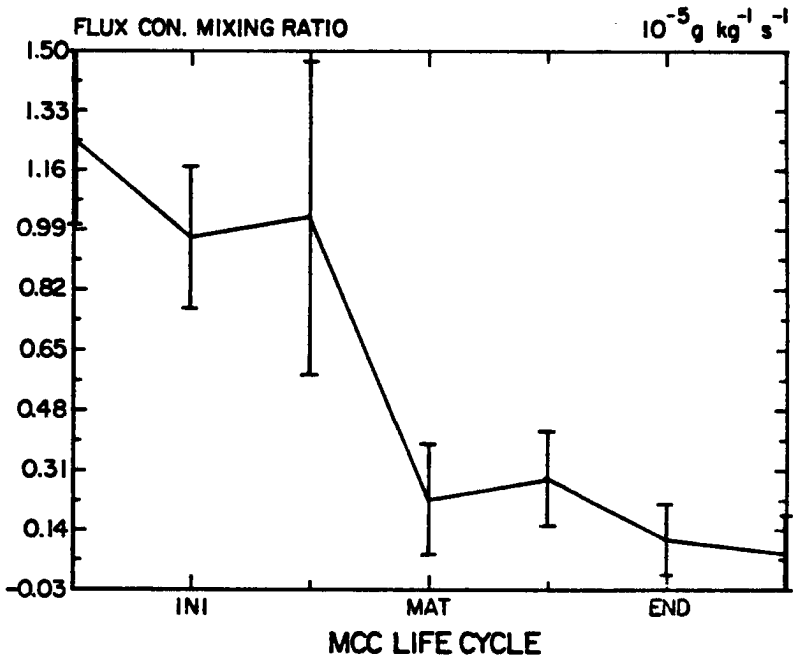

Fig. 4.12b. As in Fig. 4.12a, except for the moisture advection plus moisture divergence. Units: 10^{-5} g kg^{-1} s^{-1}.

flux convergence of available moist static energy. Fig. 4.13 shows that FCE exhibits a peak value (negative value of Eq. (1)) at the pre-MCC stage, but that it still maintains a high magnitude (negative FCE) before the MCC grows to continuously support the system development.

4.2.2 Conditional and potential instability evolution

The conditional instability calculation can be clearly addressed by the Convective Available Potential Energy (CAPE), which is defined as the positive energy of a parcel rising from the surface through the extent of the cloud (Moncrieff and Miller, 1976). In a practical sense, it is evaluated from the Lifting Condensation Level (LCL) to the Equilibrium Level (EL) where the lifted parcel is no longer warmer than its environment. Besides CAPE, the vertical cross-section of the temperature advection field can also help in identifying the warm or cold advection -- a signal of conditional instability. Some static stability indexes, e.g., total totals index, the vertical gradient of θ_e, moisture deficiency (McQueen and Pielke, 1985), bulk Richardson number, and the so-called slantwise convection Richardson number (Emanuel, 1981, 1985) have also been examined to clarify the evolution of conditional or potential instability.

After the pre-MCC stage (behaves as a meso-γ- to meso-β-scale circulations), the surface begins to cool, and CAPE is reduced drastically (Fig. 4.14). This early reduction feature indicates that the rate of CAPE dissipation by deep convection is greater than the flux of low-level energy supply. The plan view of CAPE distribution (Fig. 4.15) at the MCC initial stage shows that the maximum CAPE is located upstream of the threat area; this favors MCC build-up. The triggering of deep convection in MCCs is usually accomplished by destabilization

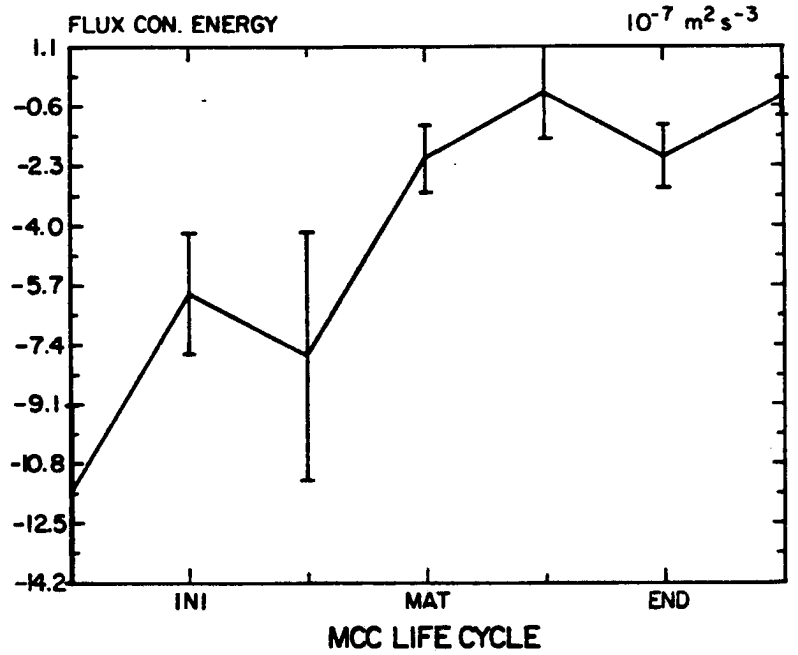

Fig. 4.13. Time evolution plot of the flux convergence energy. The value is obtained for a 9-grid-point average. Units: 10^{-7} m^2 s^{-3}.

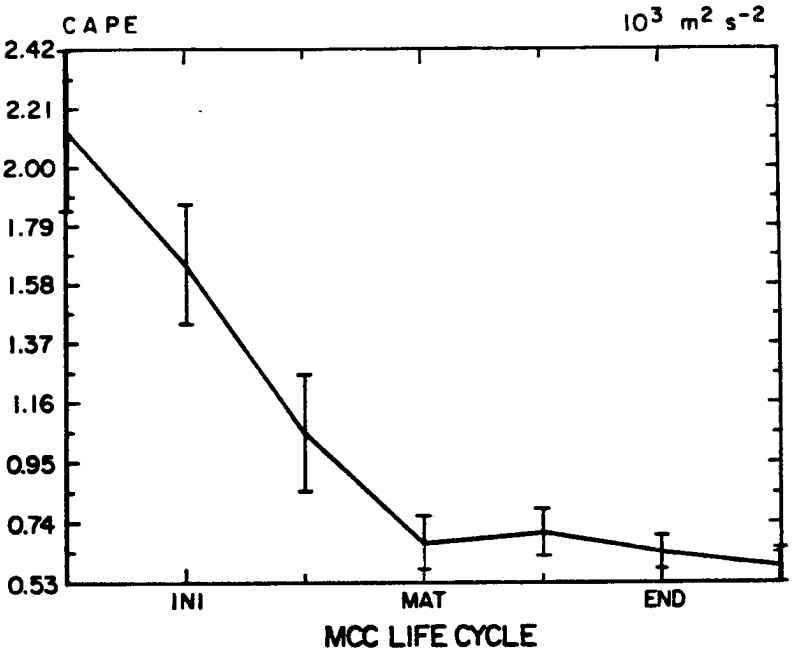

Fig. 4.14. Time evolution plot of CAPE. The value is obtained for a 9-grid-point average. Units: 10^3 m^2 s^{-2}.

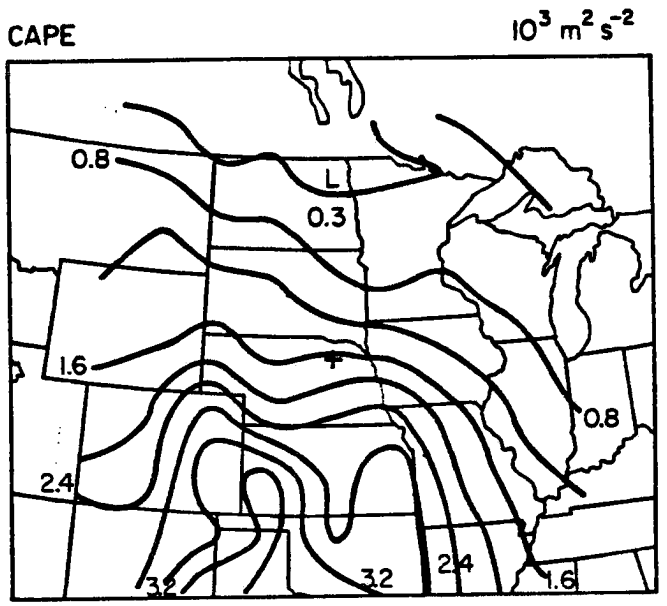

Fig. 4.15. Analysis of CAPE distribution and the 850 mb level wind vectors at the initial stage. Units: 10^3 m^2 s^{-2} and m s^{-1}.

processes such as strong low-level moisture convergence and differential temperature advection which steepens the temperature lapse rate. Indeed, the temperature advection field portrayed in Figs. 4.16a-b indicate that the MCC region experiences low level strong warm advection at the initial stage and reaches maximum value of $34^{o}C\ day^{-1}$ at the MCC maturity. However, the warm advection feature is substantially reduced and even becomes a cold advection pattern at the MCC dissipation stage (Fig. 4.17).

Notice that the total totals index (defined as follows: $TT = T_{850} + T_{d850} - 2T_{500}$) exhibits an early maximum (Fig. 4.18) of magniyude $50^{o}C$ which indicates that a distinct pocket of unstable air has narrowed into the mesoscale region before the MCC forms. The total totals index value is generally high before the MCC growth stage. Any value of total totals index > 44 indicates a favorable environment for deep convection, i.e., warm moist air present at 850 mb level and cold air at 500 mb level. The secondary maximum for total totals index that occurs at the mature stage reflects the low-level moistening produced by precipitation plus the mid-level cooling resulting from the intrusion of low θ_e air (Fig. 4.6). Moreover, another parameter, the vertical gradient of θ_e, can be evaluated by the difference in θ_e between low and middle levels. This quantity may indicate the strength of mesoscale updrafts and downdrafts. Fig. 4.19 shows an early maximum in the vertical gradient of θ_e at the pre-MCC stage; it then tapers off, mainly due to the decreased low-level supply after the MCC reaches maturity. The short-term recovering of θ_e noticeable at the growth stage (about 6 hours after the pre-MCC stage) suggests that a meso-β-scale wave disturbance (wavelength about 100 km and period about 4-6 hours) does

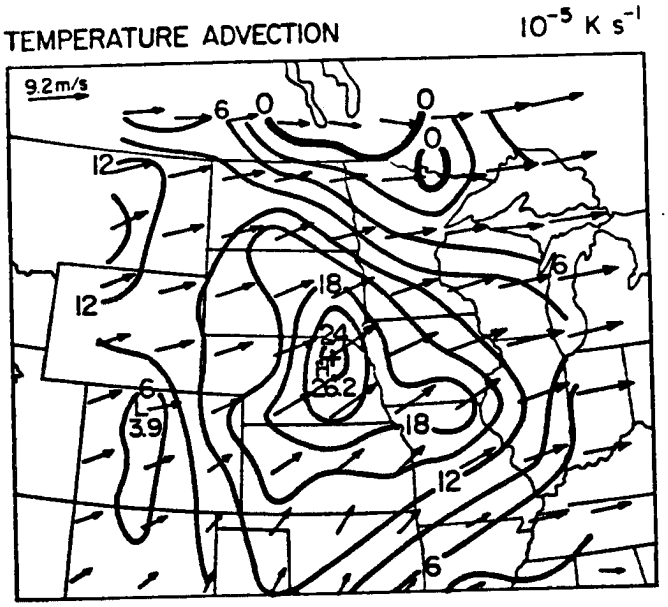

Fig. 4.16a. Analysis of 700 mb level temperature advection and wind vectors at the initial stage. Units: 10^{-5} K s^{-1} and m s^{-1}.

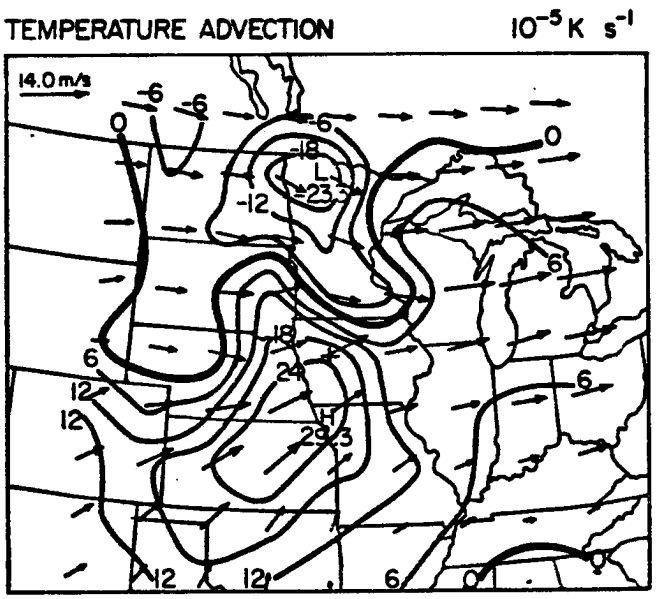

Fig. 4.16b. As in Fig. 4.16a, except for the mature stage. Units: 10^{-5} K s^{-1} and m s^{-1}.

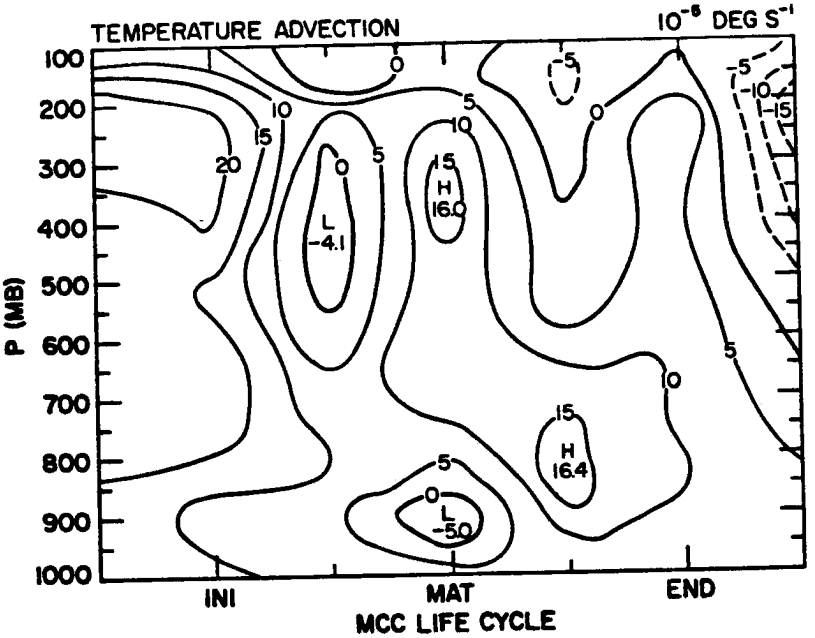

Fig. 4.17. Height-time plot of the temperature advection. The value is obtained for a 9-grid-point average every 50 mb. Units: 10^{-5} K s^{-1}.

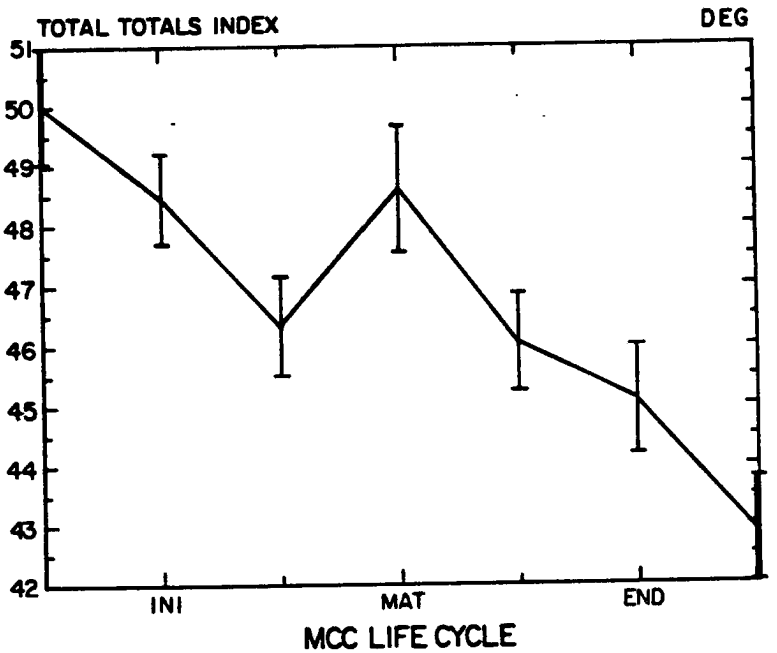

Fig. 4.18. Time evolution plot of the total totals index distribution. The value is obtained for a 9-grid-point average. Units: K.

exist which bears some resemblance to Tripoli's (1986) Rocky Mountain convection cycle simulation. This kind of disturbance frequently appears in the following analyzed fields; it may result from the inadequate sample size of the composite MCC.

The difference between the saturated equivalent potential temperature (θ_{es}) and the equivalent potential temperature (θ_e) gives the magnitude of moisture deficiency. The vertical integral of this quantity shows how moist the troposphere is through the depth of potentially unstable atmosphere; the more positive its value, the less moisture is available in the layer. Fig. 4.20 indicates that the moisture deficiency reaches its maximum magnitude before the MCC forms (pre-MCC sub-period) because of the drying effect of the early deep convection in lower layers (note that the convective activity prevails mainly before the MCC growth stage). After the MCC initial sub-period, the moisture deficiency decreases, reflecting the fact that the moistening process is performed through moisture convergence and vertical transport by meso-β convective elements.

Based on the encouraging work of Weisman and Klemp (1982, 1984) in discriminating thunderstorm types, the bulk Richardson number [CAPE (wind shear)$^{-1}$] was calculated. The typical environmental value of the bulk Richardson number for MCCs herein ranges in the hundreds; comparable values have been found by Bluestein and Jain (1985) for multicellular storms. However, this number exhibits a maximum value at the MCC's initial stage; it then falls off during MCC growth and mature stages. The time evolution of the bulk Richardson number (not shown) is basically dependent upon the distribution of CAPE; wind shear variations are too weak to control the distribution of bulk Richardson number.

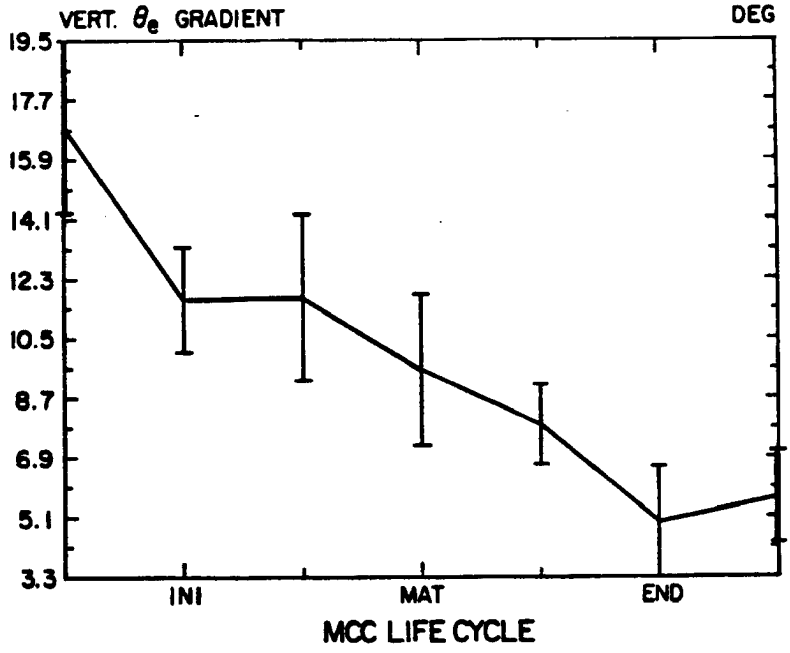

Fig. 4.19. Time evolution plot of the vertical difference of the equivalent potential temperature. The value is obtained for a 9-grid-point average. Units: K.

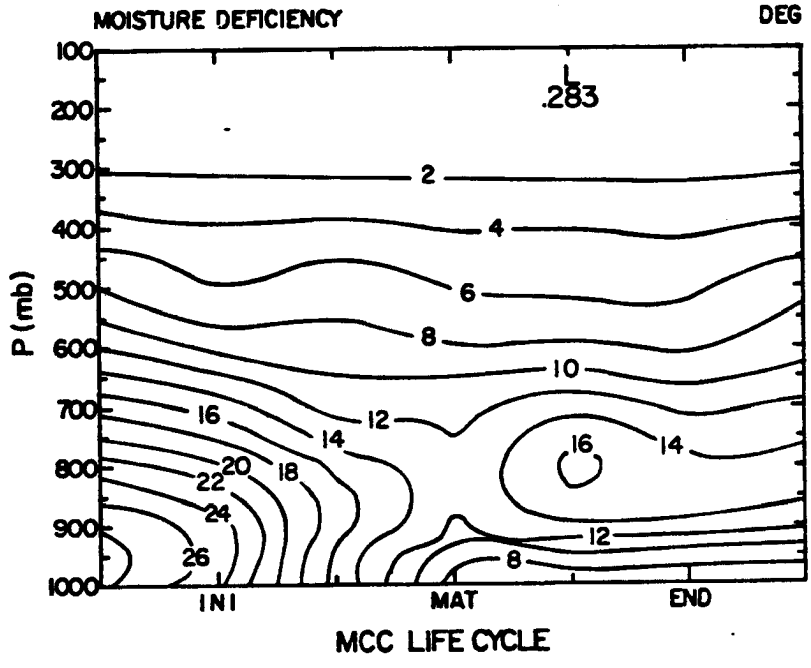

Fig. 4.20. Height-time plot of the moisture deficiency. The value is obtained for a 9-grid-point average. Units: K.

The slantwise convection instability (Emanuel, 1985; Thorpe,1986) was also examined (not shown) to evaluate its applicability to MCC evolution. However, slantwise instability only marginally exists in the upper troposphere at the mature and dissipation stages -- the time when the upper-level anticyclonic vorticity and inertial instability mostly develop.

4.2.3 Lifting mechanisms evolution

Although the large-scale environment may provide certain lifting mechanisms, the crucial issue is still whether there exist some sort of "mesoscale organizers" which favor a particular location under the umbrella of synoptic-scale support in the MCC breeding ground. Thus, a "mesoscale organizer" is responsible for helping to narrow and overlay highly moist air with conditional or potential unstable air within a mesoscale region. The following mechanisms are thought to be the possible "mesoscale organizers" because these mesoscale features ultimately serve as local forcing mechanisms or triggers to release the preexisting potential instability.

(a) Low-level jet: The calculated wind component at 850 mb level (Figs. 4.21a-c) verifies that the low-level jet (LLJ) is located on the upstream side of the MCC centroid throughout the MCC life-cycle. These wind components also show that the LLJ veers with time and exhibits maximum intensity during the MCC mature stage. The strongest wind of the LLJ usually occurs on the south side of the threat area, which provides the convergence of mass, moisture, and heat for the MCC. The LLJ is closely tied to the MCC's evolution because it supplies the necessary heat, moisture, and momentum needed to increase kinetic and thermodynamic energy. Maddox (1985) investigated low-level wind

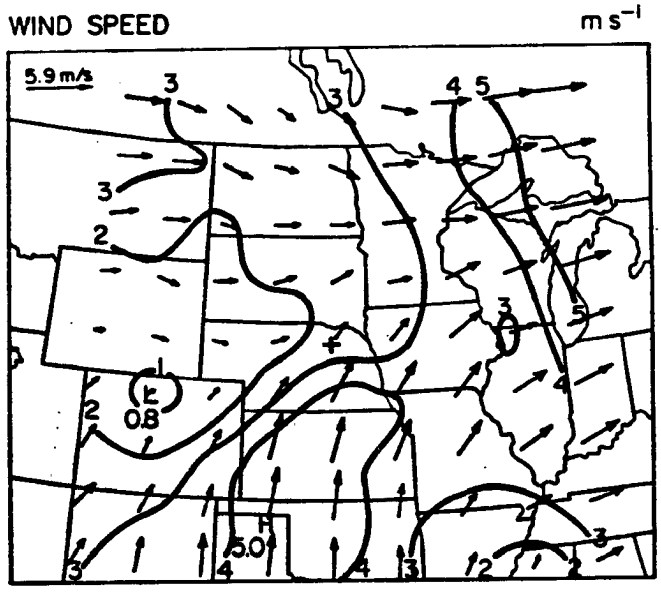

Fig. 4.21a. Analysis of horizontal wind components for the 850 mb level at the initial stage. Units: m s^{-1}.

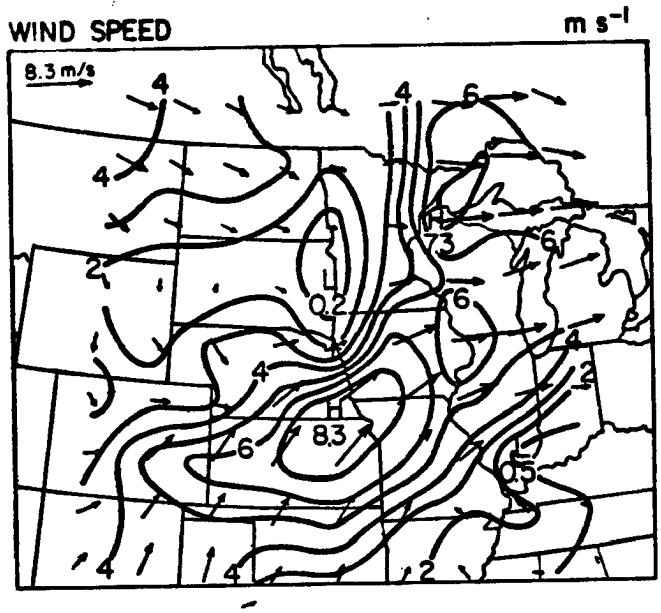

Fig. 4.21b. As in Fig. 4.21a, except for the growth stage. Units: m s^{-1}.

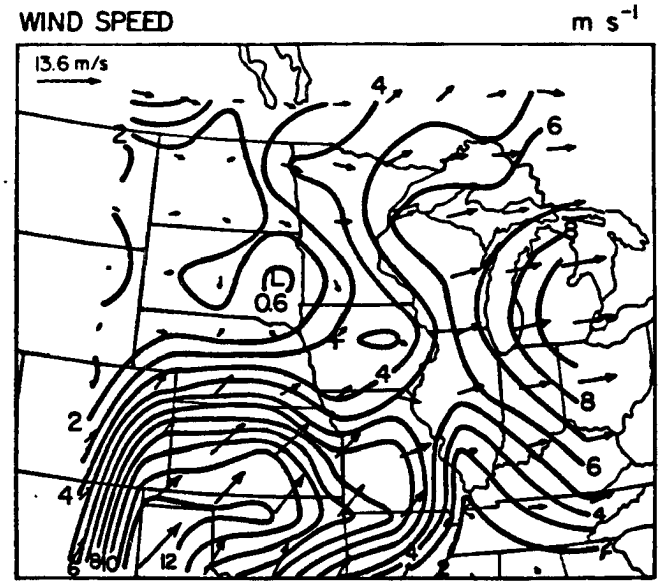

Fig. 4.21c. As in Fig. 4.21a, except for the mature stage. Units: m s^{-1}.

variations in AIMCS and found that the LLJ was located at 0.6 km above ground level and reached its maximum intensity of 16 m s^{-1} during 08-12 GMT (roughly the MCC mature to dissipation sub-period in this study).

(b) Upper-level jet: MCCs tend to occur on the anticyclonic side of a broad, weak, westerly jet stream (Maddox,1981). Generally speaking, the MCC centroid is located relatively to the right rear side of the upper-level jet (Figs. 4.22a-4.22c). This configuration more or less matches the favorable location of the "entrance zone" criterion as suggested by Uccellini and Johnson (1979) and Matthews (1983).

(c) Mid-level "jet-like" inflow: The mid-level "jet-like" inflow or rear inflow jet is found at about 600 mb in the vicinity of the upstream side of the MCC centroid (Fig. 4.23a). Storm-relative inflow occurs at the rear of the MCC, and this inflow usually exists around the melting level (Fig. 4.23b, very close to the transition level as defined by Knupp, 1985). It is generally thought that the mid-level inflow jet in tropical (Houze and Rappaport, 1984) and mid-latitude MCSs (Ogura and Liou, 1980) feeds the mesoscale downdraft beneath the stratiform cloud layer. However, this rear inflow jet may be a manifestation of the mid-level convergence created by enhanced convective heating above the melting level as suggested by Orlanski and Ross (1984); the heating could be in response to radiative destabilization and ice-phase-related heating (Cotton and Anthes, 1986). Moreover, as suggested by Chen (1986), the mid-level jet may feed into and mix with the low-level up-down downdraft (Knupp, 1985). Knupp and Cotton (1986) suggested that the mid-level inflow jet may enhance surface convergence due to the increased downshear branch of this up-down downdraft near the surface. Raymond and Wilkening (1985) also

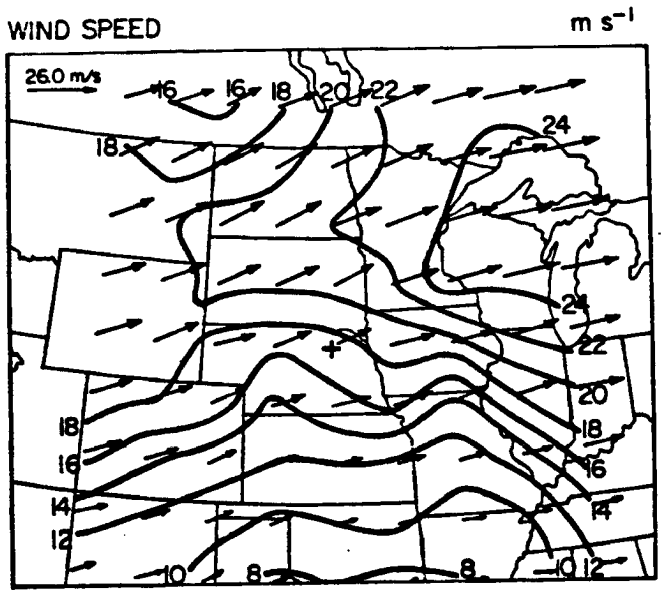

Fig. 4.22a. Analysis of horizontal wind components for the 200 mb level at the initial stage. Units: m s^{-1}.

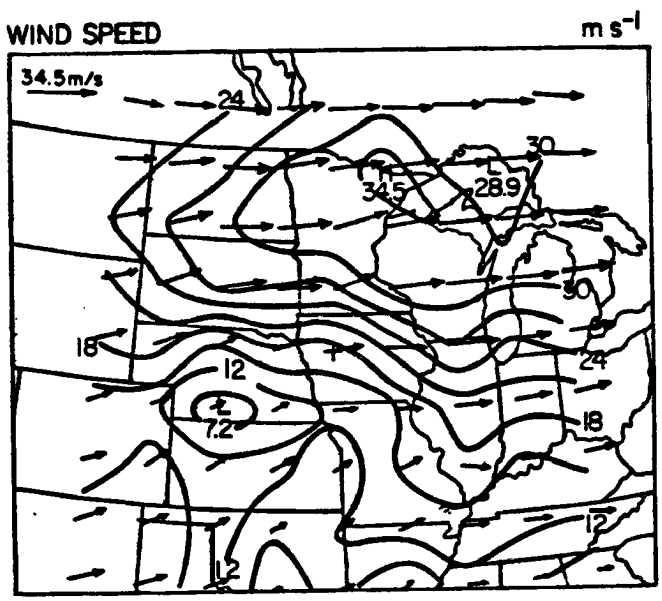

Fig. 4.22b. As in Fig. 4.22a, except for the mature stage. Units: m s^{-1}.

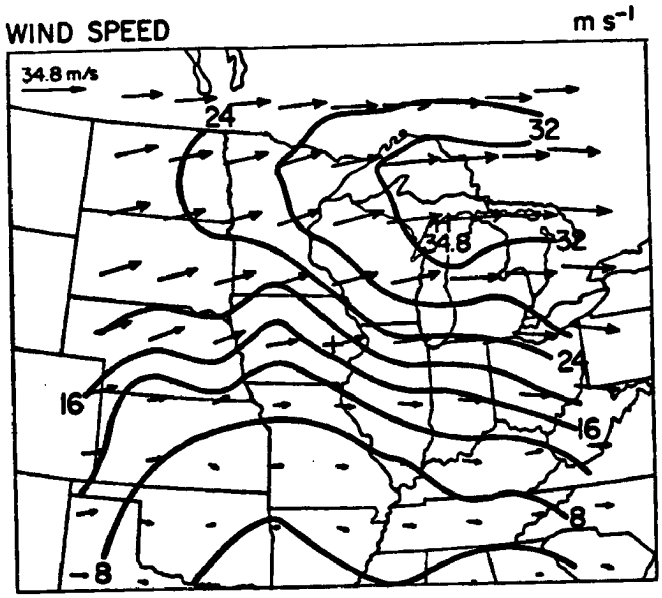

Fig. 4.22c. As in Fig. 4.22a, except for the dissipation stage. Units: m s^{-1}.

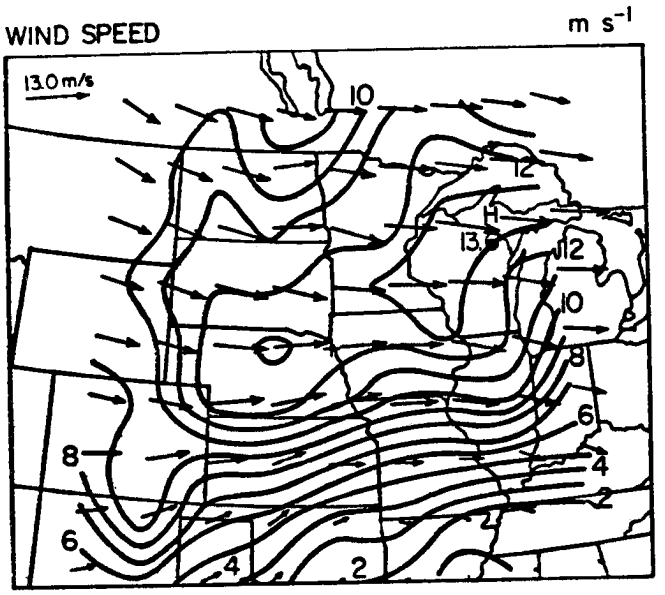

Fig. 4.23a. Analysis of horizontal wind components for the 600 mb level at the growth stage. Units: m s^{-1}.

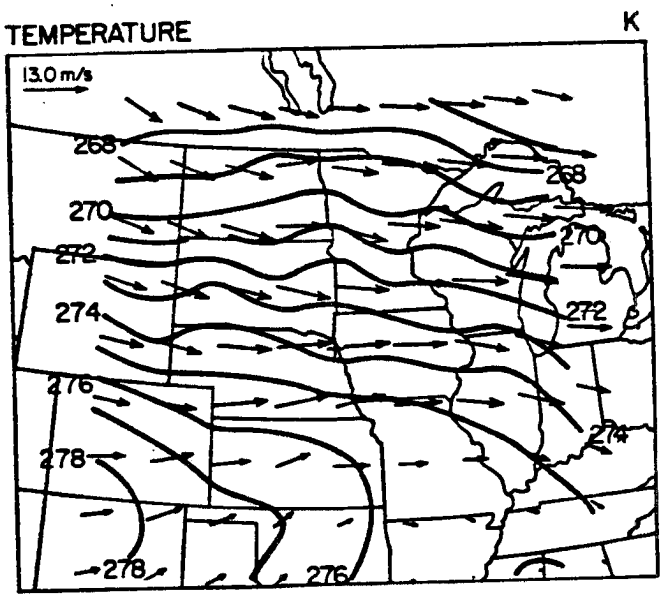

Fig. 4.23b. Analysis of temperature field for the 600 mb level at the growth stage. Units: K.

found in their thunderstorm study that the mid-level inflow fed downdrafts rather than updrafts.

(d) Low- to mid-level short-wave trough: The 700 and 500 mb levels geopotential height fields indicate that a significant synoptic-scale to mesoscale trough occurs nearby and southwest of the MCC centroid at the MCC growth stage (Fig. 4.24; see also Section 4.4.1). This also suggests that localized mid-level enhancement of moisture content and vorticity could occur through the trough forcing.

(e) 700 mb level confluent flow: The 700 mb level wind vector at the MCC initial stage (Fig. 4.25) clearly demonstrates that confluent flow is focused into the vicinity of MCC centroid. The confluent asymptote acts to concentrate the mass and moisture conducive to upward motion. In fact, this level usually fills with high-moisture-content air and experiences maximum evaporation conducive to the development of the mesoscale updrafts and downdrafts. The confluent flow feature found here is similar to that found in the dual MCC settings studied by Rocketwood et al. (1984). McAnelly and Cotton (1986) also revealed from the analysis of several MCC cases that individual meso-β convective elements tended to follow the 700 mb level confluent flow and merge to form an MCC. Based on some field forecasting experiences of Cotton and McAnelly (personal communication) during the AIMCS and O-K Pre-STORM periods, this low-level confluent flow seems to be a very powerful tool for MCC prediction.

(f) Upper-level diffluent flow: By the same token, the significant upper-level tropospheric diffluent flow induces vertical motion and leads to lower stratospheric air intruding into the upper troposphere. Fig. 4.22a depicts this unique upper-level diffluent flow at the MCC

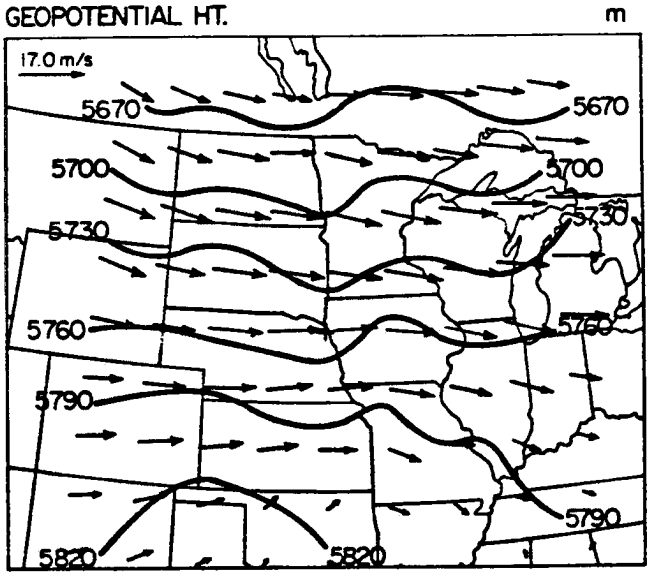

Fig. 4.24. Analysis of geopotential height and horizontal wind components for the 500 mb level at the initial stage. Units: m and m s^{-1}.

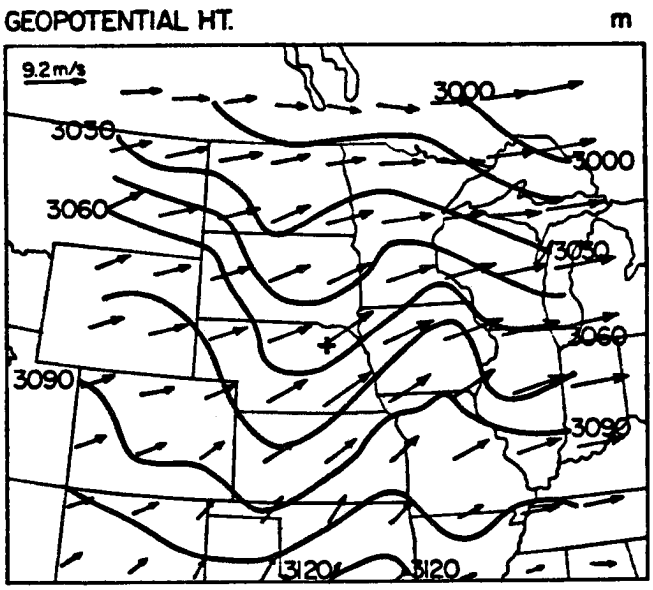

Fig. 4.25. Analysis of horizontal wind components for the 700 mb level at the initial stage. Units: m s^{-1}.

initial stage; this feature is present up to the MCC mature stage (Fig. 4.22b).

4.3 Kinematic structure of MCC evolution

The kinematic structure of an MCC can be clarified by calculating the system-relative flow fields. The MCC velocity is determined either from the detailed MCC track (see Table A.2) or from the average mid-level flow near the MCC centroid, and this velocity is subtrated from the ground-referenced (or Eulerian) grid-point velocity values to give system-relative (or Lagrangian) velocities.

4.3.1 System-relative flow fields

The calculation of a relative flow field helps to represent the real impact of MCC inflows and outflows relative to the system motion. The unique structures deduced from the system-relative motion are addressed in comparison with the basic "rotated-case".

As seen in Fig. 4.26, a relative easterly flow of 12-16 m s^{-1} streams into the storm in advance of the MCC in the lower levels, similar to Gamache and Houze's (1982) squall-line observations during GATE. It also shows the presence of a relative westerly flow of 7 m s^{-1} in the upper levels from the rear side which spans the MCC's later life-cycle. However, the mid-level inflow increases by 4.4 m s^{-1} between the initial and growth stages and reaches its maximum intensity at the MCC's growth stage (cf. Fig. 4.27). The wind component in this diagram was obtained from the 3 X 3 grid-mesh areally-averaged centering at one grid-point west of the MCC centroid; the approach attempts to identify the sources of flow. When the wind component was calculated from the same method but centering at one grid-point east of the MCC centroid; the mid-level flow (not shown) is much less than the mid-level

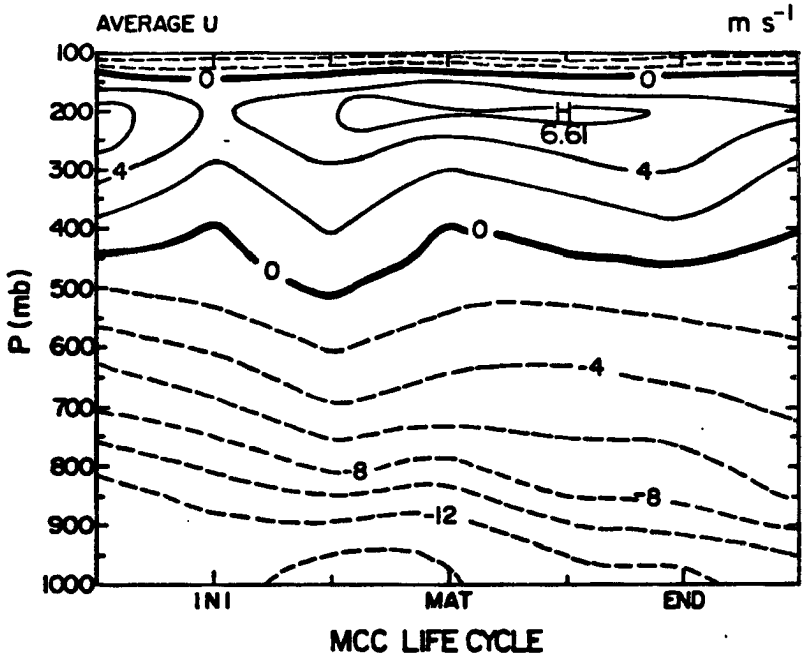

Fig. 4.26. Height-time plot of the composited value of the wind component along individual MCC tracks. The wind is obtained by applying a 9-grid-point area average over a 6^{o} X 6^{o} lat.-long. domain every 50 mb. The coordinate has been rotated along the MCC track; a positive u-value represents a tail wind. Units: m s^{-1}.

inflow shown in Fig. 4.27. In addition, Fig. 4.28 (same as Fig. 4.27, except centerated at one grid-point south of the MCC centroid) of relative v-component flow illustrates that a strong southerly flow at 850 mb level prevails over the MCC's southern flank (cf. also Fig. 4.21a-c) compared to a weaker southerly flow over the northern flank at the lower levels (not shown). Meanwhile, system-relative northerly flow in the upper-level troposphere is much stronger over the northern flank than the southern flank, exporting the outflow toward the energy sink region to the south. Combining the system-relative flow components illustrated in Figs. 4.27 and 4.28 gives a picture of the flow entering the MCC primarily in advance of the system and from its right flank. The moist inflow to the MCC provides a means of overcoming any slight negative buoyancy and raising the conditionally unstable air to its level of free convection.

The outstanding flow feature at 700 mb level is the pronounced cyclonic vortex in the relative flow sense (indicated in Fig. 4.29a). Above 650 mb level, the flow becomes increasingly divergent and anticyclonic. This is most obvious at 200 mb level (see Figs. 4.29b and 4.29c), where the flow is strongly anticyclonic and divergent. For the most efficient overturning of air within the cellular circulation, the upper branch of the cellular circulation moves slightly faster than the mean tropospheric flow and is a mainly diffluent and divergent region (Fig. 4.30). Generally speaking, diffluence of the upper-level wind is a common feature in both tropical and mid-latitude convective systems having extensive stratiform cloudiness.

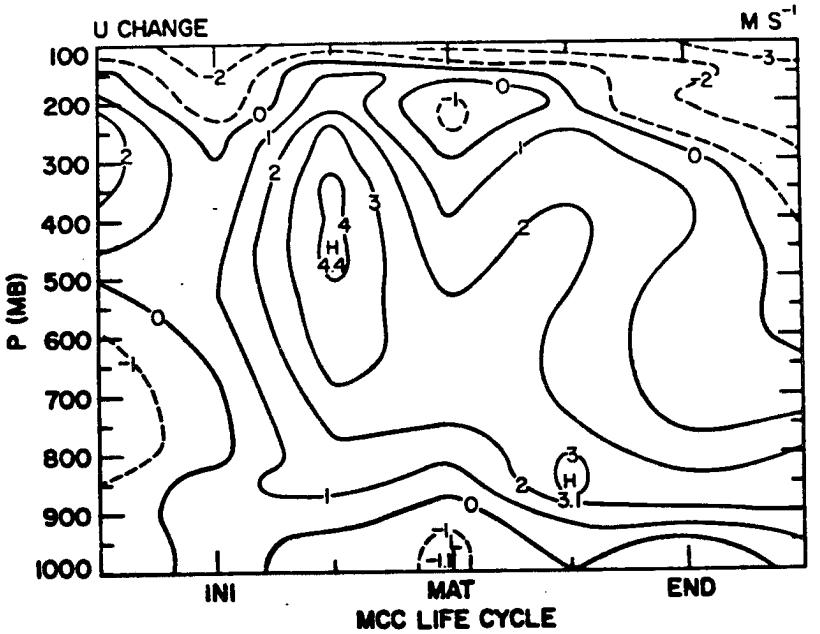

Fig. 4.27. Height-time plot of the u-component change compared to its corresponding value at the MCC-12h stage. The wind is obtained by applying a 9-grid-point area average over a 6° X 6° lat.-long. domain every 50 mb. The central point of the 9-point average is located one grid point west of the MCC centroid. Units: m s^{-1}.

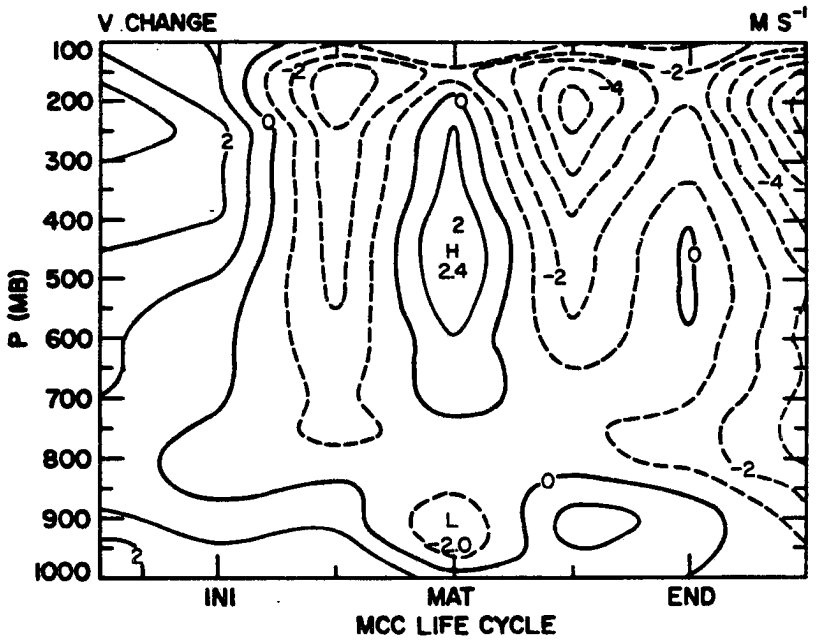

Fig. 4.28. Height-time plot of the v-component change compared to its corresponding value at the MCC-12h stage. The wind is obtained by applying a 9-grid-point area average over a 6° X 6° lat.-long. domain every 50 mb. The central point of the 9-point average is located one grid point south of the MCC centroid. Units: m s^{-1}.

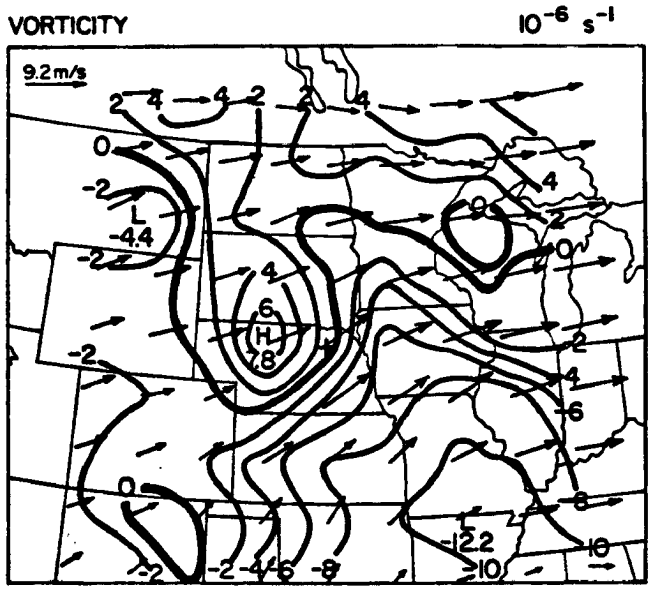

Fig. 4.29a. Analysis of the vertical component of relative vorticity and the horizontal wind components for the 700 mb level at the initial stage. Units: 10^{-6} s^{-1} and m s^{-1}.

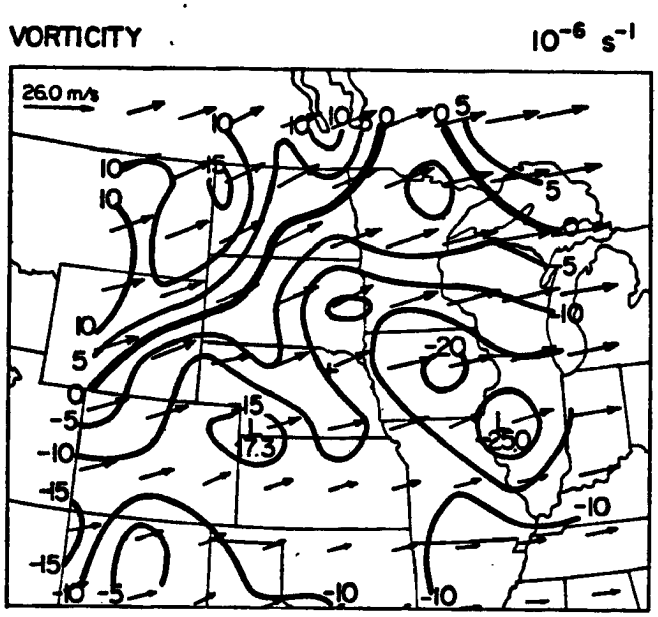

Fig. 4.29b. As in Fig. 4.29a, except for the 200 mb level. Units: 10^{-6} s^{-1} and m s^{-1}.

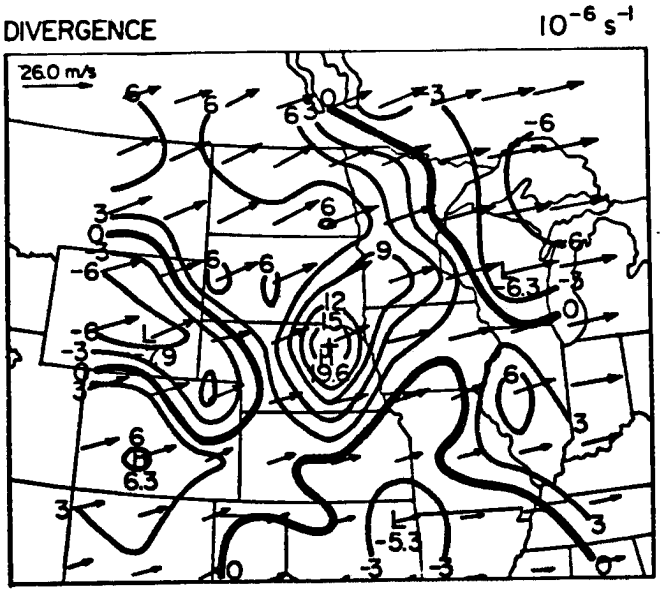

Fig. 4.29c. Analysis of the divergence field and the horizontal wind components for the 200 mb level at the initial stage. Units: 10^{-6} s^{-1} and m s^{-1}.

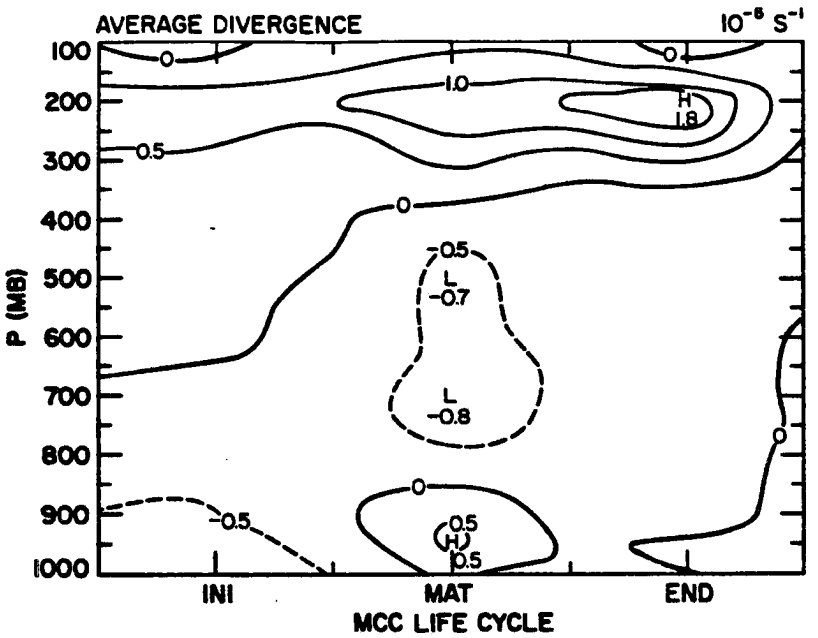

Fig. 4.30. Height-time plot of the divergence field relative to the MCC track. The horizontal coordinates have been rotated along the MCC track so that positive u and v values represent winds from the rear and right flank of the MCC, respectively. The divergence field is obtained by applying a 9-grid-point area average over a $6^{\circ} \times 6^{\circ}$ lat.-long. domain every 50 mb. Units: 10^{-5} s^{-1}.

4.4 Dynamics and thermodynamics of MCC evolution

In this section, the detailed dynamics and thermodynamics of MCC evolution are discussed. One thing which should be kept in mind is that the cumulus convection prevails in the early MCC stages, while the thick stratiform cloud shield dominates the MCC region after its growth stage. Therefore, the features of dynamics and thermodynamics related to the MCC composite system are more or less due to the meso-γ- and meso-β-scale during the early MCC life-cycle but primarily result from the meso-β- and meso-α-scale in the later stages of the MCC life-cycle. When we sampled MCC cases from the satellite imagery, we found that the ambient wind modulates the structure of the MCC cloud shield and alters the dynamics of the MCC system. Therefore, we consider the case with the entire domain of analysis was rotated along the MCC movement as a control case. The detailed dynamics and thermodynamics of the control composite MCC case are addressed in the entire Section 4.4.

4.4.1 Vertical profiles of geopotential height, temperature, and horizontal wind field

The composite chart of the surface relative vorticity (Fig. 4.31a) implies that a synoptic-scale frontal zone oriented in a NE-SW direction is situated along the MCC centroid at the time of MCC initiation. This figure should be compared with the divergence pattern (Fig. 4.31b); which indicates that the convergence zone is associated with the frontal forcing mechanism. A similar configuration was also found by Winkler and Charba (1985) in their investigation of heavy precipitation events. They indicated that the threat area occurs just northwest of the axis of a strong surface southerly wind maximum and northeast of a maximum of the strong surface moisture convergence. The horizontal display of

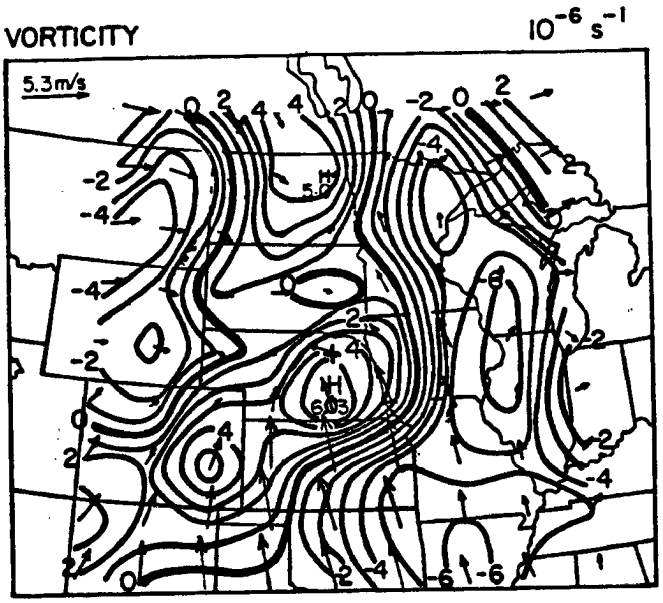

Fig. 4.31a. Analysis of the vertical component of surface relative vorticity and the surface horizontal wind components relative to the MCC track at the initial stage. Units: 10^{-6} s^{-1} and m s^{-1}.

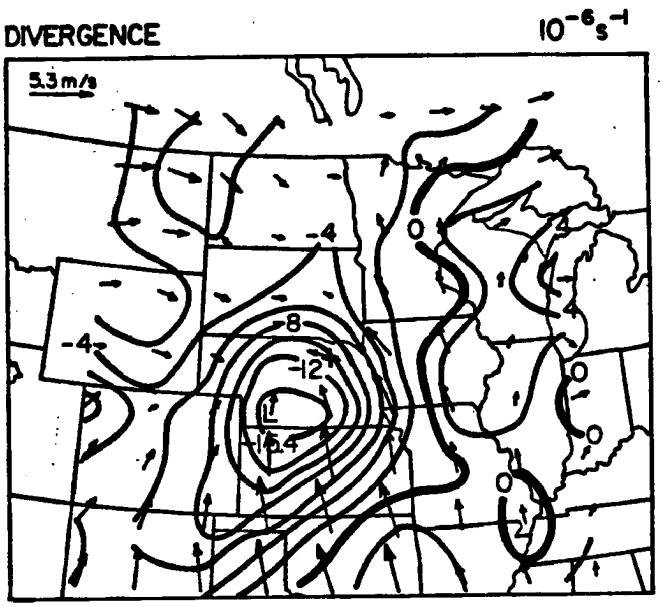

Fig. 4.31b. As in Fig. 4.31a, except for the surface divergence field. Units: 10^{-6} s^{-1} and m s^{-1}.

geopotential height field at the MCC growth stage (Fig. 4.24) indicates that certain mesoscale to synoptic short-wave troughs accompanied the MCC in the mid-level troposphere. The presence of an advancing trough near the MCC's centroid implies that baroclinicity exists which may serve as a lifting mechanism. The above discussions confirm the fact that the entire composite MCC life-cycle is linked to the eastward progression of a weak, mid-tropospheric, meso-α-scale short-wave trough as suggested by Maddox (1983). Incidentally, the geopotential height and wind contours appear to reflect the presence of both the short-wave and a local perturbation so that the location of the trough is not precisely defined. Moreover, the domain average of meridional sensible heat transport has been calculated in an attempt to verify whether MCCs, like tropical cloud clusters, are primarily barotropic. Consistent with the results obtained by Wetzel et al. (1983), Fig. 4.32 shows that this meridional heat transport has a small magnitude, implying that the MCC is akin to tropical cloud clusters in this aspect.

In order to examine the thermodynamic structure of the MCC, the corresponding temperature fields are displayed. Fig. 4.33a indicate that the MCC exhibits a cold-core structure in the upper troposphere to lower stratosphere at the mature stage as suggested by Maddox (1983). This cold-core feature near the MCC centroid reflects the persistent meso-α-scale lifting and the longwave radiational cooling. Fig. 4.33b shows that the MCC possesses a warm-core structure in most of the mid- to upper-level troposphere resulting from the heating released by deep convection plus subsidence warming.

The time evolution of the average temperature field (Fig. 4.34) clearly demonstrates the feature of four layers of temperature anomaly

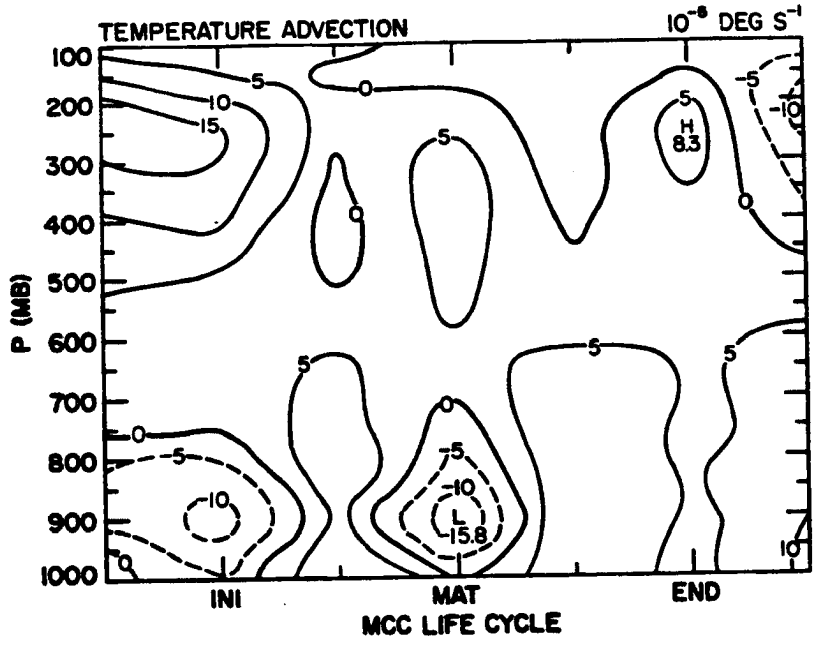

Fig. 4.32. As in Fig. 4.17, except that the winds are system-relative. Units: 10^{-5} °C s^{-1}.

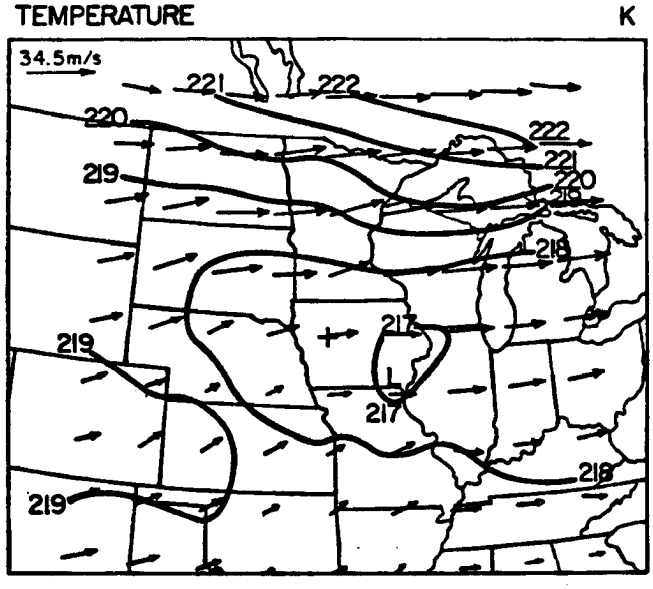

Fig. 4.33a. Analysis of temperature and horizontal wind components for the 200 mb level at the mature stage. Units: K and m s^{-1}.

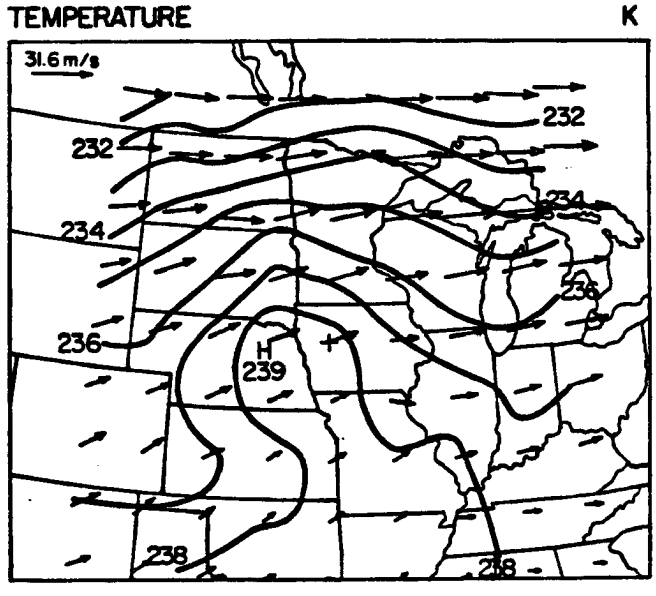

Fig. 4.33b. As in Fig. 4.33a, except for the 300 mb level. Units: K and m s^{-1}.

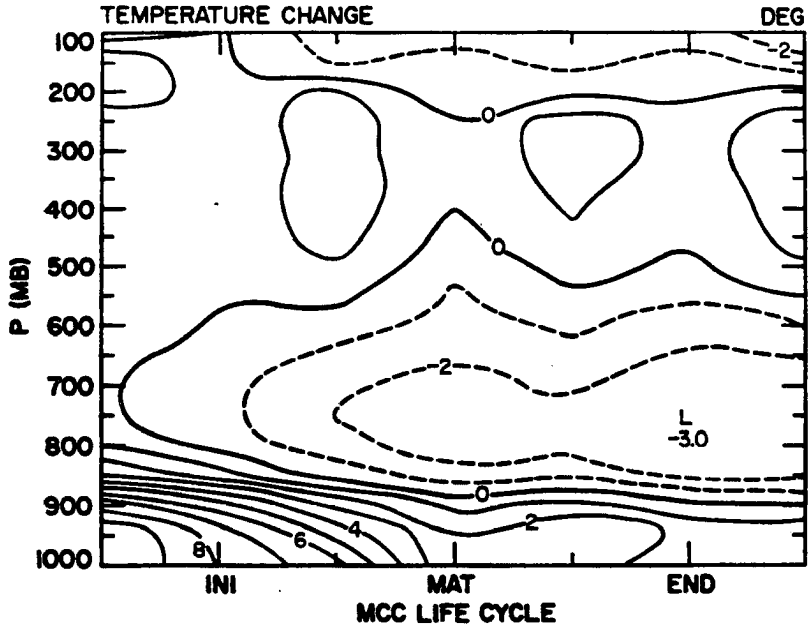

Fig. 4.34. Height-time plot of the temperature change compared to its corresponding value at the MCC-12h stage. The diurnal temperature variations was excluded. The temperature field is obtained by applying a 9-grid-point area average over a 6^{o} X 6^{o} lat.-long. domain every 50 mb. Units: K.

pattern. The layer below 800 mb level shows a warming trend throughout the entire MCC life-cycle (the diurnal temperature variations have been removed before the temperature change is calculated). This warmer temperature is probably due to the warm temperature advection (discussed later) in the early MCC stage, since the warming by adiabatic compression in the mesoscale downdraft offsets the cooling by evaporation of raindrops once the MCC reaches its maturity. In fact, Johnson and Young (1983) found a similar lower-tropospheric warming in their investigation of MCS. They argued that the diabatic processes of melting and evaporation in the lower troposphere yield a negative heating, but the atmospheric response is a warming due to the adiabatic warming overcompensating evaporative cooling beneath the stratiform clouds.

Just above the lower tropospheric warming layer, a very deep cooling layer is present, which extends from 800 mb to 500 mb level. Because the MCC exhibits a mean upward motion (Fig. 4.39a) in this layer, the adiabatic cooling probably prevails. The cooling also cancels much of the convective heating in this layer. Note that this cooling is enhanced after the MCC reaches maturity when the mesoscale downdraft prevails; it also explains the much deeper cooling layer found in the MCC's mature stage. Other factors which possibly explain or contribute to this low- to mid-level cooling were suggested by Gamache and Houze (1985). The cooling may have been the result of negatively buoyant cloud-top air being detrained from the tops of the relatively shallow convective cells. However, Rosenthal (1980) pointed out that if the base of a mesoscale updraft becomes unsaturated as a result of the convergence of dry air into its base, then dry stable ascent will occur

and produce a cool layer at the base of the mesoscale updraft of thick stratiform cloud.

Above the cool layer described, an upper tropospheric layer of warm air is located between the 500 mb and 200 mb levels. Apparently, this warm layer is associated with the mesoscale updraft of thick stratiform cloud, embedded deep convection, ice-phase latent heating, subsidence warming, and adiabatic cooling of mean upward motion. Above this warm layer, the region is characterized by a cooling trend. This cooling feature may be explained by either convective overshooting of individual cumulonimbus clouds or by the divergence of longwave radiative flux at the top of the stratiform cloud as suggested by Johnson and Kriete (1982). Fritsch and Brown (1982) also revealed that adiabatic cooling due to mesoscale ascent can alone account for the observed cooling aloft. Their calculations suggested that cooling by detrainment from convective towers actually reduces the cooling effect by mesoscale ascent because mesoscale subsidence warming occurs in response to the convective updrafts.

As far as the horizontal wind distribution is concerned, the low-level jet at 850 mb level increases in speed slightly (compared to pre-MCC stage) and veers to a more southwestern flank of the MCC region at the initial stage (Fig. 4.21a). Thus, a LLJ is a recurrent feature of the MCC's precursor environment which impinges upon the MCC region. The flow at 700 mb level has strengthened into a west-southwesterly jet over the mature MCC region. The veering of the low-level wind at the mature stage (Fig. 4.21c) presumably reflects both the advancing short-wave trough and the inertial oscillation induced by the rapid reduction of eddy viscosity at nightfall. This LLJ has weakened after the MCC decay

stage, thus reducing the supply of warm moist fuel to the system. The 200 mb level flow (Fig. 4.22b) shows an intensified jet streak downstream and to the north side of the MCC centroid (which reaches a maximum intensity at MCC maturity). Moreover, at the mature stage, the maximum u-component deceleration is slightly upwind of the MCC centroid (Fig. 4.35) due to the "obstacle blocking" effect caused by the mesohigh aloft. The west-east cross-section of the u-component at MCC maturity suggests that the distance from maximum to minimum wind speeds is on the order of 600-800 km, i.e., the MCC horizontal scale. This evidence, along with the meridional extent of the thick stratiform cloud, suggests that while the upper short-wave trough signal does affect the values of the u-component, some of the deceleration is of MCC origin.

4.4.2 Divergence field at various levels

The traditional Kuo scheme (Kuo, 1965, 1974) of cumulus parameterization states that the total convective heating is proportional to the low-level large-scale moisture convergence. Therefore, it may be inferred that low-level convergence should be crucial to the MCC's evolution. Indeed, Frank (1978) revealed that the Intertropical Convergence Zone (ITCZ) could provide the large-scale convergence which precedes the formation of tropical mesoscale convective systems. However, Houze et al. (1981) indicated that regional circulations such as land breezes can also be a source of substantial large-scale, convergence-forced mesoscale systems.

The divergence field was altered according to O'Brien's (1970) scheme. This scheme is based on the simple hypothesis that the divergence errors increase vertically as a linear function of pressure.

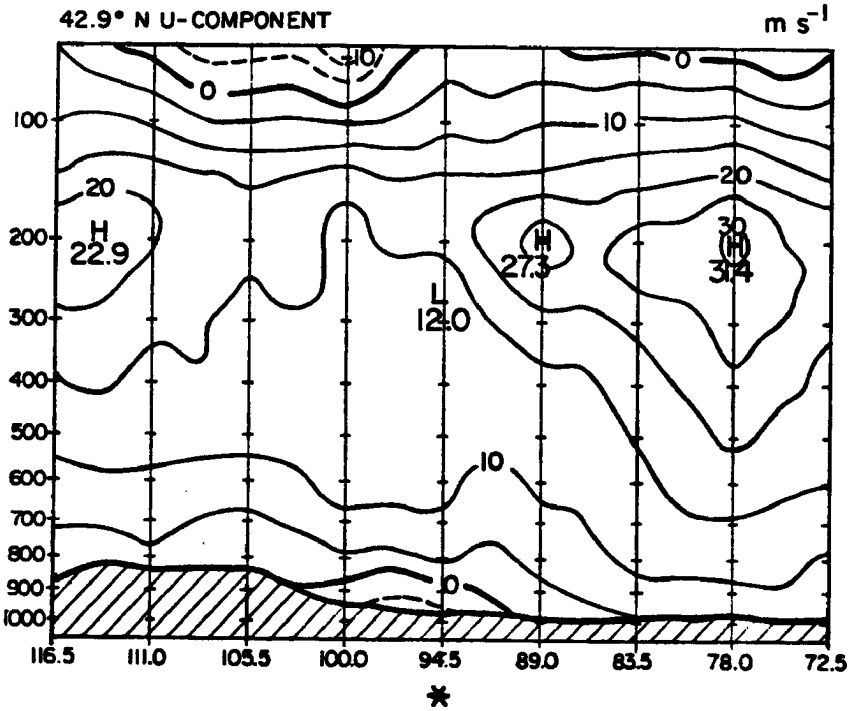

Fig. 4.35. U-component along the west-east cross-section of MCC centroid at the mature stage (rotated coordinate system). Units: m s^{-1}.

A similar mass-adjustment scheme has been successfully used in a study of a tropical squall line by Gamache and Houze (1982). The composite areally-averaged divergence and the areally-averaged divergence change (compared to the MCC-12h stage) are depicted in Figs. 4.36a and 4.36b, respectively. Areally-averaged divergence values are first obtained for each MCC case by applying a 9-grid-point average of rotated winds. The arithmetic mean of the divergence for the sample cases is then calculated for each composite MCC sub-period. We can see from Fig. 4.36a that the MCC is generally characterized by a layer of convergence up to 650-700 mb level and divergence above that throughout its early life-cycle. The low-level mass convergence not only provides the necessary large-scale moisture convergence, but also enhances the growth of meso-γ- or meso-β-scale convective elements and promotes their merger with other cells. The supporting convergence gradually deepens the moisture layer and provides an environment of enhanced potential instability. However, low-level convergence increases prior to the pre-MCC stage, indicating a lag between boundary-layer forcing and the formation of significant convection.

By the time of MCC maturity, the layer of convergence has deepened to the 400 mb level and exhibits convergence center at 500 mb level, while the layer of divergence aloft has strengthened coherently with its center located at the 200 mb level. The deeper inflow convergence is needed for intensification of the cyclonic rotation similar to that found in tropical cyclone formation (Lee, 1986). The vertical extent of the convergence zone also implies that the MCC is organized on the meso-β- to meso-α-scale rather than cumulus-scale in order to efficiently stabilize the environment. Nevertheless, a low-level region

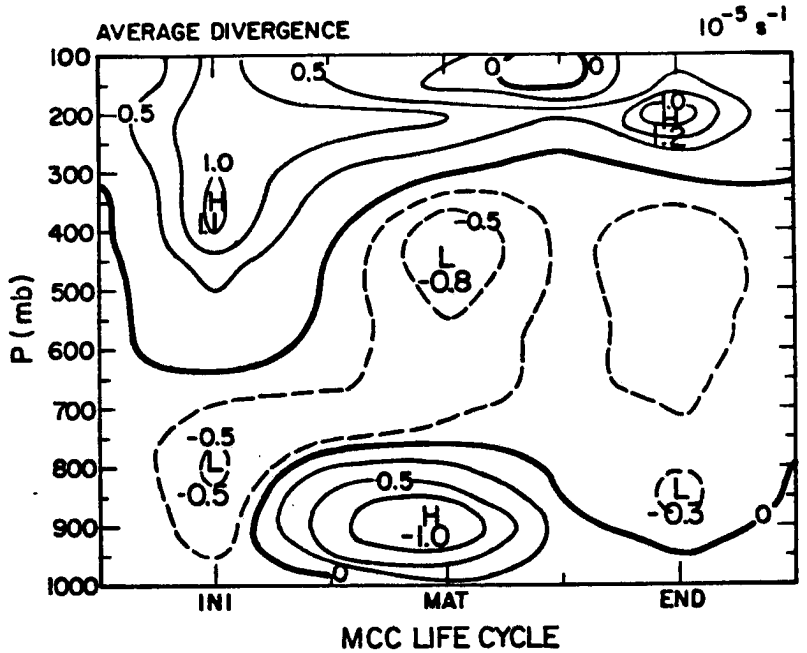

Fig. 4.36a. Height-time plot of the mean divergence field. The horizontal coordinates have been rotated along the MCC track so that positive u and v values represent winds from the rear and right flank of the MCC, respectively. The divergence field is obtained by averaging MCC cases every 50 mb for each sub-period. Units: 10^{-5} s^{-1}.

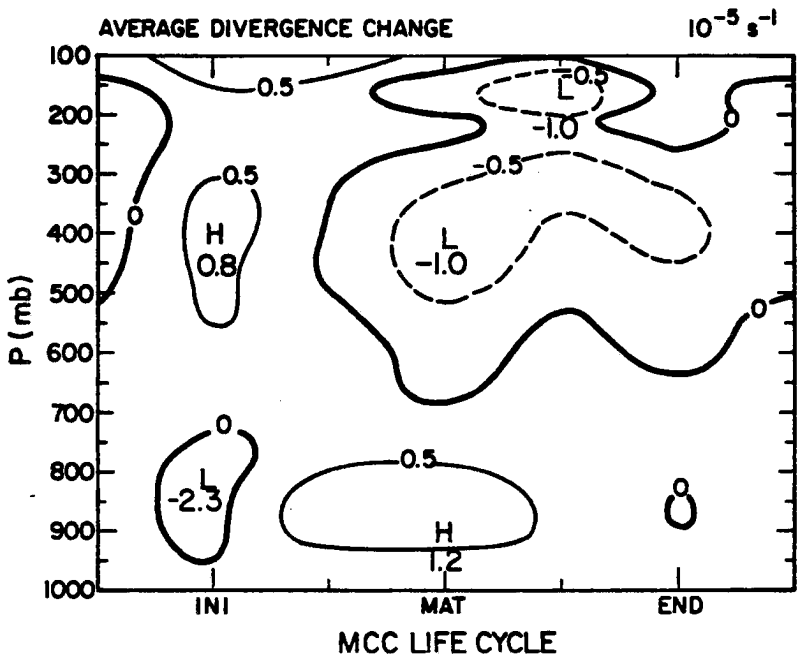

Fig. 4.36b. As in Fig. 4.36a, except for the divergence change compared to the MCC-12h stage. Units: 10^{-5} s^{-1}.

of divergence is also evident below 850 mb level during MCC maturity, presumably due to the development of a meso-high as a result of the evaporation of precipitation.

After an MCC passes maturity, the layer of mid-tropospheric convergence weakens associated with the weaker mesoscale updrafts, but the system redevelops a low-level convergence zone. It is not uncommon to detect severe weather phenomena during an MCC's dissipation period, resulting from this supporting low-level convergence and conditional or potential instability, especially in the southern flank of an MCC. Indeed, Merritt and Fritsch (1984) suggested that although an area of light precipitation slowly expands to conform to MCC dimensions, the strongest echoes occurred preferentially along the MCC's southern flank in some MCCs. Ultimately, the region of upper tropospheric divergence reaches its maximum intensity very close to the time of MCC dissipation. Thus, there is about a 6-hour lag (two sub-periods) between the time of peak low- to mid-level convergence and the subsequent peak in upper-level divergence, similar to that found in the tropical cloud clusters described by Frank (1978). The divergence pattern calculated by Tollerud and Esbensen (1985) for GATE cloud clusters exhibits similarities to results presented here.

Because the average divergence of the MCC pre-storm environment can mask changes in divergence caused by the MCC circulation, the change in divergence was calculated relative to the MCC-12h stage. We can see from Fig. 4.36b that during the early stages of the MCC life-cycle, the low-level convergence substantially increases in association with developing mid-level and upper-level divergence. This kind of divergence feature is similar to the divergence pattern over the

convective region of a tropical squall line as described by Houze and Rappaport (1984). Once the MCC reaches maturity and undergoes the later stages of its life-cycle, the low-level and upper-level divergence has intensified, accompanying an intensified mid-level convergence zone. In fact, these divergence characteristics bear a strong resemblance to the divergence pattern of the trailing stratiform region in Houze and Rappaport's study.

In order to test the statistical significance of the composite divergence field, the median divergence field was also calculated. This was done by first applying a 9-grid-point average to the divergence field for each individual MCC case. The median value (Nie et al., 1975) of the MCC cases in each sample was then obtained for each MCC sub-period. We can see that the pattern of the median divergence field (Fig. 4.36c) is generally consistent with the average or composite divergence field (Fig. 4.36a). Note again the upward translation of the convergence maximum between the initial and mature stages as well as the pronounced lower tropospheric divergence during the mature stage. This consistency of the divergence pattern between the median and mean cases and the comparable magnitudes of the two diagrams strengthens our confidence that essential features of the composite field is being accurately depicted. The change in the median divergence field relative to the MCC-12h stage was also calculated. We can see from Fig. 4.36d that during the early MCC lifetime, the low-level convergence substantially increases in association with developing mid-level and upper-level divergence. This again is similar to the corresponding average divergence change field (Fig. 4.36b).

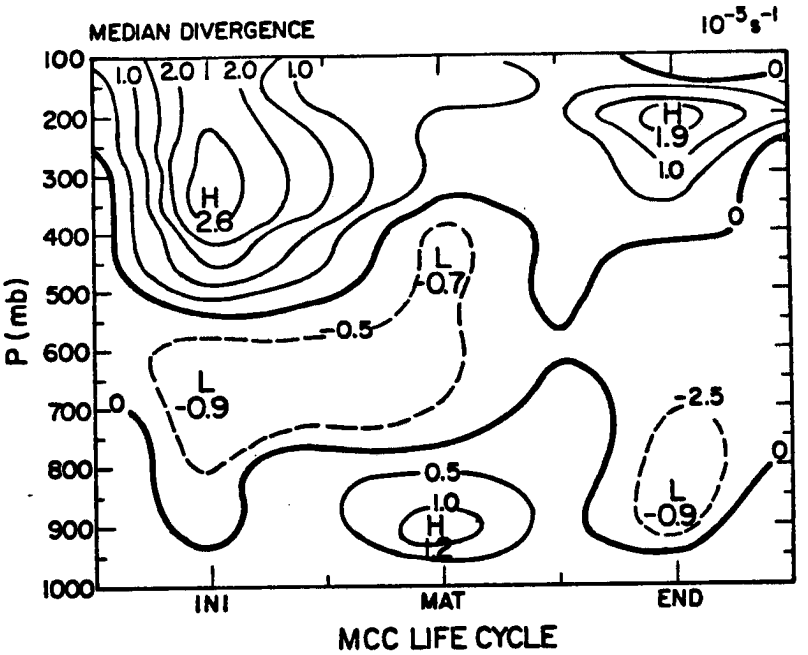

Fig. 4.36c. Height-time plot of the median divergence field. The horizontal coordinates have been rotated along the MCC track so that positive u and v values represent winds from the rear and right flank of the MCC, respectively. The divergence field is obtained by averaging MCC cases every 50 mb for each sub-period. Units: 10^{-5} s^{-1}.

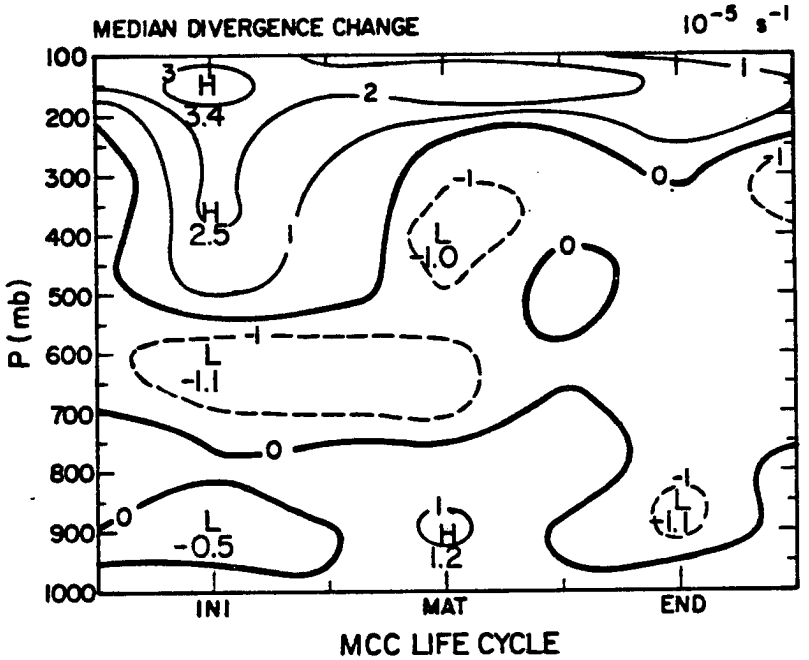

Fig. 4.36d. As in Fig. 4.36c, except for the divergence change compared to the MCC-12h stage. Units: 10^{-5} s^{-1}.

The vertical distribution of average divergence during the MCC life-cycle is presented in Fig. 4.37. We can see clearly that convergence is confined within the lower troposphere during the initial stage, but that mid-level convergence develops and reaches a maximum intensity during the mature stage at about 400 mb. As far as the upper-level troposphere is concerned, Fig. 4.37 shows an increase in divergence at about 200 mb until the dissipation stage. In fact, the divergence pattern presented here bears some resemblance to the divergence pattern of a tropical cloud cluster (Gray et al., 1982; Lee, 1986).

Time evolution plots of the average divergence at selected levels are presented in Figs. 4.38a-4.38c. Notice that the 850 mb divergence (Fig. 4.38a) which results from mesoscale downdrafts develops in the growth stage and reaches its maximum intensity at the mature stage. Because the standard deviation (Nie et al., 1975) of the average divergence is small compared to the mean value, it appears that the lower-level tropospheric divergence due to mesoscale downdrafts seen in Fig. 4.38a is a statistical significant one. Fig. 4.38b indicates that the mid-level convergence intensifies and attains a maximum intensity at the mature stage, presumably due to the upward translation of the mesoscale heating. In spite of a relatively large but still acceptable standard deviation, the persistent average divergence feature at the 200 mb level, shown in Fig. 4.38c, is evident. It is noteworthy that the maximum divergence at the dissipation stage is a significant feature. This delayed upper-level divergence is one distinguishing feature between the MCC and the tropical cloud cluster.

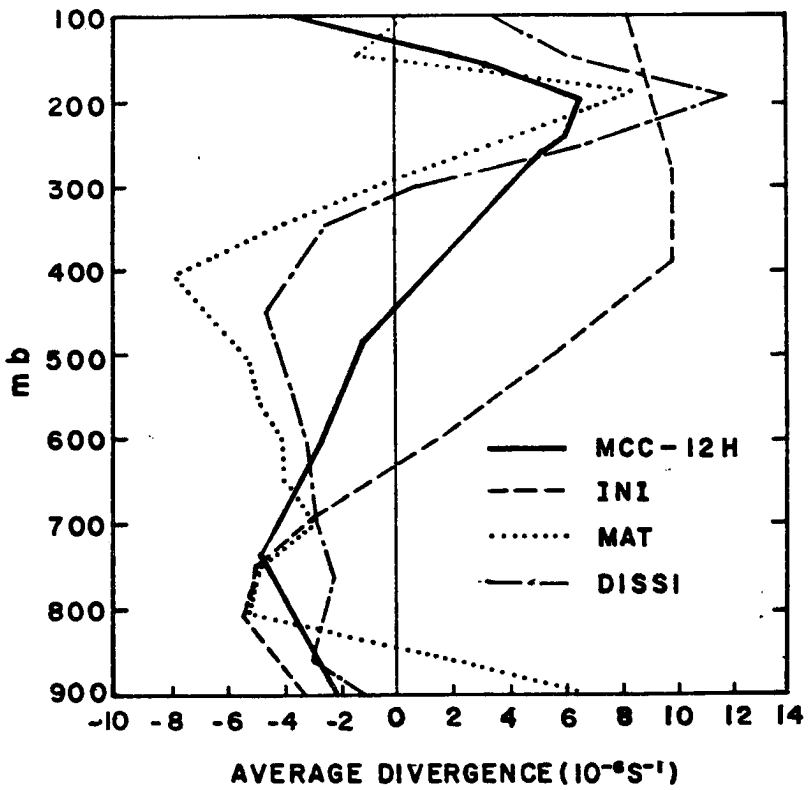

Fig. 4.37. The vertical distribution of average divergence field during the MCC-12h, initial, mature, and dissipation stages. The divergence field is obtained by averaging MCC cases every 50 mb for each sub-period. Units: 10^{-6} s^{-1}.

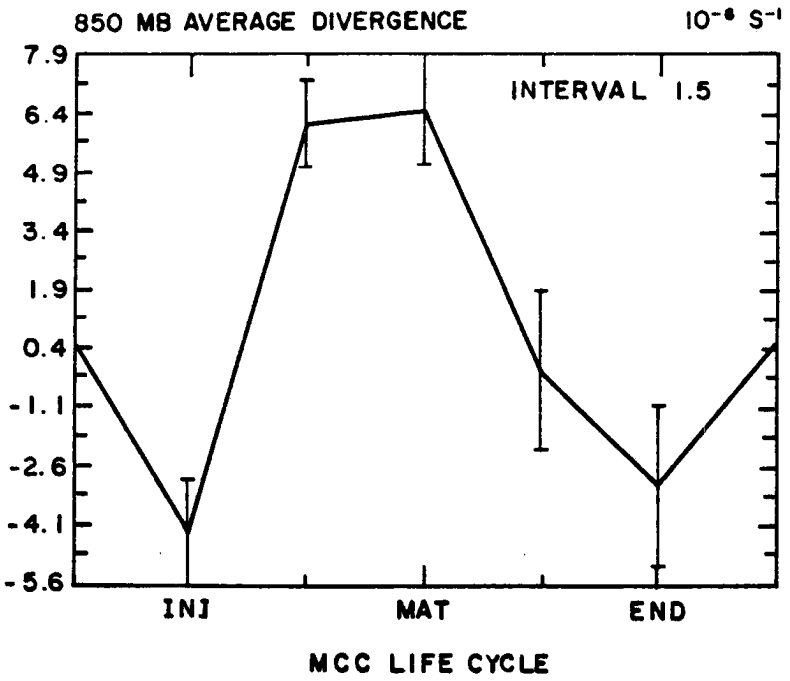

Fig. 4.38a. Time evolution plot of the average divergence at the 850 mb level. The divergence value for each MCC case is obtained by applying a 9-grid-point average. The arithmetic mean of the MCC sample is then calculated for each composite MCC sub-period. The error bars denote one standard deviation for individual MCC sub-period. Units: 10^{-6} s^{-1}.

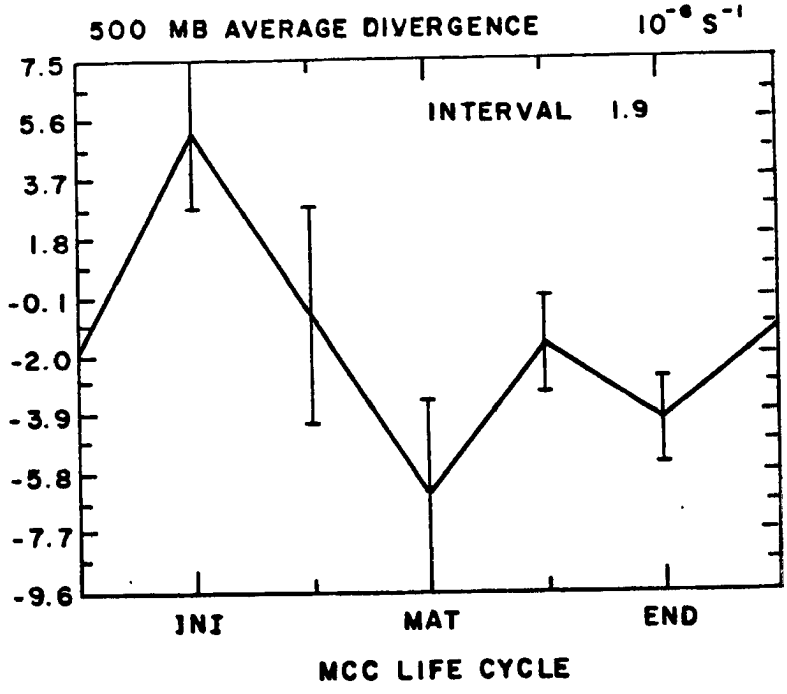

Fig. 4.38b. As in Fig. 4.38a, except for the 500 mb level. Units: 10^{-6} s^{-1}.

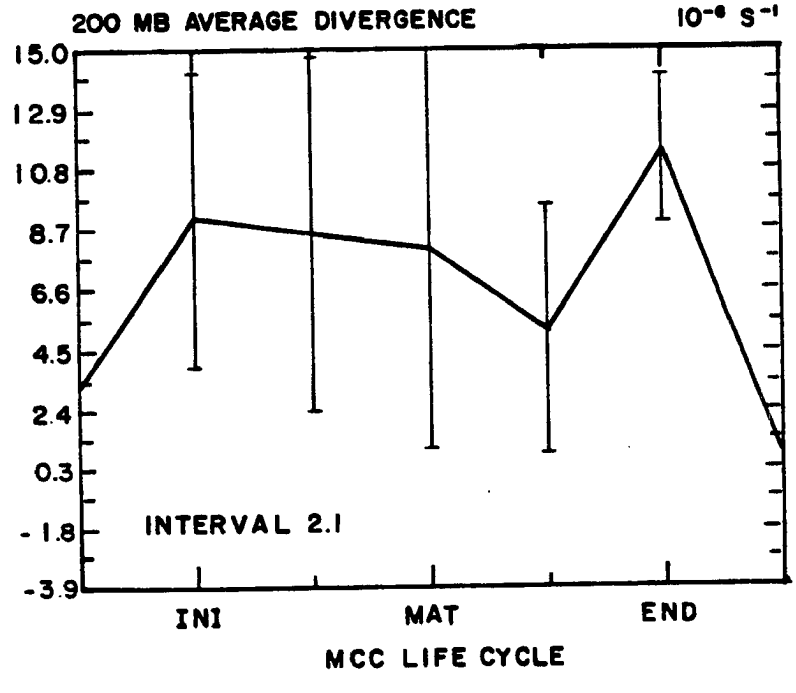

Fig. 4.38c. As in Fig. 4.38a, except for the 200 mb level. Units: 10^{-6} s^{-1}.

4.4.3 Vorticity field at various levels

The composite areally-averaged vorticity and the areally-averaged vorticity change (compared to MCC-12h stage) are shown in Figs. 4.39a and 4.39b, respectively. We see from Fig. 4.39a that the environment of the MCC is generally characterized by cyclonic vorticity below 800 mb throughout the MCC lifetime with a maximum at the 700 mb level during the growth stage. It seems that the MCC's internal dynamics start to play a more important role as the low-level vorticity increases to some extent and the MCC becomes organized. Above the 700 mb level, the MCC is basically characterized by anticyclonic flow which reaches a maximum intensity at the 200 mb level towards the end of the MCC life-cycle.

Since the average vorticity of the MCC pre-storm environment can mask changes in vorticity caused by the presence of the MCC, the change in vorticity was then calculated relative to MCC-12h stage. As seen in Fig. 4.39b, a region of positive vorticity tendency buildup between the 450 and 650 mb levels which probably results from the positive vorticity advection induced by the mid-level trough is evident during the later stages of the MCC life-cycle. Consistent with the areally-averaged vorticity distribution in Fig. 4.39a, cyclonic vorticity increases slightly (Fig. 4.39b) below the 850 mb level while substantial anticyclonic vorticity increases occur near the 200 mb level from the time of the MCC growth stage until the MCC decay stage. The major increase in cyclonic vorticity occurs near the 550 mb level. Combining the vorticity and divergence patterns, the feature of offset in the peaks of convergence (Fig. 4.36a) and vorticity (Fig. 4.39a) near middle levels (500 and 650 mb level, respectively) bears some resemblance to the squall line structure studied by Ogura and Liou (1980).

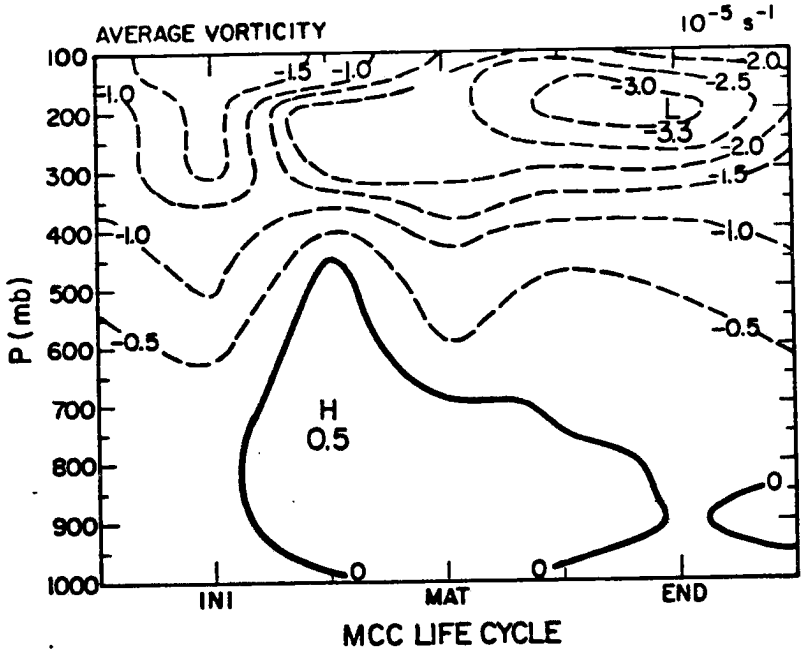

Fig. 4.39a. Height-time plot of the mean relative vorticity. The horizontal coordinates have been rotated along the MCC MCC track so that positive u and v values represent winds from the rear and right flank of the MCC, respectively. The vorticity field is obtained by averaging MCC cases every 50 mb for each sub-period. Units: 10^{-5} s^{-1}.

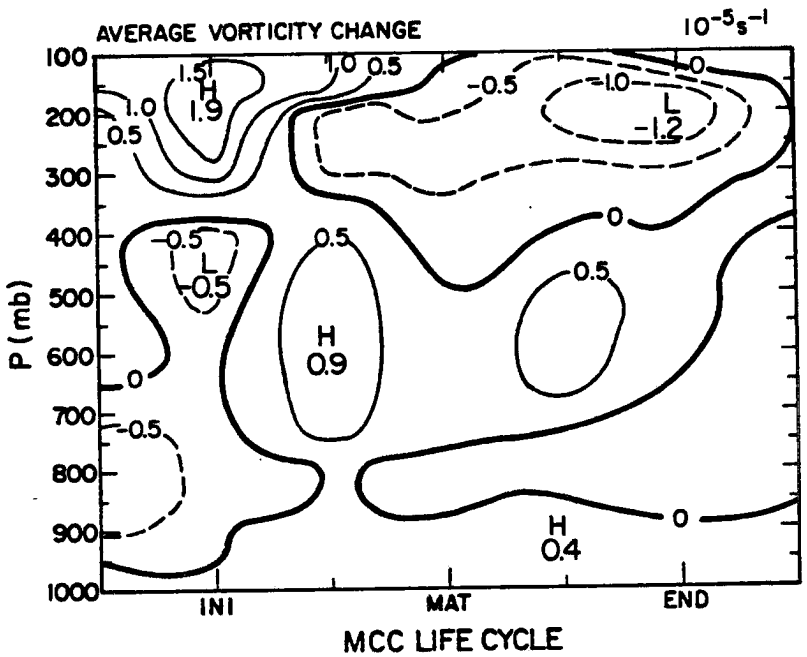

Fig. 4.39b. As in Fig. 4.39a, except for the change of vertical component of the relative vorticity compared to the MCC-12h stage. Units: 10^{-5} s^{-1}.

In order to assess the statistical significance of the relative vorticity composite, the median relative vorticity and the change of median relative vorticity are presented in Figs. 4.39c and 4.39d, respectively. We can see that the pattern of the median relative vorticity field (Fig. 4.39c) is generally consistent with the average relative vorticity field (Fig. 4.39a) in the upper troposphere with a maximum anticylonic vorticity present at the 200 mb level. However, in the lower troposphere, the median relative vorticity profile exhibits an earlier maximum in cyclonic vorticity during the initial stage at about 700 mb (in contrast to the maximum cyclonic vorticity which occurs at the growth stage in Fig. 4.39a). Also, the median relative vorticity shows intensive anticyclonic vorticity in the lower troposphere during the decay stage. The change in the median relative vorticity field was calculated relative to the MCC-12h stage. We can see from Fig. 4.39d that the low-level cyclonic vorticity increases during the initial stage in response to the low-level convergence, while the upper-level anticyclonic vorticity maximizes at the dissipation stage.

The vertical distribution of average relative vorticity during the MCC life-cycle is presented in Fig. 4.40. We can see clearly that the cyclonic vorticity is confined within the lower troposphere both before and after the initial stage. Notice that the mid-level anticyclonic vorticity decreases after the initial stage, implying the presence of a developing cyclonic vorticity which is masked by pronounced anticyclonic vorticity in the initial fields. As far as the upper-level feature is concerned, Fig. 4.40 exhibits an increase of the relative anticyclonic vorticity field until the dissipation stage at about 200 mb consistent with the divergence field (Fig. 4.37).

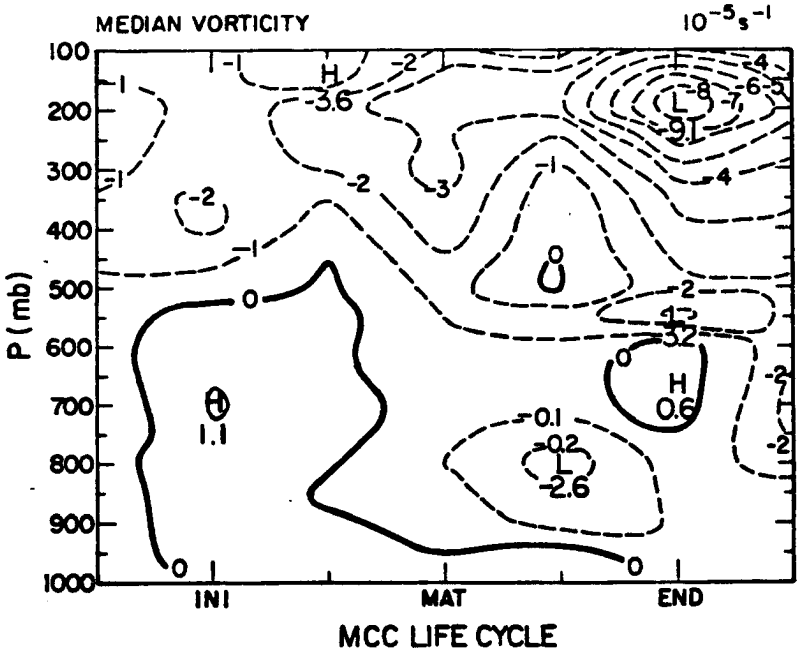

Fig. 4.39c. Height-time plot of the median relative vorticity. The horizontal coordinates have been rotated along the MCC MCC track so that positive u and v values represent winds from the rear and right flank of the MCC, respectively. The vorticity field is obtained by averaging MCC cases every 50 mb for each sub-period. Units: 10^{-5} s^{-1}.

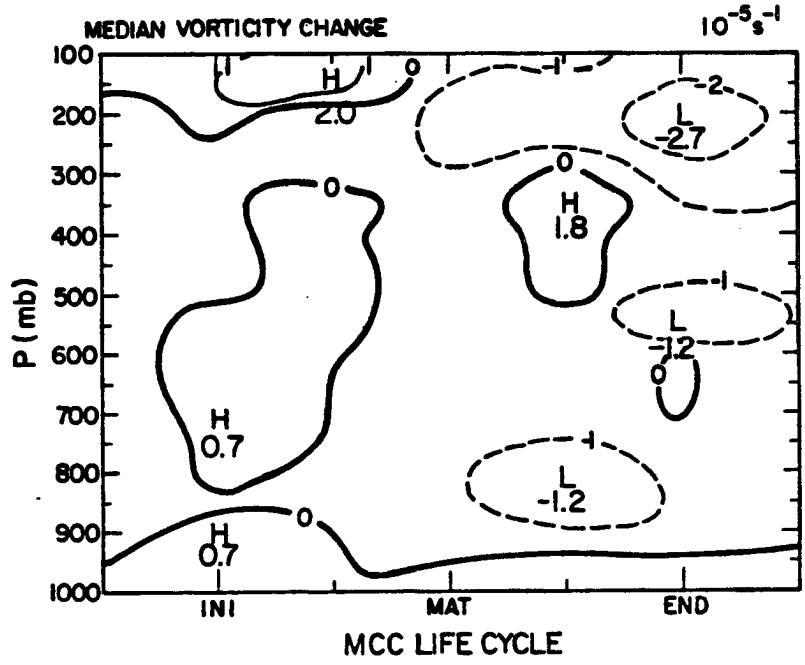

Fig. 4.39d. As in Fig. 4.39c, except for the change of vertical component of the relative vorticity compared to the MCC-12h stage. Units: 10^{-5} s^{-1}.

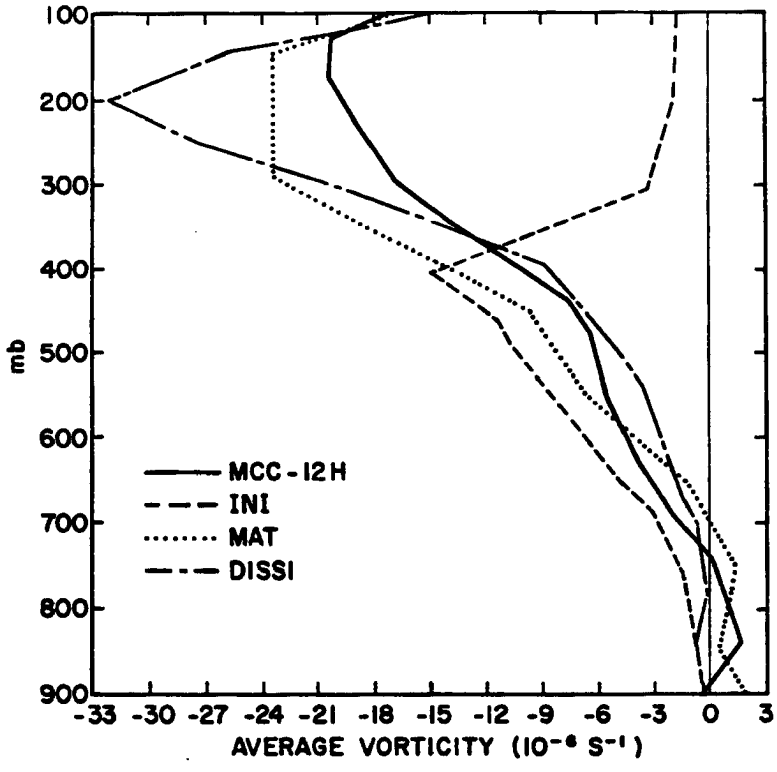

Fig. 4.40. The vertical distribution of average relative vorticity field during the MCC-12h, initial, mature, and dissipation stages. The relative vorticity field is obtained by averaging MCC cases every 50 mb for each sub-period. Units: 10^{-6} s^{-1}.

Time evolution plots of the average relative vorticity at selected levels are shown in Figs. 4.41a-4.41c along with error bars based on the standard deviation of the relative vorticity values for each level and sub-period. Notice that the 700 mb cyclonic vorticity (Fig. 4.41a) which results from the enhanced convergence attains a maximum intensity at the growth stage. Thereafter, the vorticity, an average, becomes anticyclonic but the variability is so large that a clear trend is not discernable. Possibly, the relative vorticity of an MCC system is more or less determined by the environment. Fig. 4.41b indicates that the mid-level cyclonic vorticity intensifies and attains a maximum intensity at the growth stage, presumably due to the upward translation of the mesoscale heating and convergence. Although the standard deviation of the relative vorticity is relatively large compared to the mean relative vorticity value, the persistent average anticyclonic vorticity feature at 200 mb level can be seen in Fig. 4.41c. It is note worthy that the pronounced anticyclonic vorticity of this level during the decay and the dissipation stages is significant. Again, this delayed upper-level anticyclonic vorticity is consistent with the upper-level divergence discussed earlier field (Fig. 4.38c).

The genesis potential, defined as the relative vorticity difference between lower and upper levels (Gray et al., 1982), could serve as an indicator of the efficiency of energy import versus export as well as atmospheric ventilation. Emanuel (1983) described this feature of strong vertically differentiated vorticity as a system's "dynamic flywheel" effect, such that the persistent action of an ensemble of convective elements is able to store the energy on a large scale, which in turn supports the convection. The more persistent the low-level

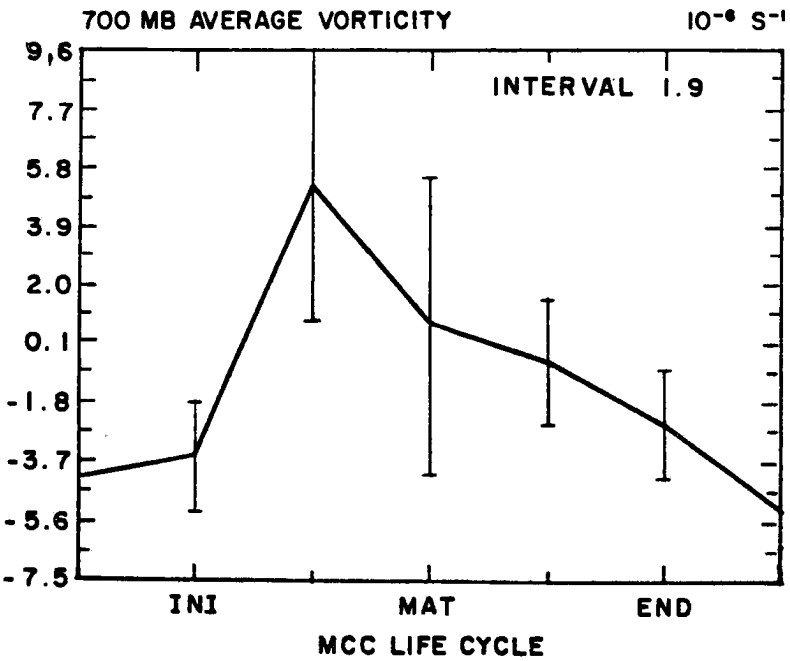

Fig. 4.41a. Time evolution plot of the average relative vorticity at the 700 mb level. The divergence value for each MCC case is obtained by applying a 9-grid-point average. The arithmetic mean of the MCC sample is then calculated for each composite MCC sub-period. The error bars denote one standard deviation for individual MCC sub-period. Units: 10^{-6} s^{-1}.

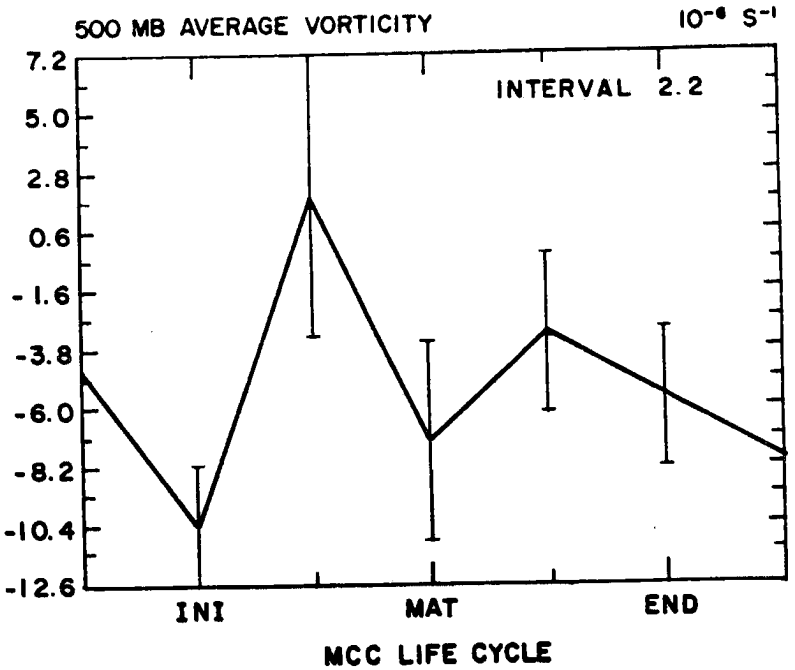

Fig. 4.41b. As in Fig. 4.41a, except for the 500 mb level. Units: 10^{-6} s^{-1}.

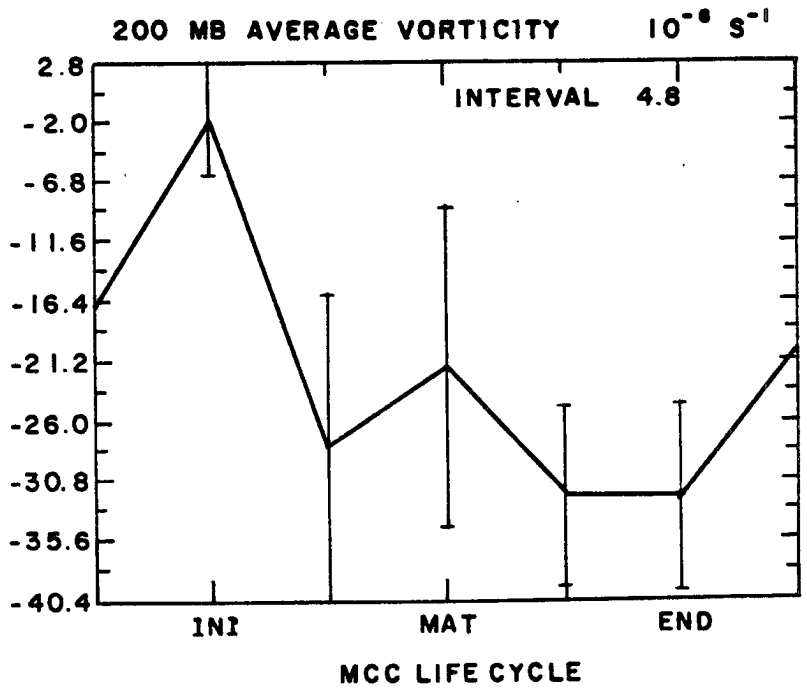

Fig. 4.41c. As in Fig. 4.41a, except for the 200 mb level. Units: 10^{-6} s^{-1}.

cyclonic and upper-level anticyclonic flow remains (i.e., the low-level cyclonic vorticity field aligned with the upper-level anticyclonic vorticity pattern), the more likely is the development of convective elements to release the potential instability. Fig. 4.42 shows that the time evolution of the genesis potential field matches the evolution of the MCC cloud shield.

4.4.4 Vertical motion field

The vertical motion field as assessed from the kinematic method (i.e., integration of the continuity equation) is a diagnostic tool to examine the net response of the atmosphere to the sum total of convective- to synoptic-scale lifting mechanisms present. Therefore, the presence of vertical motion is a demonstration of the existence of forcing mechanisms. After applying a mass-adjustment scheme (O'Brien, 1970) to the divergence calculation, the vertical velocity (ω) presented in this section was diagnosed kinematically. The lower boundary condition $\omega = 0$ was used at the p = 1000 mb level, and the upper boundary condition $\omega = 0$ was applied at the p = 100 mb level. The calculated composite vertical motion represents the combined effects of average convective-scale, mesoscale, and large-scale vertical motions. The areally-averaged composite vertical motion and areally-averaged vertical motion change (compared to MCC-12h stage) are illustrated in Figs. 4.43a-4.43b. We can see from Fig. 4.43a that the strongest average upward motion is centered near 700 mb level early in the system's life-cycle. This may be attributed to the low-level convergence which reflects the dominant contribution from deep convection. Although the individual convective updraft maximum may extend up to the 400 mb level, this phenomenon of developing an

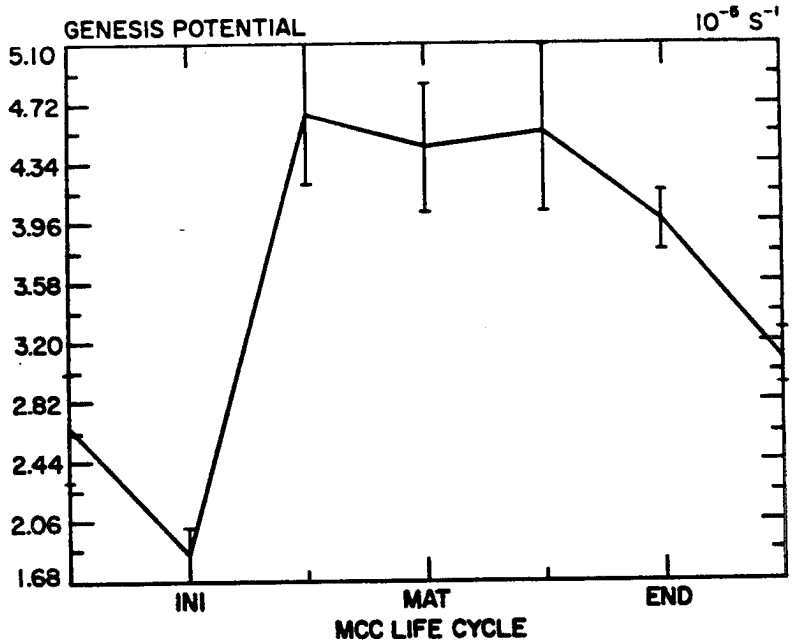

Fig. 4.42. Time evolution plot of genesis potential. The value is obtained for a 9-grid-point average. Units: 10^{-5} s^{-1}.

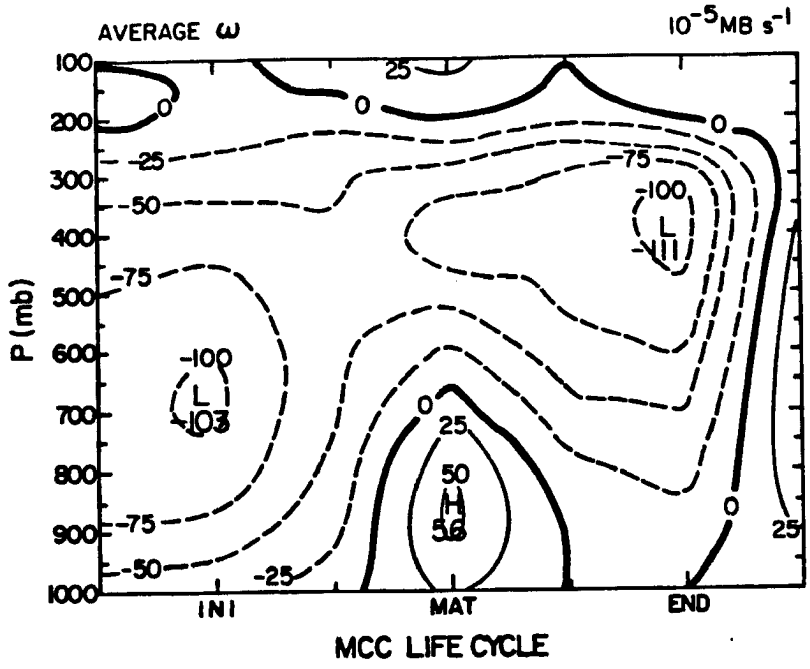

Fig. 4.43a. Height-time plot of the vertical motion. The vertical motion field is obtained by applying a 9-grid-point area average over a 6° X 6° lat.-long. domain every 50 mb. Units: 10^{-5} mb s^{-1}.

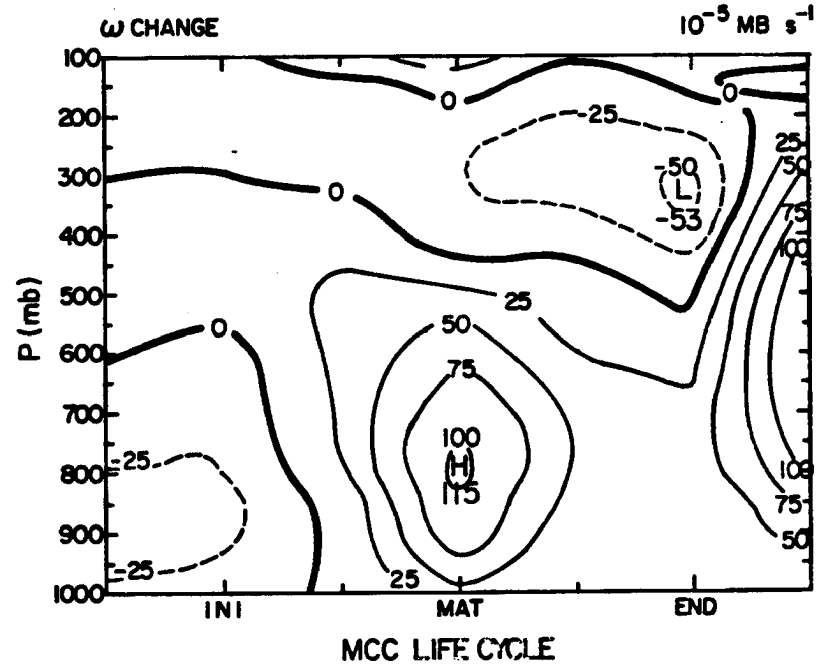

Fig. 4.43b. As in Fig. 4.43a, except for the change of vertical motion compared to the MCC-12h stage. Units: 10^{-5} mb s^{-1}.

areally-averaged low-level maximum in upward vertical motion during the early growth stage is commonly observed in tropical cloud clusters (Frank, 1978; Tollerud and Esbensen, 1985; Lee, 1986) and tropical squall lines (Houze and Rappaport, 1984; Gamache and Houze, 1985). However, Houze (1982) has shown that mesoscale anvils contribute to a peak in the convective heating in the mid to upper troposphere, whereas the peak due to cumulus heating is found in the mid to lower troposphere. The peak upward vertical velocity reaches values up to 2.37 $\mu b\ s^{-1}$ (205 mb day^{-1}) as the system evolves into the mature stage. This is due to the combined effects of deep convection and increased up-scale development of meso-β-scale convective elements. Usually, the strongest vertical transport of moist static energy is due to the meso-γ convective motions and meso-β elements. Later in the MCC life-cycle, the upward motion maximum gradually shifts upward to the 400 mb level while mesoscale updrafts prevail as a distinguishing characteristic of the thick MCC stratiform cloud shield. The upward translation of the vertical motion center is a result of the elevation in heating (see Section 5.2.2).

Kinematically, the mid-level convergence contributes to the development of the large upward velocities within the thick stratiform cloud canopy; these are tied together through the continuity equation. Molinari and Corsetti (1985) incorporated the cloud-scale and mesoscale downdrafts into a cumulus parameterization scheme in their simulation of an MCC. They reported that the upward motion maximum shifted to 400 mb level as the system matured, suggesting that upper-level heating generated the mid-level convergence and maintained the mesoscale anvil updraft. A similar upper-tropospheric maximum in upward motion has been

seen in composite analyses as well as in individual case studies of mature non-squall tropical cloud clusters (Frank, 1978; Tollerud and Esbensen, 1985). A feature which is not so evident in the tropical clusters, however, is the deep layer of downward motion below 700 mb level at the time of MCC maturity. Even during the dissipation stage, the small upward velocity (through cancellation) in the lower troposphere reflects the presence of the mesoscale downdraft as suggested by Zipser (1969, 1977) and Gamache and Houze (1982).

The height-time diagram for vertical motion change (Fig. 4.43b) indicates that the upward motion has not only intensified in the lower troposphere during the early MCC life-cycle but has also strengthened in the upper troposphere after the MCC growth stage. It also shows that downward motion develops below the 500 mb level after the MCC growth stage and that this downward motion extends to the entire troposphere by the MCC dissipation stage.

The vertical distribution of the average omega field during the MCC life-cycle is shown in Fig. 4.44. We can see clearly that mean upward motion prevails throughout the entire troposphere during the MCC life-cycle except for the lower tropospheric downward motion at the MCC mature stage. Notice that the level of the maximum upward motion lifts from 700 mb at the initial stage to 400 mb at the mature stage.

4.5 Comparison of the impact of geography on MCCs

In this section, the difference between the composite pairs constructed for orogenic and Plains MCCs are discussed.

4.5.1 Comparison between orogenic MCCs and Plains MCCs

A comparison of the mean characteristics of orogenic and Plains MCCs permits the examination of the impacts of geography on their

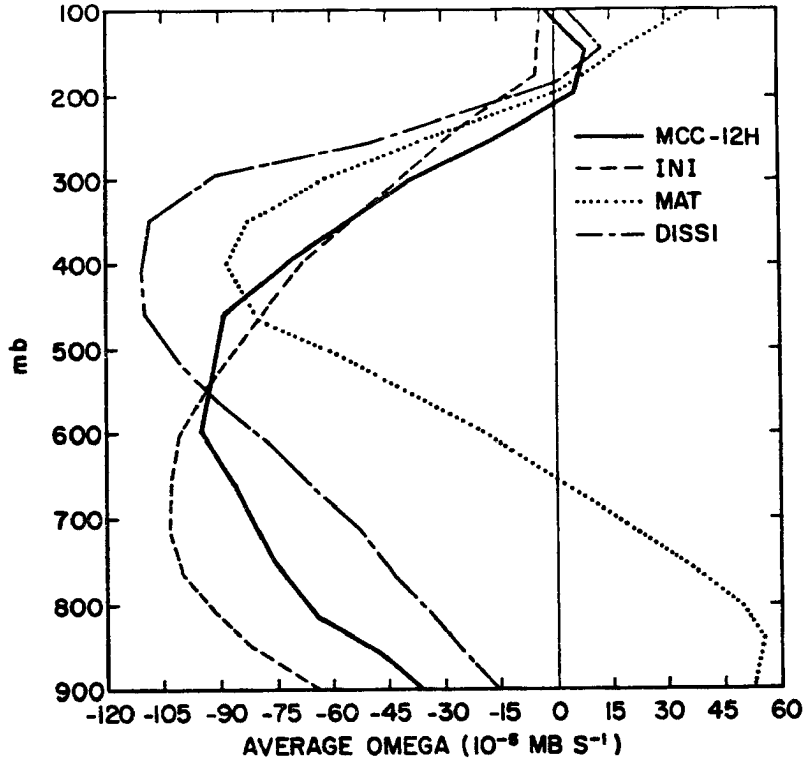

Fig. 4.44. The vertical distribution of average omega field during the MCC-12h, initial, mature, and dissipation stages. The omega field is obtained by averaging MCC cases every 50 mb for each sub-period. Units: 10^{-5} mb s^{-1}.

evolution. The fundamental causes which result in dynamical differences between the ensuing orogenic MCCs and Plains MCCs basically arise from the differential characteristics of the atmospheric background in which the MCCs are embedded. McAnelly and Cotton (1986) argued that the orogenic MCCs (WMCC) are usually formed from mountainous "hot spots" or from the intersections of multiple meso-β-scale discontinuities, while Plains MCCs (EMCC) are more or less linked to a unique meso-α- to meso-β-scale discontinuity. The time-height cross-sections of mixing ratio (Figs. 4.45a-b) and θ_e (not shown) indicate that WMCCs exhibit earlier maxima of moisture content and energy supply at the growth stage in contrast to EMCCs' maxima at their mature stage. In addition, the CAPE profiles shown in Figs. 4.46a-b illustrate that the WMCCs generally have larger values of CAPE during their early life-cycle than the EMCCs. It may be inferred that, for the WMCC case, a more random or chaotic pattern of meso-β convective elements consume less of the provided potential energy than EMCC case. The strong support from abundant moisture content and a highly potentially unstable environment possibly associated with multiple forcing mechanisms allows the WMCC to be a longer-lasting system.

The wind field distribution of these two systems (Figs. 4.47a-d) has several intriguing features. The WMCC's wind field is characterized by a weaker westerly and stronger southerly wind component, while the EMCC is associated with intensified northwesterly flow instead. These configurations imply that a WMCC is favored or is likely to occur on the western flank of an upper-level ridge while an EMCC is most likely to be found on the eastern flank. The EMCC's stronger westerly component may be due either to the orientation or to the strength of the eastern flank

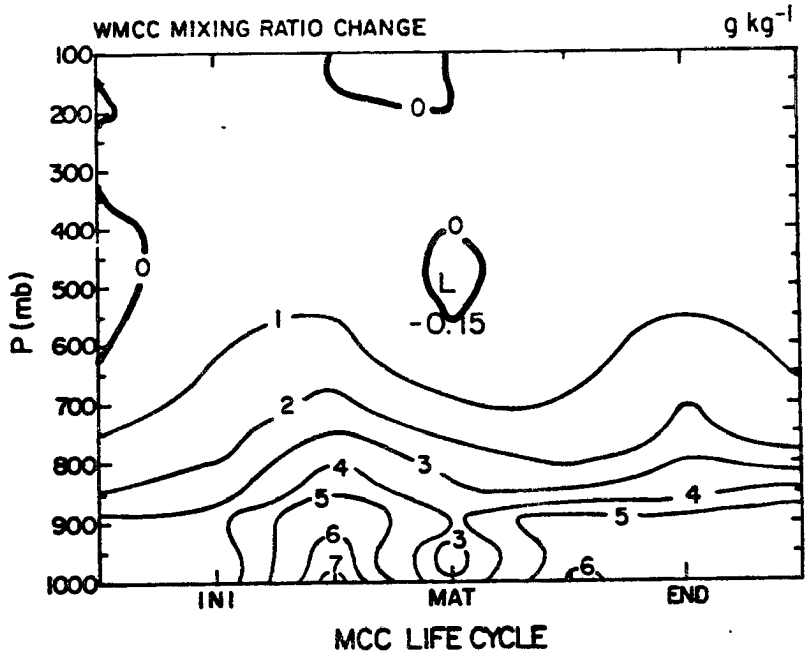

Fig. 4.45a. Height-time plot of the mixing ratio difference from its corresponding value at the MCC-12h stage for the orogenic MCCs case. The mixing ratio field is obtained by applying a 9-grid- point area average over a 6° X 6° lat.-long. domain every 50 mb. Units: g kg^{-1}.

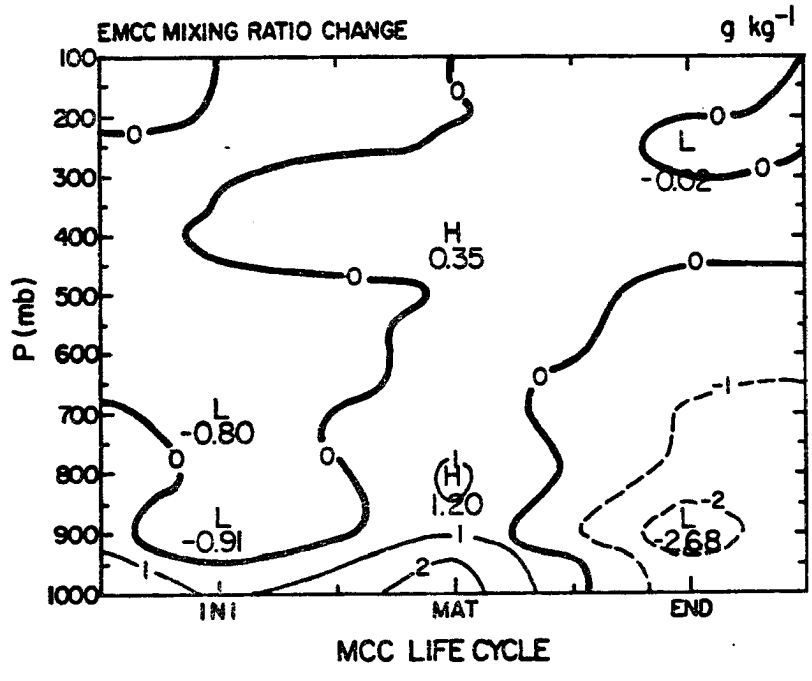

Fig. 4.45b. As in Fig. 4.45a, except for the Plains MCCs case. Units: g kg^{-1}.

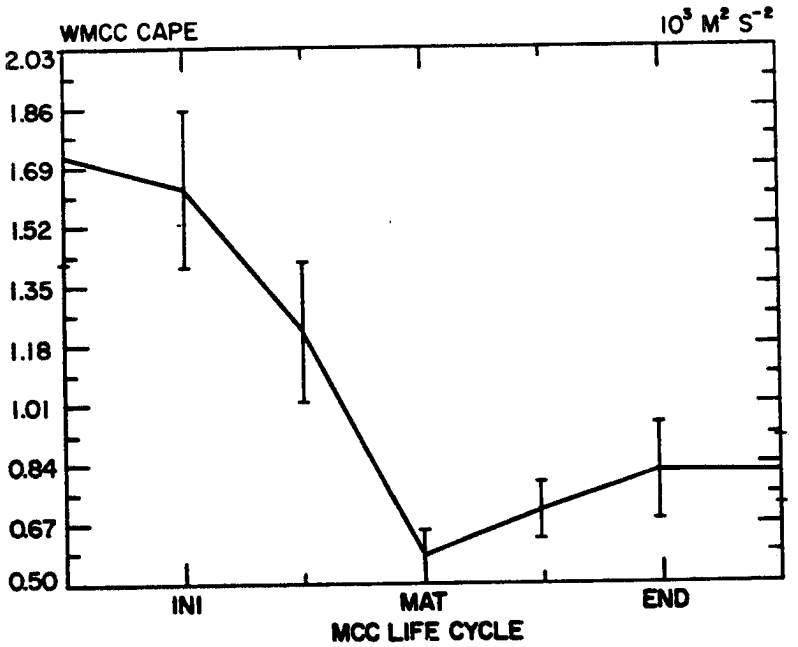

Fig. 4.46a. Time evolution plot of CAPE for the orogenic MCCs case. The value is obtained for a 9-grid-point average. Units: 10^3 m^2 s^{-2}.

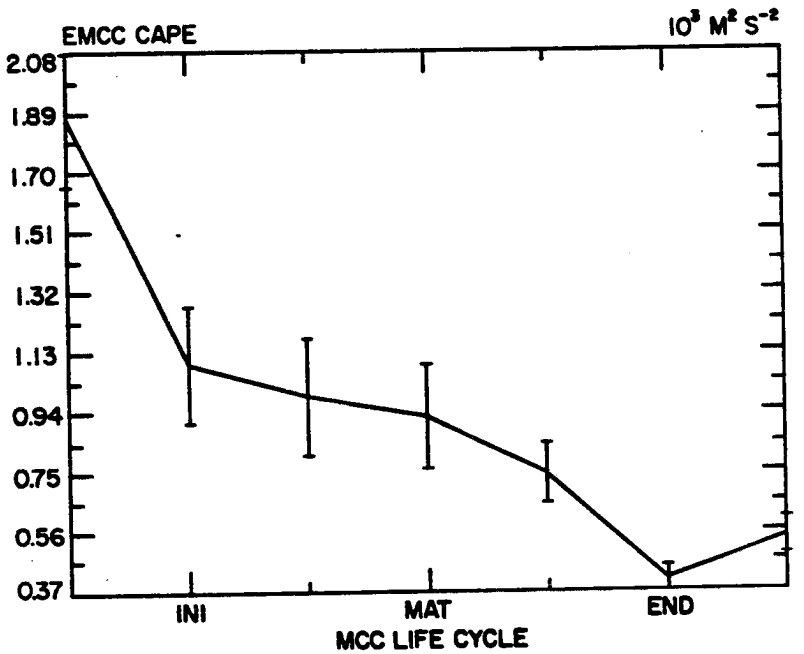

Fig. 4.46b. As in Fig. 4.46a, except for the Plains MCCs case. Units: 10^3 m^2 s^{-2}.

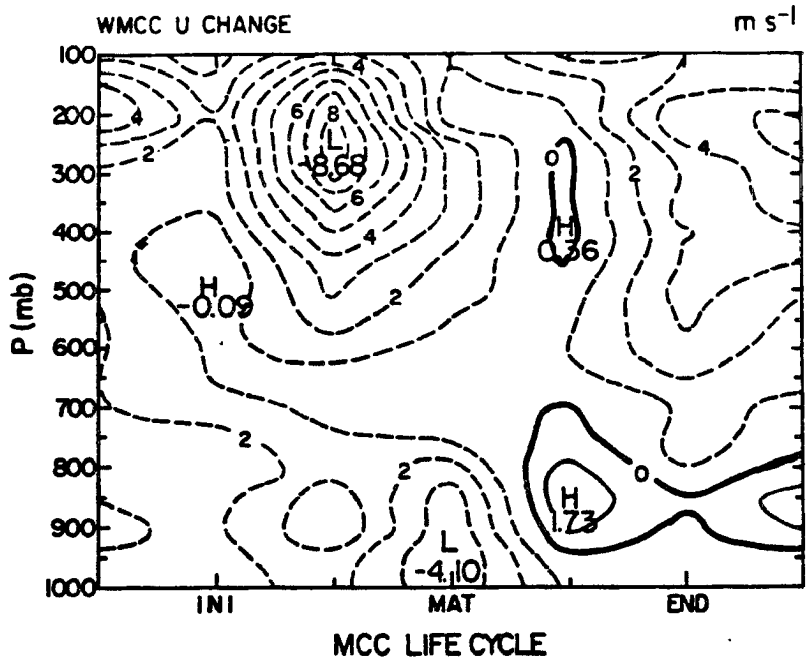

Fig. 4.47a. Height-time plot of the u-component change compared to its corresponding value at the MCC-12h stage for the orogenic MCCs case. The central point of the 9-point average is located one grid point west of the MCC centroid. Units: m s^{-1}.

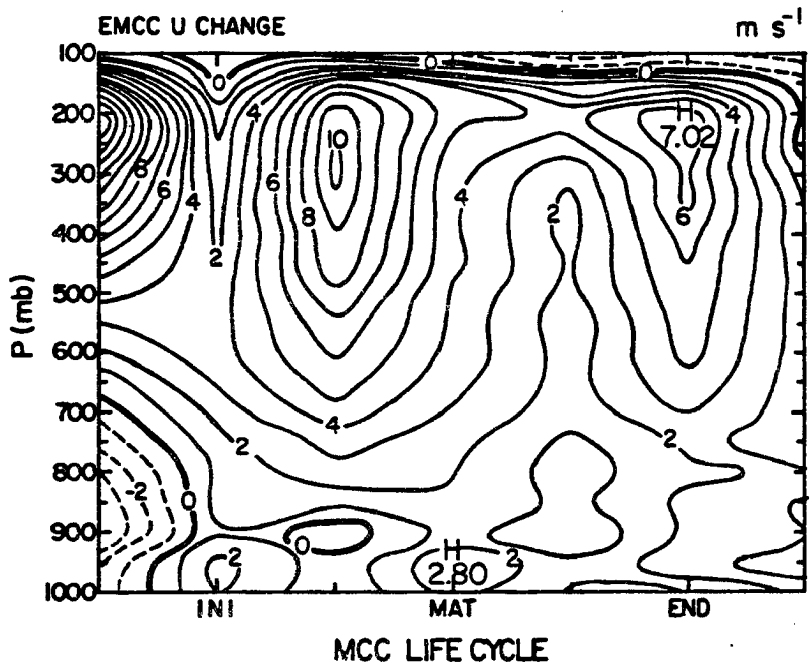

Fig. 4.47b. As in Fig. 4.47b, except for the Plains MCCs case. Units: m s^{-1}.

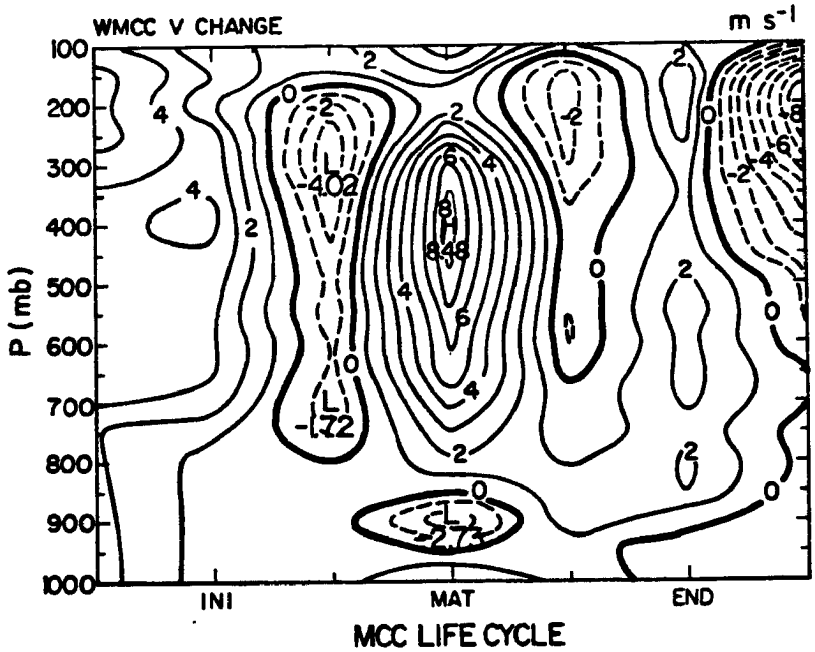

Fig. 4.47c. Height-time plot of the v-component change compared to its corresponding value at the MCC-12h stage for the orogenic MCCs case. The central point of the 9-point average is located one grid point south of the MCC centroid. Units: m s^{-1}.

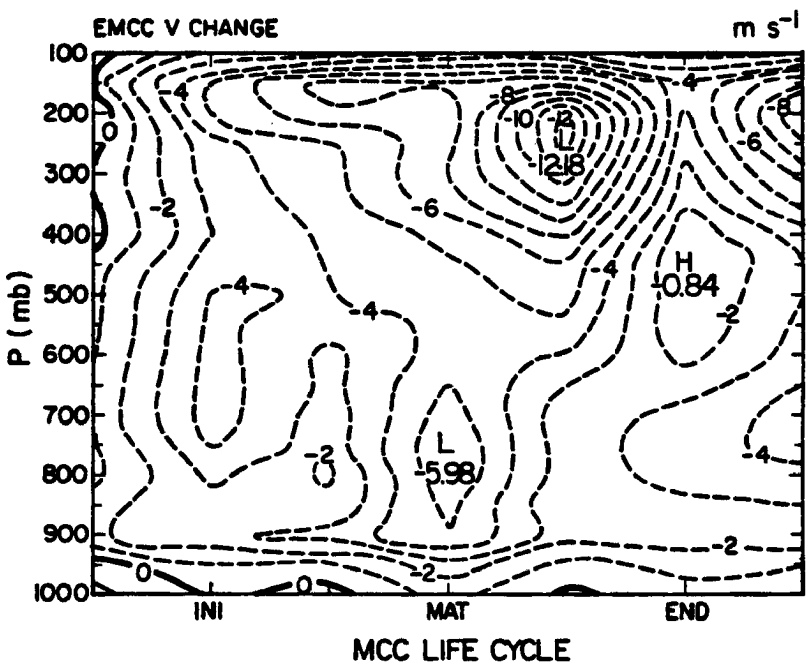

Fig. 4.47d. As in Fig. 4.47c, except for the Plains MCCs case. Units: m s^{-1}.

of the ridge. The temperature advection fields depicted in Figs. 4.48a and 4.48b support the above arguments. THe WMCC experiences widespread warm advection throughout its life-cycle; on the other hand, the EMCC is characterized by mid- to upper-level cool advection after the growth stage once it lags behind the trough. Moreover, the temperature change fields (not shown) also reflect the temperature advection pattern such that the WMCC is characterized by low- and upper-level warming while the EMCC is dominated by widespread cooling. In fact, the 1200 GMT data prior to the MCCs' initiation which was used to compare the MCC formative backgrounds shows that the nascent WMCC's centroid is located at 104^{o} west longitude on average in contrast to the EMCC's centroid which is located at 97^{o} on average. The former position lies along the eastern slope of the Rocky Mountains about 1.5 km above mean sea level, the latter is near the central Plains at an elevation of 0.5 km or so above mean sea level. Therefore, it is relatively easier for the WMCC (originated at elevated surface compared to EMCC case) to encounter warmer air which at least partly explains the warming trend.

The areally-averaged divergence field of the composite WMCC (Fig. 4.49a) indicates that the pronounced boundary-layer convergence has widened and lifted to mid-level (maxima near 700 mb and 500 mb levels) by the mature stage, then remains steady for the rest of its lifetime. In comparison, the EMCC's areally-averaged divergence field (Fig. 4.49b) shows a less intense convergence throughout its life-cycle. These configurations support the hypothesis of greater long-lasting low-level convergence support for the WMCC than the EMCC. In response to the divergence distributions, the vertical motion field of the WMCC (Fig. 4.49c) possesses a stronger upward motion maximum near 650 mb level at

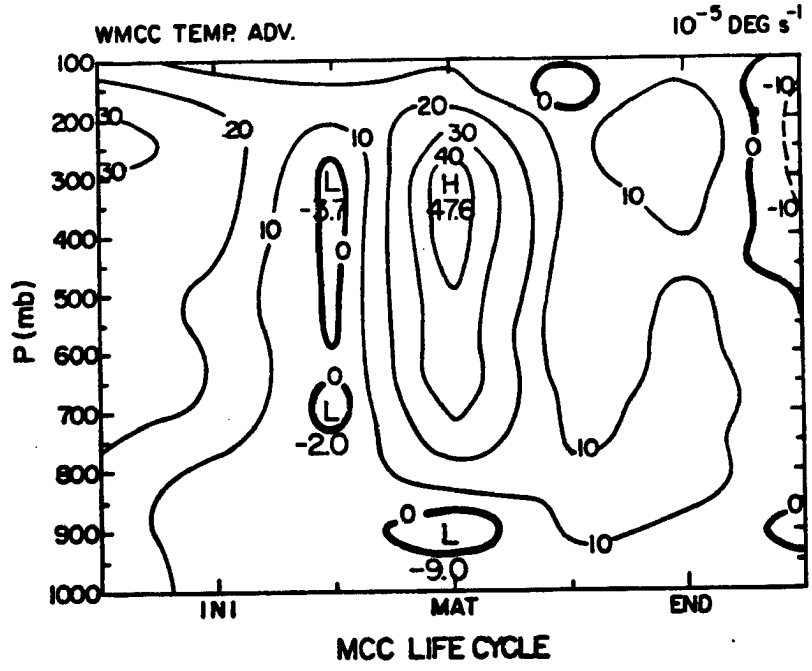

Fig. 4.48a. Height-time plot of the temperature advection for the orogenic MCCs case. The value is obtained for a 9-grid-point average every 50 mb. Units: 10^{-5} K s^{-1}.

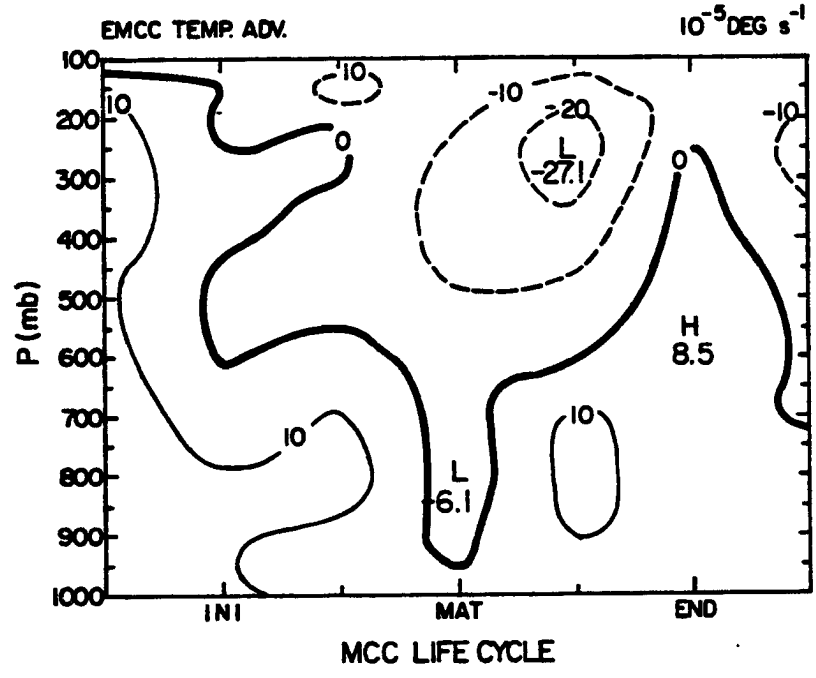

Fig. 4.48b. As in Fig. 4.48a, except for the Plains MCCs case. Units: 10^{-5} K s^{-1}.

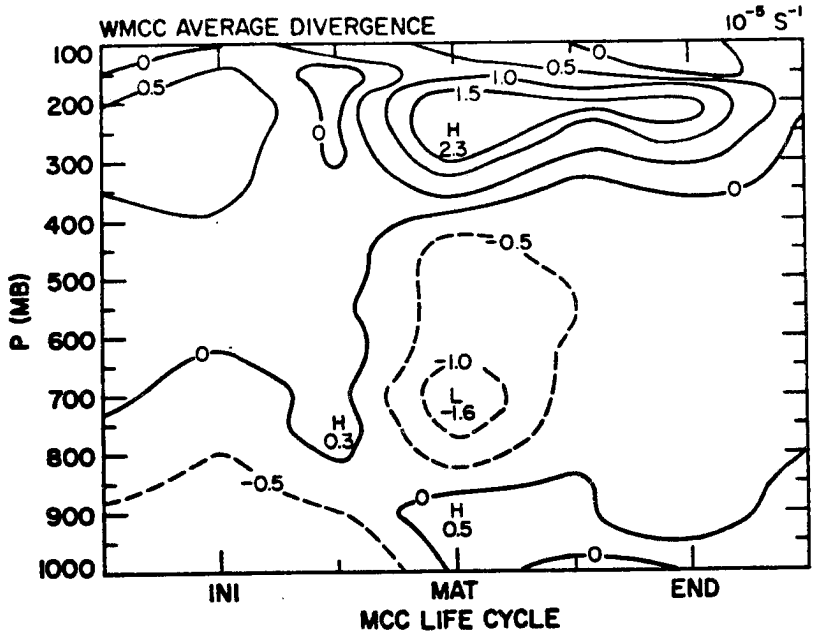

Fig. 4.49a. Height-time plot of the mean divergence field for the orogenic MCCs case. The horizontal coordinates have been rotated along the MCC MCC track. The divergence field is obtained by averaging MCC cases every 50 mb for each sub-period. Units: 10^{-5} s^{-1}.

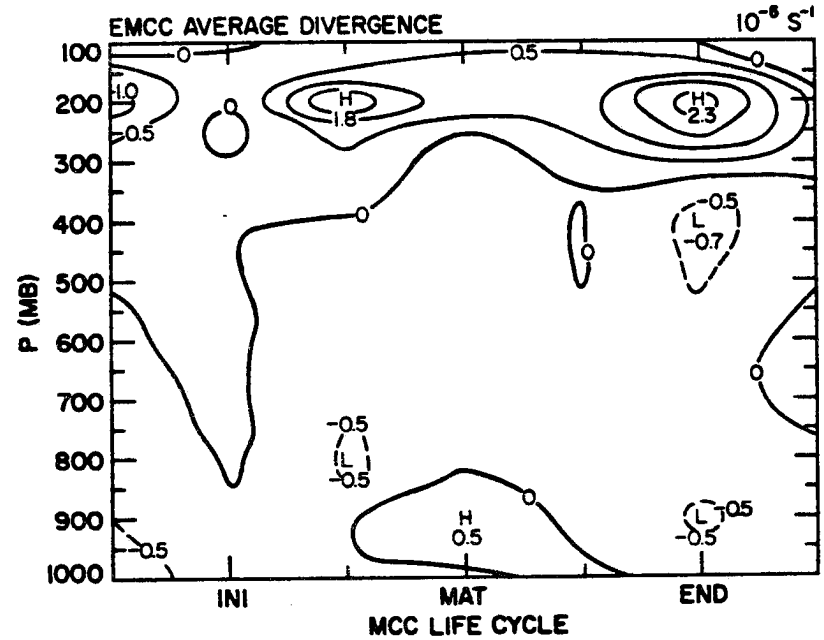

Fig. 4.49b. As in Fig. 4.49a, except for the Plains MCCs case. Units: 10^{-5} s^{-1}.

the initial stage which then gradually shifts to 400 mb level at the mature stage. The counterpart for the EMCC (Fig. 4.49d) has significant downward motion at the mature stage in association with an upward motion maximum centered at about 400 mb level at the growth and dissipation stages without the accompaniment of any upward motion center due to the absence of mid-level convergence at the mature stage. The relative vorticity fields (Figs 4.50a-b) depict an early cyclonic maximum at the growth stage for the WMCC in contrast to the EMCC whose maximum occurs at its mature stage. These features reflect that the EMCC possesses a more efficient "dynamic flywheel" at its mature stage rather than the WMCC's weaker but long-lasting feature. In summary, the WMCC owes its existence to the more moist and potentially unstable background atmosphere under weaker steering flow over a longer period. Those features support that the WMCC is characterized by a more random or chaotic pattern of meso-β-scale convective elements due to the variety of triggering mechanisms compared to the EMCC as suggested by McAnelly and Cotton (1986).

4.6 Summary

The composite results based on a coordinate system determined by the direction of MCC movement reveal a number of distinctive characteristics of the MCC's structure, dynamics, and thermodynamics during its life-cycle. It is clear that several of the contributing factors come together and interact over the threat area several hours before the ensuing MCC develops. Note that the synoptic-scale circulation provides the abundant moisture and potentially unstable environment through certain destabilization processes. The MCCs seem to be driven by a combination of dynamic and thermodynamic processes which

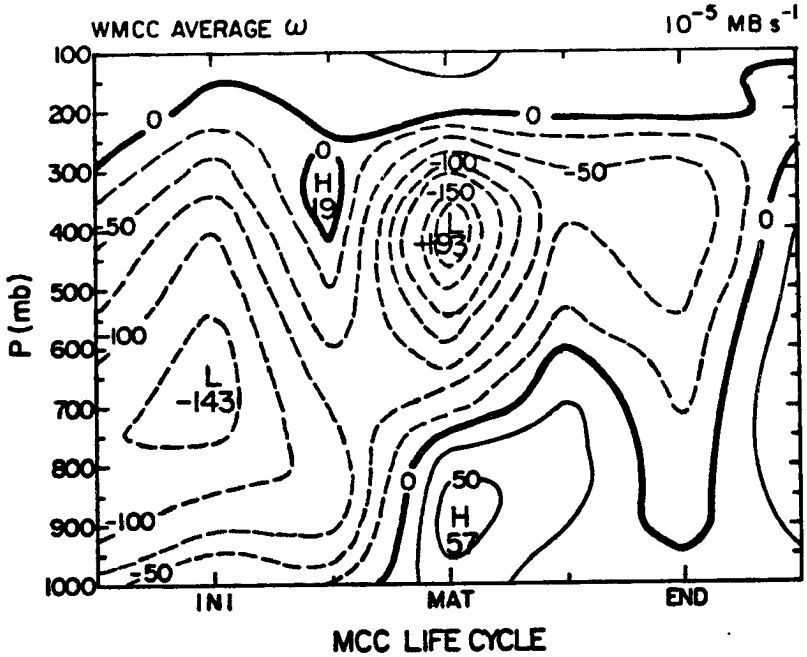

Fig. 4.49c. Height-time plot of the vertical motion for the orogenic MCCs case. The vertical motion field is obtained by applying a 9- grid-point area average over a 6^{o} X 6^{o} lat.-long. domain every 50 mb. Units: 10^{-5} mb s^{-1}.

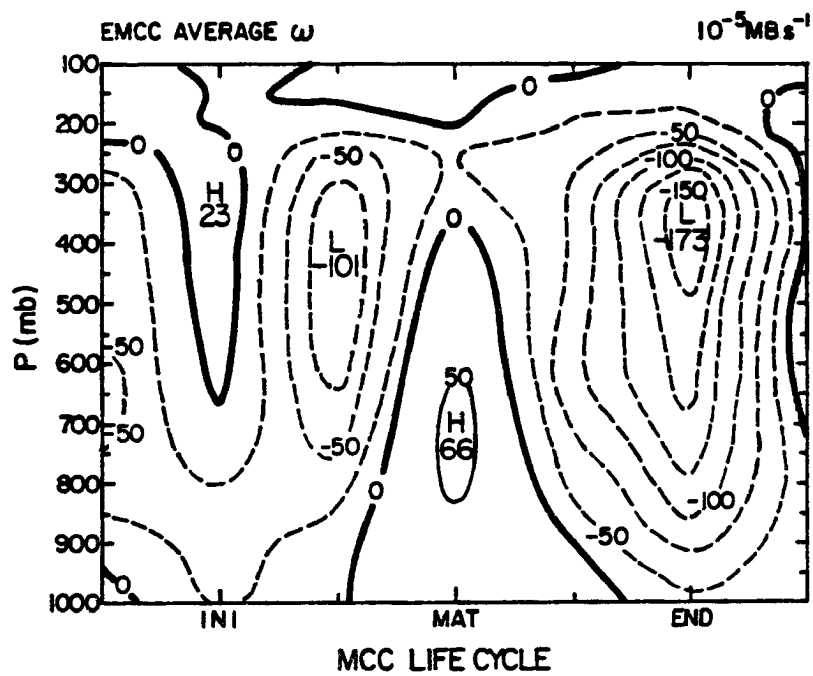

Fig. 4.49d. As in Fig. 4.49c, except for the Plains MCCs case. Units: 10^{-5} mb s^{-1}.

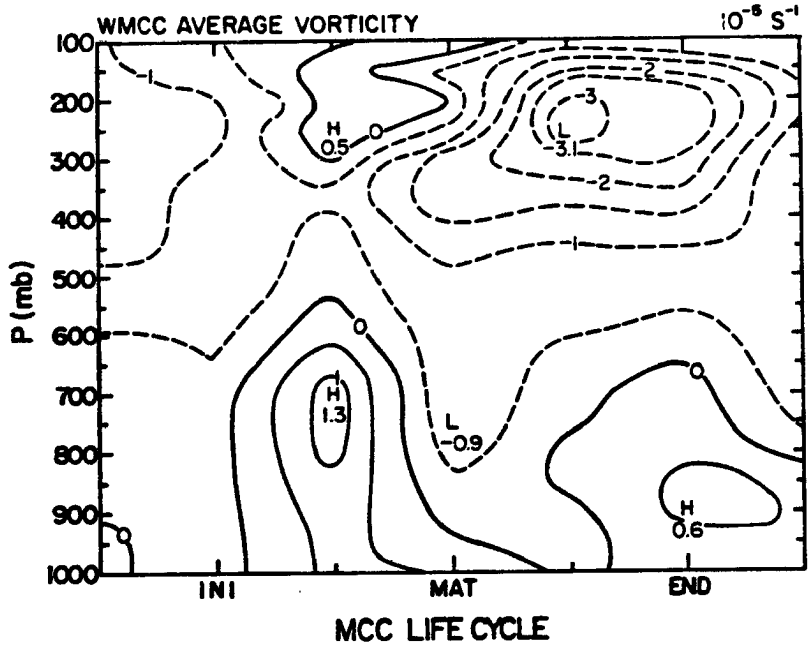

Fig. 4.50a. Height-time plot of the mean relative vorticity for the orogenic MCCs case. The horizontal coordinates have been rotated along the MCC MCC track. The vorticity field is obtained by averaging MCC cases every 50 mb for each sub-period. Units: 10^{-5} s^{-1}.

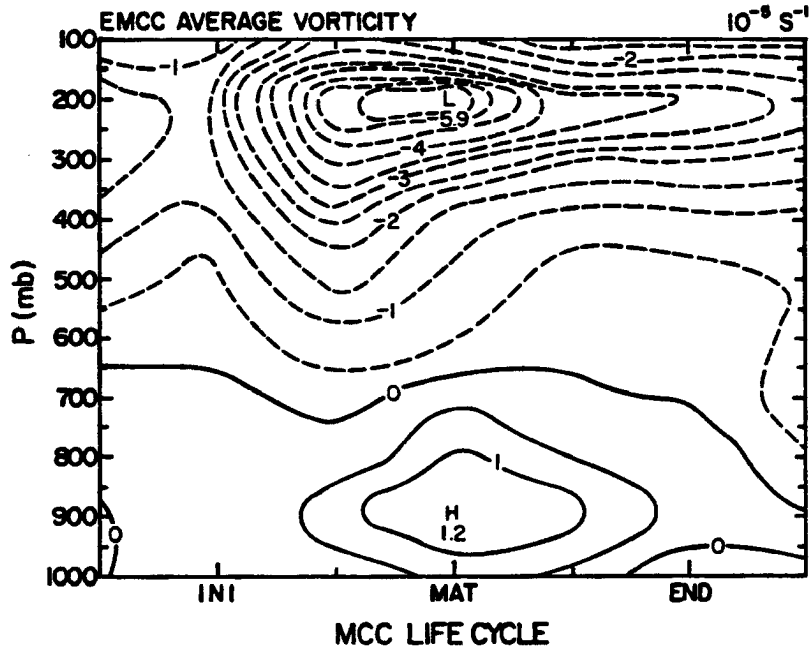

Fig. 4.50b. As in Fig. 4.50a, except for the Plains MCCs case. Units: 10^{-5} s^{-1}.

interact together. The major findings of this chapter are as follows:

1. The high horizontal θ_e gradient which exists near the MCC's centroid provides the abundant fuel supply by the growth stage for system development.
2. The CAPE reaches its maximum intensity prior to the MCC initial stage, then tapers off due to depletion by cumulus convection. It is suspected that the low-level jet acceleration may slightly offset the cumulus depletion of CAPE during the initial and growth stages.
3. The divergence pattern shows convergence limited to the lower layers in the early stages but then expanding and lifting to the middle troposphere during the MCC's growth and mature stages. The upper-level divergence increases as the system evolves and reaches its maximum intensity very close to the time of MCC dissipation. The presence of low-level mass convergence topped by upper-level mass divergence couplets helps to maintain the large flows of mass necessary to sustain the system for long periods.
4. The vorticity field analyses show the cyclonic vorticity to be confined within the surface to 700 mb layer during most of the MCC's evolution and the anticyclonic vorticity to be located exclusively in the upper troposphere. This configuration basically satisfies Emanuel's "dynamic flywheel" conceptual model for self-exciting convection.
5. Upward motion is centered near the 700 mb level early in the MCC life-cycle due to the dominant contribution from deep convection. Then the upward motion maximum gradually translates upward to the 400 mb level later in the MCC life-cycle when mesoscale updrafts prevail. However, a deep layer of downward motion below the 700 mb

level at the MCC's mature stage reflects the presence of concurrent mesoscale downdrafts.

6. The mid-level "jet-like" inflow reaches its maximum intensity at the growth stage slightly above the melting level at about 600 mb level. This mid-level "jet-like" inflow appears to play an important role in driving the mesoscale downdraft and enhancing the entire cellular circulation.
7. The system-relative flow field indicates that as the MCC moves, it is always receiving a fresh supply of moist air at low levels from the front during the early MCC life-cycle and in turn is sending a stream of drier upper-level air toward the rear.
8. The orogenic MCC owes its existence to more favorable moisture content and potentially unstable environment which lasts for a longer period than for the Plains MCC. Orogenic MCCs are also characterized by a chaotic pattern of meso-β convective elements due to the variety of triggering mechanisms.
9. The composite fields provide some evidence for the presence of "mesoscale organizers" which serve as triggers to release the preexisting potential instability. These forcing mechanisms are crucial to the MCC's initiation and development. The most likely "mesoscale organizers" are a low-level jet, an upper-level jet, a mid-level "jet-like" inflow, 700 mb level confluent flow, and a low- to mid-level trough.

5.0 MCC BUDGET EVOLUTION

In this chapter, budgets for the vertical component of relative vorticity, heat, and moisture are presented for the composite MCC discussed at the beginning of the previous chapter, i.e., the control composite based on the selected sample of MCCs.

5.1 MCC vorticity budget

This sub-section attempts to reveal the vorticity sources and sinks of a composite MCC. In addition, where there exists an imbalance in the vorticity equation when applied to the MCC, the roles of deep convection and mesoscale updrafts are discussed.

5.1.1 Vorticity budget formulation

The budget for the meso-α-scale vertical component of relative vorticity (ζ) is given by

$$\underset{(a)}{\frac{\partial \zeta}{\partial t}} + \underset{(b)}{\vec{V}\cdot\vec{\nabla}(\zeta + f)} + \underset{(c)}{\omega\frac{\partial \zeta}{\partial p}} + \underset{(d)}{(\zeta + f)\vec{\nabla}\cdot\vec{V}} + \underset{(e)}{K\cdot\vec{\nabla}\omega \times \frac{\partial \vec{V}}{\partial p}} = \underset{(f)}{R_z}, \qquad (1)$$

where ω is the vertical velocity in the p coordinate system, and R_z, the residual term, can be interpreted as the result of unresolved or subgrid-scale motions. However, any noncanceling observational errors in the terms on the left-hand side of Eq. (1) will also contribute to R_z. The terms on the left-hand side are the (a) local change term, the (b) horizontal and (c) vertical advection of absolute vorticity, (d) vorticity production by convergence (or divergence term), and the (e)

twisting term. Only those wind observations whose spatial and temporal patterns can be recognized as probable in a statistical sense can contribute significantly to the interpolated values at the grid points. Thus, we must exercise caution in interpreting the budget for the vertical component of vorticity because of the combined contributions from the variety of scales of circulation.

5.1.2 Vorticity budget of the composite MCC

Figs. 5.1a-5.1f show the height-time cross-section of each of the terms involved in Eq. (1). Based on the distribution of the residual term (Fig. 5.1f), we have confirmed earlier findings of imbalance in the vorticity equation. Generally speaking, the residual of vorticity exhibits a negative value in the lower troposphere from the MCC initial stage to the post-MCC stage. This vorticity sink (negative value of residual term) reaches its peak intensity at MCC maturity. On the other hand, the mid- to upper-level vorticity source (positive value of residual term) exists during the early, mature, and the dissipation stages of the MCC. These residuals are generally believed to result from cumulus-scale and mesoscale circulations which are not explicitly resolved by the budget analysis.

By examining the magnitude of the vorticity budget terms throughout the MCC life-cycle, we find that the divergence term (Fig. 5.1d) and the local change term (Fig. 5.1a) are basically the biggest two contributors to the imbalance in the vorticity budget equation, followed by the horizontal advection term (Fig. 5.1b). The vertical advection (Fig. 5.1c) and twisting terms (Fig. 5.1e) are at least one order of magnitude less than the others. Note that since the primary source terms are on the LHS of Eq. 5.1, a negative sign on the divergence term represents a

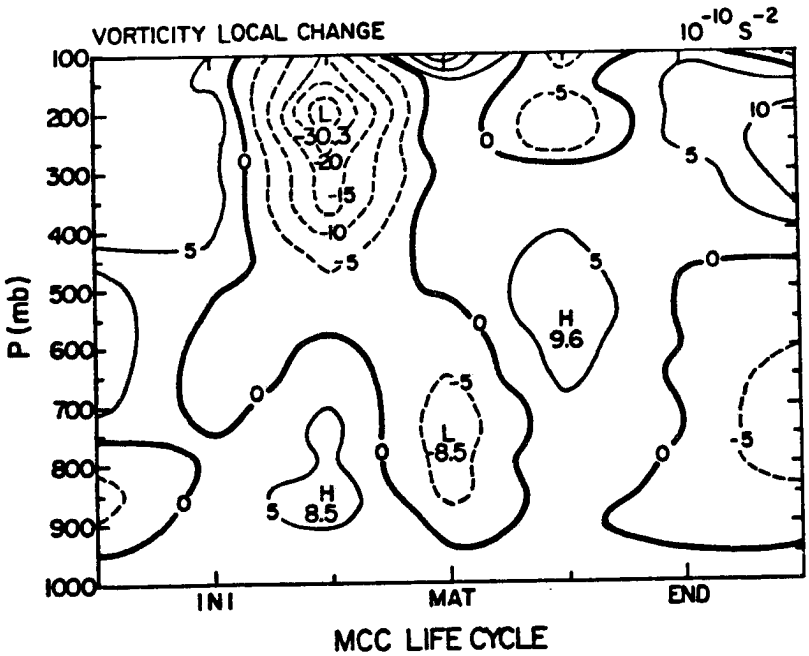

Fig. 5.1a. Height-time plot of the local vorticity time rate of change term. The vorticity change term is obtained by applying a 9-grid-point area average over a 6° x 6° lat.-long. domain every 50 mb. Units: 10^{-10} s^{-2}.

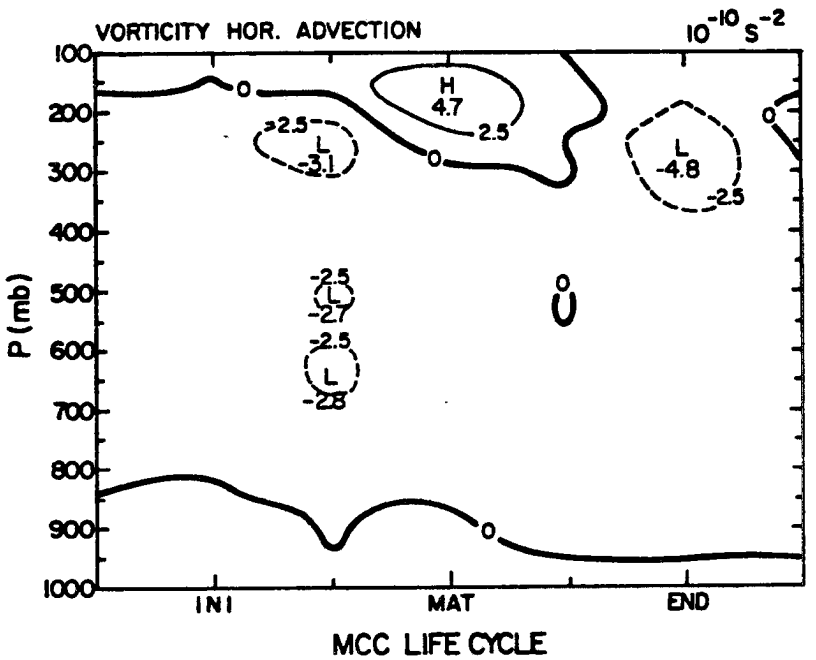

Fig. 5.1b. As in Fig. 5.1a, except for the horizontal vorticity advection term. Units: 10^{-10} s^{-2}.

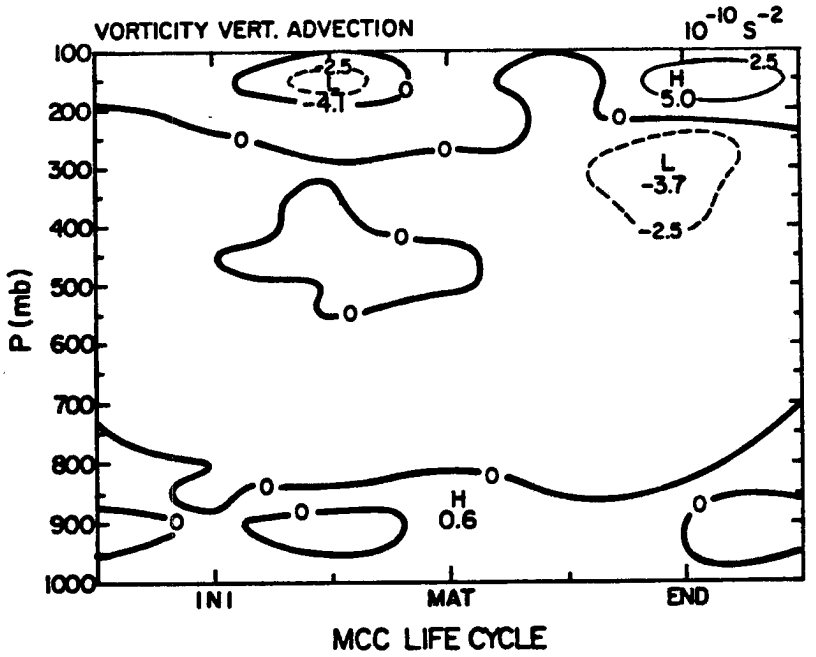

Fig. 5.1c. As in Fig. 5.1a, except for the vertical advection term. Units: 10^{-10} s^{-2}.

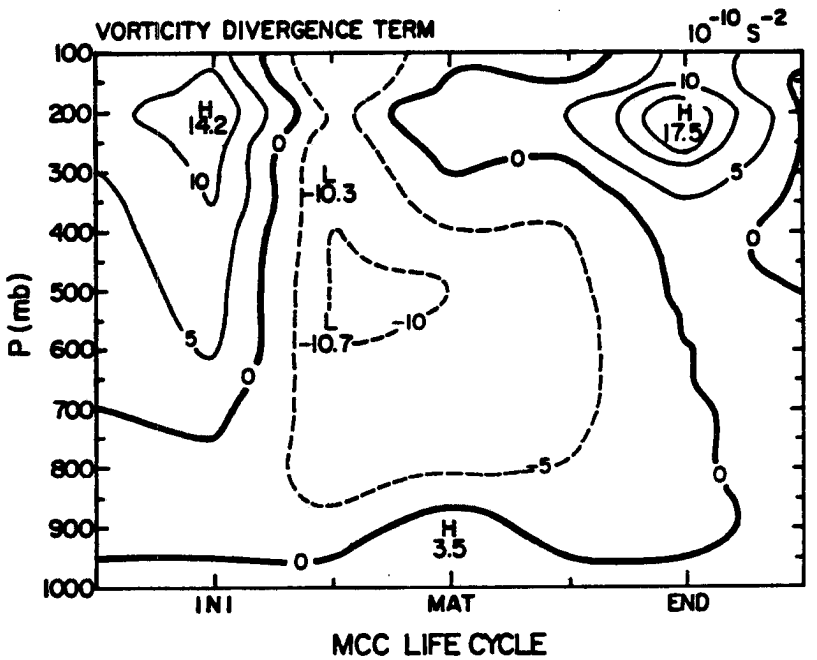

Fig. 5.1d. As in Fig. 5.1a, except for the divergence term. Units: 10^{-10} s^{-2}.

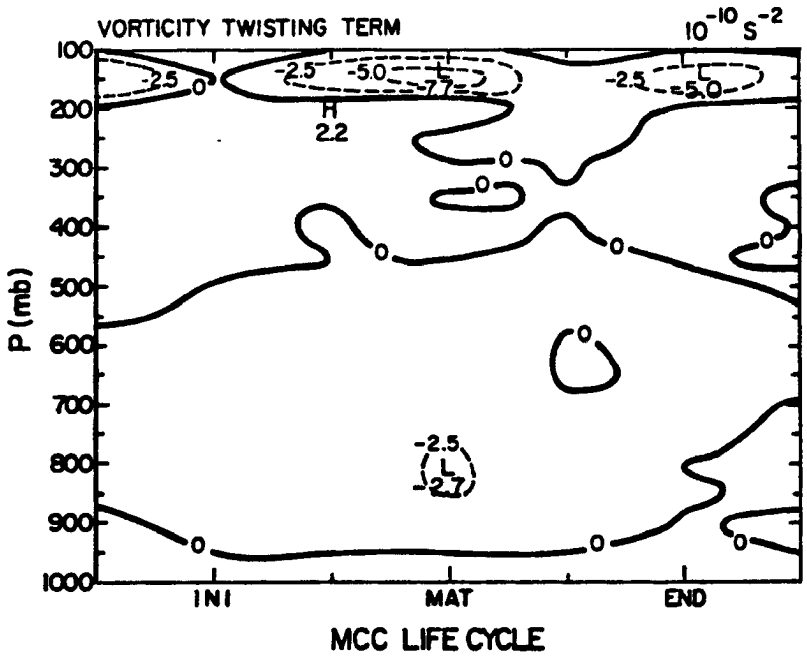

Fig. 5.1e. As in Fig. 5.1a, except for the twisting term. Units: 10^{-10} s^{-2}.

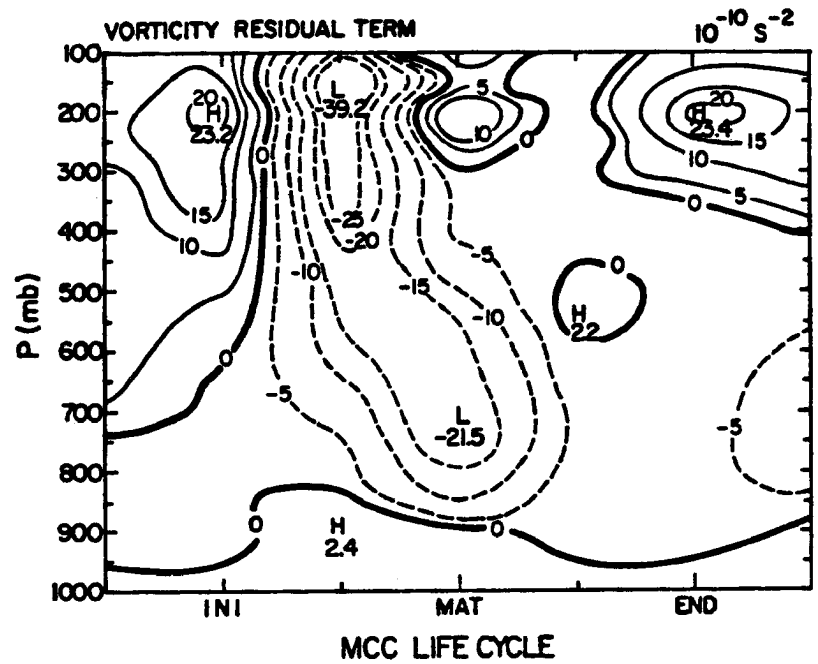

Fig. 5.1f. As in Fig. 5.1a, except for the residual term. Units: 10^{-10} s^{-2}.

contribution to cyclonic vorticity and vice versa. A visual inspection of ω and ζ in Figs. 4.43a and 4.39a shows that the relatively strong upward motion accompanying the stratiform cloud near 400 mb level after the MCC's growth stage is associated with a relatively strong decrease in the relative vorticity with height. Keeping this in mind, will make the following discussion easier to understand.

Figs. 5.2a-5.2d depict the vertical distribution of the vorticity budget terms for the pre-MCC, initial, mature, and dissipation stages, respectively. At the pre-MCC stage (Fig. 5.2a), the increase of vorticity prevail throughout most of the troposphere, resulting from the local increase of vorticity itself at all levels as well as the upper-level divergence. This imbalance implies that convective and smaller mesoscale feature are primary contributors to vorticity production during this stage. In the low-level atmosphere at the MCC initial stage (Fig. 5.2b) production of cyclonic vorticity by divergence is nearly counter balanced by local changes, principally due to the localized decrease of vorticity within the 600-700 mb layer. Upper-level anticyclonic vorticity production results from the local changes of vorticity, strong divergence aloft, and residual or convective-scale effects.

Because the thick stratiform cloud associated with cloud clusters is most evident in the growth (not shown) and mature stages (Fig. 5.2c), it is reasonable to expect that the intensified mesoscale circulations will amplify all the budget terms considerably and result in the cyclonic production below 300 mb level and anticyclonic production above 300 mb level. The cyclonic vorticity production is attributable to convective-scale contributions to the residual and to the intensified

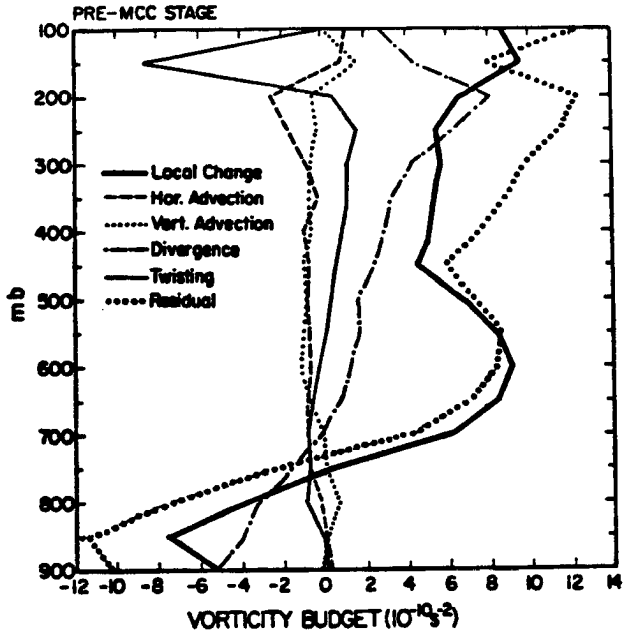

Fig. 5.2a. The vertical profile of the vorticity budget terms at the pre-MCC stage. Units: 10^{-10} s^{-2}.

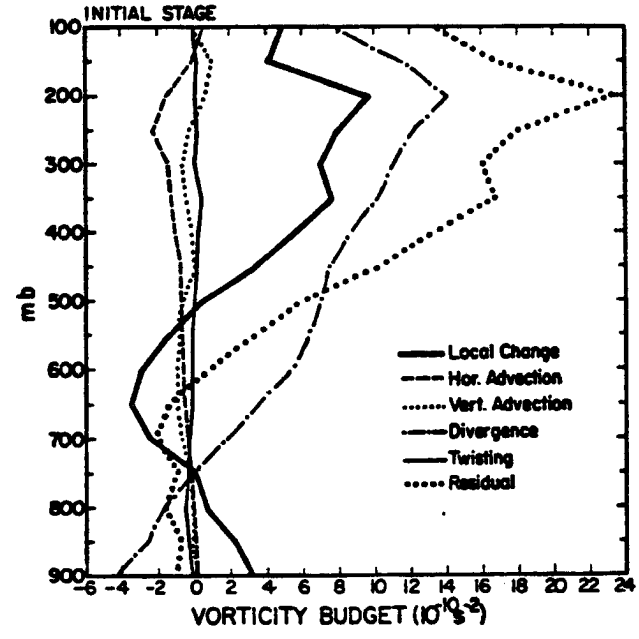

Fig. 5.2b. As in Fig. 5.2a, except for the initial stage. Units: 10^{-10} s^{-2}.

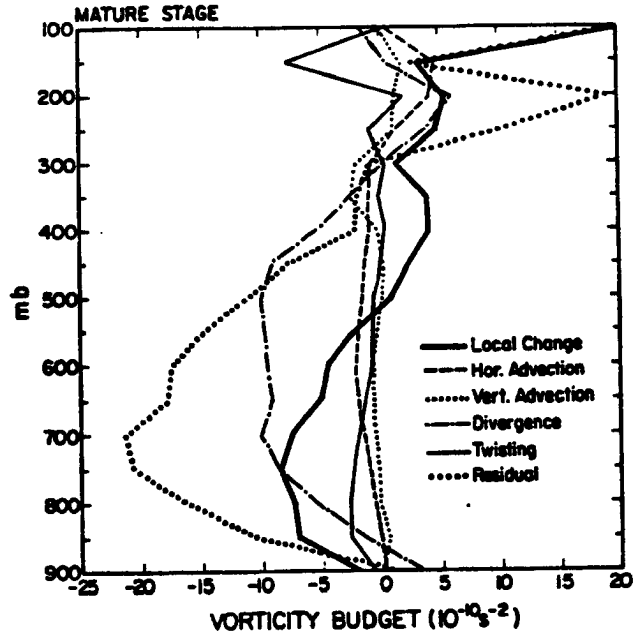

Fig. 5.2c. As in Fig. 5.2a except for the mature stage. Units: 10^{-10} s^{-2}.

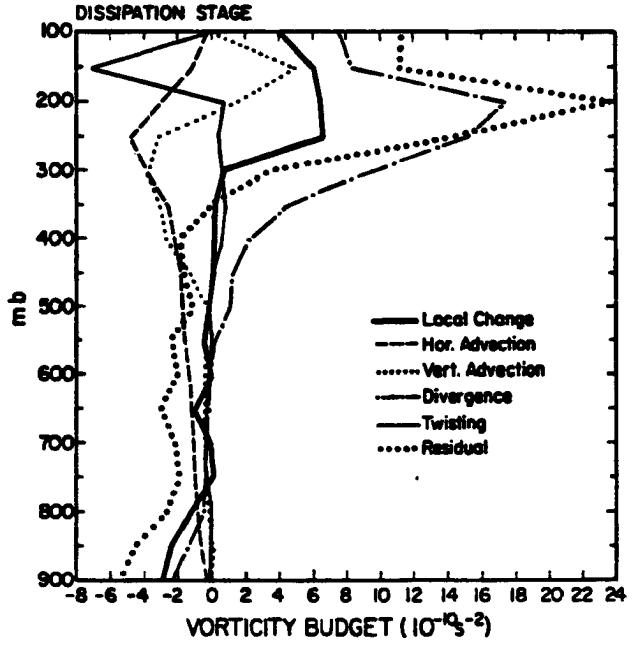

Fig. 5.2d. As in Fig. 5.2a except for the dissipation stage. Units: 10^{-10} s^{-2}.

low- to mid-level convergence and the upper-level divergence. Note that the vorticity is more or less balanced at the MCC's dissipation stage (Fig. 5.2d) in the mid-to-lower troposphere. Anticyclonic vorticity production by divergence and the residual term lingers above 300 mb level, however, in contrast to the other stages. The vorticity field clearly retains a longer "memory" of the presence of the MCC than do some of the other fields.

Analysis of west-east cross-sections of the local vorticity change term and the divergence term (not shown) at the MCC's mature stage reveal significant local vorticity change occurs upwind of the MCC centroid at middle levels; the change is characterized by a low- to mid-level increase in cyclonic and an upper-level increase of anticyclonic vorticity. The cyclonic vorticity contribution resulting from the convergence also appears upwind of the MCC centroid throughout the entire low- to mid-level troposphere. The low- to mid-level cyclonic vorticity production and upper-level anticyclonic vorticity production in the north-south cross-section was primarily due to the residual term. It is possible that the large-scale conditions, which are favorable for the development of an MCC in general, enhance deep convection along the frontal zone and hence also contribute to this upwind feature (e.g., the wavelength of upper short-wave trough is on the order of 1,000 km).

The north-south cross-section of relative vorticity at the initial stage (not shown) indicates that the anticyclonic vorticity centered at 200 mb level has intensified significantly between the MCC's initial and mature stages. Also, the intense anticyclonic vorticity center shifts to the north, while the weak anticyclonic vorticity center moves to the

south. The magnitude of the southern anticyclonic vorticity is about the same as the value of the background vorticity.

5.1.3 Comparison with other vorticity budget studies

Reed and Johnson (1974), Williams and Gray (1973), and Ruprecht and Gray (1976) also diagnosed the large-scale vorticity budget of various tropical systems and consistently found a large residual as indicated in our results. The vorticity budget residuals found in the GATE study by Esbensen et al. (1982) also show a lower-level cyclonic production and an upper-level anticyclonic production of vorticity. Reed and Johnson argued that the observed lower tropospheric cyclonic vorticity source and the upper tropospheric anticyclonic source can be attributed to the removal of vorticity-rich air from low levels and its upward transport and deposition aloft by convection. In addition, the feature of intense anticyclonic vorticity production to the north and the weak anticyclonic vorticity to the south bears some resemblance to the vorticity couplet found by Tollerud and Esbensen (1983).

5.2 MCC heat budget

5.2.1 Heat budget formulation

The effects of cumulus convection on large-scale circulations can be inferred indirectly from diagnostic budget studies (e.g., Yanai et al., 1973; Johnson, 1984; Lee, 1986). Following Yanai et al., the apparent heat source (Q_1) and the apparent moisture sink (Q_2) of a large-scale motion system are written as:

$$Q_1 = \underbrace{\frac{\partial \bar{s}}{\partial t}}_{(d)} + \underbrace{\overline{\vec{\nabla} \cdot s\vec{v}}}_{(a)} + \underbrace{\frac{\partial \overline{s\omega}}{\partial p}}_{(b)} = \underbrace{Q_R + L(c - e)}_{(c)} - \frac{\partial \overline{s'\omega'}}{\partial p}, \qquad (2)$$

$$Q_2 \equiv -L\left(\frac{\partial \bar{q}}{\partial t} + \overline{\vec{\nabla}\cdot q\vec{V}} + \frac{\partial \overline{q\omega}}{\partial p}\right) = L(c - e) + L\frac{\partial \overline{q'\omega'}}{\partial p}, \tag{3}$$

(d) (a) (b) (c)

where s is the dry static energy, $\vec{V}$ is the horizontal wind vector, ω is the vertical velocity, Q_R is the radiative cooling, c and e are the condensation and evaporation, respectively, L is the latent heat of condensation, and q is the specific humidity. The overbar here denotes a meso-α-scale horizontal average, and the prime indicates the deviation from the horizontal average. Eq. (2) shows that the apparent heating source consists of heating due to radiation, release of latent heat by net condensation, and vertical convergence of the vertical eddy transport of sensible heat. On the other hand, Eq. (3) indicates that the apparent moisture sink is due to net condensation and to vertical divergence of the vertical eddy transport of moisture. From Eqs. (2) and (3), we obtain

$$Q_1 - Q_2 - Q_R = -\frac{\partial \overline{(s' + Lq')\omega'}}{\partial p} = -\frac{\partial \overline{h'\omega'}}{\partial p}, \tag{4}$$

where $\overline{h'\omega'}$ is a measure of the vertical eddy transport of total heat and may be used to measure the activity of cumulus convection and/or mesoscale motions. The vertical integral of Eq. (4) indicates the required surface energy flux needed to balance the energy deficiency. For convenience in model calculation, Molinari (1985) evaluated the apparent heat source in terms of potential temperature rather than dry static energy. Therefore, we also use θ rather than s for the present computations, an artifice which should not significantly affect the results obtained.

5.2.2 Heat budget of the composite MCC

Because the domain center coincides with the MCC centroid, the budget study is basically carried out in a Lagrangian framework. Figs. 5.3a-5.3d show the height-time cross-section of the three right-hand-side terms of the apparent heat source (terms a, b, and c) from Eq. (2), and the corresponding apparent heat source (Q_1, term d), respectively. Note that the term Q_1 includes latent heating due to cumulus convection and to the thick stratiform cloud of the mesoscale circulation. Generally speaking, Q_1 exhibits a major heat source occurring at the 400 mb level throughout the MCC life-cycle (Fig. 5.3d). The amount of total Q_1 heating is on the order of 10-20^{o} day^{-1}. The magnitude of this heating is about five times larger than the long-term averages obtained over the large-scale domain in the tropics (Yanai et al., 1973; Johnson, 1984; Lee, 1986), and radiational cooling is therefore not dominant. In addition, a minor low-level heat source can be seen during the early MCC stages, when cumulus convection prevails. The upper-level heat source reflects the heating resulting from the mesoscale updrafts, whereas the low-level heat source indicates the significant contribution from the convective-scale systems. On the other hand, the heat sink (equivalent to -6 to -9^{o} day^{-1}) exists in the low- to mid-level troposphere after the growth stage, as a consequence of the effects of mesoscale downdrafts. Since the lifting condensation level is about 750 mb level, this low-level cooling is possibly caused by evaporation of rainfall. Both Lewis (1975) and Ninomiya (1971), who investigated case studies of squall lines and thunderstorm systems, found a similar strong low-level cooling due to the evaporation process. In Fig. 5.3d there also exists some extreme-upper-level cooling which may result from cloud-top

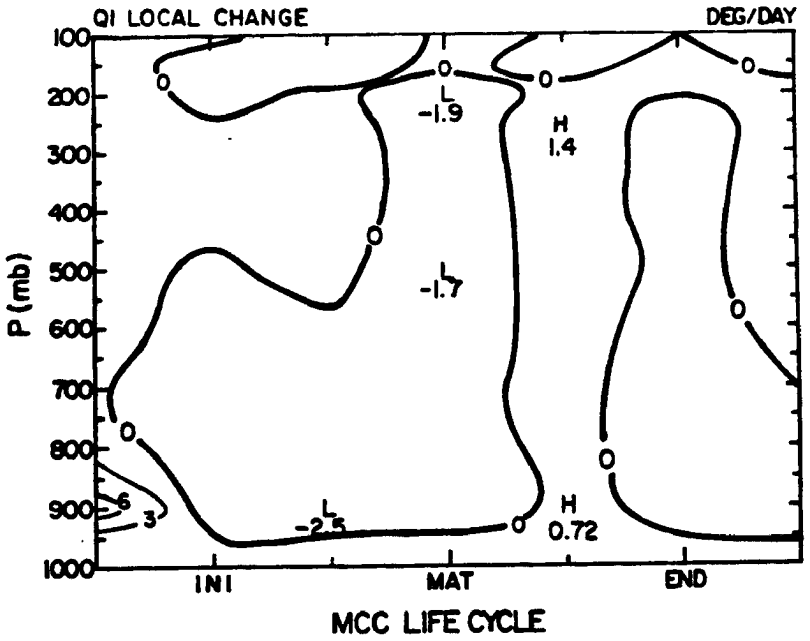

Fig. 5.3a. Height-time plot of the local heat time rate of change term. The heat change term is obtained by applying a 9-grid-point area average over a 6^{o} X 6^{o} lat.-long. domain every 50 mb. Units: K day^{-1}.

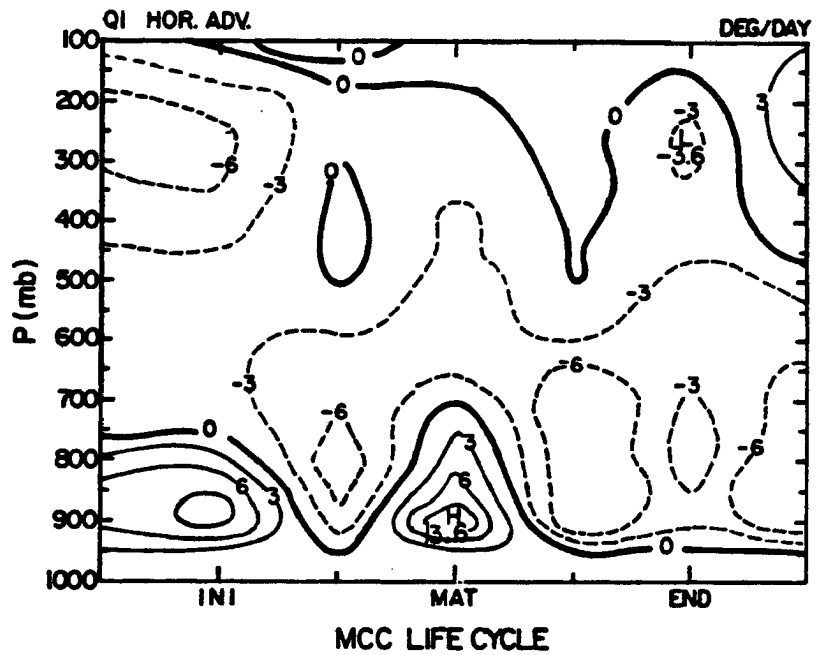

Fig. 5.3b. As in Fig. 5.3a, except for the horizontal heat advection term. Units: K day^{-1}.

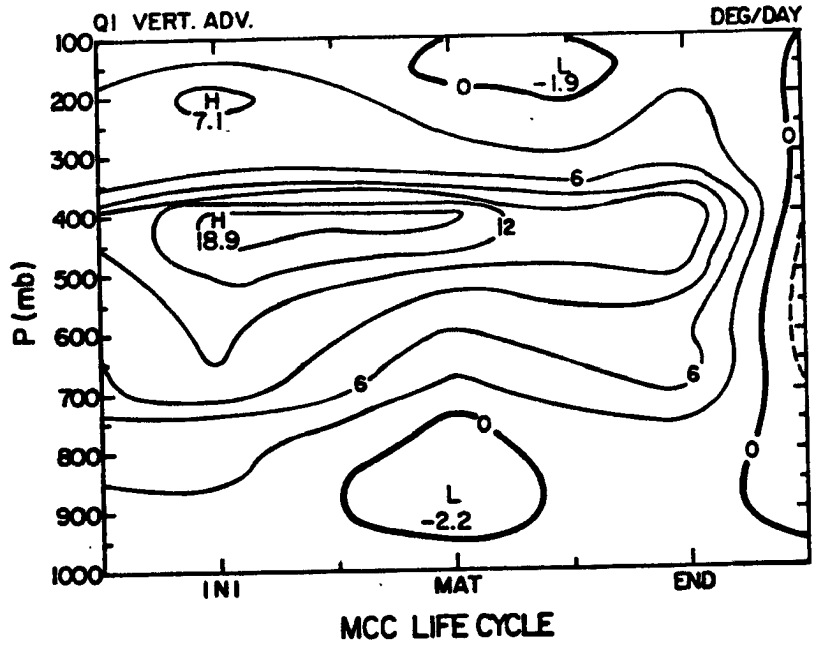

Fig. 5.3c. As in Fig. 5.3a, except for the vertical heat advection term. Units: K day^{-1}.

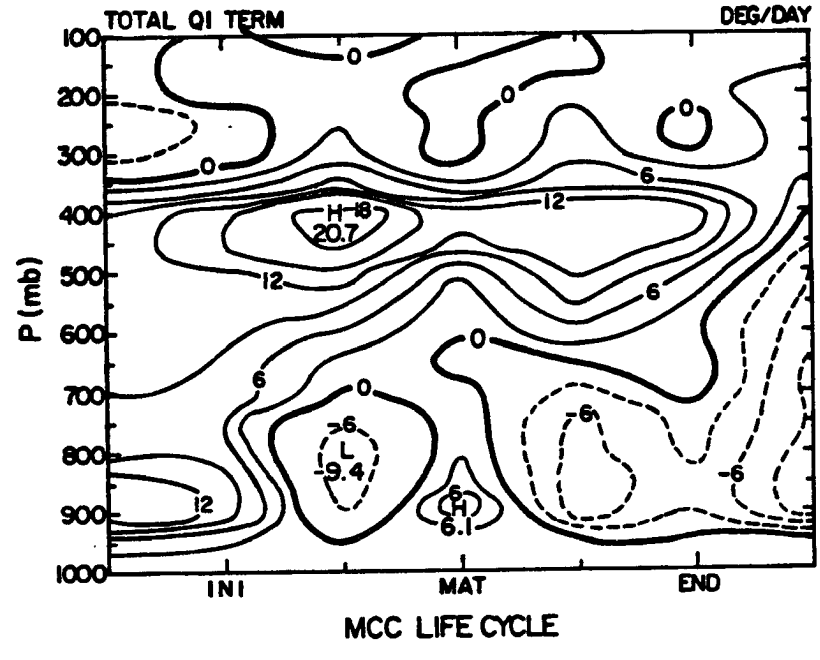

Fig. 5.3d. As in Fig. 5.3a, except for the apparent heat source term. Units: K day^{-1}.

radiational cooling, anvil evaporation, turbulent mixing of stratospheric and tropospheric air due to overshooting cumulonimbus tops, or inaccurate estimates of vertical motion near the upper boundary.

In summary, the effect of cumulus convection and mesoscale updrafts/downdrafts is to stabilize the lower and middle troposphere, based on the Q_1 profile shown here. We shall see that the local change term (Fig. 5.3a) contributes much less to the grid-scale imbalance than do the horizontal and vertical advection of heat; therefore, the imbalance between the advection terms basically determines the distribution of apparent heat source (Q_1).

Moreover, the vertical distribution of the heat budget terms involved in Eq. (2) are illustrated in Figs. 5.4a-5.4c at the initial, mature, and dissipation stages of the composite MCC, respectively. The common feature among these diagrams is the monotonic increase of the vertical dry static energy advection (equivalent to vertical potential temperature advection) with height. As the MCC develops, condensational heating increases and reaches its maximum value at the MCC growth stage. It is not surprising to find that the maximum level of the heat source coincides with the peak upward motion (see Fig. 4.43a), because the vertical advection term dominates the heat budget at upper levels. However, the horizontal advection term significantly influences the heat source (before the MCC mature stage) or heat sink (MCC dissipation stage) in the low-level troposphere.

Figs. 5.5a-5.5d show the height-time cross-section of the three right-hand-side terms of the apparent moisture sink from Eq. (3), and the corresponding total apparent moisture sink (Q_2), respectively. In

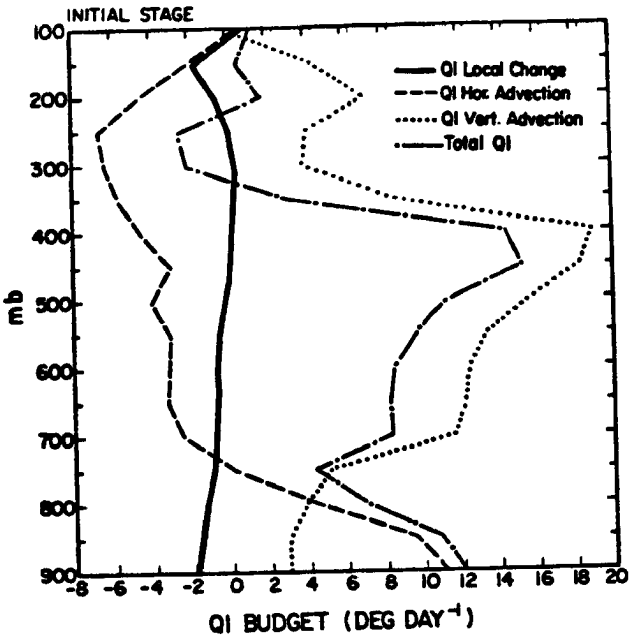

Fig. 5.4a. The vertical distribution of Q_1 budget terms at the MCC initial stage. Units: K day^{-1}.

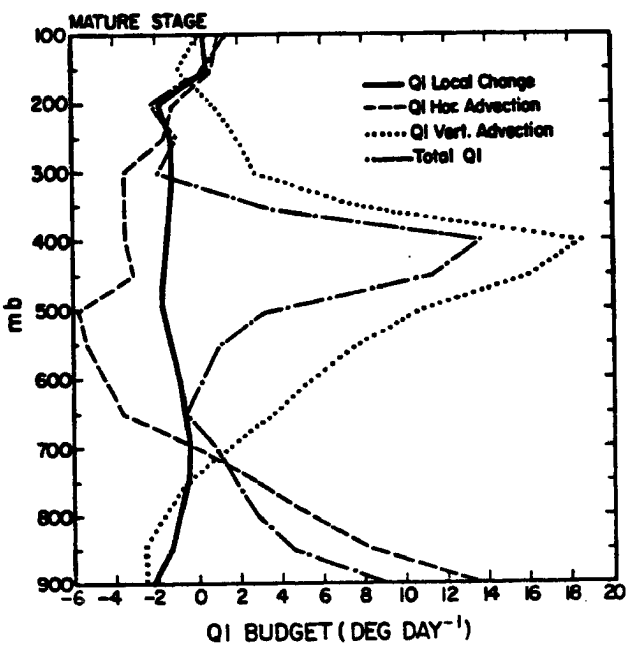

Fig. 5.4b. As in Fig. 5.4a, except for the mature stage. Units: K day^{-1}.

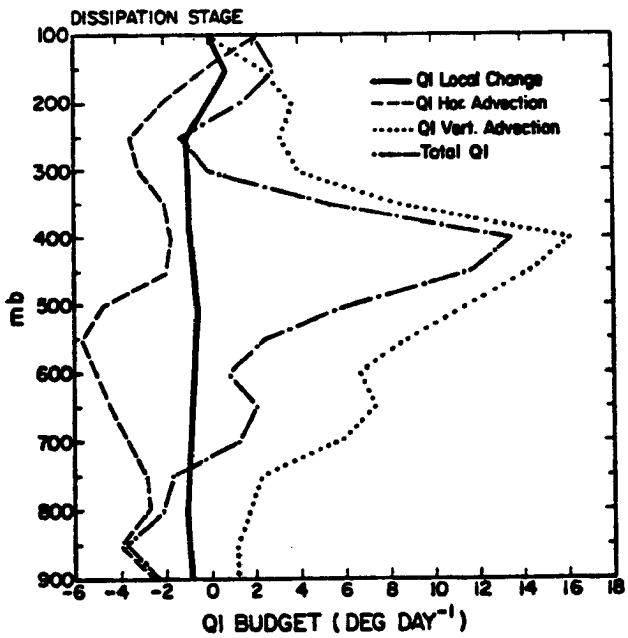

Fig. 5.4c. As in Fig. 5.4a, except for the dissipation stage. Units: K day^{-1}.

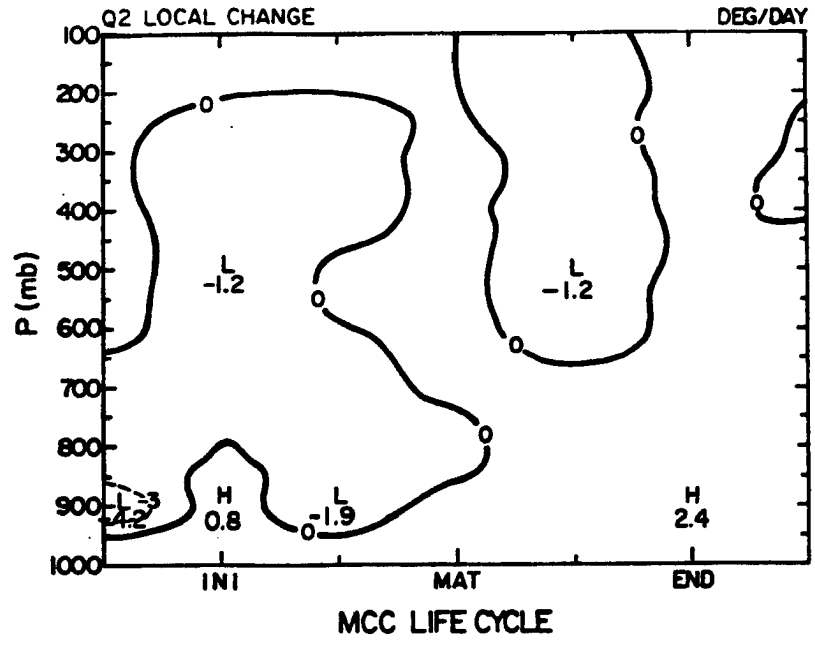

Fig. 5.5a. Height-time plot of the local moisture time rate of change term. The moisture change term is obtained by applying a 9-grid-point area average over a 6^{o} X 6^{o} lat.-long. domain every 50 mb. Units: K day^{-1}.

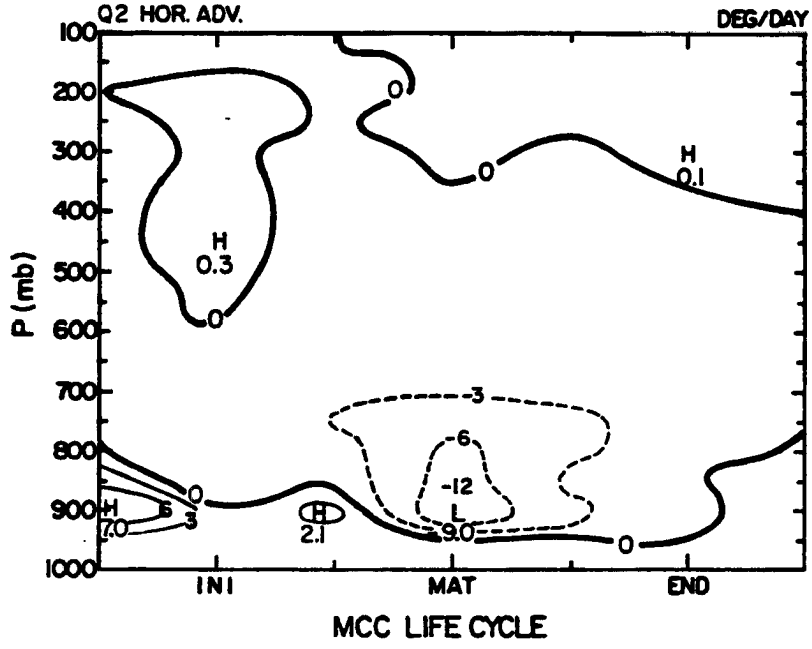

Fig. 5.5b. As in Fig. 5.5a, except for the horizontal moisture advection term. Units: K day^{-1}.

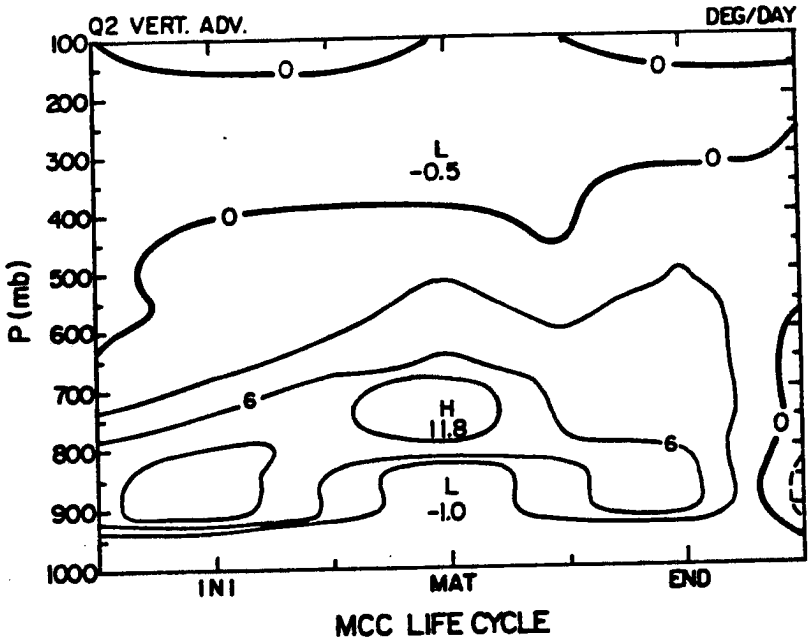

Fig. 5.5c. As in Fig. 5.5a, except for the vertical moisture advection term. Units: K day^{-1}.

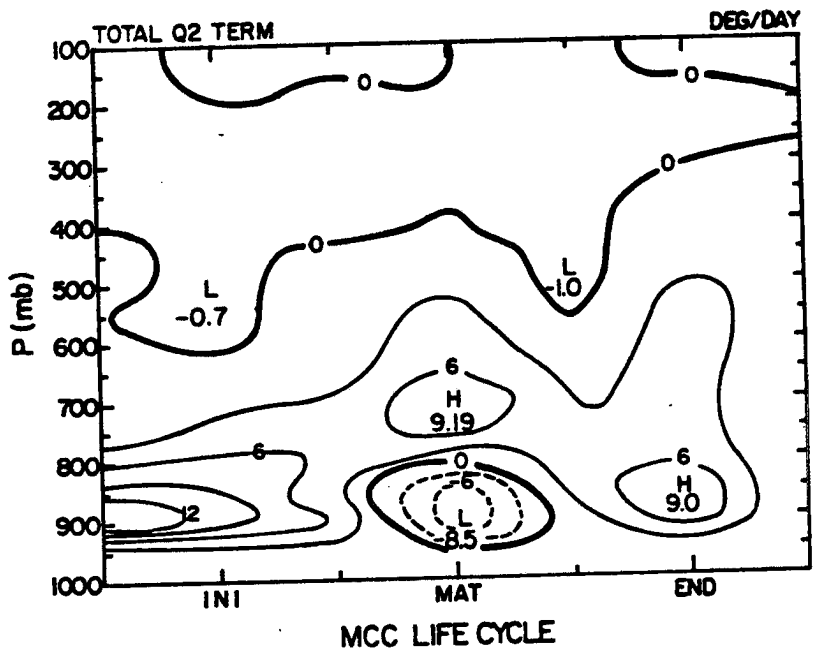

Fig. 5.5d. As in Fig. 5.5a, except for apparent moisture sink term. Units: K day^{-1}.

general, Fig. 5.5d shows that a major moisture sink (equivalent to 9-14° day^{-1}) is present below the 700 mb level throughout most of the MCC life-cycle with the exception of a moisture source which appears near the 900 mb level at the MCC mature stage. The low-level moisture sink indicates the removal of heat by evaporation and downdraft processes, whereas the low-level moisture source implies the contribution of surplus precipitation over evaporation near the ground. The vertical distribution of the Q_2 budget terms from Eq. (3) are illustrated in Figs. 5.6a-c at the initial, mature, and dissipation stages of the composite MCC, respectively. The gross feature among these diagrams is the monotonic decrease with height of each contributing moisture term because the moisture content reaches its peak value near the ground (with the exception of terms c and d at the mature stage). In fact, the vertical moisture advection term principally determines the magnitude of the moisture sink, but its contribution is partially offset by the non-negligible horizontal moisture advection term (especially at the MCC mature stage). Incidentally, as the budget area is increased from 6° X 6° latitude-longitude to 10° X 10° latitude-longitude, the magnitudes of the diagnosed terms generally decrease (not shown). This behavior bears some resemblance to the squall line investigation by Kuo and Anthes (1984b).

Fig. 5.7 depicts the height-time cross-section of the left-hand-side of Eq. (4), which results from the activity of cumulus convection and mesoscale updrafts/downdrafts. The radiative cooling rate is obtained from the mean tropospheric condition, following Cox and Griffith (1979). We see from the diagram that a heat source occurs over a deep layer in the middle to upper troposphere, accompanied by a heat

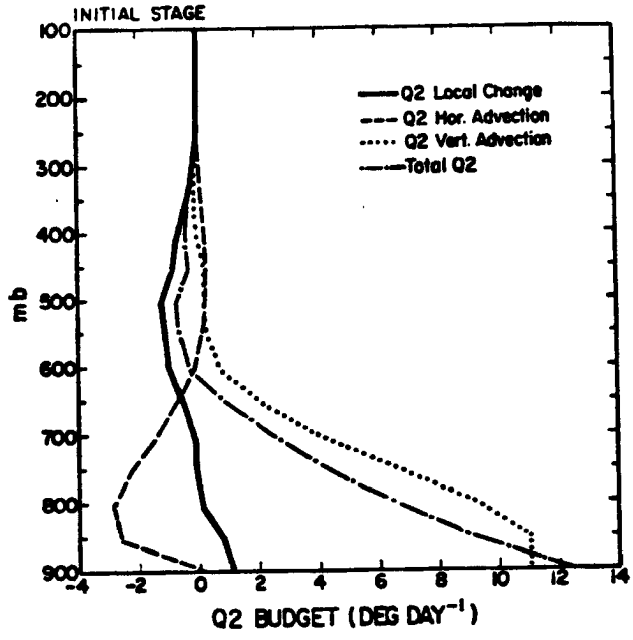

Fig. 5.6a. The vertical distribution of Q_2 budget terms at the MCC initial stage. Units: K day^{-1}.

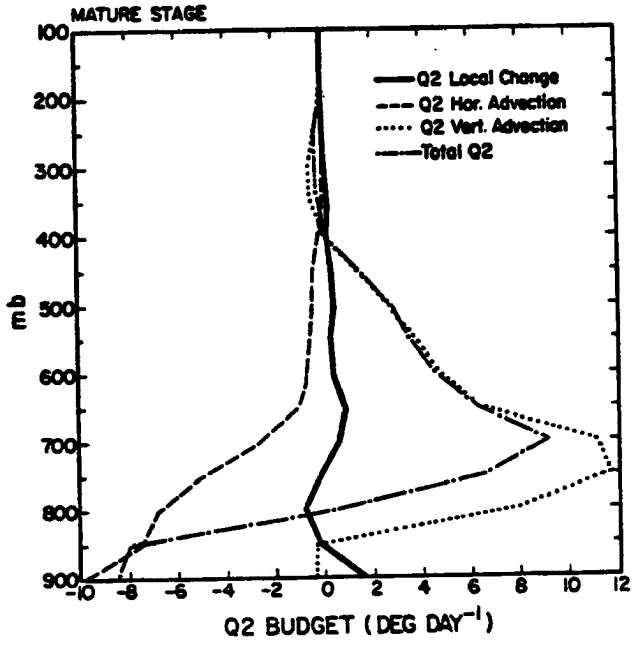

Fig. 5.6b. As in Fig. 5.6a, except for the mature stage. Units: K day^{-1}.

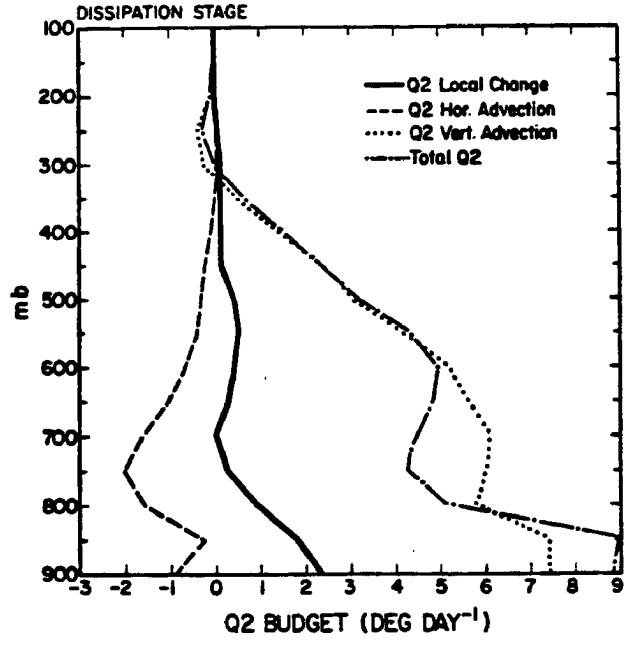

Fig. 5.6c. As in Fig. 5.6a, except for the dissipation stage. Units: K day^{-1}.

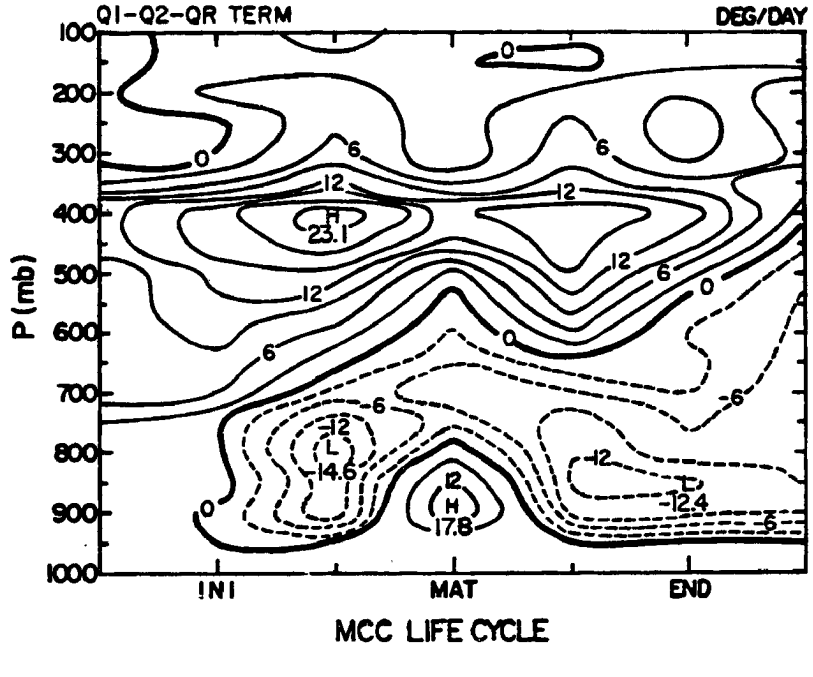

Fig. 5.7. Height-time plot of the Q_1-Q_2-Q_R term. Units: K day^{-1}.

sink in the lower layers (with the exception at the mature stage when the apparent moisture sink exceeds the apparent heat source in the presence of mesoscale downdrafts). Since the mid- to upper-level heat source is greater than the lower-level heat sink, the vertical integral of this quantity is positive (not shown). Therefore, this implies that an upward energy flux from the surface is required to balance the MCC net energy production in the upper troposphere (assuming no energy flux across the tropopause). Of course, on the time scale of MCCs, this is not likely to occur over land. The entire heating profile illustrated herein basically resembles the combined mesoscale heating and mesoscale drying proposed by Johnson (1984). In particular, the maximum heat source and minimum heat sink both occur at the MCC growth stage when meso-β convective elements prevail.

5.2.3 Comparison with other heat budget studies

Johnson (1984), in his study of winter monsoon cloud cluster heat and moisture budgets partitioned into cumulus and mesoscale components, found an intriguing feature. The total heating of Yanai et al. (1973), which has a peak near 450 mb level, was seen to be a consequence of two distinctly different circulation features: 1) the mesoscale anvil, which has a heating peak near 350 mb level and a cooling peak below 700 mb level, and 2) deep cumulus convection, which produces a heating peak centered near 600 mb level. The partitioning of the apparent moisture sink produces qualitatively similar results. The mesoscale anvil induces a drying peak near 350 mb level and a moistening peak (through evaporation) near 800 mb level. Cumulus-induced drying has a peak near 750 mb level. Thus, the double-peak structure in Q_2 is a consequence of the combined but vertically separated drying effects of two distinct

convective phenomena: mesoscale anvils and deep cumulus. These peaks occur at the levels of maximum removal of water vapor by net condensation in both cloud systems. Basically, Johnson's partitioning concept is in good agreement with the results presented here; we also found a mid- to upper-level heating due to mesoscale updrafts and a low-level mesoscale drying resulting from mesoscale downdrafts.

Esbensen and Wang (1984) studied the heat budget of a tropical cloud cluster and found strong convective activity with a very large low-level moisture sink separated in height from the region where the large-scale heating is realized during the growth stage (comparable to our Fig. 5.5d). In the mature stage, the strong development of apparent heating in the 500-600 mb layer (compared to 400 mb level in Fig. 5.4b) is evidence for the development of a dynamically active anvil. In the dissipation stage, they showed that the large-scale apparent heat source was approximately balanced by the apparent moisture sink above the freezing level (Fig. 5.7 shows an imbalance of weak mid- to upper-level heating).

Molinari and Corsetti (1985) in their simulation of an MCC showed that the larger fraction of mesoscale precipitation strongly shifts the heating and drying to the upper troposphere, similar to the Q_1 profile present here (Fig. 5.3d). Kuo and Anthes (1984a, 1984b), who investigated the heat and moisture budgets of SESAME squall lines, also showed an apparent heat source in the upper troposphere and, moisture sink in the lower troposphere with magnitudes about two times larger than the value found in this study. In addition, Akiyama (1984a, 1984b) investigated a medium-scale cloud cluster associated with a Baiu front in Asia. He showed that the structure of the cloud cluster during the

early stages resembles that of an MCC; it exhibited an apparent moisture sink in the lower troposphere and an apparent heat source in the upper troposphere.

Recently, Ogura and Jiang (1985) investigated the tropospheric heating and drying effects of an extratropical MCS. They argued that the cloud heating effect was found not to be in balance with the large-scale cooling due to the large-scale horizontal advection and storage terms, which have a dominant role in the heat and moisture budgets. Once a deep cloud developed, it tended to dry the subcloud layer through the process of dry downdrafts penetrating into the subcloud layer and updrafts removing moisture from the subcloud layer. Based on the evidence cited above, it is probably fair to conclude that a common feature of MCSs is the upper-level heating source and the low-level moisture sink.

5.3 MCC moisture budget

5.3.1 Moisture budget formulation

The water vapor budget for an MCC can be evaluated from the water vapor continuity equation

$$\bar{P} - \bar{E} = -\int_{p_{sfc}}^{p_{100}} q\vec{\nabla}\cdot\vec{V}\,\frac{dp}{g} - \int_{p_{sfc}}^{p_{100}} \vec{V}\cdot\vec{\nabla}q\,\frac{dp}{g} - \frac{\partial}{\partial t}\int_{p_{sfc}}^{p_{100}} \bar{q}\,\frac{dp}{g}\,, \qquad (5)$$

(1) (2) (3)

where q is the water vapor mixing ratio, p_{sfc} is surface pressure, and $\bar{P}$ and $\bar{E}$ are precipitation and evaporation at the surface, respectively. Here, we assume that no significant flux of water vapor occurs across 100 mb level and no storage term due to the phase change (included in residual term of $\bar{E}$). Eq. (5) states that the average rate of excess of

precipitation over evaporation at the surface plus other residual contributions -- evaporation of rain, etc. over the MCC area is provided in part by convergence of the water vapor transport, and in part by a reduction in the amount of water vapor stored in the atmosphere.

5.3.2 Moisture budget of the composite MCC

Figs. 5.8a-5.8d show the height-time cross-sections of the horizontal convergence, horizontal advection, and local decrease of mixing ratio terms from Eq. (5) as well as the sum of these three terms, which represents the net difference between the areal precipitation and evaporation, respectively. Most of the synoptic-scale to mesoscale horizontal moisture convergence (Fig. 5.8a) occurs below 700 mb level. This is due to the rapid decrease of moisture and mass convergence with height. However, the consumption of moisture Q_2 (Fig. 5.5d) is substantial up to the 600 mb level (equivalent to 9 ^{o} day^{-1}) during the mature stage. The role of synoptic-scale to mesoscale vertical motion is to transport moisture upward to support the water vapor consumption of an MCC. The horizontal convergence reaches a maximum value of 0.24 mm equivalent water vapor near the 750 mb level at the MCC mature stage.

For Fig. 5.8b the horizontal moisture advection indicates that a positive moisture advection maximum of 0.07 mm of equivalent water vapor occurs near the 700 mb level during the MCC growth stage, followed by a secondary maximum at the decay stage. Apparently, moisture advection is relatively insignificant compared to the moisture convergence term and the storage term (discussed later). Thus, the moisture convergence and storage processes dominate the moisture budget and largely balance each other by the MCC growth stage. Their difference is then partially balanced by horizontal moisture advection. However, during the later

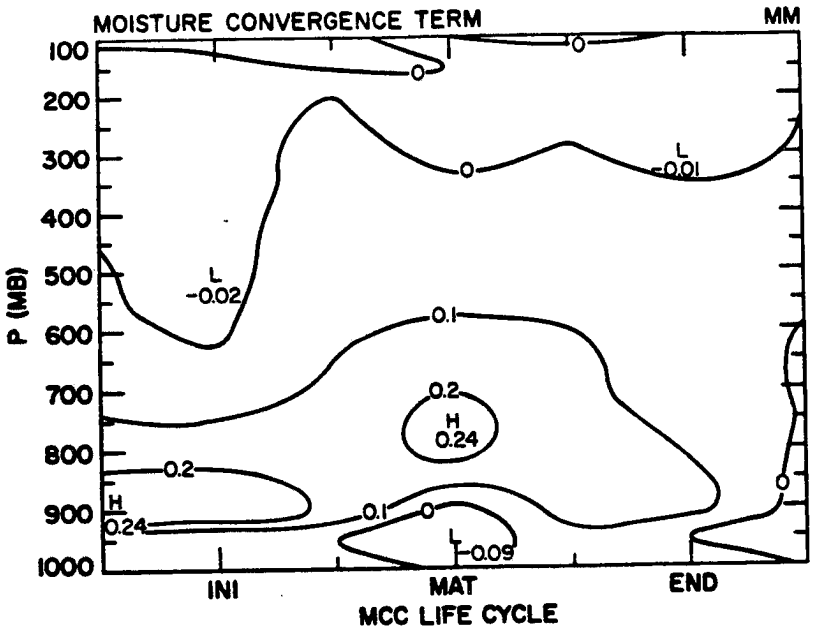

Fig. 5.8a. Height-time plot of the horizontal moisture convergence term. The moisture convergence term is obtained by applying a 9-grid-point area average over a 6^{o} X 6^{o} lat.-long. domain every 50 mb. Units: mm.

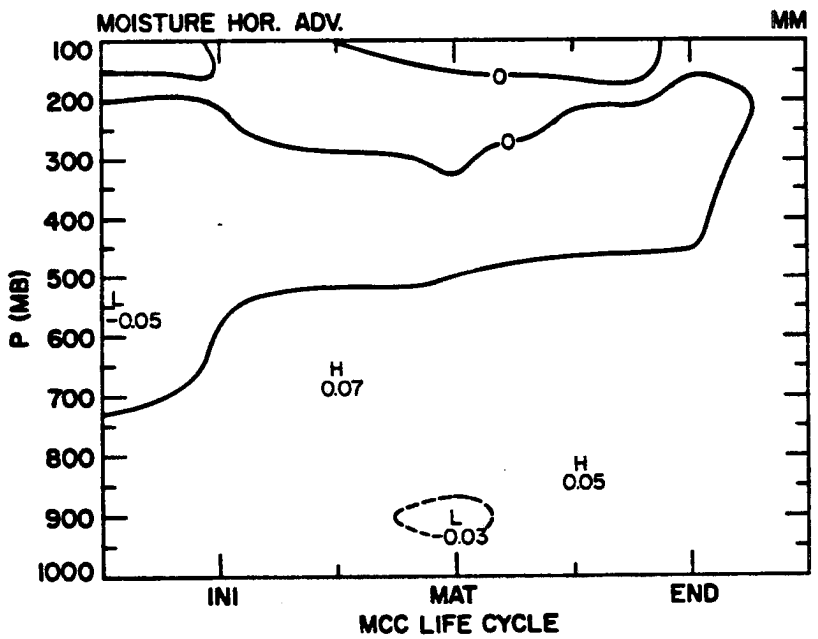

Fig. 5.8b. As in Fig. 5.8a, except for the horizontal moisture advection term. Units: mm.

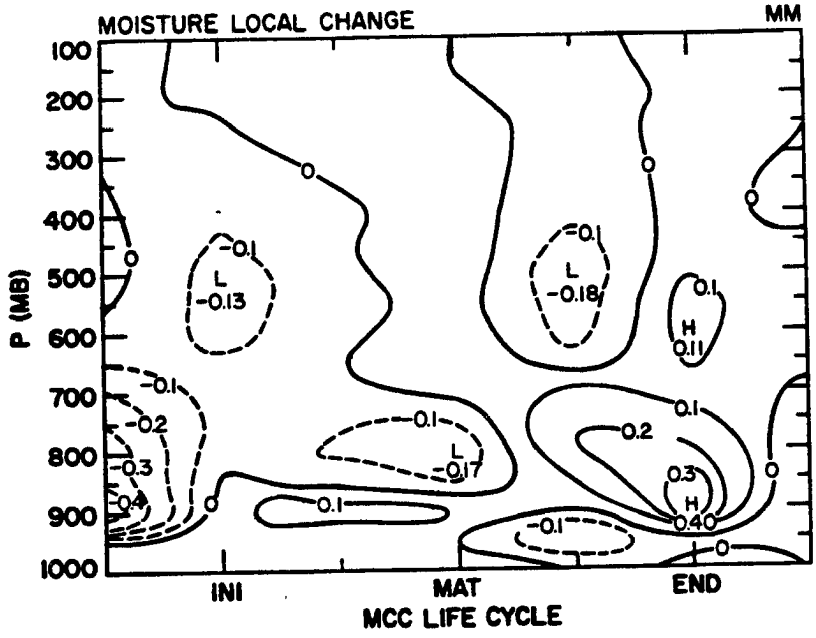

Fig. 5.8c. As in Fig. 5.8a, except for the local time rate of decrease of moisture term. Units: mm.

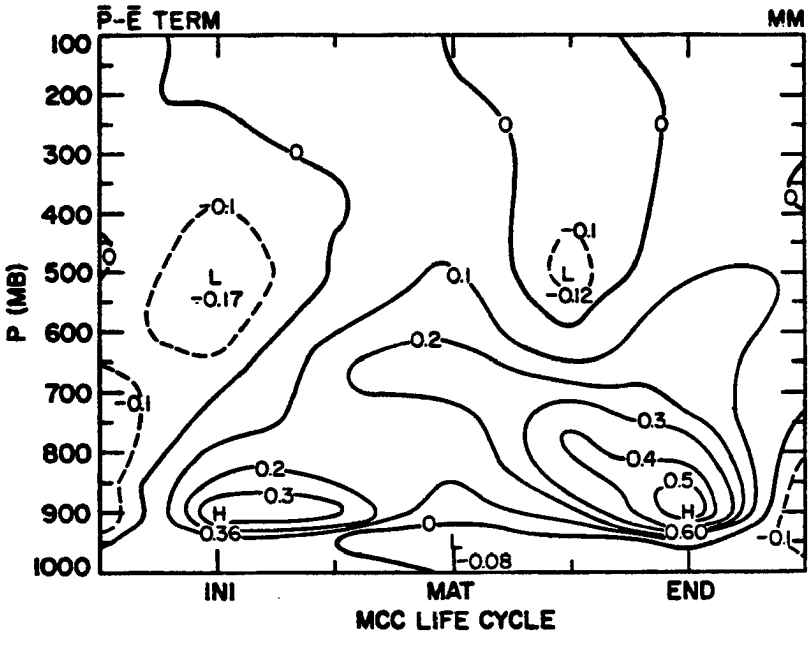

Fig. 5.8d. As in Fig. 5.8a, except for the sum of the horizontal moisture convergence, horizontal moisture advection, and local time rate of decrease of moisture terms. Units: mm.

stages of the MCC evolution, the horizontal convergence term dominates exclusively. The storage term $\partial q/\partial t$ (Fig. 5.8c) shows moistening of the large-scale environment until the MCC growth stage and drying the atmosphere after MCC maturity (with the exception of minor moistening near the ground during the decay stage). The maximum water vapor storage and depletion values are 0.4 and -0.4 mm of water vapor and both maximum occur around the 900 mb level.

Values of vertically-integrated moisture budget terms during the MCC sub-periods are presented in Table 5.1. The observed composite precipitation of each MCC sub-period was obtained from McAnelly (personal communication) who has used the same compositing dataset as this study. The evaporation term is the residual term obtained after evaluating the right-hand-side terms of Eq. (5) and using the composite precipitation data. Note that the evaporation term is the residual term which include surface evaporation as well as evaporation of water vapor, cloud water, and precipitation. However, it is impossible to distinguish among the contributions of the various source of E from our data resolution.

In fact, the primary source of water for a cumulonimbus cloud or mesoscale convective system is the flow of water vapor into the base of the cloud. As the air ascends and cools, the vapor is converted into liquid cloud droplets and some is converted into liquid or frozen precipitation elements. A portion of the water rapidly falls out as surface rainfall while some of the water is injected into the anvil portion of the cloud where it eventually evaporates or slowly settles out as steady precipitation. Some of the condensed water is evaporated from the sides of the cloud due to entrainment processes. As the cloud

decays, some of the cloud water and smaller precipitation elements will also evaporate. Another portion evaporates in the dry subcloud layer in low-level downdrafts.

Apparently, based on the analysis of Table 5.1, the moisture storage term dominates the budget balance during the early and late stages of the MCC life-cycle. This implies that any mesoscale model simulation should consider or should have the capability to handle the atmospheric storage process in order to assess the moisture structure of an evolutionary system. Unfortunately, current mesoscale models (e.g., Anthes and Warner, 1978) usually lack this ability. Budgetary calculations over the MCC area indicate that water vapor is also made available by MCC-scale convergence besides the above-mentioned storage term, with evaporation and moist horizontal advection playing smaller but by no means negligible roles.

The results of the water vapor budget shown in Table 5.1 can also be percentages shown in Table 5.2. Of each 100 units of water vapor (sum of the horizontal convergence, horizontal advection, and evaporation) made available to the MCC, the calculation shows that 47 come from MCC-scale mass convergence, 18 from MCC-scale moisture advection, and 35 from evaporation during the MCC initial stage. Of this total, 41 units are used to moisten the atmosphere, and 59 fall as precipitation. However, at MCC maturity, 60 units come from the mass convergence, -29 units from dry advection, and 69 units are contributed by the dominating evaporation from the surface, water vapor, cloud water, and precipitation. Note that of this total, the precipitation efficiency reaches 113% such that the moist atmosphere provides an extra 13% from its accumulated storage through a number of precipitation processes.

Table 5.1. The water vapor budget and its comparison with observed precipitation during MCC volution. Units in depth of liquid water (mm).

Subperiod	1 $\overline{-q}\,\overline{\vec{\nabla}\cdot\vec{V}}$	2 $\overline{-\vec{V}\cdot\vec{\nabla}q}$	3 $-\frac{\partial\bar{q}}{\partial t}$	1+2+3 $\bar{P}-\bar{E}$	Observed $\bar{P}$	Calculated $\bar{E}$
PRE-MCC	1.505	1.227	-3.078	-0.346	0.580	0.926
INIT.	1.238	0.464	-1.060	0.641	1.549	0.908
GROW.	2.125	0.176	-0.712	1.589	2.614	1.025
MAT.	1.620	-0.781	0.348	1.187	3.017	1.830
DECAY	1.824	-0.357	-0.403	1.065	2.575	1.510
DISSI.	1.192	0.027	-0.716	0.503	1.545	1.042
POST-MCC	-0.119	0.268	-1.028	-0.879	0.967	1.846

Table 5.2. The water vapor budget during MCC evolution. Units in %.

Subperiod	1 $\overline{-q}\,\overline{\vec{\nabla}\cdot\vec{V}}$	2 $\overline{-\vec{V}\cdot\vec{\nabla}q}$	1+2 $\overline{-\vec{\nabla}\cdot\vec{V}q}$	3 $-\frac{\partial\bar{q}}{\partial t}$	$\bar{P}$	$\bar{E}$
PRE-MCC	41.1	33.6	74.7	-84.1	15.9	25.3
INIT.	47.4	17.8	65.2	-40.6	59.4	34.8
GROW.	63.9	5.3	69.2	-21.4	78.6	30.8
MAT.	60.7	-29.3	31.4	13.0	113.0	68.6
DECAY	61.3	-12.0	49.3	-13.5	86.5	50.7
DISSI.	52.7	1.2	53.9	-31.7	68.3	46.1
POST-MCC	-6.0	11.9	5.9	-51.5	48.5	94.1

In fact, the atmospheric storage term (Table 5.1) has accumulated since the pre-MCC stage to ensure the highest precipitation efficiency once the MCC reaches its maturity. A precipitation efficiency greater than 100% suggests that the value of the parameter b (partition coefficient for moistening the atmosphere) in Kuo's (1965, 1974) cumulus parameterization scheme may be negative in the real atmosphere. It should also be kept in mind that part of the precipitation that actually falls from the mesoscale anvil systems is produced in cumulus updrafts and is transferred to the anvil by the mesoscale circulation (Leary and Houze, 1980; Gamache and Houze, 1983).

At the MCC dissipation stage, although the mass convergence continuously provides the moisture for the system (54%), the evaporation process still contributes a significant amount of water vapor (46%) into the atmosphere. However, mesoscale downdrafts remove the accumulating vapor in a highly efficient process whereby nearly 68% of the water vapor made available by horizontal transport and evaporation falls as precipitation. Incidentally, the decrease of the mass convergence is offset by reduced precipitation at the post-MCC stage to such an extent that precipitation efficiency drops to only 49%.

The water vapor budget shows that evaporation contributes a high percentage to the MCC system. This may result in part from the assumption of no storge term of liquid- and ice-phases in Eq. (5). Therefore, the residual term of evaporation includes the surface vapor evaporation, evaporation of precipitation, and evaporation of cloud water. Only a mesoscale model including phase change (e.g., Tripoli, 1986) can provide the partioned contribution of the evaporation in detail.

5.3.3 Comparison with other moisture budget studies

Bosart and Sanders (1981) investigated the water budget of a long-lived MCS in the Johnstown flood and showed that the water vapor was provided principally by storm-scale convergence but also to a lesser degree by atmospheric storage. They indicated that the precipitation efficiency was nearly 90%, which is similar to our result for the MCC later stages, but with the precipitation rate about four times larger than the value presented here. Thompson et al. (1979) investigated the precipitation in synoptic-scale waves in the tropical Atlantic during Phase III of GATE. They found that of 100 units of water vapor made available, 83 units came from moisture convergence and 17 units came from surface evaporation (more or less similar to our MCC early stage); they also found that 6 of these units are used to moisten the atmosphere, while 94 precipitate. However, their precipitation efficiency of 94% bears some resemblance to our findings at the MCC decay stage. As an indication of the relative contribution of the various water sinks for a severe squall line thunderstorm, Newton (1966) estimated that between 45-53% of the water vapor entering the updraft reaches the ground as precipitation, while about 40% is evaporated in downdrafts and about 10% is injected into the anvil porton of the cloud. In fact, his result bears some resemblance to our findings of the contribution of evaporation.

5.4 Summary

Budgetary calculations averaged over the composite MCC area show that the residual of grid-scale vorticity exhibits a vorticity sink in the lower troposphere from the initial to post-MCC stage which reaches its maximum intensity at MCC maturity. On the other hand, a mid- to

upper-level vorticity source exists during the early and dissipation stages of MCC. The imbalance in the vorticity budget results principally from the non-cancellation between the divergence and local change terms.

The heat budget for the composite MCC indicates that the total apparent heating Q_1 exhibits a major heat source equivalent to 10-20° day^{-1} at about the 400 mb level which occurs throughout the MCC life-cycle; there is also a minor low-level heat source during the MCC early stages while cumulus convection prevails. However, a heat sink of magnitude of -6 to -9° day^{-1} exists in the low- to mid-level troposphere after the growth stage. Among the terms involved in the heat budget, the local change term is considerably smaller than the horizontal and vertical advections terms; thus, the imbalance between the advection terms basically determines the distribution of the total apparent heat source. In general, the total apparent drying Q_2 shows a major moisture sink equivalent to -9 to -14° day^{-1} which occurs below the 700 mb level throughout most of the MCC life-cycle although a moisture source appears near the 900 mb level during the MCC mature stage. Since the mid- to upper-level heat source contribution is greater than the lower level's heat sink, some amount of the energy flux from the surface is required to balance the MCC net energy export in the upper troposphere.

Water vapor budget calculations over the composite MCC area indicate that water vapor is provided by MCC-scale convergence and the atmospheric storage term, with evaporation and moist horizontal advection playing smaller but by no means negligible roles. Of each 100 units of water vapor made available to the MCC, 47 come from MCC-scale mass convergence, 18 from MCC-scale moist advection, and 35 from

evaporation of water vapor, cloud water, and precipitation at the MCC initial stage. Of this total, 41 units are used to moisten the atmosphere, and 59 fall as precipitation. However, during the MCC mature stage, the precipitation efficiency reaches 113% such that the moist atmosphere provides an extra 13% from its storage, which was accumulated since the early stages of the MCC. The water vapor budget study suggests that the atmospheric storage process is significant enough over MCC spatial and temporal scales such that numerical models could not reflect the real atmospheric processes without considering this effect.

6.0 THE INFLUENCE OF ENVIRONMENTAL CONDITIONS ON MCC GENESIS AND DEVELOPMENT

The primary purpose of this chapter is to investigate some hypothetical mechanisms for MCC genesis and development via a composite study. Based on an examination of the structural, dynamic, and thermodynamic evolution of the composite MCC presented at the beginning of Chapter 4, together with conclusions from the budget studies of Chapter 5, certain MCC genesis and development mechanisms are hypothesized.

6.1 Geostrophic adjustment process related to MCC genesis and development

6.1.1 Geostrophic adjustment process

The problem of geostrophic adjustment is to determine the final adjusted state and the transient states which occur when atmospheric flows mutually adjust the pressure field and the momentum field to a state of geostrophic balance. Applications of the geostrophic adjustment concept to an MCC study can be addressed as follows.

It is assumed that the latent heat release from cumulus or mesoscale updrafts has a direct feedback to the rotational flow. Ooyama (1982) and Frank (1983) presented the following general definition of the Rossby radius of deformation (R'):

$$R' = N H / [(\zeta + f)^{0.5} (2 V / R + f)^{0.5}], \qquad (1)$$

where N is the Brunt-Vaisala frequency, H is the scale height of the circulation, ζ is the relative vorticity, f is the Coriolis parameter, V is the rotational component of the wind, and R is the radius of curvature. The Rossby radius of deformation is derived from consideration of the relative resistance of the atmosphere to vertical displacements resulting from static stability and to horizontal displacements resulting from inertial stability. Alternatively, the Rossby radius deformation with basic flow can be rewritten (as suggested by Schubert, personal communication) as follows:

$$R' = C_n / [(\zeta + f)^{0.5} (2 V / R + f)^{0.5}], \quad (2)$$

where C_n is the inertia-gravity wave speed of the corresponding vertical mode.

Fig. 6.1, based on Frank (1983), defines three regimes classified according to their horizontal length scale (L) and Rossby radius of deformation (R'). Region I includes small-scale turbulence and individual convective cells and clouds. Region II (or the dynamically small regime where $L < R'$) encompasses circulations with significantly unbalanced flow in which the divergent component is no longer a secondary circulation and may even be the primary mode. Region III (or the dynamically large regime where $L > R'$) is the nearly balanced flow regime where large-scale circulations evolve slowly, and secondary circulations are largely controlled by the primary circulations.

During the geostrophic adjustment process for dynamically small systems, the mass field tends to adjust to the rotational wind fields as suggested by Schubert et al. (1980) in their barotropic modeling study. On the other hand, the rotational wind fields adjust to the mass field

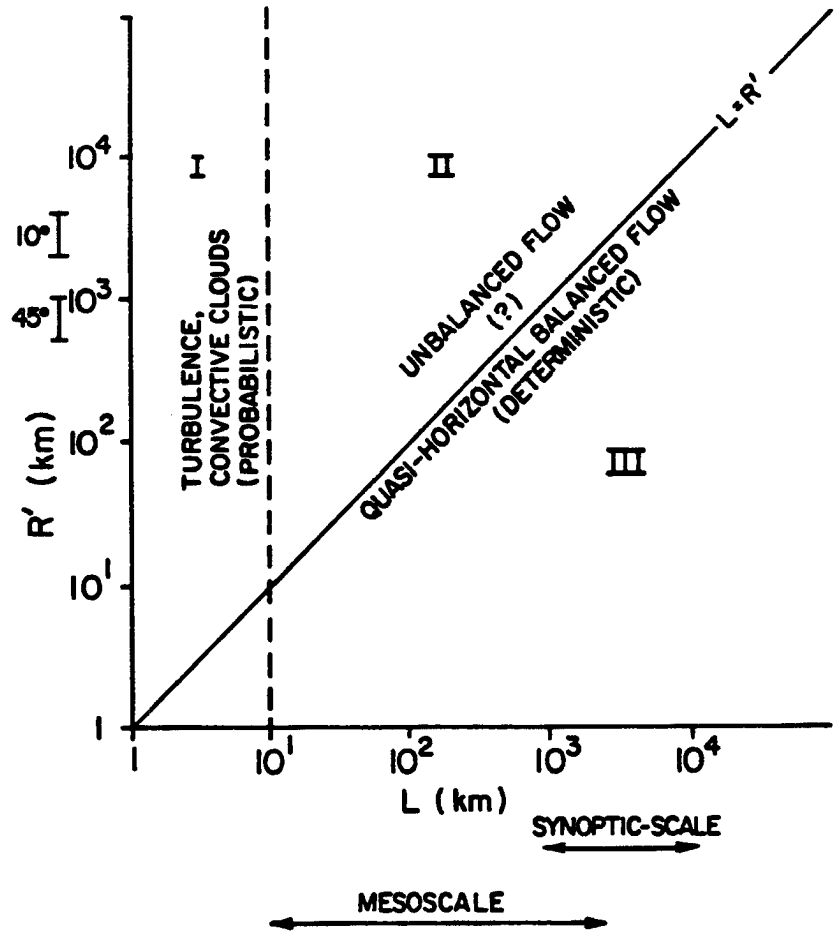

Fig. 6.1. Schematic of relationships between horizontal scale (L), the Rossby radius of deformation (R'), and modes of circulation. Typical values of R' for systems at latitudes 10° and 45° are indicated. [Adapted from Frank, 1983.]

for dynamically large systems. As a system develops, the localized relative vorticity and/or 2V/R (i.e., the mean vorticity of a system) increase comparable to f within the system area, and the mesoscale system is stiffened by the increase of absolute vorticity and inertial stability. In other words, the Rossby radius of deformation decreases locally; thus, the lower scale limit for the quasi-balanced flow is brought down closer to the mesoscale. Note that, in the tropics, a small change in ζ or 2V/R causes a large percentage change of R'. However, in the middle latitudes, a small change in ζ or 2V/R results in a smaller variation of R' in contrast (due to the dominanting role of Coriolis parameter in determining R'). If this reduction of the radius of deformation were continued, the deterministic dynamics of the balanced flow would begin to take over the control of the mesoscale convection.

Moreover, Schubert and Hack (1983) applied the transformed Eliassen balanced vortex model in a hurricane modeling study. They revealed that the change of a system from the dynamically small regime to the dynamically large regime implies a corresponding change in heating efficiency and internal circulations. They further pointed out that a relatively smaller Rossby radius signifies a stronger rotational constraint and a relative tendency for adjustment of wind to pressure. Additionally, Schubert and Hack proved that the terms "strong rotational constraint" and "adjustment of wind to pressure" were synonymous with "efficient heating". It is first necessary, however, to decide on the representative levels of the Rossby radius of deformation for a system. Then, we attempt to find out which physical

processes causes a shrinking or reduction of the radius of deformation if such a reduction occurs.

Emanuel (1983) noted that the atmospheric response to convective heating can be divided into transient and balanced modes. Typically, the transient response will take the form of an inertia-gravity wave within the Rossby radius of deformation. On the other hand, the steady response to localized heating is generally assumed to involve subsidence and concomitant adiabatic warming adjacent to the heat source. Usually, the atmospheric responds to convective heating in a balanced way beyond the Rossby radius of deformation. Thus, convective heating in disturbances larger than R' will excite less gravity wave energy, and more gravity energy will be projected onto the geostrophically-balanced flow. In fact, most of the energy released from cumulus convection to the system is transported horizontally and vertically as internal gravity wave energy. The retained portion of the heating acts to build a meso-α-scale circulation on the scale of the Rossby radius of deformation. Emanuel also showed the time scale of the balanced response to be on the order of a pendulum day.

Tripoli (1986) concluded from his MCS simulations that the internal gravity wave energy in such systems is largely transported into the stratosphere by vertical propagation during the daytime. At night, however, enhanced destabilization of the upper layer's stratiform cloud by longwave radiation traps a greater portion of the internal gravity wave energy. As a result, the concentrated cellular circulation initiates several meso-β-scale systems from the action of the emitted trapped internal waves. These act to weaken the core and spread the upward motion through the meso-α-scale circulation.

Based on the conclusions of Chapters 4 and 5, we see that low-level convergence is a necessary condition for MCC genesis. During the early stages of the MCC life-cycle, the system is characterized by the development of deep convection which has a lower level of maximum upward motion and a lower level of maximum heating. Up-scale development during the MCC growth and mature stages is characterized by wide-spread thick stratiform cloud in the upper troposphere. Observational evidence shows that the formation of this elevated stratiform cloud shield is accompanied by an upward shift in the level of maximum upward motion and maximum heating from about 700 mb to 400 mb level. Anthes and Keyser (1979), in their simulation of a mid-latitude cyclone, suggested that a higher proportion of convective heating in the lower troposphere contributed to the deepening of the mesoscale system, but the greater upper-level heating stabilized the atmosphere and caused the system to undergo slower development or weakening. It seems to be that an upward shift in the level of convective heating may weaken the overall convective intensity of an MCC but favor its up-scale growth to a larger-scale mesoscale system.

Fulton (1980) found that the extent of geostrophic adjustment depended strongly on the vertical structure of the initial conditions. He showed that as the initial bubble moved higher in the troposphere, the relative contributions of the higher wavenumber modes became smaller. His results show some resemblance to the heating profile of the early MCC stages. Hack and Schubert (1986) investigated the influence of the vertical heating profile on the development of a tropical cyclone. They found that there is a tendency for a larger percentage of the kinetic energy to be projected onto larger horizontal

scales of motion when the heating maximum is shifted into the upper troposphere. Their conclusion may apply to the MCC growth and mature stages.

Based on the apparent linkage between the heating profile and the MCC evolution, we hypothesize that the vertical level of the Rossby radius of deformation should be chosen in the low to middle tropospheric levels so as to detect the influence of both cumulus and mesoscale systems. This will allow determination of whether the Rossby radius deformation of a system is reduced during the MCC genesis and development stages.

6.1.2 Calculation of Rossby radius of deformation

We evaluated the Rossby radius of deformation through Eq. (2) by using 30 m s^{-1} for the phase speed of the inertia-gravity wave (C_n) as computed by Tripoli (1986) in his mesoscale model. The west-east cross-section of the Rossby radius deformation (Figs. 6.2a-d) generally exhibits a common feature of smaller radius in the lower troposphere and a slightly larger value aloft. Owing to the larger value of f compared to the relative vorticity and the mean vorticity (i.e., 2V/R) of the MCC in mid-latitudes, small changes in the relative vorticity or the rotational component of the wind result in little change in the magnitude of the Rossby radius of deformation. Although the change of radius is insignificant longitudinally during the MCC-12h stage (Fig. 6.2a), the plan view of Rossby radius deformation at the 700 mb level (Fig. 6.3a) still shows a relative minimum value of 310 km near the MCC centroid. This low value of the Rossby radius results mainly from the cyclonic vorticity, but the inertial stability also contributes. As the system evolves, the tendency for reduction of the Rossby radius of

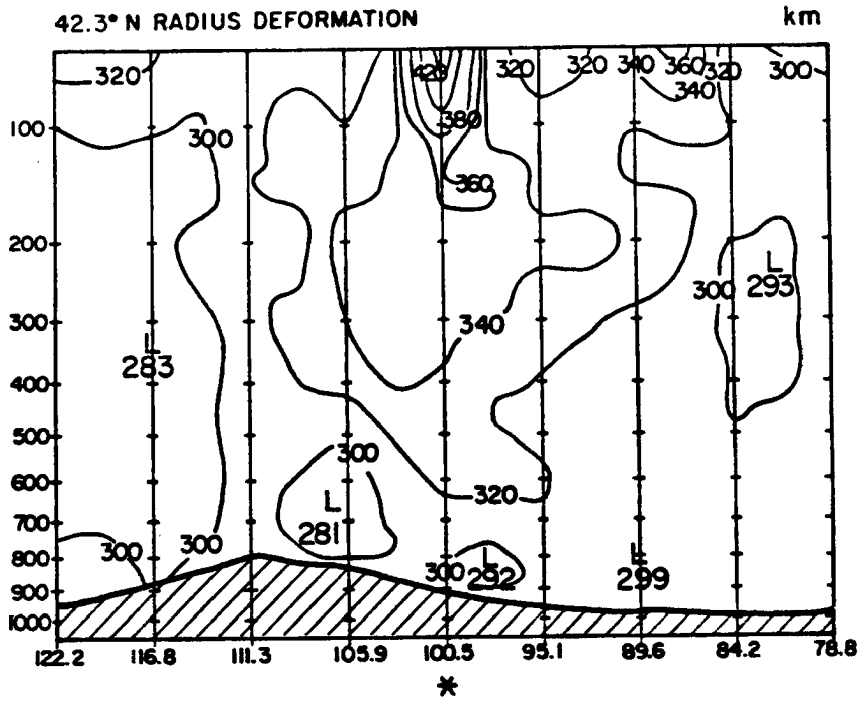

Fig. 6.2a. Rossby radius of deformation along the west-east cross-section through the MCC centroid at the MCC-12h stage. Units: km.

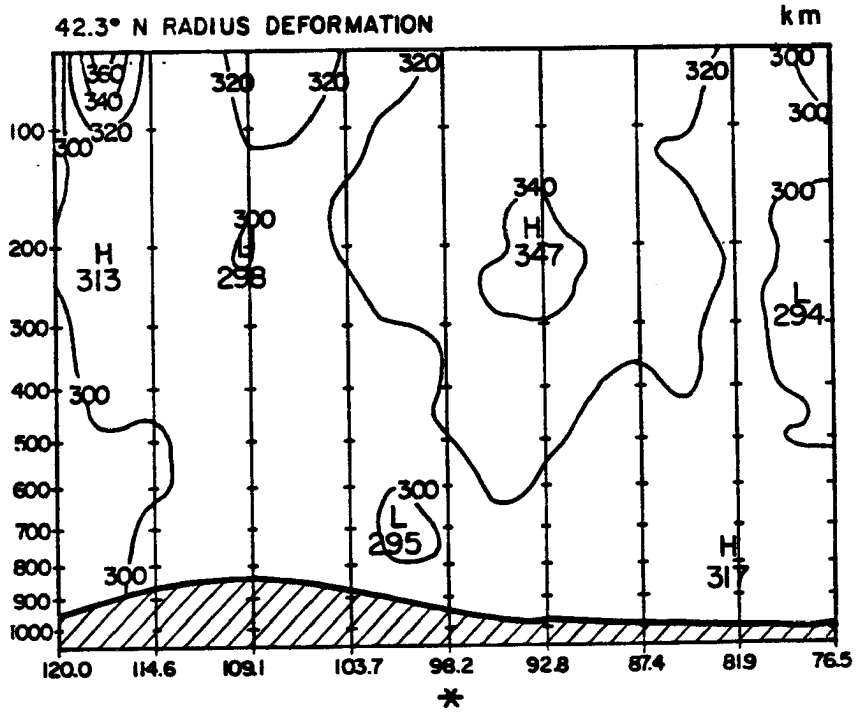

Fig. 6.2b. As in Fig. 6.2a, except for the initial stage. Units: km.

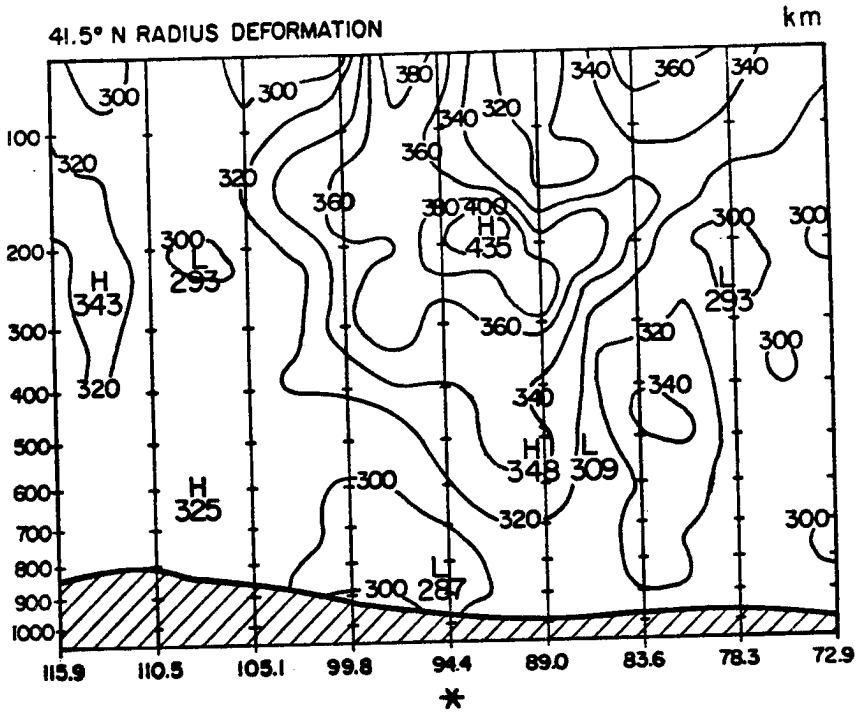

Fig. 6.2c. As in Fig. 6.2a, except for the growth stage. Units: km.

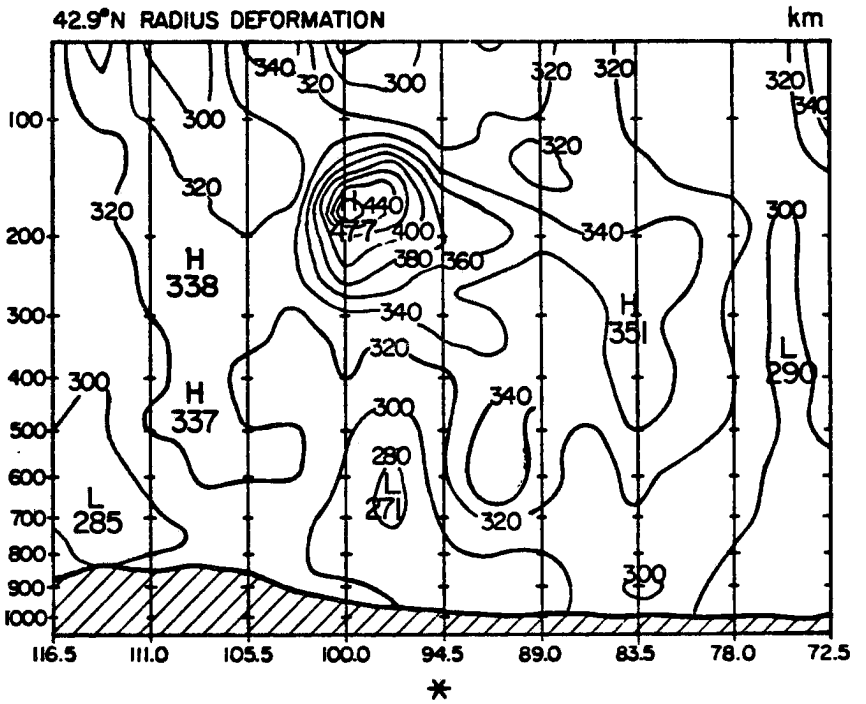

Fig. 6.2d. As in Fig. 6.2a, except for the mature stage. Units: km.

deformation is maintained within the lower troposphere, reflecting the presence of cyclonic vorticity. During the MCC growth stage (Fig. 6.3b), the Rossby radius of deformation decreases to a minimum value of 290 km, responding to the presence of the most intense vortex. However, the Rossby radius at the mature stage (Fig. 6.3c) returns to an average magnitude of 300 km due to the lower-level cyclonic vorticity center lagging behind the MCC centroid. Fig. 6.3d shows a relative minimum of the Rossby radius of deformation at the 400 mb level -- the level of maximum heating and upward motion, since mesoscale updrafts prevail during the MCC mature stage.

The time evolution chart of the ratio of Rossby radius of deformation relative to its value of MCC-12h stage is illustrated in Fig. 6.4. We can see that the ratio is less than 1 (i.e., smaller than the value of MCC-12h stage) below the 800 mb level during most of the MCC life-cycle. Note that the Rossby radius of deformation ratio at the 400 mb level decreases slightly between the growth and mature stages; this decrease can be attributed to the weaker anticyclonic vorticity at the time of MCC maturity (Fig. 4.39a). The results presented herein imply that, unlike a tropical cyclone (Lee, 1986), the MCC does not modulate the inertial stability (discussed later) significantly during its life-cycle. Consequently, the ratio of Rossby radius of deformation is near unity during the MCC life-cycle; reflecting the absolute vorticity and the inertial stability vary over a small range compared to f. In summary, the profile of Rossby radius of deformation is mainly subject to the initial distribution of the vertical component of vorticity such that the Rossby radius of deformation exhibits a smaller value in the lower troposphere and reaches a minimum during the MCC

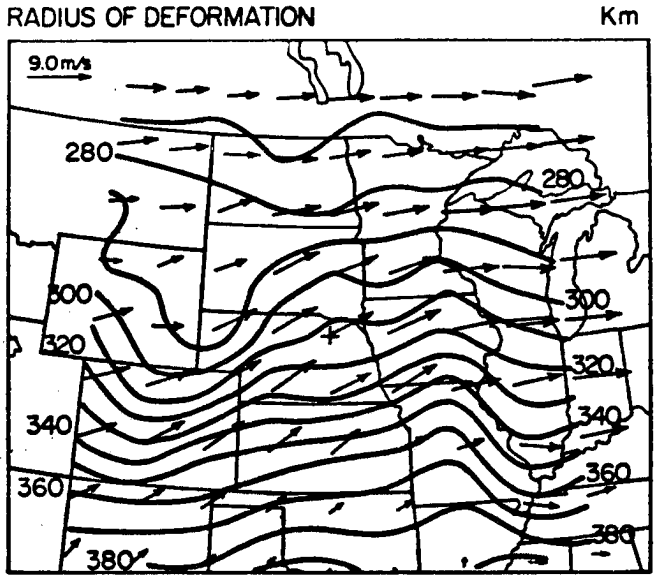

Fig. 6.3a. Analysis of 700 mb level Rossby radius of deformation and wind vectors at the MCC-12h stage. Units: km and m s^{-1}.

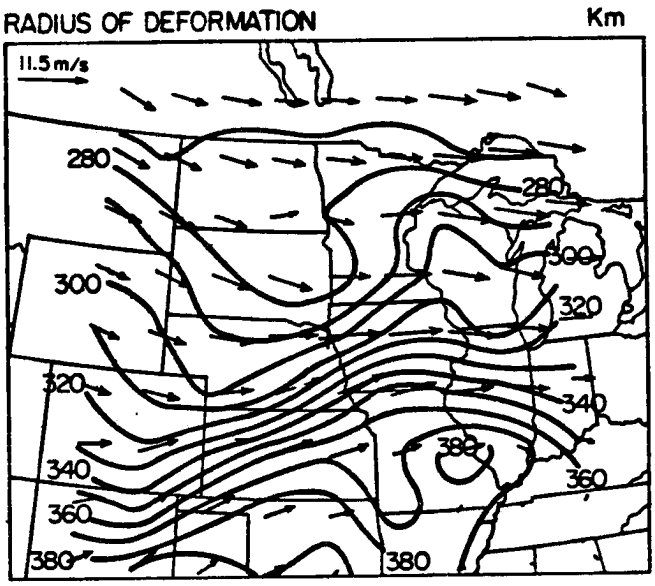

Fig. 6.3b. As in Fig. 6.3a, except for the growth stage. Units: km and m s^{-1}.

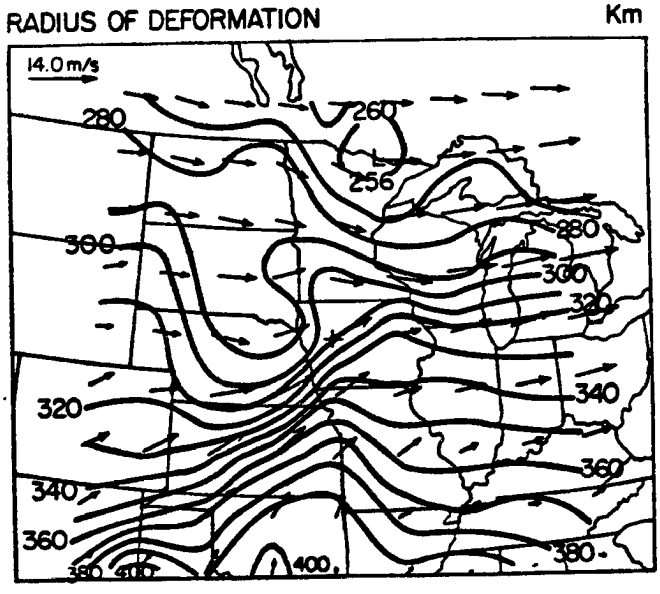

Fig. 6.3c. As in Fig. 6.3a, except for the mature stage. Units: km and m s^{-1}.

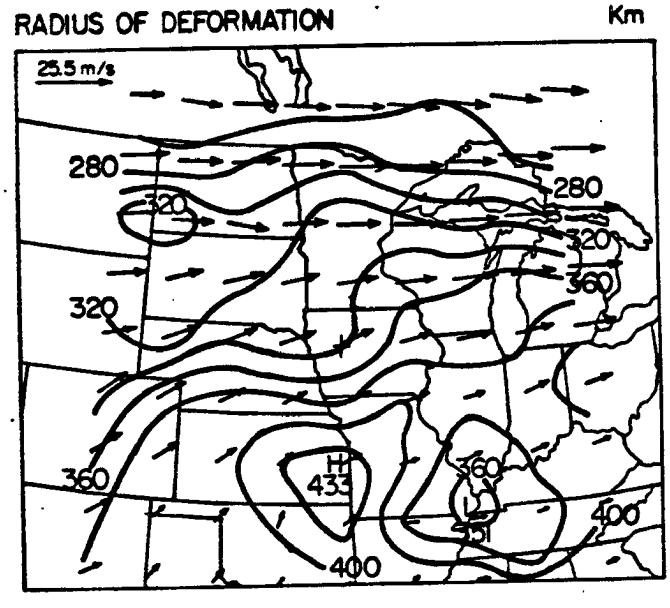

Fig. 6.3d. As in Fig. 6.3c, except for the 400 mb level. Units: km and m s^{-1}.

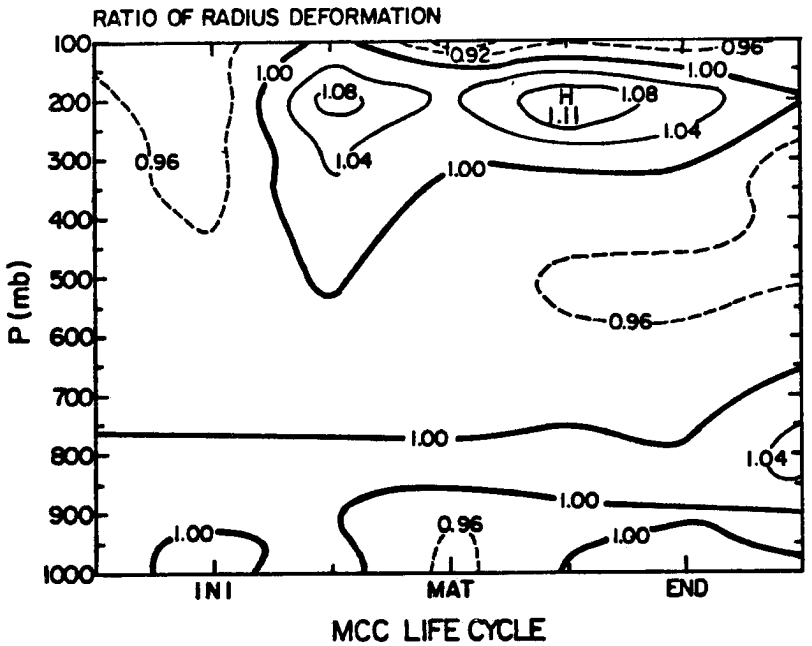

Fig. 6.4. Height-time plot of the Rossby radius of deformation ratio. The Rossby radius of deformation is obtained by applying a 9-grid-point area average over a 6^{o} X 6^{o} lat.-long. domain every 50 mb. Units: none.

growth to mature stages due to the presence of 700-mb level short-wave trough. In fact, the contribution of f is dominant over the cyclonic vorticity (caused by the production of short-wave trough) in controlling the Rossby radius of deformation. Nevertheless, a reduction of Rossby radius of deformation also occurs in the mid- to upper-level troposphere during MCC maturity, in response to the mesoscale updrafts. Evidence obtained from field experiments of Cotton (less than 5°C, personal communication) during the AIMCS and O-K Pre-STORM periods also shows that the upper-level heating during MCC development is not as strong as in tropical cyclones (about 10°C, Gray et al., 1982; Lee, 1986); therefore, the reduction of the Rossby radius of deformation will not be significant compared to that of the tropical cyclone shown by Schubert and Hack (1983).

6.2 Static stability and wind shear threshold

From the last section, we understand from the concept of Rossby radius of deformation that the dynamic structure of an MCC can modulate the system evolution. Apparently, the thermodynamic variations of the MCC alter the system in some aspects. The static stability and inertial stability are discussed in this section.

6.2.1 Static stability associated with MCC evolution

The radiative effect of the thick stratiform cloud increases in its importance to the MCC system dynamics and thermodynamics as nightfall approaches. During the nighttime, the destabilization resulting from the cloud-top longwave radiational cooling and cloud-base longwave radiational warming is significantly greater. In general, this destabilization has some influence on vertically trapping the inertia-

gravity wave energy emitted by the convection core within the troposphere (Tripoli, 1986).

Fig 6.5 shows that the MCC is characterized by a relative lower inertial stability [evaluated according to the denominator in Eq. (2)] in the upper-level troposphere than lower levels due to the anticyclonic vorticity there. Within the entire vertical column, the MCC exhibits relatively higher inertial stability (cyclonic vorticity in the lower layers and weak anticyclonic vorticity aloft) during its early stages due to the dominant low-level forcing. Gradually, the inertial stability decreases at the mature stage because of the dominant upper-level forcing.

The static stability is calculated after Holton (1979) as follows:

$$S = \frac{T}{\theta}\frac{\partial \theta}{\partial z}, \tag{3}$$

where T is the temperature, θ is the potential temperature, and z is the vertical coordinate. Fig. 6.6a illustrates the time evolution of the static stability evaluated in the mid- to upper-level troposphere (averaged over 500-200 mb layer). This diagram clearly indicates the MCC is less stable (i.e., the lapse-rate difference between dry adiabatic and the real atmosphere is about $2^{o}C\ km^{-1}$) during its growth stage. The destabilization results from a decrease of the vertical potential temperature gradient (lowering the Brunt-Vaisala frequency) in the region below the tropopause. In fact, the convective heating resulting from the up-scale development of the meso-β convective elements and the merger of anvil clouds is responsible for this destabilization (Tripoli, 1986).

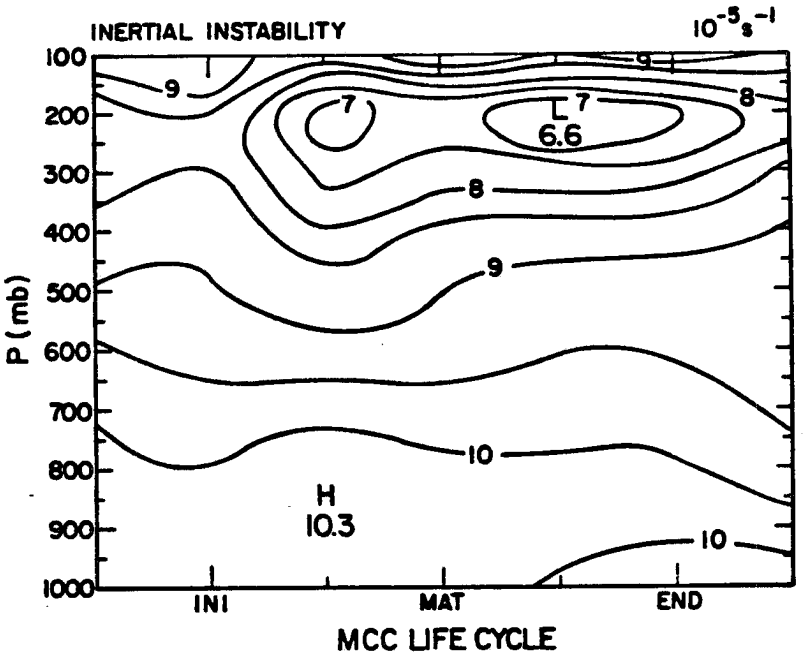

Fig. 6.5. Height-time plot of the inertial stability. The inertial stability is obtained by applying a 9-grid-point area average over a 6° X 6° lat.-long. domain every 50 mb. Units: 10^{-5} s^{-1}.

The static stability in the lower stratosphere (evaluated over 200-100 mb layer, Fig. 6.6b) generally shows a reverse trend compared to its upper-tropospheric counterpart. The MCC system is stable in this layer after the pre-MCC stage and reaches its most stable extent at the mature stage. Note that the mid- to upper-level troposphere is being destabilized one period (roughly 3 hours) prior to the lower stratospheric stabilization -- this time allows the atmosphere to adjust and respond. The time evolution of the static stability of the marginal MCCs (not shown), in contrast, does not show the feature of anvil cloud destabilization until the dissipation stage (probably due to the upper-level warm temperature advection below the thick stratiform cloud).

In summary, the atmospheric destabilization process results from the decrease of the inertial stability and the static stability during the MCC growth to mature stages. The destabilization, in turn, enhances the vertically trapping of the inertia-gravity wave energy emitted by convection cores within the troposphere and possibly contributes to a projection of greater convective heating on the meso-α-scale by triggering more widespread convection (Tripoli, 1986).

6.2.2 Wind shear associated with MCC evolution

Weisman and Klemp (1982, 1984) investigated the dependence of convection storm type on buoyancy and characteristics of the environmental wind field. A general relationship between wind shear and buoyancy was expressed in terms of a bulk Richardson number R as follows:

$$R = \frac{CAPE}{1/2[\bar{U}_6 - \bar{U}_{0.5})^2 + (\bar{V}_6 - \bar{V}_{0.5})^2]} \qquad (4)$$

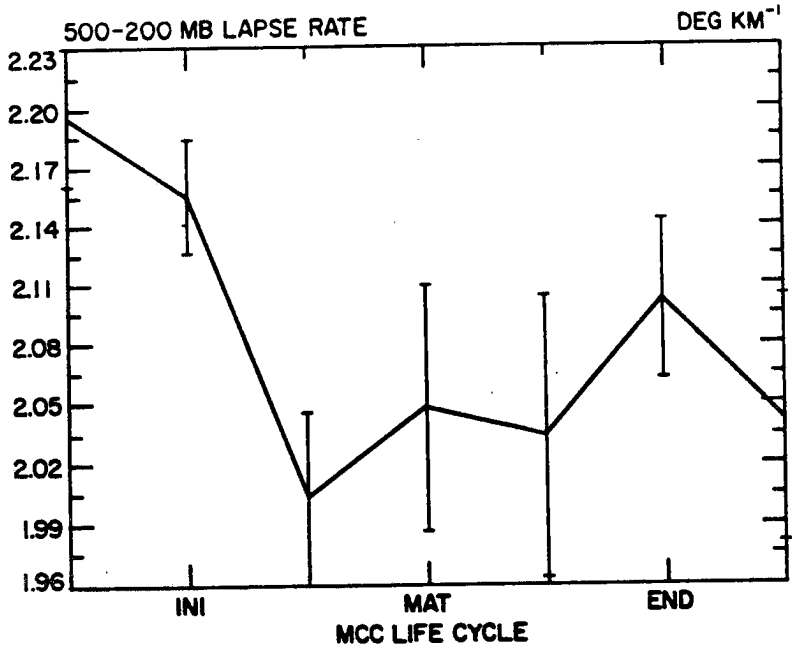

Fig. 6.6a. Time evolution plot of 500-200 mb layer static stability. The layer mean value is calculated by averaging over 9 grid points every 50 mb. The error-bar represents one plus/minus standard deviation of the 9-point average. Units: K km^{-1}.

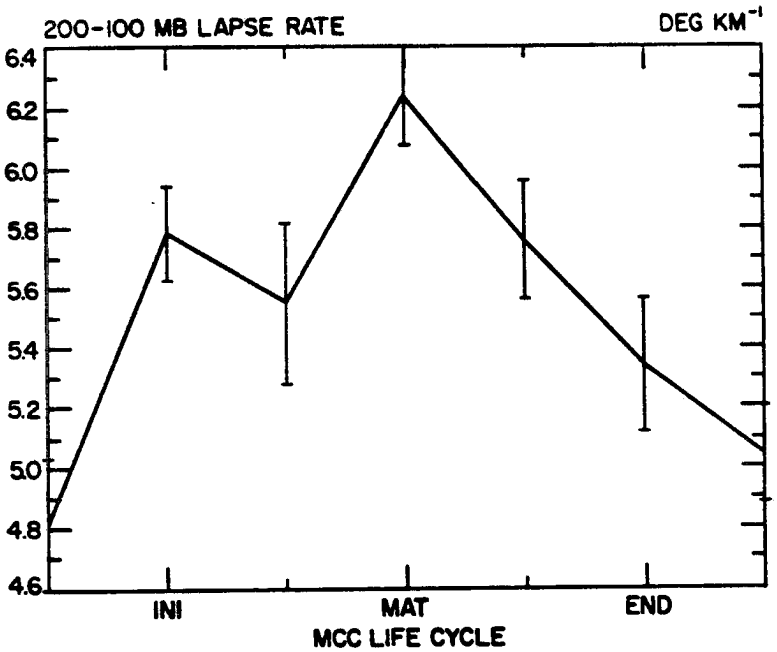

Fig. 6.6b. As in Fig. 6.6a, except for the 200-100 mb layer. Units: K km^{-1}.

where CAPE is as defined in Section 4.2.2, and $\bar{U}_6$ and $\bar{U}_{0.5}$ represent density-weighted mean wind speed taken over the lowest 6 and 0.5 km of the profile. The denominator of R is a measure of the wind shear (calculated by the wind speed difference between two levels) in the lower half of troposphere; it can also be considered a measure of the inflow kinetic energy made available to the storm by the vertical wind shear (Moncrieff and Green, 1972).

Fig. 6.7a indicates that the wind shear of low- to mid-level (calculated by the wind speed difference between 850 and 500 mb levels) reaches a maximum value of 7.7 m s^{-1} between 6 and 0.5 km from the surface during the growth stage -- the time when the mid-level "jet-like" inflow prevails. Fig. 6.8 further illustrates that the maximum wind shear occurs in the vicinity of the upstream side of the MCC centroid. Thus, a mid-level "jet-like" inflow feeds in low θ_e air for explosive system development. Frank (1978) found that the wind shear between 950 to 650 mb level for tropical cloud clusters is 6 m s^{-1} (contrasting to that for tropical squall lines of 13 m s^{-1}); this is compatible with the magnitude of wind shear presented herein. Again, the main distinguishing feature between an environment capable of sustaining a squall line versus an MCC is that MCCs prevail in low shear environments, while squall lines are favored in strongly sheared conditions.

Strong vertical wind shear in the upper troposphere tends to prevent the accumulation of the enthalpy in a vertical column needed for deep convection, thus hindering the development of the MCC. Therefore, the occurrence of an MCC is favored in a low-wind-shear environment. However, the mid- to upper-level wind shear (measured the wind speed

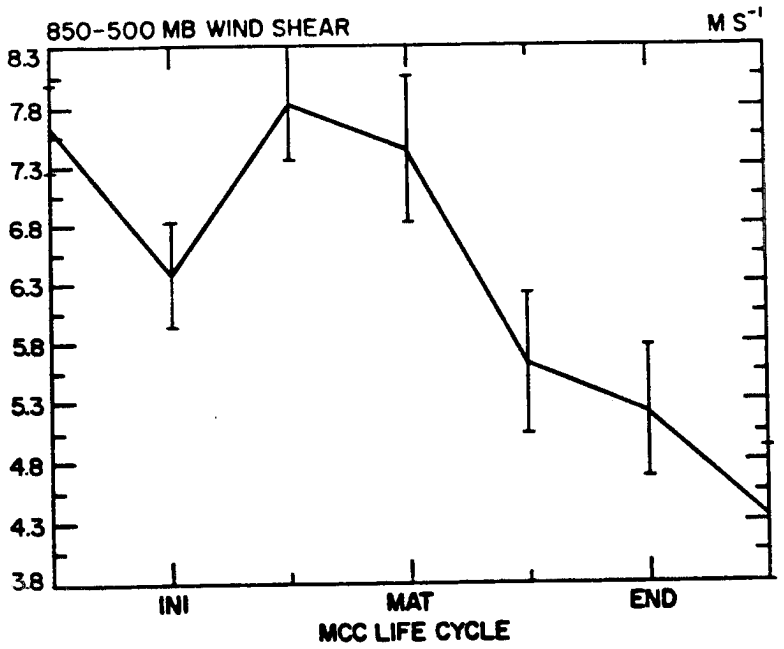

Fig. 6.7a. Height-time plot of the 850-500 mb layer wind shear. Units: m s^{-1}.

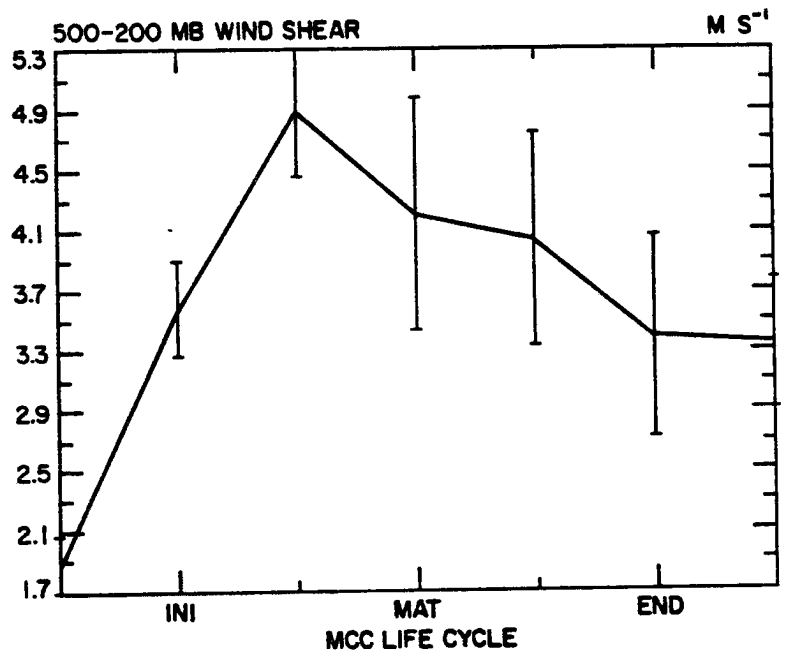

Fig. 6.7b. As in Fig. 6.7a, except for the 500-200 mb layer. Units: m s^{-1}.

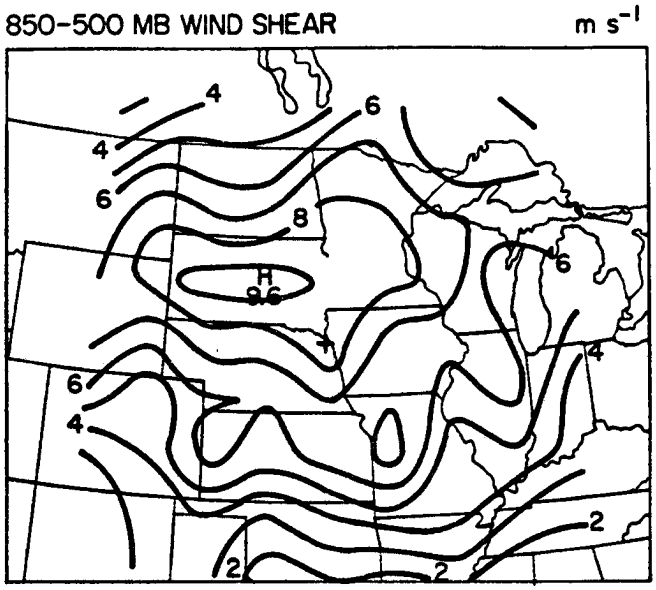

Fig. 6.8. Analysis of 850-500 mb layer wind shear at the growth stage. Units: m s^{-1}.

difference in the 500-200 mb layer, Fig. 6.7b) shows a wind shear peak with a moderate magnitude at the growth stage. Probably, the higher wind shear is caused by the enhanced upper-level jet stream resulting from the MCC's own circulation rather than by preexisting environmental conditions. However, the wind shear significantly increases at the mature stage, resulting mainly from the intrusion of a mid-level trough or partially from the late development of mid-level inflow. Incidentally, Merritt and Fritsch (1984) found that the meso-β convective elements tended to move along the orientation of the mean cloud-layer shear vector, i.e., the 850-300 mb layer thickness contours.

Weisman and Klemp (1982) found that for a given amount of buoyancy, weak wind shear produces short-lived single cells. Low to moderate wind shear produces secondary cell development similar to multicellular storms, while moderate to strong wind shears were associated with split or supercell type storms. Their results suggest that a range of bulk Richardson numbers probably exists during the MCC evolution because genesis of an MCC involves the up-scale development of meso-γ- and meso-β-scale systems during the early stages. Generally, values of the bulk Richardson number of the composite MCC (not shown) are in the hundreds range; comparable values have been found by Bluestein and Jain (1985) for multicellular storms. It was shown in Chapter 4 showed that the profile of the bulk Richardson number basically depends on the local variation of CAPE; wind shear distribution are not too critical in controlling the distribution of bulk Richardson number over the MCC lifecycle.

In summary, an MCC is favored in a weak vertical wind shear environment in comparison to squall line systems. However, the internal

dynamics of an MCC induces a slightly larger low- to mid-level wind shear during the growth stage.

6.3 Tropopause temperature threshold

To some extent, the initial growth and expansion of the upper layer's mesoscale stratiform cloud is accomplished by the incorporation of cloud and precipitation debris from dissipating cumulonimbi into a large-scale rain system (Leary and Houze, 1979). Johnson and Kriete (1982) found that the cold anomalies of 2-3^{o}C above Winter MONEX mesoscale stratiform clouds appeared to be centered 1-2 km above the mesoscale stratiform cloud top. Like those cloud clusters found in tropical regions, Maddox (1981) inferred that the duration and intensity of a mid-latitude MCC positively correlated to the area of -53^{o}C IR temperature such that the colder the tropopause temperature is, the higher the cumulus convection penetrates. Nehrkorn (1985) used a Wave-CISK model to examine prefrontal squall line formation and pointed out that the systems growth rate decreases with decreasing static stability of the stratosphere. His result implies that a colder tropopause temperature (i.e., increased static stability in the lower stratosphere) favored development of the meso-scale wave trapping. In fact, Heymsfield and Blackmer (1985) confirmed a common feature that there is a tendency for colder tropopause temperatures to be associated with higher tropopauses. Also, Emanuel's dynamic flywheel (or Carnot cycle) concept may be appliable to explain the favored development for the meso-scale system.

The above-mentioned evidence seems to provide some linkages between the tropopause temperature (or tropopause height) and the development of a mesoscale stratiform cloud system. It appears that the colder

tropopause may enhance the convective updraft and consequently the mesoscale downdraft through the coalescence and/or ice phase diffusion, accretion, and aggregate growth within the mesoscale-enhanced vertical moisture flux region. Therefore, it is postulated that the tropopause temperature (which, in turn, determines the upper tropospheric or lower stratospheric static stability) may have some connection to MCC genesis and development.

Based on the U. S. Department of Commerce and U. S. Department of Defense (1969) definition, the tropopause level is selected at a pressure of 500 mb or less as follows:

(1) The lowest level, with respect to altitude, at which the temperature lapse rate decreases to $2^{o}C\ km^{-1}$ or less.

(2) The lowest level at which the average lapse rate from this level to any point within the next higher two km does not exceed $2^{o}C\ km^{-1}$.

The horizontal plan view of the tropopause temperature at the MCC-12h stage is shown in Fig. 6.9a. We see that a cool pool is located on the upstream side of the MCC centroid such that it advects cooler air into the threat area and destabilizes the pre-MCC environment. As the MCC evolves, the cooling trend at the tropopause is maintained until the pre-MCC stage, as depicted by the chart of tropopause temperature variation (Fig. 6.10). Note that the diurnal temperature change is negligible (less than $0.3^{o}C$ near the tropopause) so that the tropopause cooling prior to the MCC initiation is meaningful. During the MCC initial to mature stages, convective heating contributes to the tropopause warming before the stratiform cloud shield spreads out horizontally. The tremendous difference in tropopause temperature ($5^{o}C$)

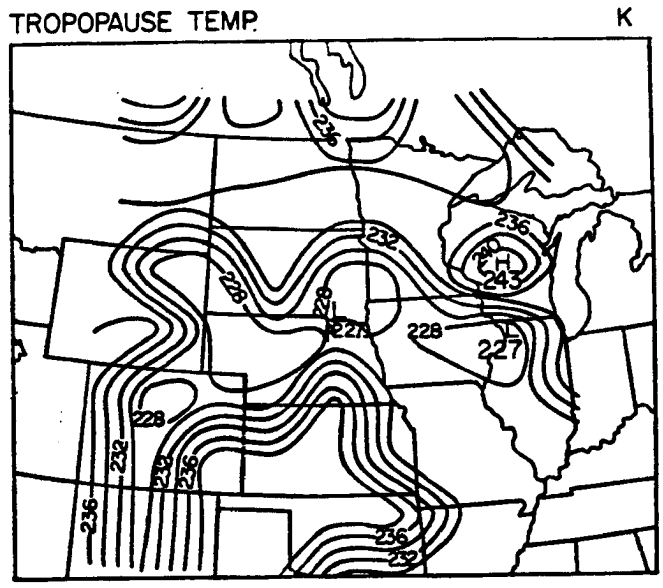

Fig. 6.9a. Analysis of temperature field and wind vectors for the tropopause at the MCC-12h stage. Units: K and m s^{-1}.

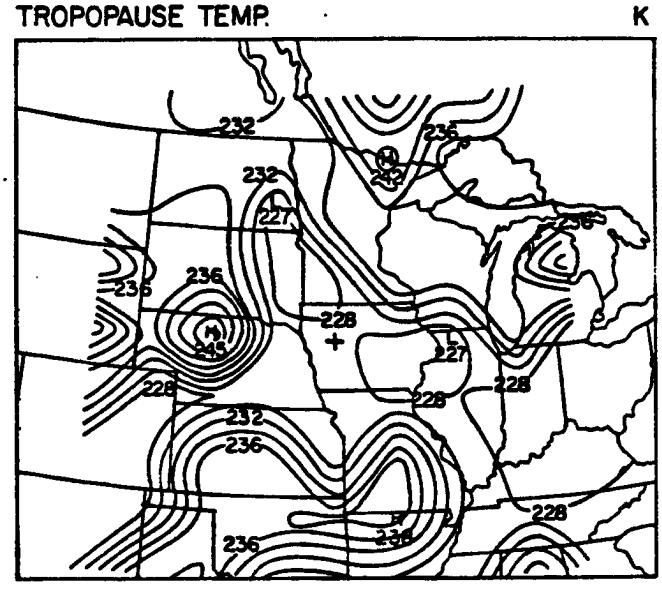

Fig. 6.9b. As in Fig. 6.9a, except for the mature stage. Units: K and m s^{-1}.

at MCC maturity apparently reflects the domination of the upper troposphere at nighttime by the well-developed cloud shield. This concentration of tropopause cooling in the vicinity of the MCC is clearly illustrated by the horizontal plan view in Fig. 6.9b. Although the tropopause cooling reaches its peak intensity at the time of MCC maturity, the environment continuously maintains a cool tropopause until the post-MCC stage (Fig. 6.10), reflecting the presence of the mesoscale cloud shield.

Generally, the tropopause height changes in step with the perturbation of the tropopause temperature, as found by Heymsfield and Blackmer (1985). The tropopause height has risen about 0.9 km at the time of MCC maturity as compared to the MCC-12h stage (Fig. 6.11). Also, the rise of the tropopause is tightly focused at the MCC centroid as shown in the horizontal plan view (Fig. 6.12). This concentration of tropopause cooling and lifting strengthens our confidence in being able to accurately detect the tropopause level and illustrates the phenomena of the tropopause cooling and elevation associated with the formation of the cloud shield.

6.4 Summary

In this chapter, we have proposed some environmental conditions which are favorable for MCC genesis and development. Prior to MCC initiation, the preexisting cool tropopause located to the upstream side of the threat area provides a destabilized upper troposphere in the pre-MCC environment. Within the lower troposphere, the large-scale circulation continuously supplies a convergence of moist and potentially unstable air into the threat area for triggering the deep convection.

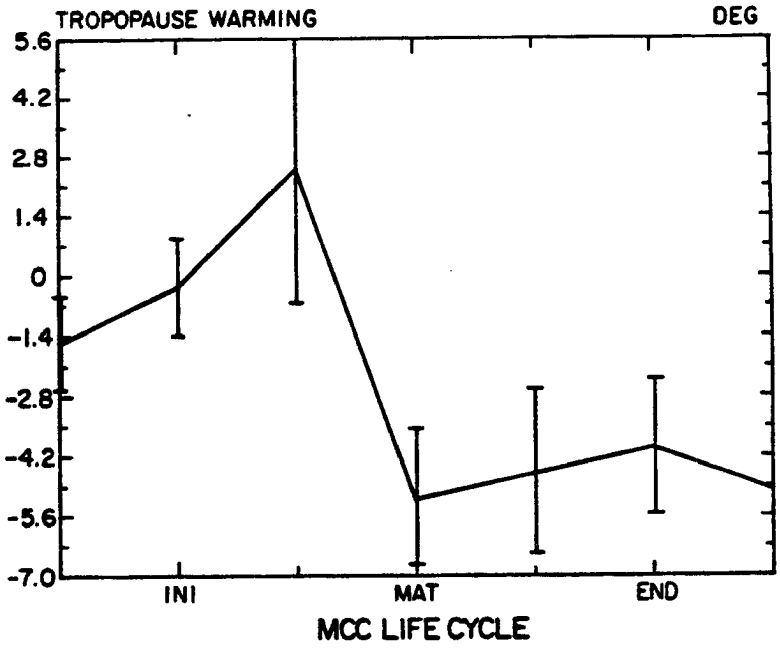

Fig. 6.10. Time evolution plot of the tropopause temperature change compared to the MCC-12h stage. The value is obtained for a 9-grid-point average. Units: K.

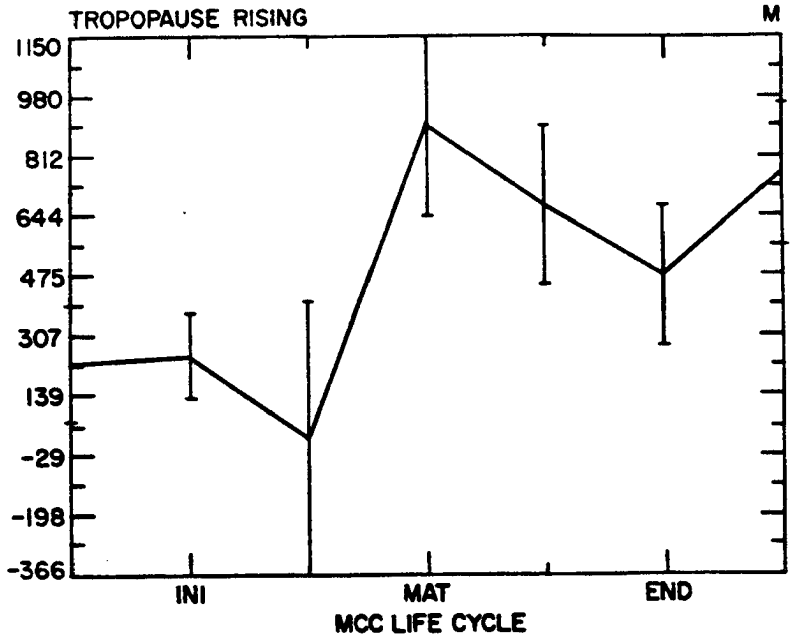

Fig. 6.11. Time evolution plot of the tropopause height change compared to the MCC-12h stage. The value is obtained for a 9-grid-point average. Units: m.

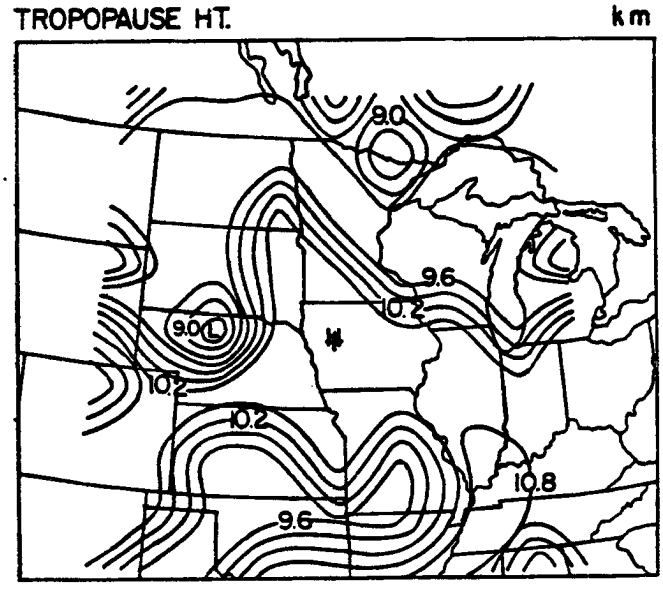

Fig. 6.12. Analysis of geopotential height and wind vectors for the tropopause at the mature stage. Units: km and $m\ s^{-1}$.

During the early stages of the MCC, the low-level cyclonic circulation is enhanced through convergence, convective heating, and some mesoscale forcing mechanisms (e.g., LLJ or low-level confluent flow). The localized cyclonic vorticity increases the inertial stability and reduces the Rossby radius of deformation, thus providing an efficient source of heating in the lower troposphere. This highly efficient heating should occur in the presence of weak vertical wind shear throughout the entire vertical column.

However, during the MCC growth stage, the low- and mid-level convergence associated with enhanced internal circulation maintains a smaller Rossby radius of deformation. Meanwhile, the MCC circulation experiences a geostrophic imbalance in the upper-level troposphere which is associated with a significant ageostrophic wind and which enhances the ascending motion. The longwave radiational cooling at the stratiform cloud top and warming at the cloud base destabilizes the upper-level tropospheric environment and results in an enhanced internal circulation.

Once the MCC reaches maturity, the mesoscale anvil dominates the upper tropospheric heating, which also helps in maintaining a reduced Rossby radius of deformation in the mid- to upper-level troposphere. The tropopause cooling and lifting reaches its maximum intensity, reflecting the influence of the mesoscale cloud shield.

7.0 A CONCEPTUAL MODEL OF MCC EVOLUTION

The primary purpose of this chapter is to describe a conceptual model of MCC evolution. This model is based on a synthesis of the composite analysis results for MCC structure, dynamics, thermodynamics, and the environmental conditions favoring MCC genesis and development, all of which were discussed in previous chapters.

7.1 Methodology for constructing a conceptual model

A conceptual model of the MCC life-cycle can be constructed primarily from analysis of the composite MCC structure discussed in Chapter 4. Certain characteristics of the MCC weather system should be detectable in the composite data set -- in particular, convectively-induced meso-α-scale temperature, height, and horizontal wind perturbations -- because the Barnes objective analysis scheme which has been used will retain the synoptic- to meso-α-scale aspects of the MCC composite data set while suppressing both short- and long-wavelength "noise".

In order to determine the evolution of the dynamic and thermodynamic structure of an MCC system, we have focused on the variations of moisture content, potential instability, and forcing mechanisms during the MCC life-cycle. The vorticity, heat, and moisture budgets constructed for the composite MCC provide additional information about MCC dynamics and thermodynamics. Environmental conditions which appear to favor MCC genesis and development have also been generated from the composite results, and these have been incorporated into the

conceptual model of MCC evolution as well. Incidentally, the following conceptual model of the evolution of a composite MCC was validated and modified through examination of the independent set of MCC cases from 1984.

7.2 Conceptual model of MCC evolution

The presence of cumulus- to meso-scale updrafts/downdrafts provides a mechanism to stabilize the atmosphere through warming in the upper troposphere and cooling in the lower troposphere. On the other hand, many large-scale processes destabilize the convective or mesoscale systems. The upper troposphere experiences cooling and relative drying due to long-wave radiative divergence or adiabatic ascent while the lower troposphere experiences warming and moistening due to surface heat flux, short-wave radiative convergence, adiabatic descent, and moisture convergence. Stabilizing and destabilizing processes compete simultaneously, thereby determining the timing and intensity of the deep convection embedded in the mesoscale convective system. During the early stages of the MCC life-cycle, the system environment is dominated by destabilizing processes such as strong low-level moisture convergence, low-level warm temperature advection, long-wave divergence and short-wave radiative convergence. However, during the growth and mature stages, the MCC environment is characterized by stabilizing processes due to the presence of prevailing mesoscale circulations. Based on the results of previous chapters, a conceptual model of the MCC scenerio may be formulated as follows.

Pre-MCC Stage

During the pre-MCC stage, several synoptic-scale features come together over the threat area several hours before the ensuing MCC

develops. The preexisting cool tropopause located on the upstream side of the threat area provides a destabilized upper-level troposphere in the pre-MCC environment. Within the lower troposphere, the synoptic-scale circulation drives the convergence of moist, potentially unstable air over the threat area which then triggers deep convection. In fact, the genesis of MCC is supported by a maximum intensity of CAPE over the threat area at the pre-MCC stage before the CAPE is quickly depleted by deep convection as the MCC forms.

Note that the positions of the surface front, horizontal moist axis, low-level jet, 500 mb vorticity trough, and upper-level diffluence zone are focused together over a mesoscale region in association with the favorable conditions of a preexisting cool tropopause and weak vertical wind shear. The MCC is thus driven by a combination of interacting dynamic and thermodynamic processes.

MCC Initial Stage

During the MCC initial stage, the system usually develops in the vicinity of the surface frontal zone. The MCC then moves with the mid-level steering flow and experiences a moist inflow in the lower troposphere to compensate for the energy export at upper levels. Weak vertical wind shear with the wind veering with height is a feature commonly present over the MCC threat area which aids in the development of more intense updrafts inside the core of the MCC. The presence of a low-level convergence and upper-level divergence couplet helps in maintaining the inflow and outflow of mass necessary for long periods of sustained deep convection while the attendent release of latent heat further enhances the low- to mid-level convergence, thus continously providing fuel for the MCC system.

At the initial stage, an MCC receives a fresh supply of moist air at low levels from the front side of the system and in turn sends an upper-level stream of drier air toward the rear side of the system. The MCC is characterized by maximum upward motion near the 700 mb level due to the dominant contribution from the convection-induced convergence and heating which carries the necessary energy upward and supports the system's initiation and further development.

The MCC exhibits a major apparent heat source equivalent to 9-12°C day^{-1} which is centered at about the 850 mb level and which results from mesoscale circulations as well as a minor low-level heat source due to the prevailing cumulus convection. The initiation of an MCC is largely driven by MCC-scale moisture convergence in the lower troposphere which is then transported to upper levels through deep convection. Precipitation efficiency is about 59%. The remaining 41% of the moisture is used to moisten the atmosphere in order to maintain MCC development.

The composite MCC behaves as a vorticity sink in the lower troposphere and as a vorticity source in the upper troposphere at the initial stage. This imbalance can be attributed to the removal of vorticity-rich air from low levels and its upward transport and deposition aloft by convection. The composite MCC initially exhibits cyclonic vorticity confined within the surface-to-700-mb layer and anticyclonic vorticity located exclusively in the upper troposphere. This configuration basically satisfies Emanuel's (1983) "dynamic flywheel" conceptual model for self-exciting convection. The low-level cyclonic circulation is enhanced through low-level mass convergence, convective heating, and some mesoscale forcing mechanisms (e.g., a LLJ

or low-level confluent flow). The localized cyclonic vorticity increases the inertial stability and reduces the Rossby radius of deformation, slightly enhancing the efficiency of heating within the low to middle troposphere.

The presence of "mesoscale organizers" which serve as triggers to release the preexisting potential instability are crucial to the MCC's initiation. The following "mesoscale organizers" were apparent in the composite MCC: a low-level jet, an upper-level jet, a mid-level "jet-like" inflow, 700 mb level confluent flow, and a low- to mid-level trough.

MCC Growth Stage

During the MCC growth stage, the high θ_e gradient between the low- and mid-level troposphere in the vicinity of the MCC centroid provides an abundant fuel supply from the lower troposphere as well as a potentially unstable environment for system development. The low-level convergence zone expands and lifts to the middle troposphere in association with an upward motion maximum at 400 mb, reflecting the dominance of mesoscale updrafts. In response to the upward shift in heating level associated with the mid-level convergence, a mid-level "jet-like" inflow develops which reaches its maximum intensity during the growth stage slightly above the melting level at about 500 mb. This mid-level "jet-like" inflow appears to play an important role in driving the mesoscale downdraft and thus enhances the entire cellular circulation. Longwave radiative cooling at the top of the growing stratiform shield and warming at its base destabilizes the upper-level tropospheric environment and results in enhancing the internal circulation in the MCC (see Figs. 4.27 and 4.28).

During the MCC growth stage, the low- and mid-level convergence associated with the enhanced internal circulation maintains a reduced Rossby radius of deformation. Meanwhile the MCC circulation induces a geostrophic imbalance in the upper-level troposphere; the resulting significant ageostrophic wind enhances the ascending motion. The dynamic structure of the composite MCC shows that the cyclonic vorticity still to be confined within the surface-to-700-mb layer and the anticyclonic vorticity to be located exclusively in the upper troposphere. Again, this configuration basically satisfies Emanuel's "dynamic flywheel" conceptual model for a self-exciting convection. The convective feedbacks through the development of elevated convective heating are also instrumental to the development of MCCs. Although the precipitation efficiency (79%) is high during the growth stage, there is additional atmospheric storage of water substance.

MCC Mature Stage

Once the MCC reaches its mature stage, the mesoscale altostratus cloud dominates the upper tropospheric heating. Tropopause cooling and rising reaches its maximum intensity at the mature stage, reflecting the contribution of longwave radiative cooling by the upper-level cloud shield and mesoscale ascent. The MCC is maintained by intensified mid-level convergence in association with a developing mid-level meso-cyclone in which mesoscale updrafts mostly prevail. However, a deep layer of downward motion below the 700 mb level which acts as an apparent moisture source at the MCC mature stage reflects the presence of concurrent mesoscale downdrafts. The low- to mid-level cyclonic vorticity and the upper-level anticyclonic vorticity continuously

maintain the "dynamic flywheel" mechanism for sustaining the convective system.

Also, the MCC now exhibits an apparent heat sink equivalent to -6 to $-9^{o}C\ day^{-1}$ in the low- to mid-level troposphere (cf. initial stage). Since the contribution of the mid- to upper-level heat source is greater than the low-level heat sink, a portion of energy flux from the surface is required to balance the MCC net energy export from the upper troposphere. As well, during the MCC mature stage, 31 units of the total moisture supply come from horizontal transport and 69 units are supplied by evaporation of cloud water and precipitation. However, the precipitation efficiency reaches 113% at this stage (precipitation rate also reaches its maximum intensity) such that the cloudy atmosphere provides an extra 13% from its supply of water which had been accumulated during the earlier MCC stages. The water vapor budget study thus suggests that the storage of water substance is important over the MCC spatial and temporal scales.

MCC Decay Stage

During the decay stage, the MCC moves eastward into a region characterized by reduced low-level moisture support, and less potentially unstable stratification or weaker forcing mechanisms (e.g., weaker LLJ); those unfavorable conditions gradually lead to the demise of the MCC system. At this stage the composite MCC exhibits a weak sink of vorticity in the lower troposphere and a weak source of vorticity in the mid- to upper-level troposphere, reflecting the lingering convection embedded in the system. Although some forcing mechanisms may still exist (resulting in the upper-level upward motion), the weakening "dynamic flywheel" mechanism due to the decrease of cyclonic vorticity

in the lower troposphere cannot efficiently support self-exciting convection. The area covered by the mesoscale cloud shield begins to shrink during this stage.

MCC Dissipation and Post-MCC Stages

During the dissipation and post-MCC stages, the MCC moves further eastward into a region characterized by little low-level moisture support, weak potentially unstable stratification, and weak or none existent forcing mechanisms; those unfavorable conditions eventually lead to the demise of the MCC system primarily due to the reduction in fuel supply. Also, the cyclonic vorticity in the lower troposphere is insufficient to support the "dynamic flywheel" mechanism for sustaining the convective system.

8.0 CONCLUSIONS AND RECOMMENDATIONS FOR FURTHER RESEARCH

In this final chapter, the major conclusions regarding the nature of the composite MCC and recommendations for future research are presented.

8.1 Primary findings

The purpose of the research presented herein is to fill in the gaps between rawinsonde observation "snapshots" of an evolving MCC, and thereby to build a four-dimensional picture of an MCC. This study focuses primarily on the evolution of system structure, dynamics, and thermodynamics in conjunction with the budgets for the vorticity, heat, and moisture of the composite MCC.

The results of the composite MCC analysis presented in previous chapters lead to a number of fruitful conclusions regarding characteristics of the composite MCC. The major findings are as follows:

1. At the pre-MCC stage, several favorable synoptic-scale conditions come together over the threat area several hours before the ensuing MCC develops. These include the preexisting cool tropopause on the upstream side, weak vertical wind shear, and a synoptic-scale convergence of high moisture content, and potentially unstable air in the lower troposphere.
2. The CAPE reaches its maximum intensity at the pre-MCC stage, then tapers off due to consumption by cumulus convection.

3. The composite MCC exhibits convergence limited to the lower layers in the early stages but which then expands and lifts to the middle troposphere during the MCC's growth and mature stages. The upper-level divergence increases as the system evolves and reaches its maximum intensity very close to the time of MCC dissipation. The presence of low-level mass convergence overlaid by upper-level mass divergence simultaneously helps to maintain the mass inflow and outflow necessary to sustain the system.
4. The composite MCC is characterized by cyclonic vorticity confined within the surface to 700-mb layer during most of the MCC's evolution and anticyclonic vorticity located exclusively in the upper troposphere. This configuration basically satisfies Emanuel's "dynamic flywheel" conceptual model for self-exciting convection.
5. Upward motion in the composite MCC is centered near the 700-mb level early in the MCC life-cycle due to the dominant contribution from deep convection. The upward motion maximum then gradually rises to the 400-mb level later in the MCC life-cycle when mesoscale updrafts prevail. However, a deep layer of downward motion below the 700 mb level at the MCC's mature stage reflects the presence of concurrent mesoscale downdrafts.
6. The mid-level "jet-like" inflow reaches its maximum intensity at the growth stage slightly above the melting level at about 600 mb. This mid-level "jet-like" inflow appears to play an important role in supporting the mesoscale downdraft and enhancing the entire cellular circulation.
7. The system-relative flow field indicates that as the MCC moves, it is always receiving a fresh supply of moist air at low levels from

the front side during its early life-cycle and in turn is sending a stream of drier upper-level air toward the rear side.

8. The composite fields provide some evidence for the presence of "mesoscale organizers" which serve as triggers to release the preexisting potential instability. These forcing mechanisms are crucial to the MCC's genesis and development. The most likely "mesoscale organizers" are a low-level jet, an upper-level jet, a mid-level "jet-like" inflow, 700-mb level confluent flow, and a low- to mid-level trough.
9. Cumulus- to meso-scale updrafts/downdrafts provide a mechanism to stabilize the atmosphere through warming in the upper troposphere and cooling in the lower troposphere. These stabilization processes compete simultaneously with the environmental destabilization processes; therefore, they determine the timing and the intensity of deep convection embedded in the mesoscale convective system.
10. The MCC system usually develops in the vicinity of a surface frontal zone; it then moves with the mid-level steering flow and experiences a highly moist inflow in the lower troposphere to compensate for energy export from the upper tropospheric levels.
11. During the early stages of the MCC life-cycle, the system exhibits a reduced Rossby radius of deformation due to enhanced cyclonic vorticity in the lower troposphere. This smaller Rossby radius of deformation can slightly enhance the efficiency of convective heating in the low- to mid-level troposphere.
12. The vorticity budget of the composite MCC shows that the residual grid-scale vorticity exhibits a decrease of cyclonic vorticity in the lower troposphere from the initial to post-MCC stages which

reaches its maximum rate at the MCC mature stage. On the other hand, a mid- to upper-level decrease of anticyclonic vorticity exists during the MCC early and dissipation stages.

13. The heat budget for the composite MCC indicates that the total apparent heating function Q_1 exhibits a major heat source of 10-20°C day^{-1} at about the 400-mb level which occurs throughout the MCC life-cycle; there is also a minor low-level heat source during the MCC early stages while cumulus convection prevails. However, a heat sink of magnitude of -6 to -9°C day^{-1} exists in the low- to mid-level troposphere after the growth stage. In addition, the total apparent drying Q_2 shows a major moisture sink equivalent to -9 to -14°C day^{-1} which occurs below the 700-mb level throughout most of the MCC life-cycle, although a moisture source appears near the 900-mb level during the MCC mature stage. Since the mid- to upper-level heat source is greater than the lower level's heat sink, some amount of the energy flux from the surface is required to balance the MCC net energy production in the upper troposphere.

14. Water vapor budget calculations over the composite MCC area indicate that water vapor is mainly provided by MCC-scale convergence and the atmospheric storage term. At the MCC mature stage, the precipitation efficiency reaches 113%, such that the moist atmosphere provides an extra 13% from its storage, which is accumulated from the early stages of the MCC life-cycle.

15. During the MCC growth stage, the MCC circulation induces a geostrophic imbalance in the upper-level troposphere, resulting in a significant ageostrophic wind which then enhances the ascending motion. The longwave radiative cooling in the stratiform cloud top

and warming in the cloud base destabilize the upper-level troposphere environment and result in an enhanced internal circulation.

16. Once the MCC reaches maturity, the mesoscale cloud shield dominates the upper tropospheric heating and also helps in maintaining a reduced Rossby radius of deformation in the mid- to upper-level troposphere. The tropopause cooling and rising reach their maximum intensity at this point, reflecting the influence of the mesoscale cloud shield.

8.2 Recommendations for future research

1. Although enhanced IR satellite imagery during the period June to August of 1977-1984 has been compiled to develop the composite MCC, these images which encompass the life-cycles of 134 MCCs are still far from complete. We might extend our data set from April until September of 1977-1986. Based on this more complete data set, some more detailed classification for the composite MCC could be carried out. For instance, we might classify MCCs by their associated weather patterns, such as the synoptic, frontal, and mesohigh types as suggested by Merrit and Fritsch (1984).
2. Another possibility is to collect and composite similar pre-frontal squall line and non-prefrontal mid-latitude squalls cases. Using the same procedure to composite their structural, dynamic, and thermodynamic evolution, it should then be valuable to compare those results with those for the composite MCC presented herein.
3. Three-hour surface observations for each sample MCC could be blended with the regular rawinsonde data to provide better time resolution in the surface analysis. In fact, in order to completely understand

the kinematic structure of the composite MCC, a kinetic energy budget and a momentum budget could also be constructed. In addition, the radar summary of each MCC sampled can provide certain information useful for determining the vertical heating structure, which in turn would help in choosing the representative level (or levels) of the Rossby radius of deformation.

4. Moreover, observations of the detailed structure of an MCC should help to assess the MCC's evolution. Therefore, major field experiments which employ special observational networks of finer scale than those routinely provided by the National Weather Service are necessary for probing the detailed life-cycle of an MCC. Experiments like the U. S. national STormscale Operational and Research Meteorology (STORM) program or the Taiwan Area Mesoscale EXperiment (TAMEX, scheduled on May-June, 1987) program should provide more detailed temporal and spatial resolution of an evolving Mesoscale Convective System from its thunderstorm roots until full development, and the resulting data sets should permit the detailed analyses required to elucidate questions concerning the up-scale development of meso-β convective elements.

5. Although the composite MCC provide invaluable insights of dynamical structure and its evolution, however, some detailed physical processes need to be further identified solely by a numerical or analytic model. For instance, the significance of middle-level "jet-like" inflow to the MCC development, needs to be examined. Sensitivity tests of the effects of the upward shift of the heating level on the MCC evolution and the variations of MCC heating efficiency during the MCC lifecycle need to be examined as well as

examinations of the distinguishable contributions of the various source of evaporation in MCC-scale water vapor budget nees to be evaluated.

6. The composite MCC, in general, exhibits many structural, dynamic and thermodynamic features in commom with tropical cloud clusters. However, the MCC exhibits a maximum upper-level divergence during the dissipation stage instead of the mature stage as found in tropical cloud clusters (Gray et al., 1982). The physical mechanisms responsible for the different evolution of the divergence fields between these two systems needs to be further examined.

REFERENCES

Achtemeier, G. L., 1986: The impact of data boundaries upon a successive corrections objective analysis of limited-area datasets. Mon. Wea. Rev., 114, 40-49.

Akiyama, T., 1984a: A medium-scale cloud cluster in a Baiu front. Part I: Evolution process and fine structure. J. Meteor. Soc. Japan, 62, 485-503.

_____, 1984b: A medium-scale cloud cluster in a Baiu front. Part II: Thermal and kinematic fields and heat budget. J. Meteor. Soc. Japan, 62, 505-520.

Anthes, R. A., and T. T. Warner, 1978: Development of hydrodynamic models suitable for air pollution and other mesometeorological studies. Mon. Wea. Rev., 106, 1045-1078.

_____, and D. Keyser, 1979: Tests of a fine-mesh model over Europe and the United States. Mon. Wea. Rev., 107, 287-300.

Banta, R. M., 1984: Daytime boundary-layer evolution over mountainous terrains. Part I: Observations of the dry circulations. Mon. Wea. Rev., 112, 340-356.

Banta, R. M., and C. L. Barker, 1984: On the nowcasting of mountain-generated thunderstorm system. Preprint, Nowcasting II symposium, Norrkoping, Sweden, 3-7 Sept. 1984.

Barlow, W., 1985: Analysis of Iowa MCC events of 1982-1983. 14th Conference on Severe Local Storms, Indianapolis, IN., Oct. 29-Nov. 1, 1985. 318-321.

Barnes, S. L., 1973: Mesoscale objective map analysis using weighted time-series observations. NOAA Technical Memorandum ERL NSSL-62, 38 pp.

Blackadar, A. K., 1957: Boundary layer wind maxima and their significance for the growth of nocturnal inversions. Bull. Amer. Meteor. Soc., 38, 283-290.

Bluestein, H. B., 1985: An observational study of a mesoscale area of convection under weak synoptic-scale forcing. Mon. Wea. Rev., 113, 520-538.

_____, and M. H. Jain, 1985: The formation of mesoscale lines of precipitation: Severe squall lines in Oklahoma during the spring. J. Atmos. Sci. 42, 1711-1732.

Bosart, L. F., and F. Sanders, 1981: The Johnstown flood of July 1977: A long-lived convective system. J. Atmos. Sci., 38, 1616-1642.

Brill, K. F., L. W. Uccellini, R. P. Burkhart, T. T. Warner, and R. A. Anthes, 1985: Numerical simulations of a transverse indirect circulation and low-level jet in the exit region of an upper-level jet. J. Atmos. Sci., 42, 1306-1320.

Brown, J. M., 1979: Mesoscale unsaturated downdrafts driven by rainfall evaporation: A numerical study. J. Atmos. Sci., 36, 313-338.

Chappell, C. F., 1985: Requisite conditions for the generation of stationary thunderstorm systems having attendant excessive rains. 6th Conference on hydrometeorology, Indianapolis, IN., Oct 29-Nov. 1 1985. 221-225.

Charba, J., 1974: Application of gravity current model to analysis of squall line gust front. Mon. Wea. Rev., 102, 140-156.

Chen, S., 1986: Simulation of the stratiform region of a mesoscale convective system. M.S. Thesis, Colorado State University, Dept. of Atmospheric Science, Fort Collins, CO 80523, 118 pp.

Churchill, D. D., and R. A. Houze, Jr., 1984: Development and structure of winter monsoon cloud clusters on 10 December 1978. J. Atmos. Sci, 41, 933-960.

Clark, J. D., 1983: The GOES User's Guide. U.S. Department of Commerce National Oceanic and Atmospheric Adminstration, National Environmental Satellite, Data, and Information Service. Washington DC.

Cotton, W. R., 1983: Up-scale development of moist convective systems. Lecture for course on mesoscale meteorology. 30 May-10 June 1983, Pinnarpsbaden, Sweden.

_____, R. L. George, and K. R. Knupp, 1982: An intense, quasi-steady thunderstorm over mountainous terrain. Part I: Evolution of the storm-initiating mesoscale circulation. J. Atmos. Sci., 39, 328-342.

_____, R. L. George, P. J. Wetzel, and R. L. McAnelly, 1983a: A long-lived mesoscale convective complex. Part I: The mountain-generated component. Mon. Wea. Rev., 111, 1893-1918.

_____, E. E. Hindman, G. Tripoli, R. L. McAnelly, C. Chen, C. Tremback, P. Flatau, and K. Knupp, 1983b: Model cloud relationships. Final report of AFGL-TR-84-0028 to Air Force Geophysics Laboratory Air Force Systems Command, United States Air Force Hanscom AFB, Massachusetts 01731.

_____, and R. A. Anthes, 1986: The dynamics of clouds and mesoscale meteorological system. To be published by Academic Press, New York.

Cox, S. K., and K. T. Griffith, 1979: Estimates of radiative divergence during Part II. Analysis of the Phase III results. J. Atmos. Sci., 36, 586-601.

Cressman, G. P., 1959: An operational objective analysis system. Mon. Wea. Rev., 87, 367-374.

Crysler, K. A., R. A. Maddox, B. M. Muller, and L. R. Hoxit, 1981: Climatology of heavy precipitation and flash flooding for various regions of the United states. NOAA-ERL report.

Culverwell, A. H., 1982: An analysis of moisture sources and circulation field associated with an MCC episode. M.S. Thesis, Colorado State University, Dept. of Atmospheric Science, Fort Collins, CO 80523, 291 pp.

Daley, R., 1984: Objective analysis and initialization. Note from AT707 taught in fall 1984. Department of Atmospheric Science, Colorado State University.

Doswell, C. A., 1977: Obtaining meteorological significant divergence fields through the filtering property of objective analysis. Mon. Wea. Rev., 105, 885-892.

Dudhia, J. and M. W. Moncrieff, 1986: A numerical simulation of quasi-stationary tropical convection bands. Submit to J. Atmos. Sci.

Emanuel, K. A., 1983: Elementary aspects of the interaction between cumulus convection and the large-scale environment. D. K. Lilly and T. Gal-Chen, Mesoscale Meteorology-Theories, Observation and Models, 551-575.

_____, 1985: Frontal circulation in the presence of small moist symmetric stability. J. Atmos. Sci., 42, 1062-1071.

_____, and F. Sanders, 1983: Mesoscale meteorology. Rev. of Geophy. and Space Physics, 21, No. 5, 1027-1042.

Esbensen S. K., E. I. Tollerud, and J.-H. Chu, 1982: Cloud-cluster-scale circulation and the vorticity budget of synoptic-scale waves over the eastern Atlantic Intertropical Convergence Zone. Mon. Wea. Rev., 110, 1677-1692.

_____, and J.-T. Wang, 1984: Heat boudget analysis and the synoptic environment of GATE cloud clusters. 15th Conference on Hurricanes and Tropical Meteorology, Jan. 9-13, 1984, Miami, Fla.

Foltz, G. S., 1976: Diurnal variation of the tropospheric energy budget. Atmospheric Science paper No. 262, Colorado State University.

Frank, W. M., 1978: The life cycles of GATE convective systems. J. Atmos. Sci., 35, 1256-1264.

_____, 1983: The cumulus parameterization problem. Mon. Wea. Rev., 111, 1859-1871.

_____, 1983: The structure and energetics of the East Atlantic Intertropical Convergence Zone. J. Atmos. Sci., 40, 1916-1929.

Fritsch, J. M., and C. F. Chappell, 1980: Numerical prediction of convective driven mesoscale pressure systems. Part II: Mesoscale model. J. Atmos. Sci., 37, 1734-1762.

_____, and R. A. Maddox, 1981: Convectively driven mesoscale weather system aloft. Part I: Observations. J. Appl. Meteor., 20, 9-19.

_____, and J. M. Brown, 1982: On the generation of convectively driven mesohighs aloft. Mon. Wea. Rev., 110, 1554-1563.

Fuelberg, H. E., and G. J. Jedlovec, 1982: A subsynoptic-scale kinetic energy analysis of the Red River Valley tornado outbreak (AVE-SESAME I). Mon. Wea. Rev., 110, 2005-2024.

_____, and M. F. Printy, 1984: A kinetic energy analysis of the meso-β scale severe storm environments. J. Atmos. Sci., 41, 3212-3226.

Fulton, S. R., 1980: Geostrophic adjustment in a stratified atmosphere. M.S. Thesis, Colorado State University, Dept. of Atmospheric Science, Fort Collins, CO 80523, 92 pp.

_____, and W. H. Schubert, 1985: Vertical normal mode transforms: theory and application. Mon. Wea. Rev., 113, 647-658.

Gamache, J. F., and R. A. Houze, Jr., 1982: Mesoscale air motions associated with a tropical squall line. Mon. Wea. Rev., 110, 118-135.

_____, and _____, 1983: Water budget of a mesoscale convective system in the tropics. J. Atmos. Sci, 40, 1835-1850.

_____, and _____, 1985: Further analysis of the composite wind and thermodynamic structure of the 12 September GATE squall line. Mon. Wea. Rev., 113, 1241-1259.

George, R. L., 1979: Evolution of mesoscale convective system over mountainous terrain. Colorado State Univ. Atm. Sci. Paper No. 318, Ft. Collins, 160 pp.

Gray, W. M., and R. W. Jacobson, Jr., 1977: Diurnal variations of deep cumulus convection. Mon. Wea. Rev., 105, 1171-1188.

_____, E. Buzzell, and G. Burton, 1982: Tropical cyclone and related meteorological data sets available at CSU and their utilization. Dept. of Atmos. Sci., CSU, 186 pp.

Hack, J. J., and W. H. Schubert, 1986: On the nonlinear response of a atmospheric vortices to heating by organized cumulus convection. Submitted to J. Atmos. Sci.

Heymsfield, G. M., and R. H. Blackmer, 1985: Characteristics of midwest severe storm anvils. 14th Conference on Severe Local Storms, Indianapolis, IN., Oct. 29-Nov. 1, 1985. 85-88.

Holton, J. R., 1979: An introduction to dynamic meteorology. Academic Press, New York, 49-51.

Houze, Jr. R. A., 1982: Cloud clusters and large-scale vertical motions in the tropics. J. Meteor. Soc. Japan, 60, 396-409.

_____, S. G. Geotis, F. D. Marks, Jr. and A. K. West, 1981: Winter monsoon convection in the vicinity of north Borneo. Part I: structure and time variation of the clouds and precipitation. Mon. Wea. Rev., 109, 1595-1614.

_____, and E. N. Rappaport, 1984: Air motions and precipitation structure of an early summer squall line over the eastern tropical Atlantic. J. Atmos. Sci., 41, 553-574.

Johnson, R. H., 1982: Vertical motion in near-equatorial winter monsoon convection. J. Meteor. Soc. Japan, 60, 682-690.

_____, 1984: Partitioning tropical heat and moisture budgets into cumulus and mesoscale components: Implications for cumulus parameterization. Mon. Wea. Rev., 112, 1590-1601.

_____, and D. C. Kriete, 1982: Thermodynamic and circulation characteristics of winter monsoon tropical mesoscale convection. Mon. Wea. Rev., 110, 1898-1911.

_____, and G. S. Young, 1983: Heat and moisture budgets of tropical mesoscale anvil clouds. J. Atmos. Sci., 40, 2138-2147.

Kane, R. J., C. R. Chelius, and J. M. Fritsch, 1985: The precipitation characteristics of mesoscale convective weather systems. 6th Conference on hydrometeorology, Indianapolis, IN., Oct 29-Nov. 1 1985. 205-211.

Klemp, J. B., and R. B. Wilhelmson, 1978: The simulation of three dimensional convective storm dynamics. J. Atmos. Sci., 35, 1070-1096.

Knupp, K. R., 1985: Precipitating convective cloud downdraft structure: A synthesis of observations and modeling. Ph. D. Dissertation, Department of Atmospheric Science, Colorado State University, Fort Collins, Colorado 80523, 296 pp.

_____, and W. R. Cotton, 1986: Internal structure of a small mesoscale system. Submitted for publication to Mon. Wea. Rev.

Koch, S. E., 1985: Ability of a regional-scale model to predict the genesis of intense mesoscale convective system. Mon. Wea. Rev., 113, 1693-1713.

Kuo, H. L., 1965: On formation and intensification of tropical cyclones through latent heat release by cumulus convection. J. Atmos. Sci., 22, 40-63.

_____, 1974: Further studies of the parameterization of the influence of cumulus convection on large-scale flow. J. Atmos. Sci., 31, 1232-1240.

Kuo, Y.-H., and R. A. Anthes, 1984a: Accuracy of diagnostic heat and moisture budgets using SESAME-79 field data as revealed by observing system simulation experiments. Mon. Wea. Rev., 112, 1465-1481.

_____, 1984b: Mesoscale budgets of heat and moisture in a convective system over the central United States. Mon. Wea. Rev., 112, 1482-1497.

Leary, C. A., and R. A. Houze, Jr., 1979: The structure and evolution of convection in a tropical cloud cluster. J. Atmos. Sci., 36, 437-457.

_____, and _____, 1980: The contribution of mesoscale motions to the mass and heat fluxes of an intense tropical convective system. J. Atmos. Sci., 37, 784-796.

_____, and E. N. Rappaport, 1983: Internal structure of a mesoscale convective complex. Preprints, 21st Conf. on Radar Meteorology, Amer. Meteor. Soc., 19-23 September, Edmonton, Alberta, 70-77.

Lee, C.-S., 1986: An observational study of tropical cloud cluster evolution and cyclogenesis in the western north Pacific. Ph. D. Dissertation, Department of Atmospheric Science, Colorado State University, Fort Collins, Colorado 80523, 243 pp.

Lewis, J. M., 1975: Test of Ogura-Cho model on a prefrontal squall line case. Mon. Wea. Rev., 103, 764-778.

Maddox, R. A., 1980: Mesoscale convective complexes. Bull. Amer. Meteor. Soc., 61, 1374-1387.

_____, 1981: The structure and lifecycle of midlatitude mesoscale convective complexes. Ph. D. Dissertation, Department of Atmospheric Science, Colorado State University, Fort Collins, Colorado 80523, 171 pp.

_____, 1983: Large-scale meteorological conditions associated with midlatitude, mesoscale convective complexes. Mon. Wea. Rev., 111, 1475-1493.

_____, 1985: The relation of diurnal, low-level wind variations to summertime severe thunderstorms. 14th Conference on Severe Local Storms, Indianapolis, IN., Oct. 29-Nov. 1, 1985. 202-207.

_____, C. F. Chappell and L. R. Hoxit, 1979: Synoptic and meso-α-scale aspects of flash flood events. Bull. Amer. Meteor. Soc., 60, 115-123.

_____, D. J. Perkey and J. M. Fritsch, 1981: Evolution of upper tropospheric features during the development of a mesoscale convective complex. J. Atmos. Sci., 38, 1664-1674.

_____, and C. A. Doswell, III, 1982: An examination of jet stream configurations, 500 mb vorticity advection and low-level thermal advection patterns during extended periods of intense convection. Mon. Wea. Rev., 110, 184-197.

Matthews, D. A., 1983: Analysis and classification of mesoscale cloud and precipitation systems. Ph. D. Dissertation, Department of Atmospheric Science, Colorado State University, Fort Collins, Colorado 80523, 422 pp.

McAnelly, R. L. and W. R. Cotton, 1986: Meso-β-scale characteristics of the meso-α-scale convective complex. Mon. Wea. Rev., To be published in August.

McBride, J. L., and W. M. Gray, 1980: Mass divergence in tropical weather systems, Part I: Diurnal variation. Quart. J. R. Met. Soc., 106, 501-516.

_____, and R. Zehr, 1981: Observational analysis of tropical cyclone formation. Part II: Comparison of non-developing versus developing systems. J. Atmos. Sci., 38, 1132-1151.

McNab, A. L., 1976: Mesoscale characteristics of cumulus convection. M.S. Thesis, Department of Atmospheric Science, Colorado State University, Fort Collins, Colorado 80523, 187pp.

McQueen, J. T. and R. A. Pielke, 1985: A Numerical and climatological investigation of deep convection cloud patterns in south Florida. Submit to Mon. Wea. Rev.

Means, L. L., 1952: On thunderstorm forecasting in central United States. Mon. Wea. Rev., 80, 165-189.

Merritt, J. H., and J. M. Fritsch, 1984: On the movement of the heavy precipitation areas of mid-latitude mesoscale convective complexes. Preprints, 10th Conf. on Wea. Forecasting and Analysis, Amer. Meteor. Soc., 25-29 June, Clearwater Beach, Florida, 529-536.

Molinari, J., 1985: A general form of Kuo's cumulus parameterization. Mon. Wea. Rev., 113, 1411-1416.

_____, and T. Corsetti, 1985: Incorporation of cloud-scale and mesoscale downdrafts into a cumulus parameterization: Results of one- and three-dimensional integrations. Mon. Wea. Rev., 113, 485-501.

Moncrieff, M. W., and J. S. A. Green, 1972: The propagation and transfer properties of steady convective overturning in shear. Quart. J. Roy. Meteor. Soc., 98, 336-353.

_____, and M. J. Miller, 1976: The dynamics and simulation of tropical cumulonimbus and squall lines. Quart. J. Roy. Meteor., 102, 373-394.

Nehrkorn, T., 1985: WAVE-CISK in a baroclinic basic state. Dissertation of Ph. D. at M.I.T. 171 pp.

Newton, C. W., 1950: Structure and mechanism of the prefrontal squall line. line. J. Meteor., 8, 210-222.

_____, 1966: Circulations in large sheared cumulonimbus. Tellus, 18, 699-712.

_____, and H. R. Newton, 1959: Dynamical interactions between large convective clouds and environment with vertical shear. J. Meteor., 16, 483-496.

Nie, N. H., C. H. Hull, J. G. Jenkins, K. Steinbrenner, and D. H. Bent, 1975: Statistical package for social science, second edition. McGraw-Hill, New York, 675pp.

Ninomiya, K., 1971: Dynamical analysis of outflow from tornado-producing thunderstorms as revealed by ATS III pictures. J. Appl. Meteor., 10, 275-294.

O'Brien, J. J., 1970: Alternative solutions to the classical vertical velocity problem. J. Atmos. Sci., 9, 197-203.

Ogura, Y., and M.- T. Liou, 1980: The structure of a midlatitude squall line: A case study. J. Atmos. Sci., 37, 553-567.

_____, and J.- Y. Jiang, 1985: A modeling study of heating and drying effects of convective clouds in an extratropical mesoscale convective system. J. Atmos. Sci., 42, 2478-2492.

Ooyama, K., 1982: Conceptual evolution of the theory and modeling of the tropical cyclone. J. Meteoro. Soc. Japan, 60, 369-379.

Orlanski, I., 1975: A rational subdivision of scales for atmospheric processes. Bull. Amer. Meteor. Soc., 56, 527-530.

_____, and B. B. Ross, 1984: The evolution of an observed cold front. Part II. Mesoscale dynamics. J. Atmos. Sci., 41, 1669-1703.

Palmen, E., and C. W. Newton, 1969: Atmospheric Circulation Systems. Academic Press, New York, 390-425, 523-560.

Perkey, D. J., and R. A. Maddox, 1985: A numerical investigation of a mesoscale convective system. Mon. Wea. Rev., 113, 553-566.

Pielke, R. A., 1984: Mesoscale Meteorological Modeling. Academic Press, New York, 612 pp.

Purdom, J. F. W., 1976: Some uses of high-resolution GOES imagery in the mesoscale forecasting of convection and its behavior. Mon. Wea. Rev., 104, 1474-1483.

_____ and K. Marcus, 1982: Thunderstorm trigger mechanisms over the southeastern United States. 12th Conf. on Severe Local Storms, Jan. 11-15, 1982, San Antonio, Texas, 487-488.

Raymond, D. J., 1978: Instability of the low-level jet and severe storm formation J. Atmos. Sci., 35, 2274-2280.

_____, 1984: A wave-CISK model of squall lines. J. Atmos. Sci., 41, 1946-1958.

_____, 1986: On the interaction of mesoscale convective systems. Submit to J. Atmos. Sci.

_____, and M. Wilkening, 1985: Characteristics of mountain-induced thunderstorms and cumulus congestus clouds from budget measurements. J. Atmos. Sci., 42, 773-783.

Reed, R. J., 1979: Cyclogenesis in polar air streams. Mon. Wea. Rev., 107, 38-52.

_____, and R. H. Johnson 1974: The vorticity budget of synoptic-scale wave disturbances in the tropical western Pacific. J. Atmos. Sci., 31, 1784-1790.

_____, and E. E. Recker, 1971: Structure and properties of synopic-scale wave disturbances in the equatorial western Pacific. J. Atmos. Sci., 28, 1117-1133.

Robertson, F. R., and P. J. Smith, 1980: The kinetic energy budgets of two severe storm producing extratropical cyclones. Mon. Wea. Rev, 108, 127-143.

Rockwood, A. A., D. L. Bartels, and R. A. Maddox, 1984: Precipitation characteristics of a dual mesoscale convective complex. NOAA Technical Memorandum, ERL ESG-6, 50 pp.

Rodger, D. M., R. A. Maddox, and K. W. Howard, 1985: A long-lived heavy rain-producing meso-α convective system. 6th Conference on Hydrometeorology, Indianapolis, IN., Oct. 29-Nov. 1, 1985. 212-215.

Rosenthal, S. L. 1980: Numerical simulation of tropical cyclone development with latent heat release by the resolvable scales, II. Propagating small-scale features observed in the pre-hurricane phase. Tech. Rep. ERL413-AOML29, NOAA Environ. Res. Lab., Boulder, CO, 43 p. [NTIS PE81-176588.]

Ruprecht, E., and W. M. Gray, 1976: Analysis of satellite-observed tropical cloud clusters. I: Wind and dynamic fields. Tellus, 28, 391-413.

Sanders, F. and K. A. Emanuuel, 1977: The momentum budget and temporal evolution of a mesoscale convective system. J. Atmos. Sci., 34, 322-330.

_____ and L. F. Bosart, 1985: Mesoscale structure in the megalopolitan snowstorm of 11-12 February 1983. Part I: Frontogenetical forcing and symmetric instability. J. Atmos. Sci., 42, 1050-1061.

Schlesinger, R. E., 1980: A three-dimensional numerical model of an isolated thunderstorm. Part II: Dynamics of updraft splitting and mesovortex couplet evolution. J. Atmos. Sci., 37, 395-420.

Schmidt, J. M., 1985: Structure and evolution of a squall line with an embedded supercell. M.S. Thesis, Department of Atmospheric Science, Colorado State University, Fort Collins, Colorado 80523, 141 pp.

Schubert, W. H., J. J. Hack, P. L. Silva Dias, and S. R. Fulton, 1980: Geostrophic adjustment in an axisymmetric vortex. J. Atmos. Sci., 37, 1464-1484.

Shapiro, M. A., 1982: Mesoscale weather systems of the central United States. CIRES/NOAA. 78 pp.

Song, J.-L., 1986: A numerical investigation of Florida's sea breeze - Cumulonimbus interactions. Ph. D. Dissertation, Department of Atmospheric Science, Colorado State University, Fort Collins, Colorado 80523, 187 pp.

Tao, W.-K., and J. Simpson, 1984: Cloud interactions and merging: Numerical simulations. J. Atmos. Sci., 41, 2901-2917.

Thompson, Jr. R. M., S. W. Payne, E. E. Recker and R. J. Reed, 1979: Structure and properties of synoptic-scale disturbances in the intertropical convergence zone of the eastern Atlantic. J. Atmos. Sci., 36, 53-72.

Thorpe, A. J. , 1986: The role of precipitating convection on the dynamics of synoptic scale systems. THE WMO/AMS/UCS INTERNATIONAL WORKSHOP ON RAIN-PRODUCING SYSTEMS IN THE TROPICS AND THE EXTRA-TROPICS, San Jose, Costa Rica, 21-25 July 1986, 67-74.

Tollerud, E. I., and S. K. Esbensen, 1983: An observational study of the upper-tropospheric vorticity fields in GATE cloud clusters. Mon. Wea. Rev., 111, 2161-2175.

_____, 1985: A Composite life cycle of nonsquall mesoscale convective systems over the tropical ocean. Part I: Kinematic fields. J. Atmos. Sci., 42, 823-837.

Toth, J. J., and R. H. Johnson, 1985: Summer surface flow characteristics over northeast Colorado. Mon. Wea. Rev., 113, 1458-1469.

Tripoli, G. J., 1986: A numerical study of the morphology of a orogenic mesoscale convective syatem. Ph. D. Dissertation, Department of Atmospheric Science, Colorado State University, Fort Collins, Colorado 80523.

_____, and W. R. Cotton, 1980: A numerical investigation of several factors contributing to the observed variable intensity of deep convection over South Florida. J. Appl. Meteor., 19, 1037-1063.

Uccellini, L. W., 1975: A case study of apparent gravity wave initiation of severe convective storm. Mon. Wea. Rev., 103, 497-513.

_____, and D. R. Johnson, 1979: The coupling of upper and lower tropospheric jet streaks and implications for the development of severe convective storms. Mon. Wea. Rev., 107, 682-703.

Ulanski, S. and M. Garstang, 1978: The role of surface divergence and vorticity in the lifecycle of convective rainfall, Part I: Observation and analysis. J. Atmos. Sci., 35, 1047-1062.

U.S. Weather Bureau and U.S. Corps of Engineers, 1947: Thunderstorm rainfall. Hydrometeorological Report No. 5, Parts 1 and 2. Waterways Experiment Station, Vicksburg, Mississipppi, U.S. Government Document C30.44:5, 331 pp (plus 155 figs).

Wallace, J. M., 1975: diurnal variations in precipitation and thunderstorm frequency over the coterminous United States. Mon. Wea. Rev., 103, 406-419.

_____, and P. V. Hobbs, 1977: Atmospheric Science, An Introductory Survey. Academic Press, 467 pp.

Watson, A. I., and D. O. Blanchard, 1984: The relationship between total area divergence and convective precipitation in south Florida. Mon. Wea. Rev., 112, 673-685.

Weisman, M. L., and J. B. Klemp, 1982: The dependence of numerically simulated convective storms on vertical wind shear and buoyancy. Mon. Wea. Rev, 110, 504-520.

_____, and _____, 1984: The structure and classification of numerically simulated convective storms in directionally varying wind shears. Mon. Wea. Rev., 112, 2479-2498.

Wetzel, P. J., 1973: Moisture sources and flow patterns during the northeast Colorado hail season. M.S. Thesis, Department of Atmospheric Science, Colorado State University, Fort Collins, Colorado 80523, 90 pp.

_____, W. R. Cotton and R. L. McAnelly, 1983: A long-lived mesoscale convective complex. Part II: Evolution and structure of the mature complex. Mon. Wea. Rev., 111, 1919-1937.

Williams, K. T., and W. M. Gray, 1973: A statistical analysis of satellite- observed trade wind cloud clusters in the western North Pacific. Tellus, 21, 323-336.

Winkler, J. A., and J. P. Charba, 1985: Composite surface fields associated with summertime heavy rainstorms in the central United States. 6th Conference on hydrometeorology, Indianapolis, IN., Oct 29-Nov. 1 1985. 212-215.

Yanai, M., S. Esbensen and J. H. Chu, 1973: Determination of bulk properties of tropical cloud cluster from large scale heat and moisture budget. J. Atmos. Sci., 30, 611-627.

Zhang, D.-L., and J. M. Fritsch, 1985: Numerical simulation of mesoscale convective systems: The Johnstown Flood of July 1977. Preprints, 7th Conference on Numerical Weather Prediction, 17-20 June 1985, Montreal, Q. P., Canada, 245-250.

Zipser, E. J., 1969: The role of organized unsaturated convective downdrafts in the structure and rapid decay of an equatorial disturbance. J. Appl. Meteor., 8, 799-814.

_____, 1977: Mesoscale and convective-scale downdrafts as distinct components of squall line structure. Mon. Wea. Rev., 105, 1568-1589.

APPENDIX A. DETAILED PROCEDURE FOR MCC SCREENING

Due to the natural variability of MCC's, some of these systems may be in the early stages of initiation or within several hours of maturity at the time the standard 0000 GMT soundings are taken. Furthermore, some systems may be at, or be two to four hours beyond or before, the MCC dissipation stage at the time the standard 1200 GMT soundings are taken. However, even though high-time-resolution soundings may be lacking, the large number of MCC samples available permits the development of a composite model of the MCC life-cycle.

First of all, working maps were constructed for each MCC from the available satellite images to relate the satellite-viewed storm system to other meteorological fields. MCC centroid positions were marked every 3 hours plus on the working map along with outlines of the $-32^{\circ}C$ and $-53^{\circ}C$ areas at the system peak. The latter showed areas with IR temperature colder than $-32^{\circ}C$ and $-53^{\circ}C$, respectively. Planimetric estimates were then made by counting the number of grid space points within the outlines which yielded either direct on-the-hour areas or interpolated from off-the-hour IR maps which were acquired from the Weather Research Program of NOAA-ERL. Fig. A.1 illustrates the evolution of one MCC as seen in GOES-East imagery. Satellite-image enhanced features utilized in this study were the IR isotherms of -32 and $-53^{\circ}C$ [following Maddox (1980)] and the light-shaded interior anvil regions which are indicative of overshooting thunderstorm activity (Clark, 1983). Although Maddox (1980) used the size of both $-32^{\circ}C$ and

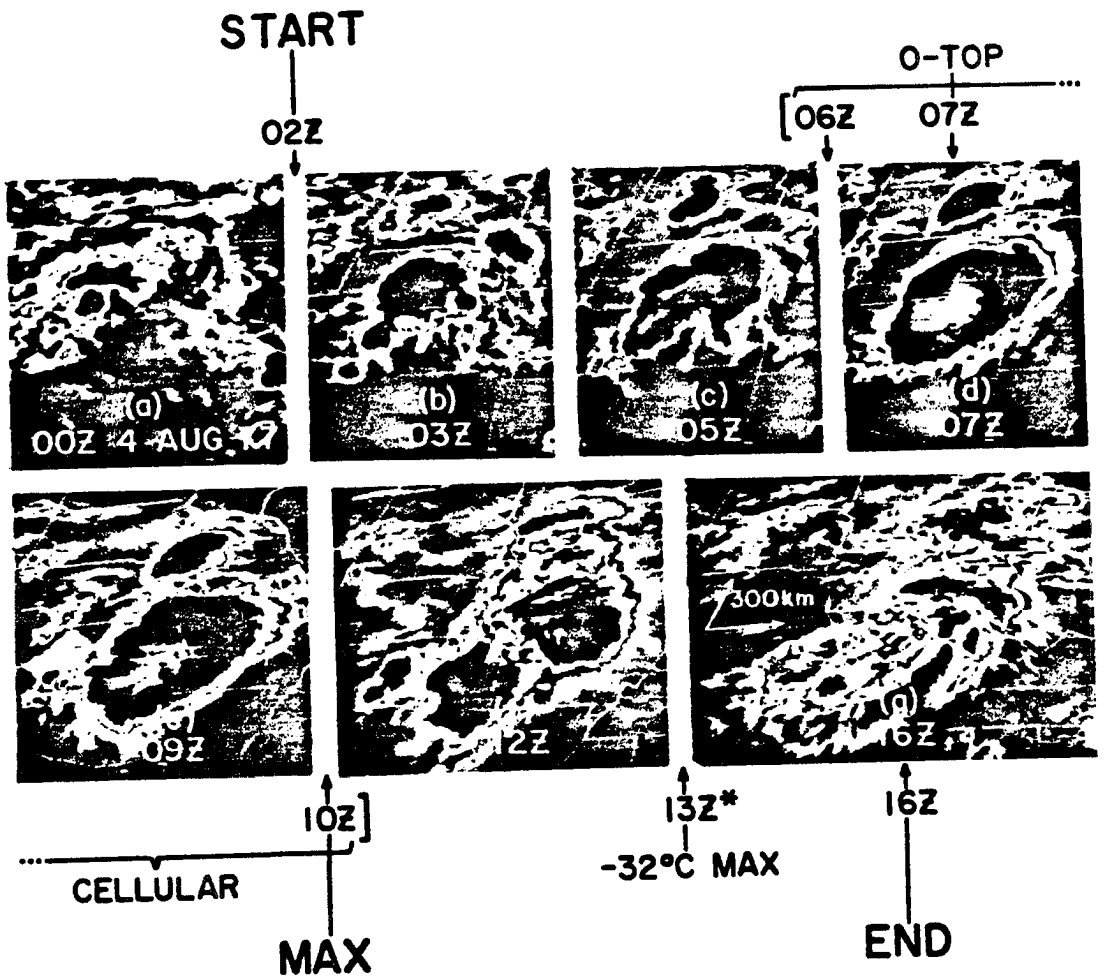

Fig. A.1. Enhanced IR GOES-East satellite images spanning the life-cycle of a sampling MCC through the night of 3-4 Aug 1977. Central Standard Time is 6 h earlier than the indicated GMT time. The stepped shades of medium gray, light gray, dark grey and black are thresholds for areas with IR temperatures colder than -32, -42, -53 and -59°C, respectively. Temperatures progressively colder than -63°C appear as a gradual black-to-white shade. The life-cycle terminology is described in the text.

$-53^{\circ}C$ IR temperature areas as MCC benchmarks, analyses of MCC hourly precipitation by Kane et al. (1985) and McAnelly and Cotton (1986) suggest that most of the rainfall occurs beneath the colder cloud-top area, whereas the $-32^{\circ}C$ area is largely a non-precipitating anvil. Therefore, we have based our definitions solely on the $-53^{\circ}C$ area.

Based on the hourly IR measurements, we define an MCC to be "initiating" when the contiguous area within the $-53^{\circ}C$ IR isotherm first exceeds 50,000 km^2, to be reaching its "maturity" when this area attains its largest size, and to be "dissipating" when this area first becomes less than 50,000 km^2. We believe our MCC case selection and MCC definition agree totally with the rationale behind the stringent (though somewhat arbitrary) criteria adopted by Maddox (1980).

In addition to these objective areally-defined periods in the MCC life-cycle, a meso-α "cellular" stage is defined more subjectively as the period after the system has apparently unified into a single meso-α "cell" and during which the $-53^{\circ}C$ IR contour is relatively smooth and circular. Within the "cellular" stage, the time of maximum "overshooting-top" activity is defined subjectively to be when the light-shaded anvil interior reaches its largest and coldest extent. These points in the MCC life-cycle were determined to the nearest half hour. Times given for life-cycle periods correspond to the period midpoint.

One hundred thirty-four MCC cases are tabulated for an eight-year period (1977-1984) in Table A.1. The assigned case numbers refer to the chronological order of the MCCs listed in Table A.1. The cases have been screened both according to how large and "classical" the MCC appears to be and by considering nearby meso-β- to meso-α-scale

activities as undesirable "contaminants" to the meso-α environment of the MCC. According to an individual case's evolution, duration, size, cellular characteristics, and proximity to other mesoscale convection, each MCC was graded for compilation purposes according to a subjective "MCC purity scale" which consisted of ten categories ranging from 0 to 9. For example, category 9 was reserved for the "perfect" MCC case, characterized by a large maximum cloud-shield size, a long-lived mature stage, an ideal "cellular" appearance, little environmental contamination, and a clear evolution through its life-cycle. By the same token, category 0 was reserved for MCC cases having a particularly complex or "messy" evolution, an irregular "cellular" appearance, a short-lived mature stage, and/or small cloud-top areal coverage at the time of maximum extent. Labels used in Table A.1 are:

Case Number: the chronologically-ordered MCC identification number

Date: year, month, and day of the MCC initial stage (yymmdd)

Rank: category on the "MCC purity scale" from 0 to 9

First Storm: time of the first thunderstorm detection from satellite; a negative value denotes time before 0000 GMT on the specific date

Init: time (GMT) of the MCC initial stage (midpoint)

Mat: time (GMT) of MCC mature stage (midpoint)

Dissi: time (GMT) of MCC dissipation stage (midpoint)

Cell. Init: time (GMT) of initiation for cellular cloud; 9999 denotes data unavailable

O-Top: time (GMT) of maximum overshooting top

Cell. Term: time (GMT) of termination for cellular cloud

Table A.1 Mesoscale Convective Complexes during 1977-1984.

Case Number	Date	Rank	Time (GMT) First Storm	Init	Mat	Dissi	Cell. Init	Cell. O-Top	Cell. Term	Maximum cloud-top area ($\times 10^3$ km^2) $\leq -32^\circ$C	$\leq -52^\circ$C
1	770804	8	-0400	0130	1000	1530	0600	0700	1000	340	580
2	770805	5	-0600	0100	0900	1630	0600	0700	0900	252	374
3	770806	7	-0800	0100	0700	1330	0500	0600	0700	238	381
4	770807	4	-0900	-0200	0000	0430	-0100	-0100	0000	108	156
5	770807	1	-0300	0400	0645	1230	0500	0500	0800	103	187
6	770807	8	0300	0645	1200	1700	0800	1000	1100	239	322
7	770808	7	0300	0500	1200	1800	0600	0900	1100	307	516
8	770809	3	-0400	0130	0400	1000	0100	0300	0500	139	193
9	770809	6	0130	0545	1100	1500	0800	0900	1100	307	478
10	770809	1	-0600	0330	0545	1100	0400	0500	0600	90	139
11	770810	2	-0600	0000	0400	0730	0200	0300	0500	138	182
12	780614	1	-0430	0500	1100	1400	0930	1030	1230	999	235
13	780620	2	-0430	-0100	0530	1300	9999	9999	9999	999	546
14	780624	5	-0600	-0200	0500	0800	0300	0330	0500	170	300
15	780625	2	-0100	0200	0400	0730	0300	0400	0430	160	167
16	780625	2	-0300	0430	1000	1300	0700	0900	0930	270	446
17	780630	8	-0600	0000	0600	1100	0500	0500	0800	250	322
18	780701	8	-0400	-0100	0400	1000	0200	0400	0700	240	262
19	780702	2	-0500	0030	0800	1030	0700	0330	0800	126	271
20	780704	7	-0400	0400	1200	1700	0800	1000	1500	190	262
21	780706	7	-0530	-0100	0430	0800	0200	0430	0600	333	454
22	780706	5	0100	0700	1100	1330	0800	1030	1100	150	233
23	780709	2	-0400	0300	0630	1130	0500	0530	0600	162	190
24	780713	4	0130	0700	1000	1600	0600	0800	1000	90	186
25	780715	7	-0700	0000	0500	0830	0000	0430	0530	216	326
26	780720	5	-0300	0500	0800	1200	0600	0600	0800	126	238
27	780721	6	-1200	-0500	-0200	0100	-0600	-0400	-0200	140	999
28	780721	8	-0530	0100	0800	1200	0600	0630	1000	160	243
29	780722	3	-0430	-0100	0630	1000	0300	0400	0600	190	429
30	780817	2	0100	1100	1230	1800	1200	1300	1500	60	216
31	780818	6	-0700	0100	0400	0800	0130	0330	0430	160	382
32	780823	7	-0600	-0230	0430	0830	0330	0330	0500	230	338
33	780823	7	-0430	0000	0800	1600	0430	0800	1000	250	375
34	780824	6	-0630	0130	0700	0900	0300	0330	0730	70	150
35	780826	8	-1200	-0300	0100	0930	-0300	0000	0300	140	239
36	790616	4	-0400	0000	0500	0830	0200	0300	0400	70	165
37	790616	6	-0400	0600	1130	2700	0800	9999	1500	240	342
38	790619	7	0030	0800	1230	1930	1000	9999	1730	180	257
39	790622	6	-0430	0100	0600	1200	0230	0500	0600	190	349
40	790623	0	-0430	-0100	0330	0630	0100	0300	0400	100	150

Table A.1 Mesoscale Convective Complexes during 1977-1984 (Continued).

Case Number	Date	Rank	Time (GMT) First Storms	Init.	Mat.	Dissi.	Cell. Init.	Cell. O-Top	Cell. Term	Maximum cloud-top area ($\times 10^3$ km^2) $\leq -32^\circ$C	$\leq -52^\circ$C
41	790623	2	-0200	0000	0300	1030	0100	0300	0500	110	167
42	790627	4	-0030	0230	0600	0930	0430	0430	0600	170	233
43	790627	3	-0700	0300	0930	1300	0730	0900	1200	110	198
44	790628	8	-0830	0700	1000	1430	0800	0830	0930	160	235
45	790705	8	-0400	-0030	0630	1000	-0100	0500	0730	180	378
46	790709	3	-0230	0600	0830	1400	0600	0800	1230	110	180
47	790712	9	-0300	0200	0900	1500	0430	0800	0900	210	245
48	790715	8	-0800	0230	0915	1400	0600	0600	1000	310	490
49	790723	2	-0530	0200	0600	1000	0430	0430	0600	100	189
50	790730	7	-0230	0430	0900	1300	0600	0900	1100	230	414
51	790808	6	-0330	0100	0600	1215	0200	0415	0745	135	192
52	790829	6	-0200	0100	0800	1230	0400	0830	1000	210	340
53	790831	6	0300	0515	1015	1830	0800	0900	1000	220	330
54	800602	6	0600	0800	1500	2000	1200	1430	1530	90	240
55	800604	7	-0030	0300	0930	1600	0600	0930	1500	207	345
56	800604	7	-0330	-0030	0800	1600	0600	0800	1200	176	308
57	800605	8	-1100	-0900	-0030	0230	-0800	-0600	0030	132	260
58	800606	8	-0330	-0030	0500	1030	0200	0230	0430	218	419
59	800607	4	-0100	0400	1500	2200	1300	1500	1800	189	510
60	800608	8	-0800	-0400	0100	0430	-0200	0000	0100	265	416
61	800608	7	-0200	0230	0700	2200	0330	0500	0730	140	280
62	800609	7	-1200	-0730	-0500	-0100	-0630	-0600	-0430	120	210
63	800619	7	-0215	0730	1015	1700	0830	0845	1000	220	340
64	800620	6	-0430	0515	1045	2000	0815	0945	1115	300	460
65	800627	8	-0400	0000	0530	0900	0300	0300	0600	323	515
66	800702	1	-0015	0815	2000	2430	1800	1900	2330	126	224
67	800703	7	-0300	-0030	0400	0830	0200	0330	0500	332	489
68	800708	2	-0330	0515	0815	1100	0515	0745	0930	91	173
69	800709	0	-1200	-0500	0300	0900	0000	0300	0500	244	350
70	800709	6	0200	0630	1100	1400	0730	0930	1100	182	300
71	800714	6	-0130	0700	1115	1500	0800	1100	1200	215	344
72	800715	2	-0100	0730	0845	1900	0800	1000	1300	95	154
73	800720	8	-0400	0130	0800	1300	0300	0800	0900	288	523
74	800813	7	-0100	0200	0715	1115	0500	0630	0730	140	280
75	810608	5	-0430	-0100	0445	0830	0400	0500	0530	188	239
76	810610	3	0045	0500	1215	2000	0500	0730	1215	190	237
77	810611	6	0530	0615	1315	1900	1145	1230	1415	290	427
78	810621	1	-0445	0230	1530	1900	9999	9999	9999	188	245
79	810622	8	0430	1030	1800	2815	1030	1315	1615	370	567

Table A.1 Mesoscale Convective Complexes during 1977-1984 (Continued).

Case Number	Date	Rank	Time (GMT) First Storms Init.	Mat.	Dissi.	Cell. Init.	Cell. O-Top	Cell. Term	Maximum cloud-top area ($\times 10^3$ km^2) $\leq -32^\circ$C	$\leq -52^\circ$C
80	810623	7	-0030	0330	0700	1045	0530	0530	0700	210	304
81	810624	7	-1130	-0300	0500	1100	0445	0430	0545	300	504
82	810703	8	-0430	-0200	0400	0900	-0045	0215	0430	265	416
83	810712	6	0200	0500	1030	1630	0900	0830	1100	180	318
84	810713	7	-0445	0130	0630	0930	0430	0500	0700	156	255
85	810714	2	0100	0400	0700	0930	0400	0430	0700	125	206
86	810803	4	-0900	0315	0500	1300	0330	0500	0730	113	300
87	810805	6	-0800	0400	0645	0945	0515	0615	0745	186	309
88	810816	6	-0400	0400	0915	1130	0630	0815	1000	170	255
89	820608	7	0545	1000	1430	2400	1100	1330	2000	191	235
90	820609	6	-1200	-0830	0130	1430	-0200	0100	0330	265	294
91	820610	6	-0315	-0030	0330	0700	0100	0330	0400	197	268
92	820611	3	-0500	-0200	0830	1600	0200	0500	0900	469	733
93	820614	3	-0400	-0100	0930	1730	0800	1100	0930	207	317
94	820615	4	-0600	-0200	0400	1130	0330	0400	0830	390	602
95	820616	3	-0600	0030	0530	0900	0330	0400	0630	196	321
96	820627	5	-0500	-0100	0600	0730	0330	0330	0600	88	135
97	820627	5	-0500	0630	1130	1400	0830	1100	1200	103	188
98	820629	6	-1130	-0300	0215	0430	0045	0130	0300	122	179
99	820630	7	-0330	0030	0500	1200	0200	0400	0600	273	430
100	820702	2	-0345	0100	0330	0630	0100	0200	0330	98	158
101	820705	7	-0200	-0030	0745	1230	0100	0600	0700	329	450
102	820714	4	-0230	0100	0430	0900	0230	0230	0430	123	194
103	820718	6	0330	0530	0830	1630	0600	0630	0800	203	359
104	820719	2	-0100	0330	0730	1130	0330	0530	0700	169	244
105	820725	5	-0145	0230	0415	0930	0330	0230	0445	116	189
106	820805	7	-0200	0300	0700	1030	0300	0430	0730	223	381
107	820815	6	-0200	0445	1000	1500	0700	0930	1200	108	193
108	820827	6	-0230	0130	0630	1200	0430	0500	0830	303	469
109	820830	4	-0230	0230	0600	0900	0230	0500	0730	88	137
110	820831	4	-0300	0115	0530	0900	0330	0500	0730	118	207
111	830611	2	0100	0530	0900	1130	0630	0830	0930	98	165
112	830614	0	-0330	0100	0600	1500	0430	0800	0800	137	173
113	830620	8	0430	0730	1100	1530	0930	1000	1300	191	284
114	830622	5	-0400	0200	0530	1300	0330	0530	0630	219	366
115	830701	7	-0430	0100	1300	1700	0800	1130	1500	238	297
116	830703	6	-0400	0000	0800	1400	0400	0700	0800	168	312
117	830727	7	-0500	0100	0730	1300	0400	0700	0900	153	246
118	830813	2	-0400	-0100	0245	0800	0245	0315	0330	101	180

Table A.1 Mesoscale Convective Complexes during 1977-1984 (Continued).

Case Number	Date	Rank	Time (GMT) First Storms Init.	Mat.	Dissi.	Cell. Init.	Cell. O-Top	Cell. Term	Maximum cloud-top area ($\times 10^3$ km^2) $\leq -32^\circ$C	$\leq -52^\circ$C
119	830816	7	0530	1300	1500	2030	1400	1430	1500	96	221
120	830819	8	-0200	0730	1000	1700	0900	0830	1400	146	234
121	830823	7	-1630	-0900	-0200	0300	-0800	-0100	0030	158	257
122	830823	8	-0400	0030	0700	1330	0530	0700	0800	139	280
123	830826	6	0800	1030	1230	1630	1100	1200	1300	140	192
124	830829	3	-0200	0430	0600	1530	0400	0800	1030	90	192
125	830829	3	-0100	0500	0830	1130	0700	0800	0900	129	219
126	840606	7	-0200	0030	0400	1000	0200	0500	0630	240	370
127	840609	7	-0730	-0030	0530	1000	0230	0600	0730	284	416
128	840614	5	-0330	0200	1200	1430	1000	1100	1300	139	389
129	840615	8	0300	0730	1300	1500	1100	1130	1300	199	320
130	840715	6	-1200	-0300	0300	1000	0100	0300	0400	215	281
131	840716	8	-0600	0000	0330	0700	0200	0200	0400	159	235
132	840808	7	-0600	-0230	0430	0730	0330	0300	0600	176	271
133	840821	5	-0400	0000	0300	1200	0100	0430	0500	205	292
134	840830	5	-0330	-0100	1400	1800	0900	1200	1530	174	260

Consequently, we have chosen to determine the location in addition to the times of occurrence of an individual MCC and to delineate the stages of its life-cycle on the basis of their satellite-defined cloud shield. After MCCs were identified and classified into life-cycle stages, the next step in the compositing procedure was to establish the location of the center of the anvil clouds at each analysis time. This step begins by identifying the analysis grid point nearest the "center of mass" of the anvil clouds.

The centroid position at 3-hour intervals of 134 MCC cases are tabulated for an eight-years period (1977-1984) in Table A.2. The data format used in Table A.2 is listed as follows:

NN YYMMDD SSSS EEEE K IIFF UUUuuu VVVvvv WWWwww XXXxxx YYYyyy ZZZzzz

where the data format symbol have the following definitions:

NN: case numbered of the MCC

YY: year of the MCC

MM: month of the MCC

DD: day of the MCC

SSSS: time of occurrence of the first thunderstorm (GMT)

EEEE: time of occurrence of the MCC dissipation stage (GMT)

K: index of continuation (1 for the first line of centroid position of an MCC case, 2 for the second line of same MCC case)

II: first time of MCC position (GMT) for this line

FF: final time of MCC position (GMT) for this line

UUU: latitude of MCC centroid at time II (tenths of degree)

uuu: longitude of MCC centroid at time II (tenths of degree, omit hundreds 1 if west of 100 ^{o} W)

VVV: latitude of MCC centroid at time II + 3

vvv: longitude of MCC centroid at time II + 3

WWW: latitude of MCC centroid at time II + 6

www: longitude of MCC centroid at time II + 6

XXX: latitude of MCC centroid at time II + 9

xxx: longitude of MCC centroid at time II + 9

YYY: latitude of MCC centroid at time II + 12

yyy: longitude of MCC centroid at time II + 12

ZZZ: latitude of MCC centroid at time II + 15

zzz: longitude of MCC centroid at time II + 15

Table A.2 MCC centroid position at 3-hour intervals for period 1977-1984.

NN	YYMMDD	SSSS	EEEE	K	IIFF	UUUuuu	VVVvvv	WWWwww	XXXxxx	YYYyyy	ZZZzzz
1	770804	-0400	1530	1	2112	424050	420020	412000	402980	397954	395937
1	770804	-0400	1530	2	1518	394920	400892				
2	770805	-0600	1630	1	0015	382036	386023	392993	390975	399950	414938
2	770805	-0600	1630	2	1821	423894	428865				
3	770806	-0800	1330	1	2112	380039	376023	381013	390986	400945	407911
3	770806	-0800	1330	2	1518	409863	420796				
4	770807	-0900	0430	1	1506	398947	399931	400905	403885	400862	403824
5	770807	-0300	1230	1	2112	395045	396033	396023	395013	394000	404967
5	770807	-0300	1230	2	1515	400955					
6	770807	0300	1700	1	0318	403950	411918	414896	411881	396893	391881
6	770807	0300	1700	2	2121	386866					
7	770808	0300	1800	1	0318	431928	428916	426888	416882	415896	405897
8	770809	-0400	1000	1	2112	402958	398938	395926	394906	385890	374890
9	770809	0130	1500	1	0318	436976	434940	423948	420929	406928	406926
10	770809	-0600	1100	1	0015	379030	370019	370014	358014	347008	340000
11	770810	-0600	0730	1	1809	362052	364039	342025	342022	344018	340006
11	770810	-0600	0730	2	1212	335990					
12	780614	-0430	1400	1	0015	446022	447002	449983	451970	458956	464941
12	780614	-0430	1400	2	1818	470928					
13	780620	-0430	1300	1	1809	379023	389998	399971	403955	408936	408925
13	780620	-0430	1300	2	1218	408913	408899	407887			
14	780624	-0600	0800	1	1809	416048	424037	423020	423999	420989	414969
14	780624	-0600	0800	2	1212	404945					
15	780625	-0100	0730	1	2109	429000	433977	435956	435948	437928	
16	780625	-0300	1300	1	2112	397048	402027	405010	415990	437982	438957
16	780625	-0300	1300	2	1515	440933					
17	780630	-0600	1100	1	1809	435040	445030	454016	460990	459972	462971
17	780630	-0600	1100	2	1215	461960	457947				
18	780701	-0400	1000	1	2112	452950	452938	447912	444907	436897	430887
19	780702	-0500	1030	1	2112	413937	415920	410907	403904	398899	388888
20	780704	-0400	1700	1	0015	474107	471088	481065	489042	493009	491981
20	780704	-0400	1700	2	1818	501947					
21	780706	-0530	0800	1	1809	440975	448963	443952	444938	444927	438901
21	780706	-0530	0800	2	1212	444881					
22	780706	0100	1330	1	0315	418050	424041	426035	440009	444988	
22	780706	0100	1330	1	0315	418050	424041	426035	440009	444988	
23	780709	-0400	1130	1	0015	402970	403953	404934	400891	401866	392852
24	780713	0130	1600	1	0318	414893	413882	402869	390860	380853	375840
25	780715	-0700	0830	1	2112	400943	393928	385920	373904	353912	330920
26	780720	-0300	1200	1	2112	392045	393030	394019	406997	414979	414951
26	780720	-0300	1200	2	1515	418937					
27	780721	-1200	0100	1	1506	415937	419921	432897	427860	427850	425846
28	780721	-0530	1200	1	2112	389041	393027	404010	419997	436979	438942
28	780721	-0530	1200	2	1515	440929					
29	780722	-0430	1000	1	2112	401992	404985	408973	411963	390967	374968

Table A.2 MCC centroid position at 3-hour intervals for period 1977-1984 (Continued).

NN	YYMMDD	SSSS	EEEE	K	IIFF	UUUuuu	VVVvvv	WWWwww	XXXxxx	YYYyyy	ZZZzzz
30	780817	0100	1800	1	0318	399978	400967	400953	413908	409886	396882
30	780817	0100	1800	2	2121	384879					
31	780818	-0700	0800	1	2112	470960	475942	482930	480918	498880	506843
32	780823	-0600	0830	1	1809	470980	472964	475925	471913	465881	457852
32	780823	-0600	0830	2	1212	454840					
33	780823	-0430	1600	1	2112	442020	456007	462994	473967	473935	461902
33	780823	-0430	1600	2	1518	462871	455861				
34	780824	-0630	0900	1	2112	456914	456904	450900	450890	434871	425853
35	780826	-1200	0930	1	1809	497035	497025	500010	494000	488988	479943
35	780826	-1200	0930	2	1212	463917					
36	790616	-0400	0830	1	2112	405043	403028	396008	392987	396967	407954
37	790616	-0400	2700	1	2112	437060	442038	438018	433002	443983	446966
37	790616	-0400	2700	2	1506	460951	467930	463906	460886	448865	440846
38	790619	0030	1930	1	0621	428025	447995	461971	465955	473943	482910
38	790619	0030	1930	2	0000	485875					
39	790622	-0430	1200	1	2112	407996	404990	398972	393946	384958	387950
39	790622	-0430	1200	2	1515	380920					
40	790623	-0430	0630	1	2109	357004	353998	352992	347987	338980	
41	790623	-0200	1030	1	2112	370010	374985	373965	374950	362933	367919
42	790627	-0030	0930	1	0012	421013	423001	425998	423987	420970	
43	790627	-0700	1300	1	0015	437918	429920	423924	414928	405922	395926
44	790628	-0830	1430	1	0318	424011	402981	406968	393955	379943	374930
45	790705	-0400	1000	1	2112	398990	399982	397967	391955	391934	386912
46	790709	-0230	1400	1	0318	384030	383020	378008	364997	355993	357991
47	790712	-0300	1500	1	2112	443038	450022	450011	454988	456980	457960
47	790712	-0300	1500	2	1518	455940	457935				
48	790715	-0800	1400	1	2112	445008	435988	426987	412964	410955	397960
48	790715	-0800	1400	2	1518	386957	383961				
49	790723	-0530	1000	1	0012	387002	385994	383990	378986	374980	
50	790730	-0230	1300	1	0015	391008	400987	419962	436921	430897	424869
51	790808	-0330	1215	1	2112	447051	447024	444020	443010	443986	443955
51	790808	-0330	1215	2	1515	442920					
52	790829	-0200	1230	1	2112	413964	416948	413940	404938	394934	387933
52	790829	-0200	1230	2	1515	373928					
53	790831	0300	1830	1	0318	486990	489982	492953	487936	483905	474876
53	790831	0300	1830	2	2121	465863					
54	800602	0600	2000	1	0621	396002	410974	412941	414896	410860	400834
54	800602	0600	2000	2	0000	390800					
55	800604	-0030	1600	1	0015	413982	415968	420950	425935	416913	400888
55	800604	-0030	1600	2	1818	397870					
56	800604	-0330	1600	1	2112	472040	482030	484010	483995	487980	480972
56	800604	-0330	1600	2	1518	472960	473919				
57	800605	-1100	0230	1	1203	460990	458976	457967	448950	446930	440910
57	800605	-1100	0230	2	0606	442885					

Table A.2 MCC centroid position at 3-hour intervals for period 1977-1984 (Continued).

NN	YYMMDD	SSSS	EEEE	K	IIFF	UUUuuu	VVVvvv	WWWwww	XXXxxx	YYYyyy	ZZZzzz
58	800606	-0330	1030	1	2112	456950	459934	448902	445885	442844	444810
58	800606	-0330	1030	2	1515	446785					
59	800607	-0100	2200	1	0015	440010	441978	433955	430925	430903	427861
59	800607	-0100	2200	2	1800	415836	408802	390780			
60	800608	-0800	0430	1	1809	418893	413868	405841	385841	380812	375780
61	800608	-0200	2200	1	0015	323025	323021	329015	338996	345978	342958
61	800608	-0200	2200	2	1800	338934	334925	322908			
62	800609	-1200	-0100	1	1203	311045	313036	314025	317019	319992	323976
63	800619	-0215	1700	1	0015	375018	377000	376971	363952	353937	340920
63	800619	-0215	1700	2	1821	325918	308915				
64	800620	-0430	2000	1	0015	344006	354990	349963	348955	345940	333938
64	800620	-0430	2000	2	1800	325934	310935	300930			
65	800627	-0400	0900	1	2112	437007	445000	448985	452960	445941	442915
66	800702	-0015	2430	1	0621	405998	406987	407959	403936	395923	383914
66	800702	-0015	2430	2	0003	371903	362888				
67	800703	-0300	0830	1	0621	405998	406987	407959	403936	395923	377885
67	800703	-0300	0830	2	0012	381875	378847	376826	380802	410780	
68	800708	-0330	1100	1	0315	408038	419032	428024	436993	443974	
69	800709	-1200	0900	1	1506	415800	406810	395798	384805	375808	369814
69	800709	-1200	0900	2	0912	360770	350740				
70	800709	0200	1400	1	0318	435948	432928	430910	424888	414842	408824
71	800714	-0130	1500	1	0318	443987	462958	470930	472882	470846	467806
72	800715	-0100	1900	1	0318	399998	410983	426956	439924	446885	441848
72	800715	-0100	1900	2	2121	437802					
73	800720	-0400	1300	1	2112	423982	433952	443920	447900	448862	452824
73	800720	-0400	1300	2	1515	452788					
74	800813	-0100	1115	1	0015	454978	447948	445933	441921	440900	437880
75	810608	-0430	0830	1	2112	415935	416919	413910	403907	395900	392880
76	810610	0045	2000	1	0318	393948	386942	379930	374921	372927	374919
76	810610	0045	2000	2	2100	376927	382929				
77	810611	0530	1900	1	0318	383941	381931	386930	389955	387944	390910
77	810611	0530	1900	2	2121	391892					
78	810621	-0445	1900	1	1809	430045	416016	409001	410987	407978	405965
78	810621	-0445	1900	2	1221	400935	403930	404905	403875		
79	810622	0430	2815	1	0621	389016	387994	382968	381951	374942	368898
79	810622	0430	2815	2	0006	362860	362837	363822			
80	810623	-0030	1045	1	0015	356018	354024	343032	339042	327053	318063
81	810624	-1130	1100	1	1809	451948	444935	440930	435925	430918	412892
81	810624	-1130	1100	2	1215	404867	393852				
82	810703	-0430	0900	1	1809	401015	400013	403000	397997	388995	374984
82	810703	-0430	0900	2	1212	364977					
83	810712	0200	1630	1	0015	462050	463037	465020	466995	463968	464941
83	810712	0200	1630	2	1821	463922	460908				

Table A.2 MCC centroid position at 3-hour intervals for period 1977-1984 (Continued).

NN	YYMMDD	SSSS	EEEE	K	IIFF	UUUuuu	VVVvvv	WWWwww	XXXxxx	YYYyyy	ZZZzzz
84	810713	-0445	0930	1	2112	414061	422058	422050	425044	440023	447014
85	810714	0100	0930	1	0012	453012	463992	469981	473962	472942	
86	810803	-0900	1300	1	0015	472068	464041	462011	453993	447964	442935
87	810805	-0800	0945	1	2112	433994	426987	420977	414965	410950	406935
88	810816	-0400	1130	1	2112	370006	368999	359992	358982	356972	353961
88	810816	-0400	1130	2	1515	350938					
89	820608	0545	2400	1	0621	382960	393939	396921	395890	391868	386842
89	820608	0545	2400	2	0003	380800	360780				
90	820609	-1200	1430	1	1203	407978	413957	410946	413932	412920	408912
90	820609	-1200	1430	2	0618	404935	408924	401920	383908	373895	
91	820610	-0315	0700	1	2112	359963	360940	367919	367899	368870	373845
92	820611	-0500	1600	1	1809	305062	313049	319037	337018	352998	364978
92	820611	-0500	1600	2	1218	373950	374929	373904			
93	820614	-0400	1730	1	2112	442065	442041	444027	436003	440997	436976
93	820614	-0400	1730	2	1521	430962	430938	423911			
94	820615	-0600	1130	1	1809	403048	405030	413994	411975	417933	423907
94	820615	-0600	1130	2	1215	420857	420825				
95	820616	-0600	0900	1	1809	335984	339963	346955	346939	347920	334920
95	820616	-0600	0900	2	1212	335903					
96	820627	-0500	0730	1	2109	332012	324005	317984	310970	310960	
97	820627	-0500	1400	1	2112	356041	347033	343030	333014	328001	324991
97	820627	-0500	1400	2	1518	316980	310963				
98	820629	-1130	0430	1	1506	332952	328947	326951	326957	315950	320940
98	820629	-1130	0430	2	0909	310930					
99	820630	-0330	1200	1	2112	415044	418032	420019	418004	407003	400990
99	820630	-0330	1200	2	1515	397972					
100	820702	-0345	0630	1	2109	397998	401991	404981	405971	413973	
101	820705	-0200	1230	1	2112	462003	476990	488963	491940	497927	504920
102	820714	-0230	0900	1	2112	371024	373015	373997	371993	361996	354987
103	820718	0330	1630	1	0318	423964	426942	425915	414903	405901	396894
103	820718	0330	1630	2	2121	383891					
104	820719	-0100	1130	1	0015	407930	410910	408895	405864	392857	382848
105	820725	-0145	0930	1	0012	436058	449046	458029	464001	464969	
106	820805	-0200	1030	1	0015	414958	415945	415937	413917	402900	392887
107	820815	-0200	1500	1	0015	382978	389958	394939	384918	375909	363903
107	820815	-0200	1500	2	1818	350904					
108	820827	-0230	1200	1	2112	387949	389932	391921	384903	378873	376833
108	820827	-0230	1200	2	1515	370810					
109	820830	-0230	0900	1	2112	387003	379989	377977	371975	366963	363957
110	820831	-0300	0900	1	2112	398030	402009	402998	403981	405961	410939
111	830611	0100	1130	1	0315	365020	360011	354998	354976	354954	
112	830614	-0330	1500	1	2112	358990	357975	349971	343972	340965	340953
112	830614	-0330	1500	2	1518	330962	318952				

Table A.2 MCC centroid position at 3-hour intervals for period 1977-1984 (Continued).

NN	YYMMDD	SSSS	EEEE	K	IIFF	UUUuuu	VVVvvv	WWWwww	XXXxxx	YYYyyy	ZZZzzz
113	830620	0430	1530	1	0318	446990	442973	438966	438954	430940	432919
114	830622	-0400	1300	1	2112	459041	464008	476994	486950	493960	499908
114	830622	-0400	1300	2	1515	502860					
115	830701	-0430	1700	1	2112	437056	446026	449006	446980	440949	435918
115	830701	-0430	1700	2	1521	430890	419857	415830			
116	830703	-0400	1400	1	2112	458999	468983	474960	479930	478875	473862
116	830703	-0400	1400	2	1518	467838	464819				
117	830727	-0500	1300	1	2112	414032	421014	420001	423992	426976	480950
117	830727	-0500	1300	2	1515	481910					
118	830813	-0400	0800	1	2112	345922	340929	341940	343958	343970	345993
119	830816	0530	2030	1	0900	453020	454001	461979	463943	457920	449902
120	830819	-0200	1700	1	0015	478975	482960	481940	482885	473845	463827
120	830819	-0200	1700	2	1821	449804	435789				
121	830823	-1630	0300	1	1203	412963	413950	411940	404915	390896	389879
121	830823	-1630	0300	2	0606	385860					
122	830823	-0400	1330	1	2112	403048	415030	423014	416997	414979	411961
122	830823	-0400	1330	2	1515	404938					
123	830826	0800	1630	1	0618	450962	450940	451917	440890	429863	
124	830829	-0200	1530	1	0015	489062	493036	500020	498992	492961	484920
125	830829	-0100	1130	1	0315	469948	462946	463933	469922	470907	
126	840606	-0200	1000	1	0012	412997	437986	466966	477938	487917	
127	840609	-0730	1000	1	2112	384963	387969	395963	403950	411933	413923
128	840614	-0330	1430	1	0015	460072	467058	469039	470012	462983	464960
128	840614	-0330	1430	2	1818	459934					
129	840615	0300	1500	1	0318	431038	448036	455013	463977	458951	464925
130	840715	-1200	1000	1	1809	447946	435927	424915	412910	408906	400890
130	840715	-1200	1000	2	1215	387867	382842				
131	840716	-0600	0700	1	2109	364050	375036	378020	378003	392978	
132	840808	-0600	0730	1	1809	435954	435946	438928	438908	432889	427858
133	840821	-0400	1200	1	2112	406011	410999	414993	407982	400970	399958
133	840821	-0400	1200	2	1515	400939					
134	840830	-0330	1800	1	2112	446906	450890	453862	447843	440830	429819
134	840830	-0330	1800	2	1521	418808	404805	394794			

APPENDIX B. COMPARISON OF THE IMPACTS OF COORDINATE ROTATION, SYSTEM STRENGTH, AND SYSTEM-RELATIVE FLOW ON MCCS

In this section, the differences between the composite pairs constructed for 1) with and without rotation, 2) organized MCCs and marginal MCCs, and 3) with and without relative flow are discussed. What might be termed "control case", the composite MCC which has already been discussed in this chapter, is the organized MCCs sample for the period 1977-1983 analyzed in rotated but ground-referenced coordinate.

B.1 Comparison between rotated and non-rotated composites

The results of the coordinate rotated composite MCC (as control case) have been discussed in detail in the previous sections, therefore it is appropriate to address only the major differences between the rotated and non-rotated composites. To save space, figures for these calculations are not shown. Because the coordinate system used in the rotated case has been rotated according to the direction of the MCC track (which is more or less equivalent to the direction of the mid-level steering flow), the thermodynamic fields are not affected with regard to the rotation. Thus, the distribution of CAPE and the bulk Richardson number patterns in the non-rotated case are similar to those composites for the rotated case. The flux convergence available moist static energy (FCE) patterns resemble each other but the magnitude of non-rotated case is greater, reflecting that the low-level wind is more sensitive to the MCC movement. In essence, the genesis potential of

vorticity possesses a greater value of 6.7 X 10^{-5} s^{-1} for the non-rotated case at MCC maturity due to the stronger upper-level anticyclonic vorticity (upper-level winds in the rotated cases have smaller horizontal wind shear of $\partial u/\partial y$ term).

For the non-rotated case, the temperature advection field illustrates that warm advection prevail at MCC maturity over the boundary layer and reaches a maximum of 25.2°C X 10^{-5} s^{-1} at the MCC decay stage. However, the moisture advection field indicates that there is no dry advection in the non-rotated case at the MCC mature stage in the extreme low level instead of a lagging maximum of 34.6 X 10^{-6}g kg^{-1} s^{-1} at the decay stage. Again, the comparisons of temperature and moisture advection indicate the low-level winds are sensitive to the rotation; therefore the cold and dry advections at the MCC mature stages can be clearly addressed by the rotated case. Comparison of the u-component change fields indicates that the increase of mid-level "jet-like" inflow at the growth stage reduces to 3 m s^{-1} (compared to 4.4 m s^{-1}), and the v-component change indicates no significant variations between the two cases, implying that the MCC track (or mean steering flow) is more or less parallel to the east-west direction.

The divergence field for the non-rotated case is weaker at the mature stage and exhibits its maximum value later at the dissipation stage. The divergence field also exhibits a single lower level convergence zone without mid-level convergence. Consequently, the mid-level positive cyclonic center is absent due to the lack of mid-level convergence, but the upper-level anticyclonic vorticity maximum has intensified, reflecting that the upper-level flow is modulated in the rotated case to behave as smaller horizontal wind shear ($\partial u/\partial y$ term) in

the vorticity evaluation. Because of the vertical motion responds to the divergence field, it indicates a weaker downward motion in the extreme low-level at the mature stage for non-rotated case. Nevertheless, the upward motion reaches its maximum value at the mature stage with a much smaller magnitude of only 20 X 10^{-5} mb s^{-1}. In summary, the essential features of the dual mid-level convergence maxima and boundary-layer downdraft can be more clearly addressed by the rotating frame.

B.2 Comparison between the selected MCCs and marginal MCCs

Because the selected MCCs (organized MCCs) were characterized by longer duration, well-organized meso-β convective elements, larger cold cloud shield, and less environmental contamination than the marginal MCCs based on the compilation philosophy, differences obtained from the comparison of the two composites should be attributed to the real influence of the well-organized MCCs which modifies the synoptic background in which the MCC is embedded. The time-height cross-section of mixing ratio (Fig. B.1a vs. Fig. 4.5) shows that the significant moisture increase for the marginal MCCs is confined within the boundary layer until MCC maturity and does not extend over the entire lifetime as it does for the selected MCCs'. The mid-level mixing ratio (Fig. B.1b vs. Fig. 4.10) is monotonically increasing until the mature stage while the smaller magnitude reflects that the energy consumption by deep convection and meso-β convective elements are inefficient in the marginal MCCs case. The moisture advection field (Fig. B.1c vs. Fig. 4.12a) displays a pronounced dry advection at 850 mb level of MCC's maturity in association with the insignificant moist advection elsewhere. The θ_e distribution (Fig. B.1d vs. Fig. 4.6) depicts a

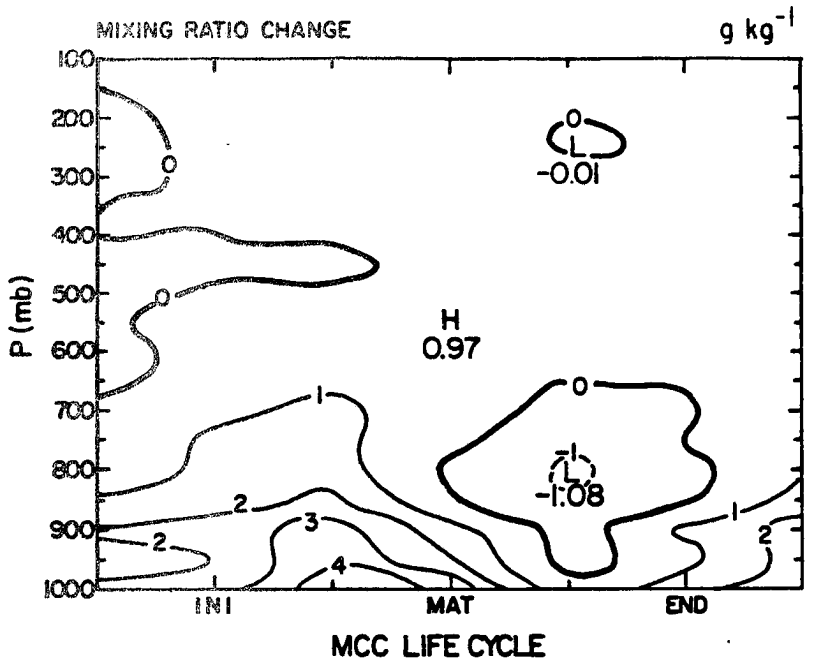

Fig. B.1a. Height-time plot of the mixing ratio difference from its corresponding value at the MCC-12h stage for the marginal case. The mixing ratio field is obtained by applying a 9-grid- point area average over a 6^{o} X 6^{o} lat.-long. domain every 50 mb. Units: g kg^{-1}.

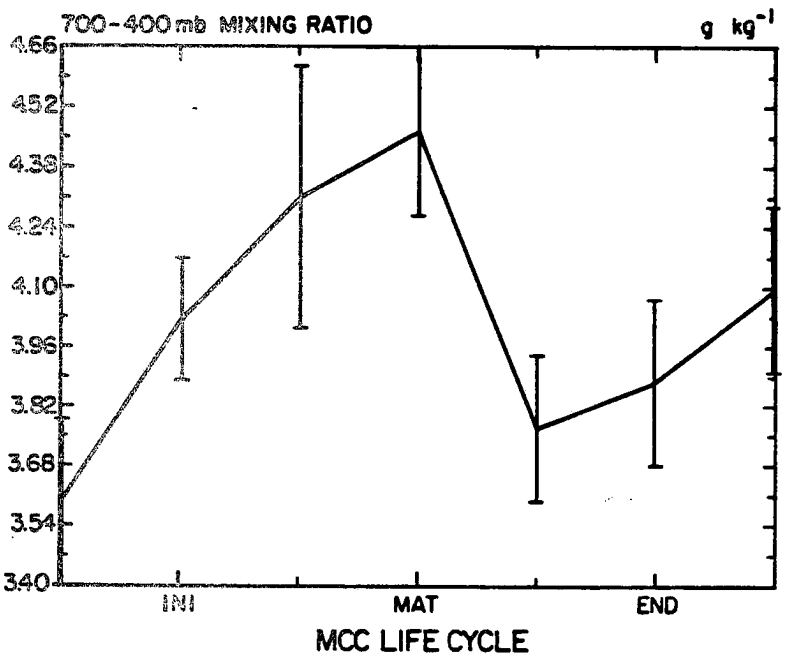

Fig. B.1b. Time evolution plot of the average 700-400 mb layer mixing ratio for the marginal case. The error-bar represents one plus/minus standard deviation of the 9-point average. Units: g kg^{-1}.

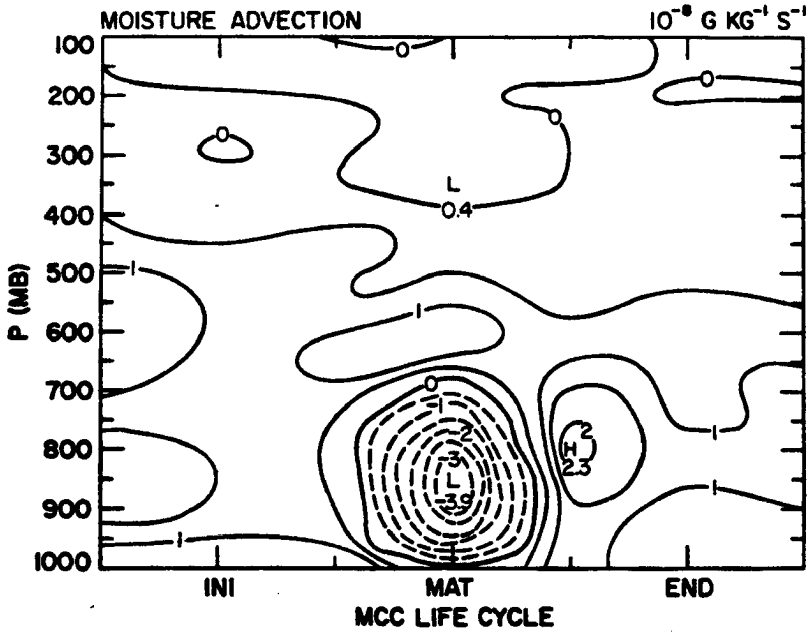

Fig. B.1c. Height-time plot of the moisture advection for the marginal case. The moisture advection field is obtained by applying a 9- grid-point area average over a 6^{o} X 6^{o} lat.-long. domain every 50 mb. Units: 10^{-3} g kg^{-1} s^{-1}.

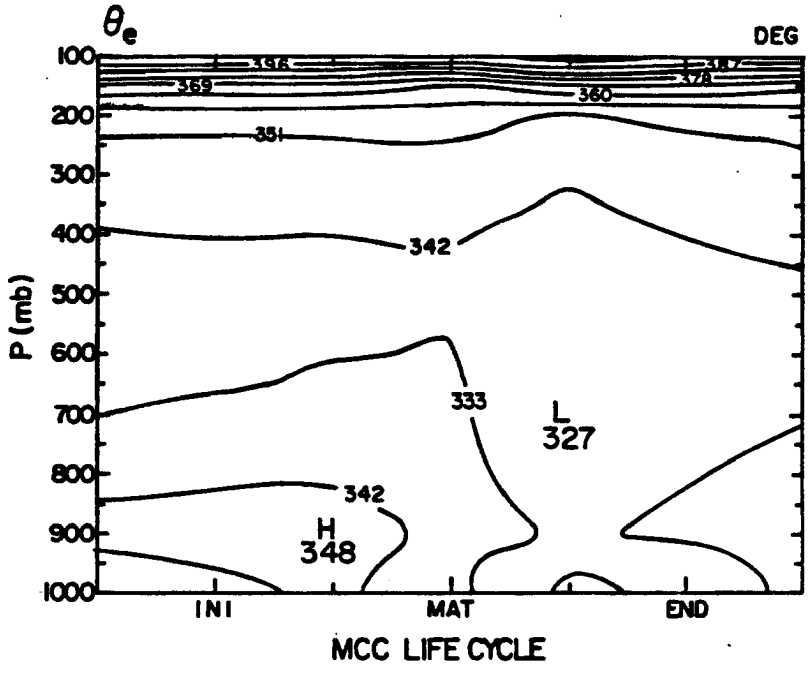

Fig. B.1d. Height-time plot of the equivalent potential temperature (θ_e) for the marginal case. The θ_e field is obtained by applying a 9-grid-point area average over a 6^{o} X 6^{o} lat.-long. domain every 50 mb. Units: K.

minimum value at 700 mb level (compared to 500 mb level for organized MCCs) during the decay stage which is associated with the evaporation process, but the early stage's extremely high θ_e maximum (348 K compared to 340 K for organized MCCs) resides in the boundary layer, implying that the low-level moisture supply is even more favored for marginal MCCs.

The total totals index distribution (not shown) indicates that the potential instability has been released after marginal MCCs initiation and reaches a minimum value at MCC maturity. Because both of the low-level moistening produced by precipitation and the mid-level cooling resulting from the intrusion of low θ_e air are weaker; it is therefore impossible to regenerate the instability during the marginal MCC's mature stage as in the organized MCC's. This fact is supported by the distribution of FCE for marginal MCCs which is smaller in magnitude than for selected MCCs', but it maximizes (negative value of FCE) at the MCC initial stage and reaches a minimum at the mature stage. In fact, the time evolution of CAPE for the marginal case exhibits a persistent high magnitude which is maintained until its growth stage (compared to the pre-MCC stage of the selected cases) and then rapidly tapers off through to the decay stage. This delayed consumption of the potential energy confirms that the deep convection or meso-β convective elements neither occupy the larger portion of marginal MCCs nor are well organized for a long period.

The u-component change (Fig. B.2 vs. Fig. 4.27) shows that the mid-level "jet-like" feature is delayed in its occurrence from the growth stage until the mature stage. The temperature advection field [advected by the full winds not the relative winds (not shown)] exhibits

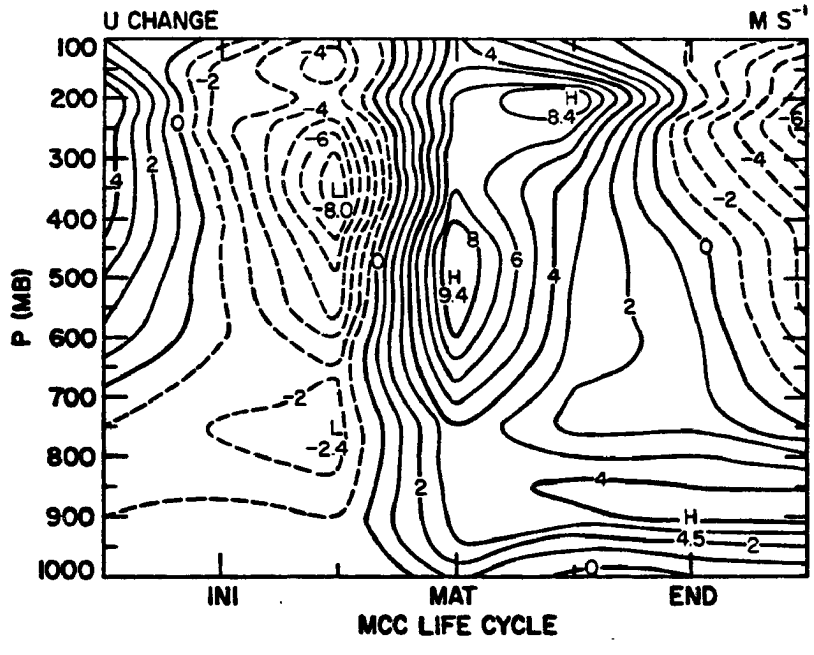

Fig. B.2. Height-time plot of the u-component change compared to its corresponding value at the MCC-12h stage for the marginal case. The wind is obtained by applying a 9-grid-point area average over a 6^{o} X 6^{o} lat.-long. domain every 50 mb. The central point of the 9-point average is located one grid point west of the MCC centroid. Units: m s^{-1}.

that weaker low-level warm advection ($12^{o}C \times 10^{-5}\ s^{-1}$) prevails for marginal MCCs except at the mature stage (offset by weak mesoscale downdraft cooling). This figure also indicates that the warm advection extending to upper levels before the growth stage is associated with a pronounced mid-level cool advection after this stage.

The areally-averaged divergence, areally-averaged vorticity, and areally-averaged vertical motion are illustrated in Figs. B.3a-B.3c (vs. Figs. 4.36a, 4.39a, and 4.43a), respectively for marginal MCCs. The low-level divergence persists after MCC maturity, while the upper-level divergence reaches its maximum intensity at the decay stage earlier and more intensely than for organized MCCs (2.5 versus $1.8 \times 10^{-5}\ s^{-1}$). The striking feature of the vorticity profile for marginal MCCs is the presence of cyclonic vorticity aloft at the growth stage which inhibits the "dynamic flywheel" effect for deep convection. Upper-level cyclonic vorticity advection is responsible for this unfavorable configuration at the growth stage; it implies that certain marginal MCCs may be initiated behind the mid-level trough. The vertical motion field for marginal MCCs depicts the upward motion center lifting from 600 mb (growth stage) to 400 mb level (mature stage). The mesoscale downdraft, however, is not significant enough to be reflected as a net downward motion until the marginal MCCs dissipation stage. These comparisons indicate that selected MCCs are supported by a deeper moist environment and low- to mid-level warm advection which allows convection or meso-β convective elements to be sustained for a longer period. Dynamically, the persistent low-level convergence and cyclonic vorticity associated with upper-level divergence and anticyclonic vorticity provide a flywheel effect for deep convection in the case of organized MCCs.

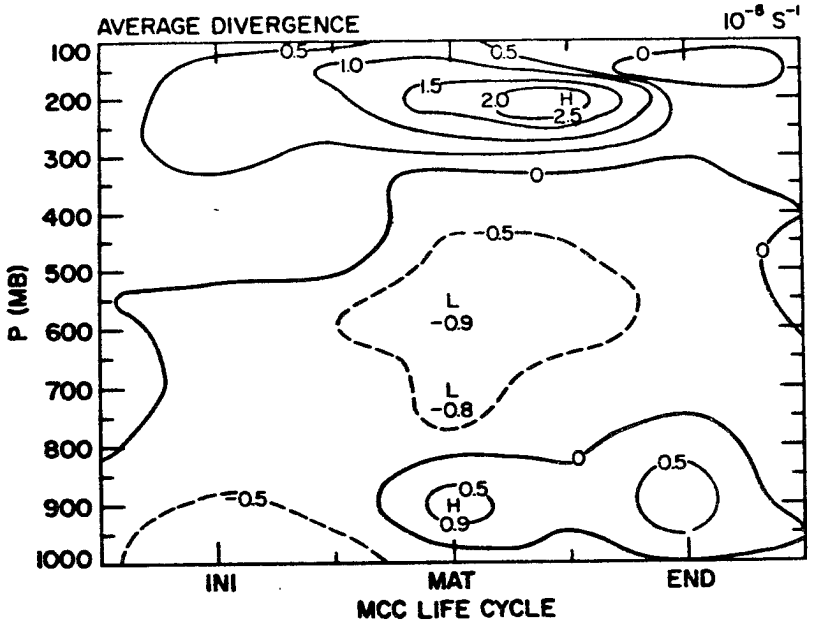

Fig. B.3a. Height-time plot of the mean divergence field for the marginal case. The horizontal coordinates have been rotated along the MCC MCC track so that positive u and v values represent winds from the rear and right flank of the MCC, respectively. The divergence field is obtained by averaging MCC cases every 50 mb for each sub-period. Units: 10^{-5} s^{-1}.

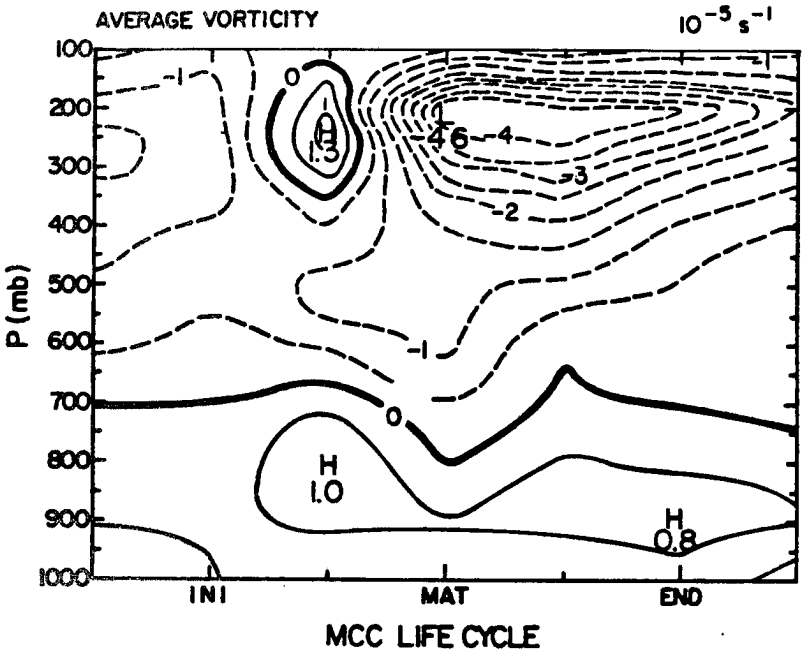

Fig. B.3b. Height-time plot of the mean relative vorticity for the marginal case. The horizontal coordinates have been rotated along the MCC MCC track so that positive u and v values represent winds from the rear and right flank of the MCC, respectively. The vorticity field is obtained by averaging MCC cases every 50 mb for each sub-period. Units: 10^{-5} s^{-1}.

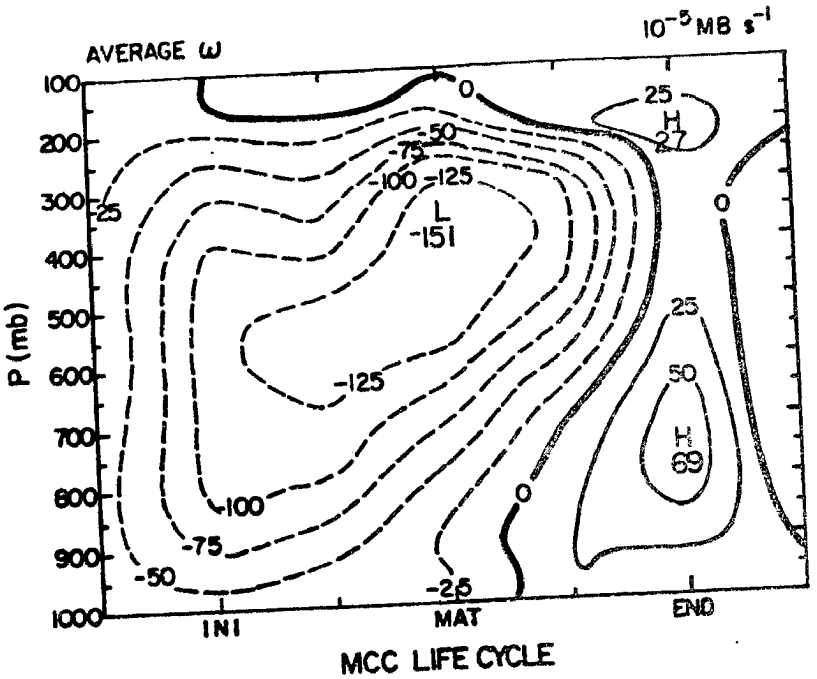

Fig. B.3c. Height-time plot of the vertical motion for the marginal case. The vertical motion field is obtained by applying a 9- grid-point area average over a $6^{\circ} \times 6^{\circ}$ lat.-long. domain every 50 mb. Units: 10^{-5} mb s^{-1}.

B.3 Comparison between ground-relative and system-relative cases

The system-relative case is calculated by subtracting the MCC centroid velocity from the horizontal wind fields. Again, the thermodynamic fields are not affected. For the sake of brevity, the figures will not be displayed. The temperature advection field depicts that the 6-hour oscillation is pronounced over both lower and upper levels but that it exhibits an out-of-phase feature between these two levels. The low-level cool advection (advected by the relative winds) at MCC maturity is as big as $-16^{o}C \times 10^{-5}$ s^{-1}. In fact, the moisture advection field shows that moist advection exclusively occurs in the boundary layer during the early part of MCC life-cycle, reflecting that the low-level relative easterly flow brings moist air towards the MCC centroid before the mature stage.

The relative u-component change shows that the mid-level "jet-like" inflow identified in the selected MCCs is reduced in magnitude from 4.4 m s^{-1} to 2.3 m s^{-1}, implying that the MCC-steering flow is above the level of mid-level "jet-like" inflow. In fact, the relative v-component change exhibits a pronounced 6-hour oscillation feature. However, a value which is 3.4 m s^{-1} larger than the MCC-12h value in the lower troposphere at the MCC decay stage resulting from the LLJ is quite striking. In essence, the system-relative calculation depicts clearly that as the MCC moves, it is always receiving a fresh supply of moist air at low levels from the east during the early MCC life-cycle and in turn is sending a stream of dry air eastward in the upper troposphere, not unlike a mid-latitude squall line.